Prediction of Miscible Fluid-Fluid Displacement in Long Pipelines

B. van Eeden

TU Delft

Prediction of Miscible Fluid-Fluid Displacement in Long Pipelines

by

B. van Eeden

to obtain the degree of Master of Science
at the Delft University of Technology,
to be defended publicly on Tuesday August 6, 2021 at 10:00 AM.

Student number:	4273710	
Project duration:	April 28, 2020 – August 6, 2021	
Thesis committee:	Prof. dr. ir. R.A.W.M. Henkes,	TU Delft, supervisor
	Dr. ir. P.I. Rosen Esquivel,	Shell Projects & Technology, supervisor
	Dr. ir. W.-P. Breugem,	TU Delft

An electronic version of this thesis is available at `http://repository.tudelft.nl/`.

TU Delft

Abstract

In the oil and gas industry it is crucial that the transport of hydrocarbons through long pipelines occurs at the most efficient and safest way. These pipelines can cover up to several tens to hundreds of kilometres. Hydrocarbons are not the only fluids present within the pipelines, often they are filled with a mixture of oil, gas, water and even sand particles. The flow phenomena associated with this multiphase mixture complicate the transport operations of the industry. The operations covered in the present study are: flushing, batch transport and hydrate inhibition.

Simulation techniques exist to reproduce the multiphase flow phenomena. However, three-dimensional Computational Fluid Dynamics (CFD) models require very much computational power and the one-dimensional two-fluid models, such as OLGA and COMPAS, are not capable of capturing all involved flow phenomena. The goal of the present study is to develop a one-dimensional model of high accuracy to reproduce miscible fluid-fluid displacements in long pipelines, in which the focus is on the displacement within the aqueous phase of a multiphase mixture. The model must be able to reproduce slip velocities and gravity currents within this aqueous phase without solving the momentum equations. Furthermore, the model must account for turbulent dispersion, mass transfer, pipeline inclination and differences in thermodynamic properties of the fluids.

Two virtual regions are created in the model in which both fluids can be present. The upper region is associated with the less dense fluid and the lower region is related to the denser fluid. The mass of the regions is tracked by a mass conservation equation. To account for the changes in the concentrations of the fluids in the regions two advection-diffusion equations are solved. These three equations are coupled by exchange terms. The velocity variables are solved by a slip relation between the regions and by a velocity equation derived from the incompressibility condition. All equations are cross-sectionally averaged to ensure the one-dimensionality of the model. To reproduce the appropriate slip interface between the regions several slip relation functions are derived. An empirical relation for the turbulent axial dispersion is implemented in the advection-diffusion equations of the two regions.

The one-dimensional miscible fluid-fluid displacement model is discretised by employing a finite volume method on a staggered grid, by using the Crank-Nicolson time integration and different schemes for the advective terms. The diffusion terms are discretised by the central approximation method. The flow variables are solved by a coupled approach using Picard's method to linearise the nonlinear terms. Moreover, the possibilities of applying Newton's method for linearisation have also been studied. The model is validated by comparing the flow solution of a single-phase advection-diffusion equation to the analytical solution of a turbulent diffusion equation. Even the flow solutions obtained on relative coarse grids turn out to be of high accuracy.

By simulating miscible fluid-fluid displacement cases it is shown that the model is able to reproduce slip velocities and gravity currents under different circumstances. A linear empirical relation for the volumetric transfer terms is derived by matching the numerical simulation results to experimental results and to CFD results of a specific miscible fluid-fluid displacement case. The CFD results were also obtained as a part of this study; thereto the Fluent CFD package was applied. The CFD results were also used to obtain the exchange terms in the one-dimensional flow model.

Acknowledgement

This study is the result of a master thesis assignment performed in collaboration with the Shell Technology centre in Amsterdam and marks the end of my time as a student at Delft University of Technology.

The thesis topic has proven to be challenging and fascinating at the same time. I have learned a lot during the thesis process and it has helped me to realise that I want to pursue a career in the field of fluid mechanics.

I would like to thank my supervisor: Prof. dr. ir. Ruud Henkes who gave me the opportunity to start with this thesis topic. Thanks for providing me with your expertise during the thesis and for challenging me when it was necessary!

Special graditude to my daily supervisor: Dr. ir. Patricio Rosen Esquivel, who often amazed me by the amount of knowledge he has in the fluid mechanics discipline. Thanks for the brainstorming sessions, guiding me towards the end, and the time you made free for me! Maybe we can keep practising your Dutch in the future!

Thanks to my friends who have let me blow off some steam during the Vrijmibo's, the cycling trips, the driving range sessings and the walks in this turbulent year!

A special thanks to my roommates: Marijn, Max and Zhouxin, who had to face me during my whole thesis journey at home. Thank you guys for letting me ventilate my thoughts and your support when I needed it, and most importantly, thanks for the Fika Tuesdays, the Hika Thursdays and the cool trips we made!

I am profoundly grateful to my parents: Anita and Richard, who have supported me no matter what I did! Thanks for the freedom to make my own choices (and my own mistakes) during my time as a student! Thanks for the amazing start you gave me in life!

In particular I would like to thank my girlfriend: Esther, who showed me that there is more in life than a master thesis. Thanks for the infinite amount of support you gave me and for disallowing me to bring my laptop on our holidays!

Thanks to everybody who have made my time as a student so much fun!

Looking forward to what the future will bring!

B. van Eeden
Rotterdam, 14 July 2021

Contents

List of Figures

List of Tables

1 Introduction

Multiphase flow is defined as flow that consists of multiple distinct phases. Such flow is seen everywhere in the world, on large nature scales in oceans and the atmosphere, to smaller scales, like estuaries where the sweet river meets the salt sea. These flowa in the oceans and atmosphere are examples of miscible flows, whereas multiphase flow normally refers to immiscible flows. In the industry, multiphase flow is observed in numerous processes of which petrochemical operations are most relevant for this study. Hydrocarbons are transported in pipelines ranging from several tens to hundreds of kilometers in lengths, both onshore well as offshore. These pipelines are filled with a mixture of oil and gas and frequently include water and sand particles. The simplest form of multiphase flow is a mixture of only two distinct phases, e.g. gas and oil. This is referred to as two-phase flow. A water-oil mixture is another example of two-phase flow.

The transportation of the hydrocarbons comes with various physics, safety and economics related challenges. The present study focusses on the challenges of modelling fluid-fluid displacement operations in pipelines, including: flushing, batch transport and hydrate inhibition.

A pipeline fluid-fluid displacement operation is an operation in which a fluid A (present in the pipeline) is displaced by another fluid B (which is introduced into the pipeline). Fluid-fluid operations operations can involve more than two fluids. While fluid B is displacing fluid A in the pipeline, the fluids can either mix into one another (these fluids are charaterised as miscible fluids), or not dissolve into one another (being immiscible fluids). For example, methanol and water are fully miscible, whereas water and oil are immiscible. The mixing region between the two fluids is called the contamination zone. The behaviour of this zone is dependent on the miscibility of the flow, the difference in thermodynamic properties between the two fluids, the pipe geometry (think of the pipe diameter and possible pipe inclinations) and the volumetric flow rate. The mixing region will change in space and time. This illustrates that the flow phenomena in the contamination zones can become very complex, as it depends on a wide range of variables. In immiscible flow, a finite interfacial tension is present between both fluids. This indicates that the mixing at molecular level will not take place between the fluids [15].

1.1. Flushing

Flushing is a common pipeline operation in oil and gas industry. For example, flushing is done after maintenance of the pipeline. After the maintenance, in order to restart the pipeline's function, it is crucial that a pressure test is carried out within the pipeline. In order to do so, all remaining oil has to be removed. One option for removing the oil is to flush the pipeline with water [7]. The displacement of oil by water is an immiscible process; i.e. the fluids do not mix. Due to the density difference between the fluids, a light oil tend to float on top of the water. The different thermodynamic properties of the fluids and the interactions at their interfaces initiate complex physical flow phenomena. A density difference induces buoyancy effects, e.g. gravity currents in horizontal pipe sections. The scaling of the forces acting on two-phase flow is explained in Section 2.5.

It is illustrative to consider how these flow phenomena initiate and evolve in two classic examples. These examples involve two-phase flow in a horizontal and vertical pipe section. In Fig. 1.1 (a) and (c) a horizontal and vertical pipe sections are displayed. Both sections are filled with water (turquoise) and oil (yellow). ρ_W and ρ_O indicate the densities of the water and the oil, respectively. The figures shows the configuration for the case in which the density of water is larger than the density of oil namely $\rho_W > \rho_O$.

Initially the flow are stagnant, and the water and oil are separated by a diaphragm. The water is placed next to the oil in the horizontal section and the water is on top of the oil in the vertical section. When the diaphragm is removed, the density difference will cause the fluids to move under the influence of gravitational acceleration [24].

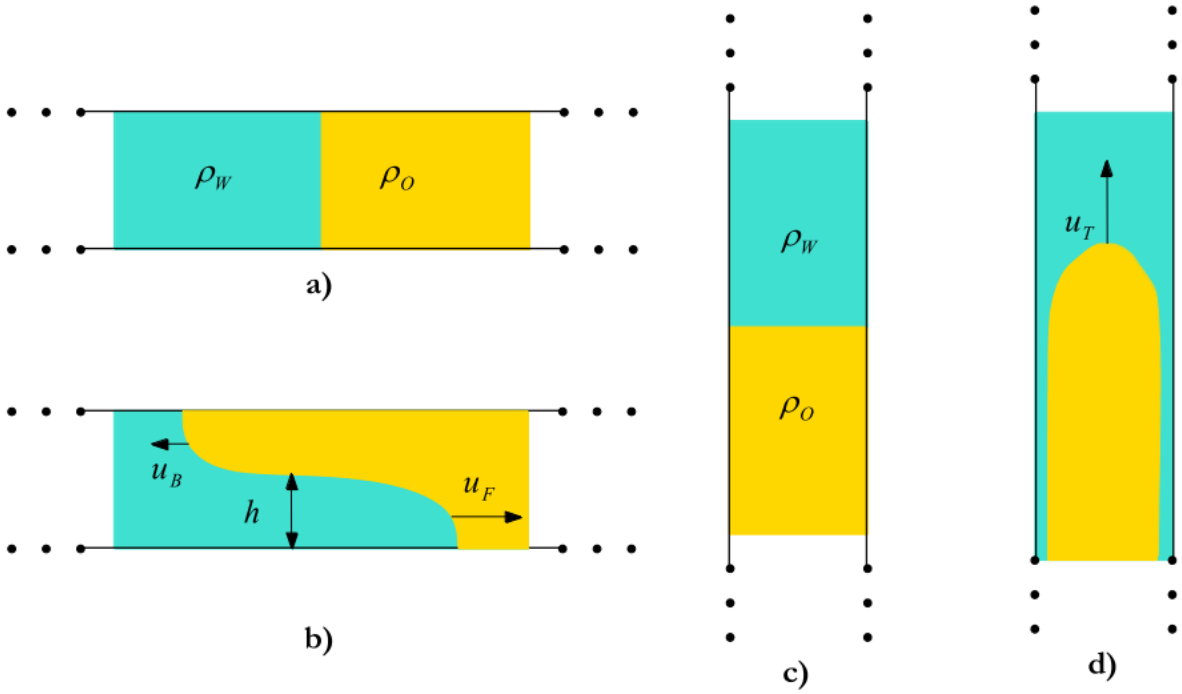

Figure 1.1: Horizontal and vertical pipe sections are filled with water and oil which are separated by a diaphragm. The water is coloured turquoise and the oil is given the colour ocher yellow. The density of water is larger than the density of oil, $\rho_W > \rho_O$, which initiates a motion when the diaphragma in (a) and (c) are removed. The Benjamin bubble is seen in (b) and in (d) the Taylor bubble is observed. The Benjamin and Taylor bubble velocity are denoted by u_B and u_T, respectively. h indicates the interface height and u_F is the velocity of the front of the water bubble [24].

For the horizontal pipe section, the gravity acts in the transverse direction. When the diaphragm is removed, an unbalance in the hydrostatic pressures is created at the interface due to the density difference. This results in water flowing under the oil, giving rise to the development of a waterfront. The oil moves in the opposite direction and starts to creep over the water, as illustrated in Fig. 1.1 (b). This type of movement initiated in a horizontal section is called a gravity current. The elongated bubble motion that arises is named the Benjamin bubble [5].

In the vertical pipe section, buoyancy forces cause the oil to move upwards, as the gravitational acceleration acts in the axial direction of the pipe. This movement is illustrated in Fig. 1.1 (d). A large elongated oil bubble rises in the pipeline segment in the form of a bullet. This type of bubble motion is named Taylor bubble [31]. The Taylor bubble fills almost the entire section when moving upwards. Eventually, the fluids in both sections will reach an equilibrium position, in which the oil will float on top of the water.

This illustrates the impact that pipe inclination can have on the flow. The formation of a bubble in an inclined pipe will feature both mechanisms; the Benjamin and Taylor bubbles. A bubble in an inclined pipe section will form a similar bubble. In Section 2.4 the mathematical relations of the Benjamin and Taylor bubble velocities will be described and explained. Similarly an expression for the bubble velocity in the case of an inclined pipe will be introduced.

Consider the V-shape pipeline sections depicted in Fig. 1.2 (a) and (b). Again, the water is depicted turquoise and the oil yellow. The flushing takes place from left to right. Initially, the pipeline is completely filled with oil. The goal of the flushing operations is to remove all oil and replace it with water. As the oil is present in an inclined pipe, both the Benjamin and the Taylor bubble mechanisms will contribute to the motion of the oil bubble. The flow of the oil bubble can work either in favour or against the flushing operation. As $\rho_W > \rho_O$, the oil bubble will oppose the flushing in the downward-inclined section, whereas it will facilitate flushing in the upward-inclined section.

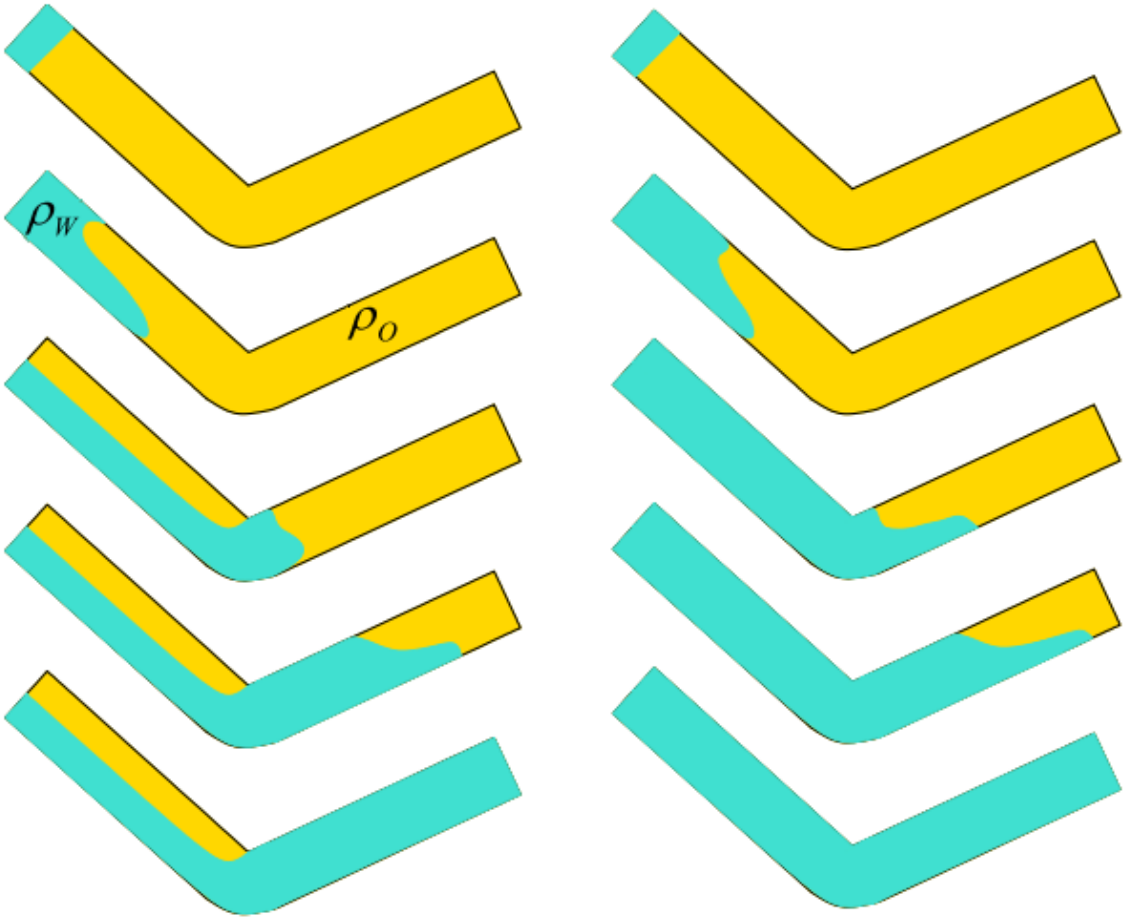

(a) Low volumetric flow rate of water

(b) High volumetric flow rate of water

Figure 1.2: A V-shape pipeline is completely filled with oil which is about to get flushed out by water. Flow is from left to right, water is turquoise and the oil is yellow. Situation (a) illustrates the effect of the oil bubble when the volumetric flow rate of water is not high enough to overcome the oil bubble velocity. The oil gets trapped in the downward-inclined section. In contrast to this, the oil gets flushed in the upward-inclined section due to the help of buoyancy. In situation (b) the volumetric flow rate of water is increased and is now able to overcome the oil bubble velocity. All oil is flushed out of the pipe section [24].

Fig. 1.2 (a) depicts the behavior for the case of a relatively low volumetric flow rate. The entrance of water generates the motion of the oil bubble. The velocity of the oil bubble is higher than the inlet velocity of the water. As a result, the oil bubble moves upwards in the downward-inclined section and the water flows underneath the bubble. The oil has formed a layer inside the section. At this volumetric flow rate, the water is not able to overcome oil-bubble velocity and the oil bubble remains trapped in the pipe section. Fig. 1.2 (b) shows the situation for a larger water volumetric flow rate. The flat interface at the start of the flushing process starts to deform and is pushed down. Though, in this case, the water flushing velocity is high enough to flush out all oil of the downward-inclined section. The water flushing velocity has overcome the oil bubble velocity. When the water reaches the upward-inclined section, it is seen that regardless of the volumetric flow rate of the water, the water is able to push out the oil as buoyancy acts in favor of the flushing operations. The interface between the water and oil is certainly not flat due to the oil bubble. The pipe inclination angle is thus a very important parameter when flushing fluids with dissimilar densities [24].

1.2. Batch transport

In the oil and gas industry, it is possible that dissimilar hydrocarbons are sent in batches through the pipelines by its operator. This is called a batch transport. For example, the transportation of the gasses, methane and propane, or the fuels, diesel and kerosene.

When two miscible fluids are transported one after the other through the same pipeline, a zone of mixed fluids is formed. Pure fluids are only observed far away from the mixing zone in the pipeline. If this type of fluids are brought together, they automatically start to dissolve. Under the absence of flow, the mixing happens due to the microscopic motion and the thermodynamic affinity of their molecules. This is a slow process that is called molecular diffusion. The rate at which this diffusion takes place is described by the molecular diffusion coefficient. This rate is formulated in Fick's first law of diffusion. Under the presence of flow, mixing will happen not only due to molecular diffusion, but also due to the motion of the fluids. In particular turbulent flow significantly enhances the mixing and disperses the fluids by the random like motion that happens at several length scales. This mechanism is known as turbulent dispersion or turbulent diffusion. The molecular diffusion and turbulent dispersion coefficients can be included into an advection-diffusion equation to predict the amount of mixing between two fluids in addition to their relative motion [7]. The mixing due to a (turbulent) axial dispersion coefficient will be explained in more detail in Section 3.3.4.

Austin and Palfrey [1] have investigated the factors that contribute to the length of the contamination zone. They concluded that mixing length of the interface between two fluids in a batch transport for a horizontal pipe section, among others, depends on:

- the Reynolds number;
- the distance travelled by the interface;
- the pipe's internal diameter;
- the fluids' thermodynamic properties (e.g. their densities and viscosities).

Laminar flow is associated with Reynolds numbers with a value of $Re < 2300$ for pipe flow. The Reynolds number is the ratio of the inertia forces and the viscous forces and helps to determine whether a flow is laminar or turbulent. The velocity profile in laminar flow has a parabolic shape [33]. As a result, the fluid near the wall moves very slowly and the residence time of particles in this region is large. The diffusion in laminar flow is primarily dependent on molecular diffusion, which results in low radial mixing in the pipeline and, therefore, a long streamwise contamination zone.

As the flow becomes fully turbulent, i.e. $Re > 6000$, the velocity profile will move to a flat shape in the centre with a small region of high radial velocity gradients near the wall. The region with high velocity gradients is called the viscous sublayer [22]. Here, the fluid is slowed down by the no-slip condition at the wall. As the Reynolds number becomes significantly large ($Re < 20,000$), the flow results in even larger velocity gradients and the thickness of the viscous sublayer becomes very thin. Therefore the residence time of fluid particles in the viscous sublayer is small in the case of turbulent flow. Together with the presence of eddies and vortices, this results in a continuous mixing of fluid which cause a higher mixing across the interface in the axial direction. This results in a higher axial dispersion coefficient which overwhelms molecular diffusion. The difference is so significant that the contribution of the molecular diffusion coefficient can be neglected in turbulent flow. Overall, the length of the contamination zone of a turbulent flow is smaller compared to a laminar flow, and the axial dispersion length decreases for increasing Reynolds number [15].

The length of the mixture region is of interest to the pipeline operator. For long horizontal pipelines, in which batch transport processes with fluids of similar densities occur, the mixture interface length s_{mix} is linearly proportional to the square root of the total length of the pipe; i.e. $s_{\text{mix}} \propto s_{\text{total}}^{\frac{1}{2}}$. According to Austin and Palfrey [1], the mixture interface length is given by:

$$s_{\text{mix}} = C\sqrt{D_H s}, \tag{1.1}$$

where C is the Palfrey coefficient, D_H the internal diameter of the pipe which is equal to the hydraulic diameter in $[m]$ and s is the axial length travelled by the front of the mixing region. Eq. (1.1) is known as the Palfrey relation. Austin and Palfrey have found that the Palfrey coefficient is a function of the mixing Reynolds number and can be approximated in two different relations, each indicating a different mixing region.

$$C = \begin{cases} C_1 = 18420 Re_{\text{mix}}^{-0.9} e^{2.192\sqrt{D_H}}, & \text{for} \quad Re_{\text{mix}} \leq Re_{\text{cr}} \\ C_2 = 11.75 Re_{\text{mix}}^{-0.1}, & \text{for} \quad Re_{\text{mix}} > Re_{\text{cr}}. \end{cases} \tag{1.2}$$

Here, Re_{mix} is the mixture Reynolds number and Re_{cr} is the critical Reynolds number at which the transition is seen between the steep and flat contimination zone.

The mixture and critial Reynolds numbers are defined as:

$$Re_{\text{mix}} = \frac{\rho_{\text{mix}} u_s D_H}{\mu_{\text{mix}}}; \quad \text{and} \quad Re_{\text{cr}} = 10000 e^{2.753\sqrt{D_H}}; \tag{1.3}$$

where ρ_{mix} and μ_{mix} are the average (mixture) density and dynamic viscosity of the fluids in $[kg/m^3]$ and $[kg/m \cdot s]$, respectively, and u_s is the total axial velocity in $[m/s]$ [15]. In Fig. 1.3, the Palfrey coefficient is depicted for a hydraulic diameter $D_H = 0.1$ $[m]$. The steep and flat region before and after the critical Reynolds number are clearly seen.

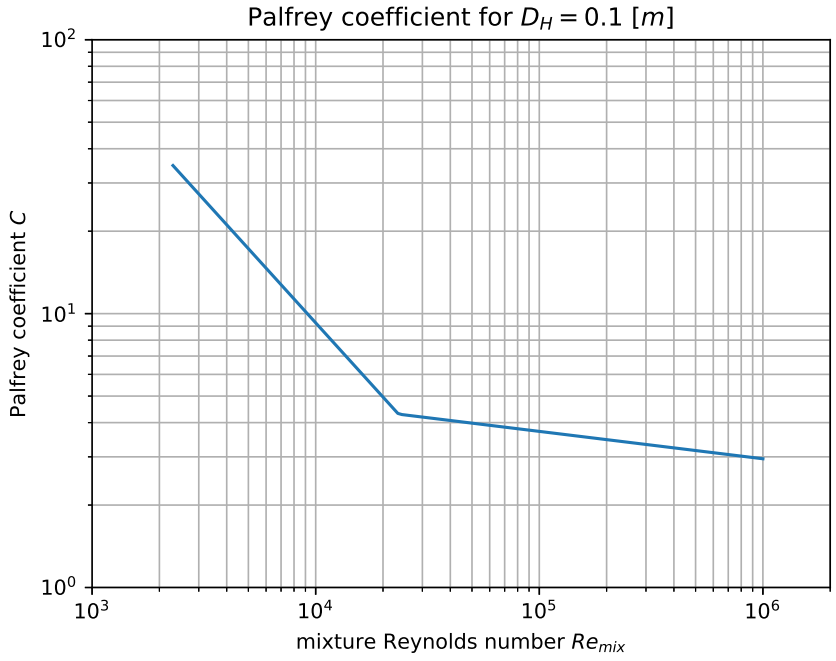

Figure 1.3: The Palfrey coefficient given in Eq. (1.2) for a hydraulic diameter of 0.1 $[m]$ on log-log scale. Below the critical Reynolds number Re_{cr}, the size of the viscous sublayer has huge impact on the magnitude of the Palfrey coefficient resulting in a steep region. The size of the viscous sublayer becomes of less importance when the mixture Reynolds number exceeds the critial Reynolds number, $Re_{\text{mix}} > Re_{\text{cr}}$, as the flow approaches piston-like flow. This is shown by the flat region of the Palfrey coefficient C.

The importance of the pipeline's diameter is shown by keeping the mixture Reynolds number constant for turbulent flow. For the same type of batch transport, the thermodynamic properties remain constant. The product of the axial velocity and the hydraulic diameter within the mixture Reynolds number is kept constant as well, but the axial velocity and hydraulic diameter parameters are allowed to be alternated. By increasing the hydraulic diameter, the axial velocity automatically has to decrease. This indicates that the radial velocity gradients become less sharp and the viscous sublayer, which was already increased in size by enlarging the pipe's diameter, will grow even more. By doing so, the mixture interface length becomes larger as well, as is demonstrated by the Palfrey relation in equation (1.1) [1].

If there is a density difference between the fluids in the batch transport operation, stratification effects can play an important role. The less dense fluid will creep over the dense fluid when it is displaced as the second fluid in the batch transport. In constrast to this, the dense fluid moves below the less dense fluid when it is displaced in the batch transport operation after the less dense fluid. Eventually, the segregated flow becomes mixed by the turbulent diffusion, and stratification effects are no longer seen further down the pipe. Before this happens, it will affect the length of the mixing region.

A modified Palfrey relation for the mixture interface length was suggested by Henkes [16] in Shell's research on the batch transport for different oil types in the Tempa Rossa project. The modified relation includes an apparent stratification length s_{strat}, which is initially present in the batch transport, and an extra apparent virtual length s_{virtual}, needed for axial mixing as a result of the stratification. The modified Palfrey relation reads:

$$s_{\text{mix}} = C\sqrt{D_H\,(s + s_{\text{virtual}})} \quad \text{and} \quad s_{\text{strat}} = C\sqrt{D_H\, s_{\text{virtual}}}. \tag{1.4}$$

In the Tempa Rossa study, experiments were executed, in which salt water was substituted by fresh water and vice versa. Fig. 1.4a shows the level of local stratification at various locations throughout a pipe section by calculating the difference of the concentration at the top minus the concentration at the bottom using electrical conductivity measurements. Fig. 1.4b shows the average of the top and bottom concentrations, this enables to visualise the mixing region passing through the measurement locations. Henkes reports a longer stratification length for the fresh water displacing the salt water, compared to salt water displacing fresh water. This is in line with the theory of stratification formation [16]. The mathematical reason for this theory is explained in Section 3.3.3.

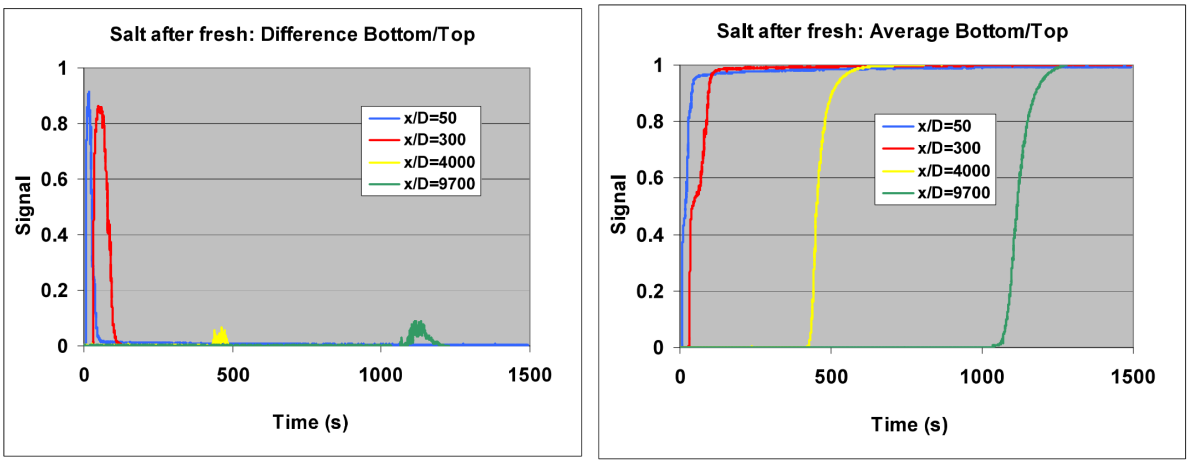

(a) stratification measurements

(b) Axial mixing measurements

Figure 1.4: The measurement results of a salt water after fresh water batch transport are given for (a) the amount of local stratification and (b) axial mixing over time for a axial velocity $u_s = 0.153\ [m/s]$, a mixture Reynolds number of $Re_{\text{mix}} = 2900$ and a Froude number of $Fr = 1.8$. The experiments were conducted in the Shell laboratory in Amsterdam to investigate the batch transport of different oil types [16].

The amount of stratification in the mixing zone depends on the Froude number. In literature, it is stated that for a Froude number above 15, stratification effects are no longer observed and are negligible. For segregated flow, the Froude number is defined as:

$$Fr = \frac{\rho_{\text{mix}}}{\Delta\rho}\frac{u_s^2}{gD_H}, \tag{1.5}$$

where the gravitational acceleration factor g is extended to $g\rho_{\text{mix}}/\Delta\rho$ to include the density differences. $\Delta\rho$ is defined as the density of the dense fluid minus the density of the less dense fluid [16].

The effect of another thermodynamic property, the viscosity, is described by Austin and Palfrey. In the example, they propose the batch transport of gasoline-gasoline types and diesel-diesel batches. The relative viscosity difference is basically equal for both batches. On the contrary, the absolute viscosity difference between the batches is not equal. The viscosity of the diesel batch is much larger than that of the gasoline batch. This results in a measured contamination zone of approximately half the size of the mixing zone of the gasoline-gasoline batch [1].

Therefore, in addition to the pipe inclination, the mentioned variables in this section have a large impact on fluid-fluid displacement as well.

1.3. Hydrate inhibition

In the offshore industry, oil and gas are produced through subsea wells. These wells are often connected to other wells via subsea manifolds, which simplify the subsea system by minimizing the use of subsea pipelines. A manifold is an arrangement of pipes and valves to combine, distribute, control and monitor the oil and gas flow. The manifolds are often connected to the tie-backs via jumpers. Tie-backs are pipelines, which connect the subsea wells to other pipelines which are already connected to existing offshore platforms. In Fig. 1.5, an example of a subsea infrastructure featuring wells, jumpers and a manifold can be seen [2].

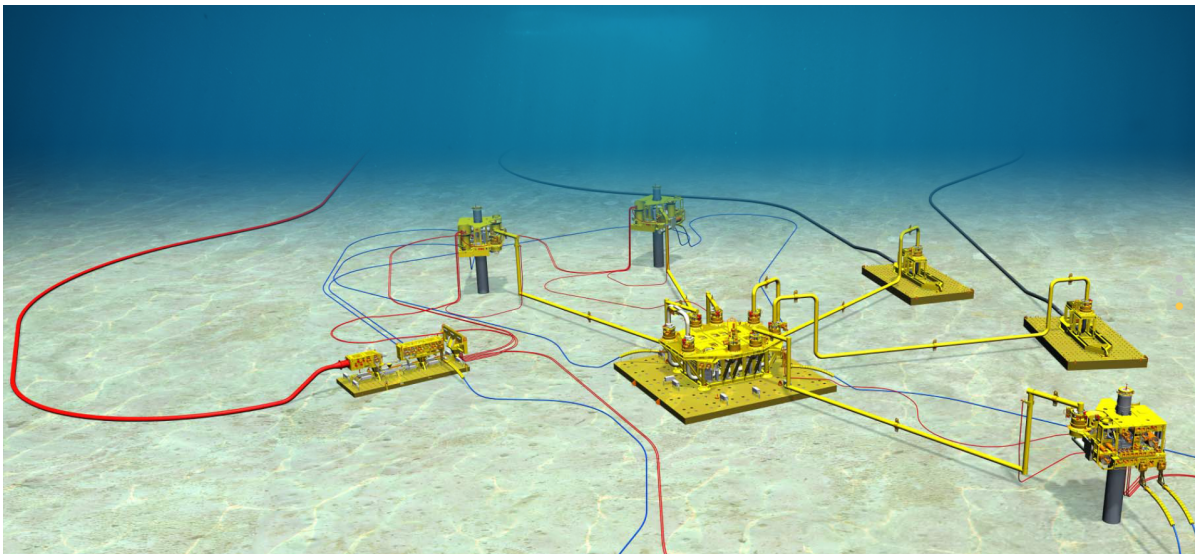

Figure 1.5: A subsea infrastructure including multiple wells connected to a manifold by jumper geometries. The tie-backs are leading in the direction of the offshore platform. Source:https://makoss.com/

During a planned or unplanned interruption of oil or gas production, the fluids in tie-backs and jumpers are in a so-called shut-in period. The duration of these periods can vary from a couple of hours to a couple of weeks. As a result, the multiphase mixture of oil, gas and water will become stagnant in the pipelines. During a shut-in period, there is a risk of hydrate formation in the tie-backs and especially the risk is higher in the jumpers as the fluids in the pipeline cool down to ambient temperatures. Gas hydrates are crystalline water-based solids that can cluster together. This can lead to fully clogged pipelines, which must be avoided in order to prevent interruptions in production and the high cost associated with the remediation of these events [7].

For hydrates to form, gas molecules have to be composed to hydrogen-bounded water molecules [28]. Due to the density differences between oil, gas and water, water is often accumulated in the horizontal sections of a jumper geometry, the so-called low spots. The accumulation of water might also happen in the tie-backs as a result of the elevation profile of the seabed. Furthermore, in order for hydrates to form the pressure needs to be high and the temperature needs to be low. The gas is produced under high pressure and the subsea infrastructure is exposed to the low ambient temperature of subsea water. The risk of hydrate formation in jumper geometries is high during the shut-in periods.

To avoid hydrate formation, several strategies have been developed by the industry. Most strategies consist of thermally insulated pipes, electrical heating of pipes and the injection of a thermodynamic inhibitor (THI) via so-called umbilicals during the shut-in period. Methanol (MeOH) is one of the commonly used THIs. It is essential that for THI to be properly dispersed and mixed in the aqueous phase to effectively prevent the formation of hydrate crystals [9][27].

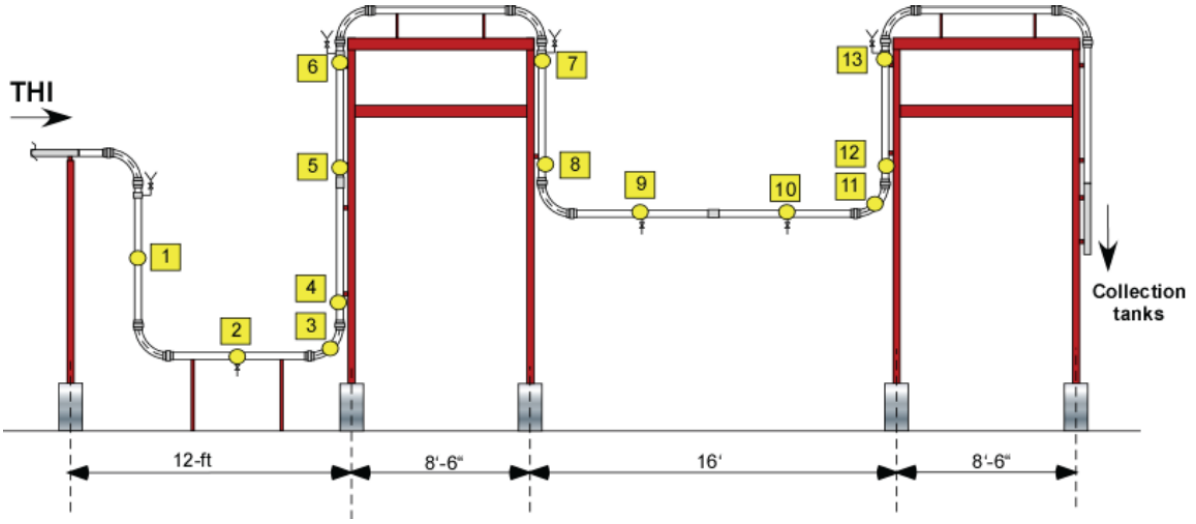

Figure 1.6: A jumper-like geometry used by Dellecase in his experiments to investigate the effect of mixing and dispersion at various volumetric flow rates for methanol inhibiting fresh or salt water. The measurement points at which a sample of the concentration of methanol is taken are represented by numbers. In the horizontal sections, the methanol concentration is measured at the top and bottom of the pipe. This allows Dellecase to measure stratification [10].

The density difference between water and the THI, together with the elevation profile of the seabed and jumper geometries can lead to locations with low methanol concentration along the pipeline. Typically, low volumetric flow rates can be achieved when injecting THI. This results in the THI, e.g. methanol, floating on top of the water rather than displacing it. It is possible that after the injection stops, the methanol is already partly flowing out of the pipeline segment without having achieved the minimum required methanol concentration at certain locations. In the best scenario, the stratification effects are minimum. The accumulated water is displaced from the pipeline by the methanol or the methanol and the water are sufficiently mixed in the water accumulation zones [15].

Frequently hydrate inhibition strategies feature overdosing with THI to prevent hydrate formation. This is a conservative approach that comes with higher operational costs, but that can also impact HSE (Health, Safety and Environment) footprint of the industry. The injection of hydrate inhibitor requires difficult logistics, onsite storage of these hazardous chemicals on the platforms and manual handling of the crew. Accurate prediction of the THI distribution along the pipeline would be beneficial for both financial and environmental reasons [27].

Dellecase investigated the effect of mixing and dispersion of methanol in fresh and salt water accumulated in a jumper-like geometry. In Fig. 1.6, a schematic illustration of his experimental jumper-like geometry is given. Dellecase has performed the experiments at various volumetric flow rates to determine its effect on the concentration distribution of methanol along the geometry. During the experiments, stratified flow was observed in the horizontal sections. The methanol was overriding the water phase. For the lowest two flow rates, the methanol concentration remains low in the horizontal sections. This indicates that water is accumulated in these low spots, even after one full jumper volume of methanol has been injected into the pipeline. Eventually, this accumulated water will be diffused out over time by the action of molecular and turbulent diffusion. However this might take a significant amount of time and a high volume of injected fluid. The flushing behaviour of methanol approaches a piston-like displacement for the highest volumetric flow rate. [10] The Dellecase experiments will be adressed again in Section 5.4 where the results of the created one-dimensional numerical model and of three-dimensional computational fluid dynamics (CFD) simulations will be compared against the experiments. The CFD simulations are reproduced in Ansys Fluent which is a commercial CFD package, these results are presented in Appendix C.

1.4. Flow patterns

It is useful to know how fluids can behave in two-phase flow. The involved flow structures between the fluids can be very complex and, therefore, flow patterns are used to categorize the two-phase flow. Three type of flow patterns are illustrated in a horizontal pipe section in Fig. 1.7. On top (1), smooth stratified flow is seen. The fluids travel in two segregated regions through the pipe in the axial direction. Due to interfacial instabilities on the surface, the smooth stratified flow becomes wavy. This flow pattern is called wavy stratified flow, (2). The instabilities between two segregated fluids of dissimilar densities caused by a slip velocity are called Kelvin-Helmholtz instabilities, which can enhance the mixing process. The instabilities can arise by inclinations in the terrain and can grow when the relative velocity between the two layers exceeds a critical threshold value. The waves can grow in amplitude until they reach the top of the pipeline. When this happens, the flow pattern changes to the type, where liquids pockets or slugs are formed together with small bubbles. This flow pattern is called slug flow or intermittent flow, (3) [7][26].

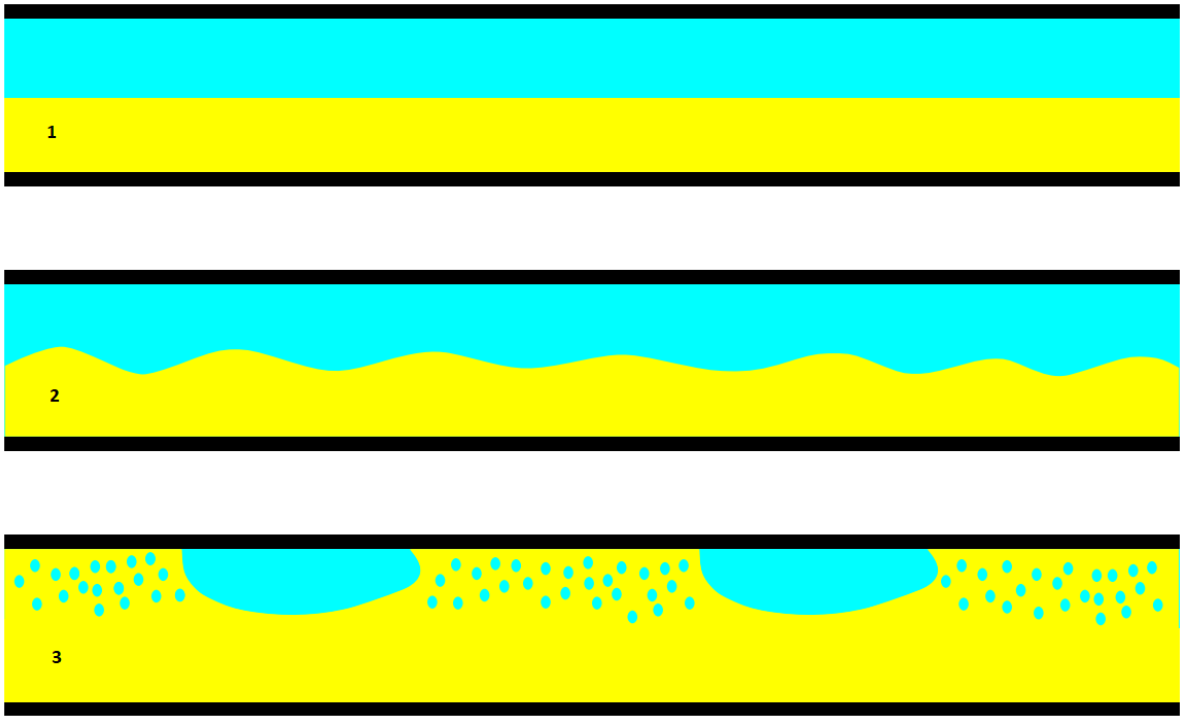

Figure 1.7: The flow patterns that could occur in two-phase flow are, among others, (1) stratified flow, (2) stratified wavy flow and (3) slug flow [26].

Shell has developed an in-house model to determine which type of flow pattern will occur for multiphase flow in pipelines. The model is called Shell Flow Correlations (SFC). SFC checks the number of phases, their fluxes and thermodynamic properties and the pipe geometry in order to determine the flow pattern. When the correct flow pattern is found, the tool to solve the multiphase flow configuration is adjusted to include the correct models for each flow pattern. These models include e.g. the momentum balance, estimated pressure drop, friction forces and interface height [29].

1.5. Modelling of two-phase flow

The modelling of two-phase flow is often a great challenge within the oil and gas industry due to complex flow phenomena and large pipeline volumes. Computational Fluid Dynamics (CFD) is capable of modelling these flow phenomena, however, three-dimensional CFD simulations have high computational costs and, therefore, are not feasible for simulating very long pipelines. By using two-dimensional CFD-simulations, larger pipeline structures can be modelled. Nonetheless, specific three-dimensional effects will not be included in the simulations. In the petrochemical industry, one-dimensional flow simulations are the most often used approach for pipeline transport.

OLGA (short for OiL and GAs simulator) has the largest global market share and was developed by Malnes and Bendiksen [4]. Shell has developed its own dynamic multiphase flow tool, called COMPAS (COmpositional MultiPhase Advanced Simulator). One-dimensional multiphase tools that are capable of modelling up to three phases, an aqueous, oil and gas phase. Nonetheless, these tools do not include an axial dispersion coefficient in their model. Furthermore, if multiple components are present in a given phase (aqueous, oil or gas), OLGA and COMPAS regard the components within a given phase as a homogeneous mixture, therefore neglecting the effect of dissimilar densities and slip velocity within the phase. OLGA includes hydraulic gradients in its momentum equations, whereas COMPAS does not have those included. The hydraulic gradients account for the variation of pressure with height (i.e. the pressure in the phases will be different, especially at the interphasial surfaces where the surface tension might cause a pressure jump). The multiphase flow equations (conservation of mass, momentum and energy) are not able to reproduce surface wave (Kelvin-Helmholtz instabilities) and gravity currents without the hydraulic gradients [15].

Haspels and Sanderse [26] examined whether it is possible to obtain the correct slip velocity using the one-dimensional averaged conservation of mass and momentum equations for slug flow. The study was meant to determine whether COMPAS could be extended to include a bubble drift model. They succeeded in their goal and reproduced a Benjamin bubble in their model. However, they had to conclude that their solution was not convenient. A lot of effort had to be delivered on the closure relations to realise the slip velocity. Bouwhuis [7] tried another approach only using the conservation of mass in a one-dimensional averaged model. The model directly incorporates a slip velocity relation to solve both velocities of the two fluids in the same phase. No momentum equation was solved in his model. The model captures the Benjamin bubble using the alternative set of equations. Besides, he did set up relations for the movement of fluids of dissimilar densities in inclined pipe sections for immiscible flow. Moreover, he started working on a miscible flow model.

Dellecase tried to reproduce his experimental results using a one-dimensional transient model and a three-dimensional CFD-model [20]. In his paper, Dellecase did not mention the name of the one-dimensional modeling tool that was used, but it is probably similar to OLGA as a monotonic concentration distribution was found for methanol along the jumper-like geometry. This indicates that the model is not capable of predicting segregation in the horizontal sections for the aqueous phase. Besides, the model was lacking a (turbulent) dispersion coefficient. The 3D CFD-simulation results show that the chosen turbulence models were not able to predict stratified flow in the low spots. The results on the non-horizontal measurement points are within 10% of the experimental data for the 3D CFD-model.

Shell investigated whether less methanol as hydrate inhibitor could be injected in the tie-backs during a shut-in. By using a CFD-model, it was concluded that OLGA was not suitable for the job in this study [27]. A three-dimensional CFD-model gave new insights on the impact of turbulent mixing, molecular diffusion and the density differences between methanol and water over time and space. The density difference was found to result in a slip velocity within the aqueous phase as a result of buoyancy forces. Only the aqueous phase was simulated in the CFD-model. The CFD-results were obtained for a relatively short pipeline section and were extrapolated using a dimensionless scaling technique. Using this ad-hoc scaling technique of the CFD-results, it was possible to improve the hydrate management strategy, nonetheless there is still a need for a model which can more comprehensively simulate the miscible fluid displacement phenomena.

1.6. Objective and approach of the present study

The goal of the present study is to develop a numerical model, able to accurately predict miscible fluid-fluid displacements within pipeline operations. The model should be able to capture the following physical phenomena:

- miscible effects; i.e. molecular and turbulent diffusion;
- stratified (separated) fluid layers, in which gravity currents induced by a density difference, could occur;
- a slip velocity between the regions influenced by buoyancy;

The model should predict the concentration of both fluids as functions of time and space along the pipeline. Moreover, it should predict how variations in the volumetric flow rate and the thermodynamic properties will affect these concentrations. The model should be able to predict the non-monotonic concentration distributions that can occur along pipelines due to the density difference between the fluids.

The model is an extention of previous work on multiphase flow models. Some learnings that are important to keep in mind are the following:

- CFD has shown to capture the most important physical phenomena for single-phase miscible fluid displacement. However, due to its computational intensity it is only practical for simulating short pipe sections. The CFD-results over relatively short pipelines can be extrapolated. Nonetheless, there is still need for a fast accurate one-dimensional model which can model long pipelines while accurately capturing the key physical phenomena.
- The relevance of density differences and the pipeline inclination effect can be captured by incorporating information related to the bubble velocities.
- Haspels and Sanderse [26] reproduced elongated bubbles in a horizontal channel using the one-dimensional momentum equation. The method is, however, not convenient, as significant efforts had to be made in the closure relations. By directly implementing a velocity relation based on the bubble velocity, together with the continuity equation in a one-dimensional immiscible model. The approach of Bouwhuis is used and this model is extented to a fully miscible model in this study [7].
- The one-dimensional dynamic simulation tools, OLGA and COMPAS, are capable of handling density differences and the interface friction between the aqueous, oil and gas phases. The hydrate inhibitor operation demands that the density differences within the aqueous phase are included in the model as well, together with a slip velocity between the fluids in this phase. The present study focusses on multiphase phenomena happening in the aqueous phase.

  Furthermore, both tools cannot simulate the growth of an axial mixing zone for miscible fluids. The only diffusion seen using OLGA and COMPAS is numerical diffusion. The amount of numerical diffusion must be minimized within the model. The model must be higher-order accurate and should include a (turbulent) diffusivity relation.

  In the momentum equation solved within OLGA, hydraulic gradients are included. These hydraulic gradients are responsible for the prediction of gravity currents. The momentum equation of COMPAS does not consist of these gradients and is, therefore, not able to reproduce the surface waves and gravity currents. As the approach of Bouwhuis is used in this study, the model does not solve a cross-sectional averaged momentum equation. Therefore, hydraulic gradients are not incorporated in this research. The prediction of the gravity currents has to be determined using other velocity relations.

Therefore, the objective of the present study is:

The development of a one-dimensional numerical model of high accuracy for miscible fluid-fluid displacement, able to predict a slip velocity and gravity currents within the aqueous phase.

The immiscible fluid displacement model from Bouwhuis [7] is used as the starting point of this study. The conservation of mass equation and two advection-diffusion equations are cross-sectionally averaged to derive the miscible equations. These equations describe the fluids behavior in space and time. A velocity equation that couples the slip velocity between the two fluids within the aqueous phase and the bubble velocity is solved in conjuction with an equation which is derived from the incompressibility condition. This set of equations is supplemented with closure relations describing the axial dispersion coefficient and the bubble velocity.

The set of equations is numerically discretised in time and space and solved in a coupled solver implemented in Python. First, a single-phase model is validated by an analytical solution for the transport equation using a new empirical relation for the axial dispersion coefficient. Thereafter, some fundamental cases are presented in a horizontal pipe and a W-shaped pipe to illustrate the model in several geometries. At last, the Dellecase experiments are simulated by the model. It is tried to reproduce and match the Dellecase results and, thereby, derive a new empirical relation for the transfer terms. If an empirical relation is found the fundamental cases are repeated to test the flow behaviour under the modified transfer terms.

Next to the Python model, a CFD-model in Ansys Fluent is set-up for two-dimensional multiphase fluid-fluid interactions in the aqueous phase. The Dellecase experiments are also reproduced in Ansys Fluent where the focus lays on the stratification effects in the horizontal section.

1.7. Outline of the report

The present report is structured as follows.

In Chapter 2 the governing equations are derived. Starting at the integral formulation, the cross-sectional averaged equation of the conservation of mass and the transport equation for both single -and multiphase flow are derived. Expressions for the effective bubble velocity are determined, and the important dimensionless numbers are introduced.

In chapter 3, the model underlying assumptions are presented as well as its limitations. The final equations are derived. Its functions for closure of the model and the axial dispersion relation are introduced.

The numerical discretisation of the governing equations is done in chapter 4. The discretisation scheme for the time derivative, the advection and diffusion terms are handled in this chapter. The stability criteria are given for the model, and it is described which choices had to be made to integrate the model in Python.

Chapter 5 starts with a validation of the numerical model for single-phase flow. The new empirical relation for the axial dispersion coefficient is validated with an analytical solution of an advection-diffusion problem. This is followed by fundamental cases to show what the model is capable of. First, cases in a horizontal pipe are investigated. The Benjamin bubble solution should be obtained and the influence of the Froude number should clearly be seen on the flow. Afterwards, the model is tested for both upward- and downward-inclined pipe geometries. Eventually, the Dellecase experiments are simulated by the model. The goal of these simulations is to derive a new empirical relation for the mass transfer term as a function of the mixture Reynolds number.

Finally, the conclusions and recommendations for future research are provided in Chapter 6 & 7.

2

Physics of miscible fluid-fluid displacement model

The equations used to model the fluid-fluid displacement phenomena are derived in this chapter. This derivation includes the conservation of mass and the transport equation for both single phase and multi-phase flow. Furthermore, the mathematical relations behind the bubble velocity are explained. Moreover, an overview of the forces acting on the two-phase flow is given together with a dimensional analysis of the important variables in the model.

All equations are cross-sectionally averaged in order to arrive to a one-dimensional model.

2.1. Averaging of three-dimensional flow

The three-dimensional equations which describe flow are called the Navier-Stokes (NS) equations. These equations are the foundations of CFD models. For turbulent flow, the NS-equations are extended with a turbulence model, like the k-ϵ model [22]. To include multiple fluids within the model, multiphase models, or a species transport model, could also be added to the CFD-model. In practice pipelines can be very long ranging from several tens up to hundreds of kilometers. Simulating such long pipelines with direct three-dimensional CFD model can easily become inpractical. Therefore, simplifications to the physical model are needed to come up with a model a model that can be solved efficiently.

One way to achieve this is averaging the governing equations over the pipeline's cross-sectional area. In this way a one-dimensional model of the governing equations can be obtained. Solving a one-dimensional model is orders of magnitude faster than a three-dimensional one. One disadvantage is that some of the information can get lost through the averaging process. Therefore measures must be taken in order to still capture the relevant mixing mechanisms.

2.1.1. Definitions

To obtain one-dimensional flow equations, the scalar and vector quantities in the conservation equations have to be cross-sectionally averaged. The volume average of a scalar quantity $f(\boldsymbol{x}, t)$ associated with an arbitrary volume Ω, is defined as:

$$\{f\}(t) := \frac{1}{V}\int_{\Omega} f(\boldsymbol{x}, t)\mathrm{d}\Omega, \tag{2.1}$$

where $V = \int_{\Omega}\mathrm{d}\Omega$ is assumed to be time-independent, i.e. the pipe geometry is rigid an it does not deform.

The area average of a scalar quantity $g(\boldsymbol{x}, t)$ associated with a surface S:

$$\langle g\rangle(t) := \frac{1}{A}\int_{S} g(\boldsymbol{x}, t)\mathrm{d}S, \tag{2.2}$$

where $A = \int_{\partial\Omega}\mathrm{d}S$, which is also assumed to be time-independent. This surface S does not necessarily have to be the cross-sectional area of the pipe.

The area average of a scalar quantity $f(\boldsymbol{x}, t)$ associated with a volume can also be defined by considering a pipe segment $V = A\Delta s$ and taking the limit of $\{f\}(t)$ as $\Delta s \to 0$.

$$\langle f \rangle(s,t) := \frac{1}{A}\int_S f(x,t)\mathrm{d}S. \tag{2.3}$$

By following this definition, the cross-sectional averaged quantity does not lose its dependency with respect to the axial direction s, since:

$$\lim_{\delta s \to 0} \{f\}(t) = \langle f \rangle(s,t) \tag{2.4}$$

Furthermore, the average of a product of functions is assumed to be equal to the product of averages [25].

$$\{fg\} \approx \{f\}\{g\} \tag{2.5}$$

The error in this approximation is on the order of D^2, where D is the pipe diameter. Sanderse [25] gives details for this derivations.

2.2. Mass Conservation equation

Two miscible fluids can interact and exchange mass with each other while flowing through the system. This results in a constantly altering mass over time at specific locations in a fixed volume. The miscible fluid-fluid displacement model has to be able to accurately track the mass changes in the system.

To explain how the mass of a fluid volume can change, the conservation of mass is first derived for single phase flow. Thereafter, this derivation is expanded to include two fluids and to elaborate on the multiphase conservation of mass principles.

The conservation of mass is given in the integral form. The integral form is the most physical form of the equations. It requires less smoothness than starting from the differential form and allows the presence of discontinuities at the interfaces, which are typically seen in multiphase flow. The cross-sectional averaging method is used to derive the one-dimensional differential form of the equations. This provides a good starting point for the derivation of the discretized equations using the Finite Volume Method (FVM) [25]. This is explained in Chapter 4.

2.2.1. Single phase flow

Consider the arbitrary pipe segment illustrated in Fig. 2.1. It contains a fluid with volume Ω fixed in time and space, which is limited by the boundaries $\partial\Omega$. The boundaries include S_1 the pipe inlet at $s = s_1$, S_2 the pipe outlet at $s = s_2$ and S_3 the pipe surface, $\partial\Omega = S_1 \cup S_2 \cup S_3$. The no-slip boundary condition is applied at the pipe surface.

An orthogonal curvilinear coordinate system is employed along a generic spatial curve, being the centreline of the pipe. Such a coordinate system is suitable for general or curved pipe flow, as well as for non-circular, expanding and constracting pipe sections. The variable s denotes the coordinate tangential to the spatial curved centerline and r and θ are the polar coordinates representing the radial and circumferential coordinates. This results in the coordinate system $\boldsymbol{x} = (s, r, \theta)$ which can be translated to the Cartesian coordinate $\boldsymbol{x} = (x, y, z)$.

The integral form of the mass conservation equation over a volume Ω bounded by $\partial\Omega$ is defined as:

$$\frac{\partial}{\partial t}\int_\Omega \rho \mathrm{d}\Omega + \int_{\partial\Omega} \rho \boldsymbol{u}\cdot\boldsymbol{n}\mathrm{d}S = 0, \tag{2.6}$$

where $\rho(\boldsymbol{x}, t)$ is the density, $\boldsymbol{u}(\boldsymbol{x}, t) = (u_s, u_r, u_\theta)$ is the velocity vector and $\boldsymbol{n}$ is the outward unit normal vector. The normal vector is perpendicularly directed to each boundary $\partial\Omega$. Note that, equation (2.6) does not include a source term, which can add or remove mass to the system.

The surface integral over $\delta\Omega$ can be splitted as follows:

$$\frac{\mathrm{d}}{\mathrm{d}t}\int_\Omega \rho \mathrm{d}\Omega + \int_{S_1} \rho \boldsymbol{u}\cdot\boldsymbol{n}\mathrm{d}S + \int_{S_2} \rho \boldsymbol{u}\cdot\boldsymbol{n}\mathrm{d}S + \int_{S_3} \rho \boldsymbol{u}\cdot\boldsymbol{n}\mathrm{d}S = 0, \tag{2.7}$$

where the outward normal vector $\boldsymbol{n}$ determines the sign of the advection terms. The first term of (2.7) is rewritten following the averaging definition of equation (2.1).

$$\frac{\mathrm{d}}{\mathrm{d}t}\int_\Omega \rho \mathrm{d}\Omega = \frac{\mathrm{d}}{\mathrm{d}t}\left(\left[\frac{1}{V}\int_\Omega \rho(\boldsymbol{x}, t)\,\mathrm{d}\Omega\right]V\right) = \frac{\mathrm{d}}{\mathrm{d}t}\left(\{\rho\}(t)\,V\right) \tag{2.8}$$

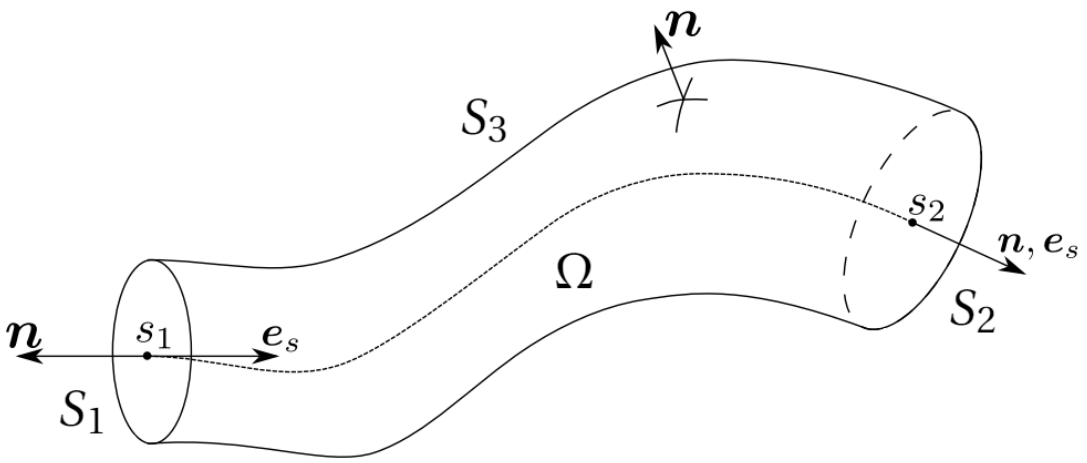

Figure 2.1: An arbitrary pipe section with a total volume Ω. The volume of interest is bounded by the two cross-sectional areas of the pipe at S_1 and S_2 and the surface pipe, S_3. The single phase flow is depicted as transparent. On each surface, the normal vector $\boldsymbol{n}$ is depicted. The unit vector $\boldsymbol{e}_s$ along the pipe axis s is illustrated on the cross-sectional surfaces of the pipe, S_1 and S_2 [7].

Note that, the volume V is independent on time and space for this pipe section. The second term of (2.7), the surface integral over S_1 is rewritten as:

$$\int_{S_1} \rho \boldsymbol{u}\cdot\boldsymbol{n}\mathrm{d}S = -\left[\frac{1}{A(s_1)}\int_{S_1}\rho\boldsymbol{u}\cdot\boldsymbol{e}_s\,\mathrm{d}S\right]A(s_1) = -\left\langle\rho u_s\right\rangle(s_1,t)\,A(s_1)\,, \tag{2.9}$$

where $\boldsymbol{e}_s$ is the unit vector tangential to the centerline of the pipe and $u_s = \boldsymbol{u}\cdot\boldsymbol{e}_s$. The normal vector $\boldsymbol{n}$ and the unit vector $\boldsymbol{e}_s$ point in opposite direction on surface S_1. Therefore, these terms result in a minus sign. Similarly, the surface integral over S_2 is rewritten.

$$\int_{S_2} \rho \boldsymbol{u}\cdot\boldsymbol{n}\mathrm{d}S = \left[\frac{1}{A(s_2)}\int_{S_2}\rho\boldsymbol{u}\cdot\boldsymbol{e}_s\,\mathrm{d}S\right]A(s_2) = \left\langle\rho u_s\right\rangle(s_2,t)\,A(s_2) \tag{2.10}$$

No flow passes the pipe surface, $\boldsymbol{u}\cdot\boldsymbol{n} = 0$. Accordingly, the fourth term of equation (2.7) does not have to be rewritten. Substituting all terms of Eq. (2.7) by the rewritten terms yields:

$$\frac{\mathrm{d}}{\mathrm{d}t}\left(\{\rho\}(t)\,V\right) + \left\langle\rho u_s\right\rangle(s_2,t)\,A(s_2) - \left\langle\rho u_s\right\rangle(s_1,t)\,A(s_1) = 0. \tag{2.11}$$

The differential form of the single-phase mass conservation equation can be obtained by taking a small finite volume $V = A\delta s$ with sides $A(s)$ and $A(s+\delta s)$.

$$\frac{\mathrm{d}}{\mathrm{d}t}\left(\{\rho\}(t)\,A\delta s\right) + \left\langle\rho u_s\right\rangle(s+\delta s,t)A(s+\delta s) - \left\langle\rho u_s\right\rangle(s,t)A(s) = 0 \tag{2.12}$$

Dividing by δs and taking the limit of $\delta s \to 0$, gives:

$$\frac{\partial}{\partial t}(\langle\rho\rangle(s,t)A(s)) + \frac{\partial}{\partial s}\left(\left\langle\rho u_s\right\rangle(s,t)A(s)\right) = 0. \tag{2.13}$$

The average of the product of functions is assumed to be equal to the product of averages which yields:

$$\begin{aligned}\frac{\partial}{\partial t}(\langle\rho\rangle(s,t)A(s)) + \frac{\partial}{\partial s}\left(\langle\rho\rangle\langle u_s\rangle(s,t)A(s)\right) = 0,\\ \frac{\partial}{\partial t}(\rho(s,t)A(s)) + \frac{\partial}{\partial s}\left(\rho(s,t)u_s(s,t)A(s)\right) = 0.\end{aligned} \tag{2.14}$$

The final differential form of the single-phase continuity equation yields:

$$\frac{\partial(\rho)}{\partial t} + \frac{1}{A}\frac{\partial(\rho u_s A)}{\partial s} = 0. \tag{2.15}$$

The cross-sectional area is independent of time, and can be taken out of the first partial derivative. The brackets and space and time variables are omitted for simplicity, but all variables should be interpreted as cross-sectional averages. Furthermore, it is assumed that [7][25]:

- the density is uniform over the cross-section;
- the streamwise velocity is much larger than the velocity contributions of the radial and circumferential components;
- the pipeline's curvature is negligible.

2.2.2. Multiphase flow

Consider the arbitrary pipe section illustrated in Fig. 2.2. Note, that this geometry is similar to the arbitrary pipe section as seen in Fig. 2.1. Again, the geometry has a fixed volume Ω in space and time.

Now, two miscible fluids of dissimilar densities are present in the volume, which results in a pipe flow that is assumed to be stratified. In stratified flow, the averaging volume is barely larger than the characteristic size of the interfacial structures [25]. The similar orthogonal curvilinear coordinate system is employed here as in Section 2.2.1.

Due to the miscible character of the two fluids, their particles can freely move along each other through the volume. Therefore, an interface formally does not exist. Nonetheless, for modeling purposes we define a virtual interface with the goal of capturing the effect of non-uniform concentration along the cross-section of the pipe. Two separate regions are introduced in the volume Ω. The regions are defined as the upper and lower region separated by a virtual interfacial surface. Both fluids can be present in all regions, each representing its own volume and mass. Thereby, the fluids contribute to the volume and mass of both regions. The change of mass in these regions is tracked via the mass conservation equation for multiphase flow.

In the following derivations we will use the following notation. The subscript $(.)_\beta$ is used to refer to the variables either in the the upper or lower region, where $\beta \in \{u, l\}$. The subscript $(.)_u$ is used for the upper region and $(.)_l$ is used for the lower region. To quantify the variables of the fluids a similar notation is used, $(.)_B$ where $B \in \{L, H\}$. $(.)_L$ is used for the light fluid and $(.)_H$ is used for the heavy fluid. Due to gravity and buoyancy effects, the light fluid particles will have the tendency to be more present in the upper region, whereas the heavy fluid will have the tendency to be more active in the lower region. Therefore, the contribution of the density of upper region, ρ_u, to the density of the light fluid ρ_L is higher than the contribution of the density of the heavy fluid ρ_H. The opposite applies for the density of the lower region ρ_l.

The volume, that is considered for the integral formulation of the multi-phase conservation of mass, is again evaluated from $s = s_1$ till $s = s_2$. The volume occupied by the upper region Ω_u, is composed out of the boundaries $\partial\Omega_u$ at

1. the cross-sectional area $S_{u,1}$ occupied by the upper region at $s = s_1$;
2. the cross-sectional area $S_{u,2}$ occupied by the upper region at $s = s_2$;
3. the pipe surface surrounded by the upper region $S_{u,3}$;
4. the interphasial surface $P_{u,l}$ between the regions from $s = s_1$ till $s = s_2$.

Similarly, the volume occupied by the lower region, Ω_l, is composed of the boundaries, $\partial\Omega_l = S_{l,1} \cup S_{l,2} \cup S_{l,3} \cup S_{u,l}$.

The cross-sectional area at distance s, following the centerline of the pipe section, is denoted by $A(s)$. The area occupied by the upper region at s_1 is defined as $A_u(s_1, t)$:

$$\int_{S_{u,1}} \mathrm{d}S := A_u(s_1, t). \tag{2.16}$$

Note that, the area occupied by the upper region is dependent on time and space. Now, the hold-up of the upper region can be introduced at $s = s_1$, which is defined as:

$$\alpha_u(s_1, t) := \frac{A_u(s_1, t)}{A(s_1)}. \tag{2.17}$$

The hold-up is defined as the ratio of the cross-sectional area occupied by that region A_β and the total cross-sectional area A. The hold-up variable is function of space and time. The hold-ups and the cross-sectional areas occupied by the regions are similarly determined at the boundaries $S_{u,2}$, $S_{l,1}$ and $S_{l,2}$.

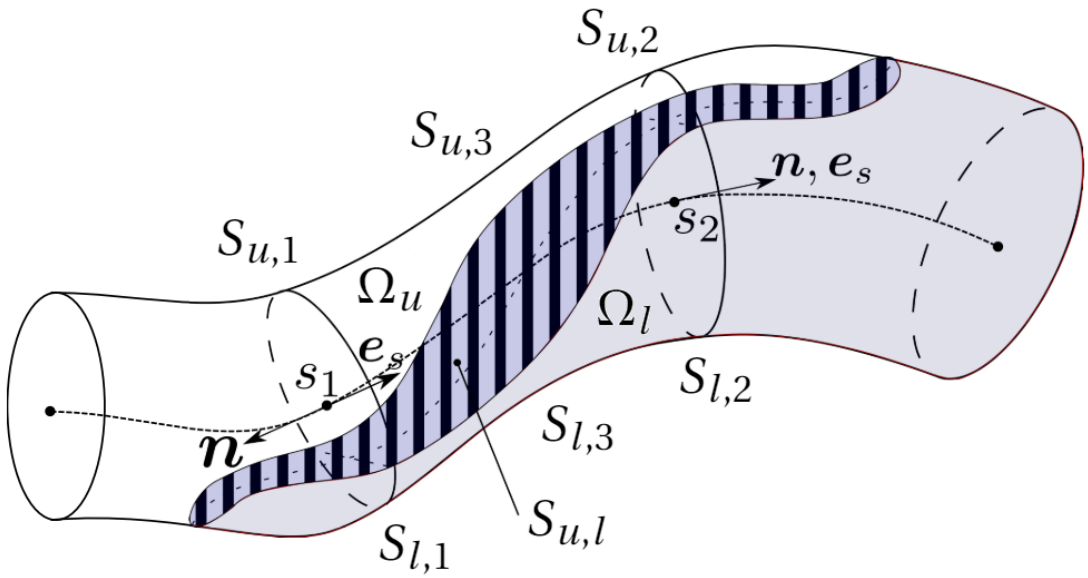

Figure 2.2: An arbitrary pipe section with two regions, both occupied by two miscible fluids. For example, the total volume of the upper region is bounded by the boundaries $\partial\Omega_l = S_{l,1} \cup S_{l,2} \cup S_{l,3} \cup S_{u,l}$. The upper region with volume Ω_u is depicted as transparent and the lower region with volume Ω_l is depicted in light grey. The interphasial surface between the two regions is striped in light blue and black [7].

The integral form of the mass conservation equation of the upper region with volume Ω_u yields:

$$\frac{\mathrm{d}}{\mathrm{d}t}\int_{\Omega_u}\rho_u \mathrm{d}\Omega + \int_{S_{u,1}}\rho_u \boldsymbol{u}_u\cdot\boldsymbol{n}\,\mathrm{d}S + \int_{S_{u,2}}\rho_u \boldsymbol{u}_u\cdot\boldsymbol{n}\,\mathrm{d}S + \int_{S_{u,3}}\rho_u \boldsymbol{u}_u\cdot\boldsymbol{n}\mathrm{d}S + \int_{S_{u,l}}\rho_u \boldsymbol{u}_u\cdot\boldsymbol{n}\mathrm{d}S = 0, \tag{2.18}$$

where $\rho_u(\boldsymbol{x},t)$ is the density of the upper region and $\boldsymbol{u}_u(\boldsymbol{x},t) = (u_{s,u}, u_{r,u}, u_{\theta,u})$ is the velocity vector in the upper region. In an analogous way to the case of single phase flow, the terms of the Eq. (2.18) are rewritten to derive the one-dimensional differential equation as follows:

$$\frac{\mathrm{d}}{\mathrm{d}t}\int_{\Omega_u}\rho_u \mathrm{d}\Omega = \frac{\mathrm{d}}{\mathrm{d}t}\left(\{\rho_u\}(t)\,V_u(s,t)\right), \tag{2.19}$$

$$\int_{S_{u,1}}\rho_u \boldsymbol{u}_u\cdot\boldsymbol{n}\mathrm{d}S = -\left[\frac{1}{A_u(s_1,t)}\int_{S_{u,1}}\rho_1 \boldsymbol{u}_u\cdot\boldsymbol{e}_s\,\mathrm{d}S\right]A_u(s_1,t) = -\left\langle\rho_u u_{s,u}\right\rangle(s_1,t)\,A_u(s_1,t), \tag{2.20}$$

$$\int_{S_{u,2}}\rho_u \boldsymbol{u}_u\cdot\boldsymbol{n}\mathrm{d}S = \left\langle\rho_u u_{s,u}\right\rangle(s_2,t)\,A_u(s_2,t), \tag{2.21}$$

$$\int_{S_{u,3}}\rho_u \boldsymbol{u}_u\cdot\boldsymbol{n}\mathrm{d}S = 0, \tag{2.22}$$

$$\int_{S_{u,l}}\rho_u \boldsymbol{u}_u\cdot\boldsymbol{n}\mathrm{d}S = \left[\frac{1}{A_{u,l}(s,t)}\int_{S_{u,l}}\rho_u \boldsymbol{u}_u\cdot\boldsymbol{n}\mathrm{d}S\right]A_{u,l}(s,t) = \langle\Psi_{lu}\rangle(s,t)\,A_{u,l}(s,t). \tag{2.23}$$

Here, $\langle\Psi_{lu}\rangle$ is the cross-sectional averaged mass transfer rate of the lower region to the upper per unit area. Its units are $[\mathrm{kg/m^2 s}]$. The mass transfer rate arises from the advective component of the mass conservation equation. It should be interpreted as the mass exchange of the light and heavy fluid from the lower region to the upper region, or vice versa. The subscript $(.)_{lu}$ is used to define the direction of the mass exchange rate. The direction from the lower to the upper region is defined as positive, as the y-coordinate is positive in this direction. In section 3.3.5, $\langle\Psi_{lu}\rangle$ is further elaborated.

$A_{u,l}$ is the area of the interphasial surface between the two regions and can be approximated by:

$$A_{u,l}(s,t) = P_{u,l}(s,t)\,\Delta s, \tag{2.24}$$

where $P_{u,l}$ is the interphasial surface length and $\Delta s = s_2 - s_1$ is the length of the arbitrary pipe section. $P_{u,l}$ is also called the interphasial perimeter and is further elaborated in section 3.3.1. The subscript $(.)_{u,l}$ is not used to assign a direction to the variable, it simply indicates that both regions are involved in the variable.

Substituting all rewritten terms back into Eq. (2.18), yields:

$$\frac{\mathrm{d}}{\mathrm{d}t}\left(\{\rho_u\}(t)\,V_u(s,t)\right) - \langle \rho_u u_{s,u}\rangle(s_1,t)\,A_u(s_1,t) + \langle \rho_u u_{s,u}\rangle(s_2,t)\,A_u(s_2,t) + \langle \Psi_{lu}\rangle(s,t)\,P_{u,l}(s,t)\,\Delta s = 0. \tag{2.25}$$

The differential form of the mass conservation equation for the upper region can be obtained by taking a small finite volume $V_u(s,t) = A_u(s,t)\delta s$ with side $A_u(s,t)$ and $A_u(s+\delta s,t)$. This results in:

$$\frac{\mathrm{d}}{\mathrm{d}t}\left(\{\rho_u\}(t)\,A_u(s,t)\delta s\right) + \langle \rho_u u_{s,u}\rangle(s+\delta s,t)\,A_u(s+\delta s,t) - \langle \rho_u u_{s,u}\rangle(s,t)\,A_u(s,t) + \langle \Psi_{lu}\rangle(s,t)\,P_{u,l}(s,t)\,\delta s = 0. \tag{2.26}$$

Dividing by δs, taking the limit $\delta s \to 0$ and substituting $A_u(s,t) = \alpha_u(s,t)A(s)$, yields:

$$\frac{\partial}{\partial t}\left(\alpha_u(s,t)\langle \rho_u\rangle(s,t)\,A(s)\right) + \frac{\partial}{\partial s}\left(\alpha_u(s,t)\langle \rho_u u_{s,u}\rangle(s,t)\,A(s)\right) + \Psi_{lu}(s,t)\,P_{u,l}(s,t) = 0. \tag{2.27}$$

Now, the differential form of the conservation of mass for the upper region is obtained.

$$\frac{\partial}{\partial t}\left(\alpha_u \rho_u A\right) + \frac{\partial}{\partial s}\left(u_{s,u}\alpha_u \rho_u A\right) + \Psi_{lu}P_{u,l} = 0 \tag{2.28}$$

Here, the averaging brackets and dependencies are omitted for readability purposes. [25] This equation can be easily extended for the case of two regions, $\beta \in \{u,l\}$. In literature, this miscible continuity equation is often called the Individual Phase Continuity Equation (IPCE) [8]. The equation reads:

$$\frac{\partial}{\partial t}\left(\alpha_\beta \rho_\beta A\right) + \frac{\partial}{\partial s}\left(u_{s,\beta}\alpha_u \rho_\beta A\right) + \Psi_{\beta_2\beta_1}P_{\beta_1,\beta_2} = 0, \tag{2.29}$$

where $\beta = \{\beta_1,\beta_2\}$ and β_1 and β_2 denote the two regions present in the domain. The IPCE for immiscible flow looks similar, but it does not contain the mass transfer term. When the sum over IPCE for the two regions is taken, the Combined Phase Continuity Equation (CPCE) is found.

In addition to the conservation of mass, Sanderse [25] derived the conservation of momentum and energy for stratified flow. The interested reader is reffered to his work.

2.3. Transport equation

The transport equation is an advection-diffusion equation which uses advection and diffusion terms to track the change of physical variables over time and space. These transferred variables could be, for example, molar concentration or temperature.

Here, the transport equation is used to track the fluid volume fractions within the region. Another term for volume fraction is concentration; both words are used interchangeably throughout the report. First, the equation is elaborated for single phase flow, after which the derivation of the transport equation is given for the case of multiphase flow.

2.3.1. Single phase flow

In the case of single phase flow the volume fraction is used to tracke the concentration of species within the single phase. For example the concentration of a coloring dye in water in space and time. In section 3.3.4, this example is addressed in the experiments carried out by Hart to determine an empirical relation for the axial dispersion coefficient.

Recall the arbitrary pipe section illustrated in Fig. 2.1 with volume Ω and bounded by $\partial\Omega = S_1 \cup S_2 \cup S_3$. The same orthogonal curvilinear coordinate system is employed with $\boldsymbol{x} = \{s, r, \theta\}$. As a starting point to obtain the one-dimensional cross-sectionally averaged transport equation, the integral form reads:

$$\frac{\partial}{\partial t}\int_{\Omega} c\,(\boldsymbol{x}, t)\,\mathrm{d}\Omega + \int_{\partial\Omega} \boldsymbol{f}\cdot\boldsymbol{n}\mathrm{d}S = 0. \tag{2.30}$$

Here, $c(\boldsymbol{x}, t)$ is the volume fraction or concentration is dimensionless $[m^3/m^3] = [-]$, $\boldsymbol{n}$ is the outward directed normal vector at the boundaries and $\boldsymbol{f}$ is the flux vector of c. The flux vector describes the amount of transport of the volume fraction across the boundaries $\partial\Omega$. It consists out of an advection and a diffusion component with unit of $[m/s]$. The advection and diffusion components are defined as:

$$f_{\text{adv}} = c\,(\boldsymbol{x}, t)\,\boldsymbol{u}\,(\boldsymbol{x}, t)\,, \tag{2.31}$$

$$f_{\text{diff}} = -\mathscr{D}(\boldsymbol{x}, t)\nabla c\,(\boldsymbol{x}, t)\,, \tag{2.32}$$

where $\boldsymbol{u}(\boldsymbol{x}, t) = u_s\cdot\boldsymbol{e}_s + u_r\cdot\boldsymbol{e}_r + u_\theta\cdot\boldsymbol{e}_\theta$ is the velocity vector, $\mathscr{D}(\boldsymbol{x}, t) = \mathscr{D}_s\cdot\boldsymbol{e}_s + \mathscr{D}_r\cdot\boldsymbol{e}_r + \mathscr{D}_\theta\cdot\boldsymbol{e}_\theta$ is the dispersion coefficient vector and $\nabla = (\partial/\partial s)\cdot\boldsymbol{e}_s + (1/r)\cdot(\partial/\partial r)\cdot\boldsymbol{e}_r + (\partial/\partial\theta)\cdot\boldsymbol{e}_\theta$ is the divergence operator vector. The (axial) dispersion coefficient is explained in detail in Section 3.3.4.

Substituting the flux vectors in the integral form of the transport equation, gives:

$$\frac{\partial}{\partial t}\int_{\Omega} c(\boldsymbol{x}, t)\mathrm{d}\Omega + \int_{\partial\Omega} c(\boldsymbol{x}, t)\boldsymbol{u}(\boldsymbol{x}, t)\cdot\boldsymbol{n}\mathrm{d}S - \int_{\partial\Omega}\mathscr{D}(\boldsymbol{x}, t)\nabla c(\boldsymbol{x}, t)\cdot\boldsymbol{n}\mathrm{d}S = 0. \tag{2.33}$$

The three terms of Eq. (2.33) are cross-sectionally averaged, as:

$$\frac{\mathrm{d}}{\mathrm{d}t}\int_{\Omega} c(\boldsymbol{x}, t)\mathrm{d}\Omega = \frac{\mathrm{d}}{\mathrm{d}t}\left(\{c\}\,(t)V\right), \tag{2.34}$$

$$\int_{\partial\Omega} c(\boldsymbol{x}, t)\boldsymbol{u}(\boldsymbol{x}, t)\cdot\boldsymbol{n}\mathrm{d}S = -\left\langle cu_s\right\rangle(s_1)\,A(s_1, t) + \left\langle cu_s\right\rangle(s_2, t)\,A(s_2)\,, \tag{2.35}$$

$$-\int_{\partial\Omega}\mathscr{D}(\boldsymbol{x}, t)\nabla c(\boldsymbol{x}, t)\cdot\boldsymbol{n}\mathrm{d}S = \left\langle\mathscr{D}_s\frac{\partial c}{\partial s}\right\rangle(s_1, t)\,A(s_1) - \left\langle\mathscr{D}_s\frac{\partial c}{\partial s}\right\rangle(s_2, t)\,A(s_2)\,. \tag{2.36}$$

The terms in equations (2.35) and (2.36) are the fluxes through the inlet area S_1 and outlet area S_2 by the advection and diffusion component, respectively. The flux through the pipe surface S_3 is zero, $\boldsymbol{u}\cdot\boldsymbol{n} = 0$. Combining all five terms, yields:

$$\begin{aligned}\frac{\mathrm{d}}{\mathrm{d}t}\left(\{c\}\,(t)V\right) - \left\langle cu_s\right\rangle(s_1, t)\,A(s_2) + \left\langle cu_s\right\rangle(s_2, t)\,A(s_1)\\ + \left\langle\mathscr{D}_s\frac{\partial c}{\partial s}\right\rangle(s_1, t)\,A(s_1) - \left\langle\mathscr{D}_s\frac{\partial c}{\partial s}\right\rangle(s_2, t)\,A(s_2) = 0.\end{aligned} \tag{2.37}$$

The differential form of the transport equation can be obtained by taking a small finite volume $V = A(s)\delta s$ with sides $A(s)$ and $A(s+\delta s)$, this results in:

$$\begin{aligned}\frac{\mathrm{d}}{\mathrm{d}t}\left(\{c\}\,(t)A(s)\delta s\right) - \left\langle cu_s\right\rangle(s, t)\,A(s) + \left\langle cu_s\right\rangle(s+\delta s, t)\,A(s+\delta s)\\ + \left\langle\mathscr{D}_s\frac{\partial c}{\partial s}\right\rangle(s, t)\,A(s) - \left\langle\mathscr{D}_s\frac{\partial c}{\partial s}\right\rangle(s+\delta s, t)\,A(s+\delta s) = 0.\end{aligned} \tag{2.38}$$

Dividing by δs, taking the limit of $\delta s \to 0$ and assuming that the average of product of functions is equal to the product of averages, yields:

$$\frac{\partial cA}{\partial t} + \frac{\partial u_s cA}{\partial s} - \frac{\partial}{\partial s}\left(\mathscr{D}_s\frac{\partial c}{\partial s}A\right) = 0. \tag{2.39}$$

This equation is the transport equation for single phase flow. The brackets and dependent variables are omitted for simplicity [7].

2.3.2. Multiphase flow

In Section 2.2.2, it was already mentioned that two created virtual regions are separated by an interfacial surface. The volume of the fluids in both regions are of interest, as these volumes are constantly changing in magnitude due to the miscible character of the fluids. The light and heavy fluid volumes in the upper and lower region are going to interact with each other. The physical model should be able to capture this effect. The multiphase flow transport equations are used to track these changes of the volume fractions over time and space.

Following the definition of the hold-up, the volume fractions of the light and heavy fluid in the upper and lower region are as follows:

- c_{Lu} denotes the volume fraction of light fluid particles in the upper region;

$$c_{Lu} := \frac{A_{Lu}}{A_u}, \tag{2.40}$$

- c_{Hu} is the volume fraction of heavy fluid particles in the upper region;

$$c_{Hu} := \frac{A_{Hu}}{A_u}, \tag{2.41}$$

- c_{Ll} is the volume fraction of light fluid particles in the lower region;

$$c_{Ll} := \frac{A_{Ll}}{A_l}, \tag{2.42}$$

- c_{Hl} is the volume fraction of heavy fluid particles in the lower region;

$$c_{Hl} := \frac{A_{Hl}}{A_l}. \tag{2.43}$$

The summation of the volume fractions in the upper and lower region are by definition equal to one, namely:

$$\frac{A_{Lu} + A_{Hu}}{A_u} = c_{Lu} + c_{Hu} = 1, \qquad \frac{A_{Ll} + A_{Hl}}{A_l} = c_{Ll} + c_{Hl} = 1. \tag{2.44}$$

The total volume fraction of the light fluid present in the system, reads:

$$\begin{aligned} c_L &:= \frac{A_{Lu} + A_{Ll}}{A} = \frac{A_{Lu}}{A_u}\frac{A_u}{A} + \frac{A_{Ll}}{A_l}\frac{A_l}{A}, \\ &= c_{Lu}\alpha_u + c_{Ll}\alpha_l. \end{aligned} \tag{2.45}$$

Similarly, the total volume fraction of the heavy fluid reads:

$$\begin{aligned} c_H &:= \frac{A_{Hu} + A_{Hl}}{A} = \frac{A_{Hu}}{A_u}\frac{A_u}{A} + \frac{A_{Hl}}{A_l}\frac{A_l}{A}, \\ &= c_{Hu}\alpha_u + c_{Hl}\alpha_l. \end{aligned} \tag{2.46}$$

Consider the arbitrary pipe section illustrated in Fig. 2.2. The pipeline is occupied by two regions with volumes Ω_u and Ω_l; and bounded by $\partial\Omega_u$ and $\partial\Omega_l$. The orthogonal curvilinear coordinate system is again employed. To derive the cross-sectionally averaged multi-phase transport equations, the derivation of the fraction of the light fluid particles in the upper region is given as an example. The concentration of the light fluid in the upper region is tracked in volume Ω_u and its boundaries $\partial\Omega$.

The integral form of the change of c_{Lu} in time and space then reads:

$$\frac{\partial}{\partial t}\int_{\Omega_u} c_{Lu}(\boldsymbol{x},t)\mathrm{d}\Omega + \int_{\partial\Omega_u} c_{Lu}(\boldsymbol{x},t)\boldsymbol{u}_u(\boldsymbol{x},t)\cdot\boldsymbol{n}\mathrm{d}S - \int_{\partial\Omega_u} \mathscr{D}_u(\boldsymbol{x},t)\nabla c_{Lu}(\boldsymbol{x},t)\cdot\boldsymbol{n}\mathrm{d}S = 0, \tag{2.47}$$

where the advection and diffusion term are responsible for the transfer of the light fluid particles in the upper region through the boundaries $\partial\Omega_u$. The terms of Eq. (2.47) are cross-sectionally averaged as:

$$\frac{\mathrm{d}}{\mathrm{d}t}\int_{\Omega_u} c_{Lu}\mathrm{d}\Omega = \frac{\mathrm{d}}{\mathrm{d}t}\left(\{c_{Lu}\}(t)V_u(s,t)\right), \tag{2.48}$$

$$\int_{\partial\Omega_u} c_{Lu}\boldsymbol{u}_u\cdot\boldsymbol{n}\mathrm{d}S = -\left\langle c_{Lu}u_{s,u}\right\rangle(s_1,t)\,A_u(s_1,t) + \left\langle c_{Lu}u_{s,u}\right\rangle(s_2,t)\,A_u(s_2,t) + \ldots \tag{2.49}$$

$$\left\langle \Psi_{\mathrm{adv}_{L,lu}}\right\rangle(s,t)P_{u,l}(s,t)\Delta s,$$

$$-\int_{\partial\Omega_u} \mathscr{D}_u\nabla c_{Lu}\cdot\boldsymbol{n}\mathrm{d}S = \left\langle \mathscr{D}_{s,u}\frac{\partial c_{Lu}}{\partial s}\right\rangle(s_1,t)\,A_u(s_1,t) - \left\langle \mathscr{D}_{s,u}\frac{\partial c_{Lu}}{\partial s}\right\rangle(s_2,t)\,A_u\left(s_{2,t}\right) - \ldots \tag{2.50}$$

$$\left\langle \Psi_{\mathrm{diff}_{L,lu}}\right\rangle(s,t)P_{u,l}(s,t)\Delta s.$$

The advection and diffusion of the volume fraction is not transferred through the pipe surface $S_{u,3}$, due to the no flux condition $\boldsymbol{u}_u\cdot\boldsymbol{n}=0$. In contrast to the multiphase mass conservation equation, both the advection and diffusion terms contribute to an exchange term. As volume is transferred, this contribution of both terms represents a volumetric flow rate with units $[m^3/s]$, which is cross-sectionally averaged to obtain the units $[m/s]$. The summation of these terms results in the cross-sectionally averaged volumetric transfer rate of the light fluid from the lower to the upper region. The subscript of the volumetric transfer rate is denoted with the subscript $(.)_{L,lu}$. L indicates, that the this term refers to the transfer of light fluid. The term lu is used to represent the direction, in this case from the lower to the upper region. Similary the subscript ul refers to transfer from the upper to the lower region.

$$\left\langle \Psi_{L,lu}\right\rangle(s,t)P_{u,l}(s,t)\Delta s = \left(\left\langle \Psi_{\mathrm{adv}_{L,lu}}\right\rangle(s,t) - \left\langle \Psi_{\mathrm{diff}_{L,lu}}\right\rangle(s,t)\right)P_{u,l}(s,t)\Delta s \tag{2.51}$$

Substituting all cross-sectionally averaged terms back into Eq. (2.47), gives:

$$\begin{gathered}\frac{\mathrm{d}}{\mathrm{d}t}\left(\{c_{Lu}\}(t)V_u(s,t)\right) - \left\langle c_{Lu}u_{s,u}\right\rangle(s_1,t)\,A_u(s_1,t) + \left\langle c_{Lu}u_{s,u}\right\rangle(s_2,t)\,A_u(s_2,t) + \ldots \\ \left\langle \mathscr{D}_{s,u}\frac{\partial c_{Lu}}{\partial s}\right\rangle(s_1,t)\,A_u(s_1,t) - \left\langle \mathscr{D}_{s,u}\frac{\partial c_{Lu}}{\partial s}\right\rangle(s_2,t)\,A_u(s_2,t) + \left\langle \Psi_{L,lu}\right\rangle(s,t)P_{u,l}(s,t)\Delta s = 0.\end{gathered} \tag{2.52}$$

The differential form of the multiphase transport equation of the volume fraction of the light particles in the upper region can be obtained, if a small finite volume $V_u(s,t) = A_u(s,t)\delta s$ is taken with sides $A_u(s,t)$ and $A_u(s+\delta s,t)$. Substituting this in equation (2.52), yields:

$$\begin{gathered}\frac{\mathrm{d}}{\mathrm{d}t}\left(\{c_{Lu}\}(t)A_u(s,t)\delta s\right) - \left\langle c_{Lu}u_{s,u}\right\rangle(s,t)\,A_u(s,t) + \left\langle c_{Lu}u_{s,1}\right\rangle(s+\delta s,t)\,A_u(s+\delta s,t) + \ldots \\ \left\langle \mathscr{D}_{s,u}\frac{\partial c_{Lu}}{\partial s}\right\rangle(s,t)\,A_u(s,t) - \left\langle \mathscr{D}_{s,u}\frac{\partial c_{Lu}}{\partial s}\right\rangle(s+\delta s,t)\,A_u(s+\delta s,t) + \left\langle \Psi_{L,lu}\right\rangle(s,t)P_{u,l}(s,t)\delta s = 0\end{gathered} \tag{2.53}$$

Dividing by δ_s and taking the limit of δ_s going to zero, results in:

$$\begin{gathered}\frac{\partial}{\partial t}\left(\langle c_{Lu}\rangle(s,t)A_u(s,t)\right) + \frac{\partial}{\partial s}\left(\langle c_{Lu}\rangle(s,t)\left\langle u_{s,u}\right\rangle(s,t)A_u(s,t)\right) - \ldots \\ \frac{\partial}{\partial s}\left(\left\langle \mathscr{D}_{s,u}\right\rangle(s,t)\frac{\partial\langle c_{Lu}\rangle}{\partial s}(s,t)A_u(s,t)\right) + \left\langle \Psi_{L,lu}\right\rangle(s,t)P_{u,l}(s,t) = 0.\end{gathered} \tag{2.54}$$

Using the assumption that the average of the product is equal to the product of averages and omitting the brackets and function arguments the equation for c_{Lu} read:

$$\frac{\partial c_{Lu}A_u}{\partial t} + \frac{\partial c_{Lu}u_{s,u}A_u}{\partial s} - \frac{\partial}{\partial s}\left(\mathscr{D}_{s,u}\frac{\partial c_{Lu}}{\partial s}A_u\right) + \Psi_{L,lu}P_{u,l} = 0. \tag{2.55}$$

Note that $A_{Lu} = c_{Lu} A_u$. In fact, this equation tracks the area occupied by the light fluid particles in the upper region.

The volume fraction of the heavy fluid in the upper region c_{Hu} can be derived as:

$$c_{Hu} = 1 - c_{Lu}. \tag{2.56}$$

The general cross-sectional averaged multiphase transport equation for the volume fraction of a fluid B is defined as:

$$\frac{\partial c_{B\beta} A_\beta}{\partial t} + \frac{\partial c_{B\beta} u_{s,\beta} A_\beta}{\partial s} - \frac{\partial}{\partial s}\left(\mathscr{D}_{s,\beta} \frac{\partial c_{B\beta}}{\partial s} A_\beta\right) + \Psi_{B,\beta_2\beta_1} P_{\beta_1,\beta 2} = 0. \tag{2.57}$$

2.4. Bubble velocities

So far, the multiphase equations are derived to track the changes of mass and volume fractions over time and space. However, a fundamental equation for the velocities of both regions is not given yet. In Section 1.6, it was already mentioned that the velocities of the upper and lower region will included through a slip velocity relation. The effective bubble velocity, which is presented at the end of this section, will serve as the basis for deriving the slip velocity relation in Section 3.2.3.

In section 1.1, the Benjamin and the Taylor bubbles were presented. These bubbles are generated by a density difference between both fluids and the gravitational acceleration acting on the fluids. An example of flushing a V-shaped pipe section was also illustrated. Here, the theory behind Benjamin and Taylor bubbles is further described and the mathematical relations of their bubble velocities are given. At last, the bubble velocity in an inclined pipe section is given.

2.4.1. Benjamin bubble

In Fig. 1.1 (a) and (c), the classic example of the formation of a Benjamin bubble of two liquids was given. This example will also serve as a fundamental case of the numerical model. The function which should help the model to reproduce this classic Benjamin bubble is given in Section 3.3.3 and the results of the numerical model of this Benjamin bubble are given in Section 5.1.

Here, the formation of the Benjamin bubble within a stagnant fluid is considered. Fig. 2.3 illustrates the formation of this elongated bubble motion. The bubble can be encountered in the petrochemical industry, when a pipe full of stagnant liquid is opened at one side. Under the action of gravity, the liquid will flow out freely from this end. After the transient effects of the start of this process are completed, it is expected that an air-filled cavity replaces the volume of the ejected liquid. This process will steadily continue along the pipe [5]. The velocity at which the front of the air bubble is travelling is known as the Benjamin bubble velocity.

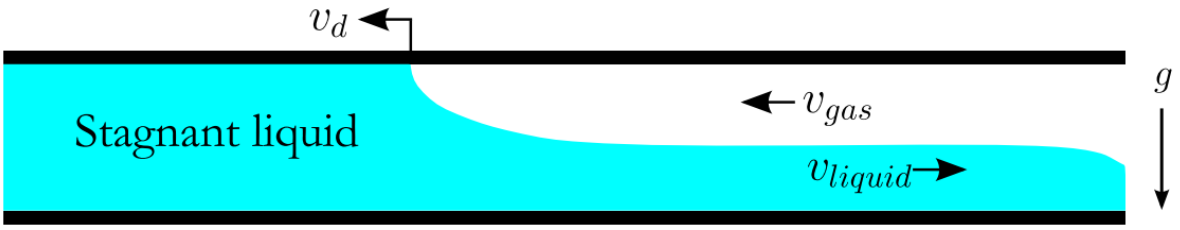

Figure 2.3: The formation of an air Benjamin bubble by opening a pipe filled with stagnant fluid. The depicted v_d indicates the bubble drift velocity, which is equal to the Benjamin bubble velocity in this scenario [26].

Benjamin [5] was the first to derive the expression for the bubble velocity and the shape of an elongated air bubble in stagnant water. First, he derived these parameters for both channel and pipe flow. To do so, he has assumed the flow to be steady. Furthermore, the effects of viscosity and the surface are assumed to be negligible. The density of air is also neglected, as the density of the liquid is much higher than the density of air. Benjamin has described the bubble configuration in a potential flow analysis, in which the frame of reference is moving with the front of the bubble. This is depicted in Fig. 2.4, where the air bubble is a stationary bubble.

The uniform velocity profiles with velocities u_1 and u_2 in Fig. 2.4 represent the velocity far upstream and downstream of the stagnant bubble. u_1 is the Benjamin bubble velocity u_B and u_2 is the water front velocity, denoted by u_F similar to the notation used in Fig. 1.1 (b). Point O is the stagnation point where the pressure is defined as the reference pressure; p_0. The red line along the interface of the bubble and yellow line along the pipe wall denote streamlines. At streamlines, Bernoulli's equation is constant.

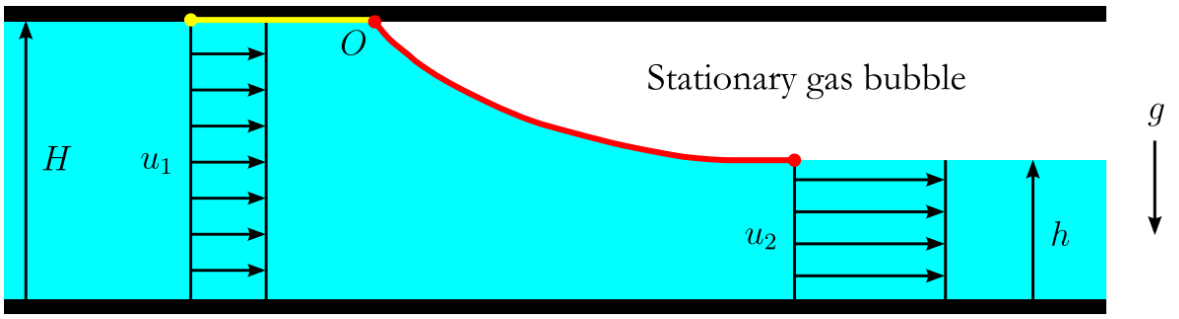

Figure 2.4: A similar configuration as is depicted in Fig. 2.3. Now, the front of the Benjamin bubble is further downstream and its movement is chosen as the frame of reference. This indicates that the air bubble is stagnant in this situation, while the water steadily moves underneath the bubbles [26].

A full derivation on the magnitudes of the velocities u_1 and u_2 and the interface height h is not given here. The interested reader is referred to Benjamin [5]. For pipe flow, Benjamin found that the magnitude of the bubble velocity could be described by the following expression:

$$u_B = 0.767\sqrt{gR}, \tag{2.58}$$

where g is the gravitational acceleration and R is the pipe's radius. The water front velocity reads:

$$u_F = 1.322\sqrt{gR}, \tag{2.59}$$

whereas the height of the interface h is:

$$h = 1.126R. \tag{2.60}$$

In the case of an air bubble traveling upstream in stagnant water, the velocity of the water front is higher than the velocity of the air bubble.

This does not hold for fluid-fluid displacements. In the classic Benjamin bubble example illustrated in Fig. 1.1, the water front moves slower than the oil bubble. Also, Benjamin extented the previous relation to include the densities of both fluids, as the density of the light fluid cannot be neglected anymore. This is done by replacing the contribution of gravity g by $\left(\Delta\rho/\rho_H\right)g$. $\Delta\rho = \rho_H - \rho_L$ is the positive density difference and ρ_H is the density of the heavy fluid [5].

The reason why the density of the heavy fluid is taken here, is illustrated by the following mathematical relation, where the limit of the density of the light fluid is taken to zero:

$$\lim_{\rho_L \to 0} \sqrt{\frac{\Delta\rho}{\rho_H} gR} = \sqrt{gR},$$

where the limit of the density of light fluid to zero indicates, that this density is again negligle with respect to the density of the heavy fluid, and that Benjamin bubble velocity must be determined by equation (2.58).

Therefore, the expression of the Benjamin bubble velocity for a fluid-fluid displacement case takes the form of:

$$u_B = 0.767\sqrt{\frac{\Delta\rho}{\rho_H} gR}, \tag{2.61}$$

and the expression of the water front velocity becomes:

$$u_F = 0.555\sqrt{\frac{\Delta\rho}{\rho_H} gR}. \tag{2.62}$$

The height of the interface h remains the same for fluid-fluid displacement as described in equation (2.60).

2.4.2. Taylor bubble

Small and large bubbles can be distinguished for a vertical pipe geometry, in which a less dense fluid rises into a denser fluid. The size of the bubble depends on the volume fraction of the less dense fluid. If the volume fraction is small, the fluid will rise in the form of small bubbles (for a gas) or droplets (in the case of a liquid). For a large volume fraction of less dense fluid, these bubbles are clustered together and form a large bubble. This type of elongated bubble has the shape of a bullet and is called a Taylor or Dumitrescu bubble. These two researchers independently derived the expression for a gas bubble rising in stagnant water. The Taylor bubble is denoted by the variable u_T [24].

To obtain the expression of the Taylor bubble, Taylor & Davies [31] and Dumitrescu [11] have made similar assumptions as Benjamin. They have neglected the density of the gas, the effects of viscosity and surface tension. The density of the stagnant water ρ_W, the pipe's radius R and the gravitational acceleration g are the only remaining physical variables. Out of these variables, the expression of the Taylor bubble is determined. To do so, a dimensional analysis is performed following the Buckingham Pi theorem [33], starting at the scaling law for the Taylor bubble:

$$u_T = C\rho_w^a R^b g^c, \tag{2.63}$$

where C is a proportionality constant and a, b and c are the exponents to guarantee the dimensional consistency of the equation.

Dumitrescu determined the proportionality constant at $C = 0.496$, by solving this flow configuration using potential flow theory [11]. The dimension of the Taylor bubble velocity is matched when $a = 0$, $b = c = \frac{1}{2}$ [24], as this results in the correct units: meters per second. The formula for the Taylor bubble velocity is:

$$u_T = 0.496\sqrt{gR}. \tag{2.64}$$

When the density of the less dense fluid is no longer negligible, equation 2.64 can be adjusted by substituting the contribution of the gravititional acceleration g by $\left(\Delta\rho/\rho_H\right)g$, so that both densities are taken into account. The Taylor bubble velocity reads:

$$u_T = 0.496\sqrt{\frac{\Delta\rho}{\rho_H}gR}. \tag{2.65}$$

2.4.3. Effective bubble velocity

In case of an inclined pipe, the velocity of the bubble velocity can be obtained by combining the expression for the Benjamin and Taylor bubbles. The inclined bubble velocity is called the effective bubble velocity, which is denoted by u_E [24].

Bendiksen [3] showed that the orthogonal projections of the Taylor and Benjamin bubble to the axial direction of the inclined pipe need to be added to approximate the effective bubble velocity. This is illustrated in Fig. 2.5, where the blue arrow represents the contribution of the Taylor bubble and the red arrow is the projection of the Benjamin bubble. The pipe inclination angle is denoted by θ.

The effective bubble velocity for fluid-fluid displacement is given as:

$$u_E = 0.767\sqrt{\frac{\Delta\rho}{\rho_H}gR}\cos(\theta) + 0.496\sqrt{\frac{\Delta\rho}{\rho_H}gR}\sin(\theta). \tag{2.66}$$

The expression is solely valid for pipe inclination angles between 0 and 90 degrees, $0 \leq \theta \leq 90$. To include downward-inclined pipes, the inclination angle is placed between absolute brackets. [24] The expression of the effective bubble velocity is given in the following short notation:

$$u_E = u_B\cos|\theta| + u_T\sin|\theta|. \tag{2.67}$$

To investigate the pipe inclination angle at which the effective bubble velocity is the highest, the derivate of u_E with respect to θ is taken. Thereafter, the derivative is equated to zero and solved for the pipe inclination angle.

$$\frac{\mathrm{d}u_E}{\mathrm{d}\theta} = (-0.767\sin|\theta| + 0.496\cos|\theta|)\sqrt{\frac{\Delta\rho}{\rho_H}gR} = 0 \tag{2.68}$$

Using this derivative, the minimum flow rate required to flush out all the remaining fluid in a pipe section can be determined [24].

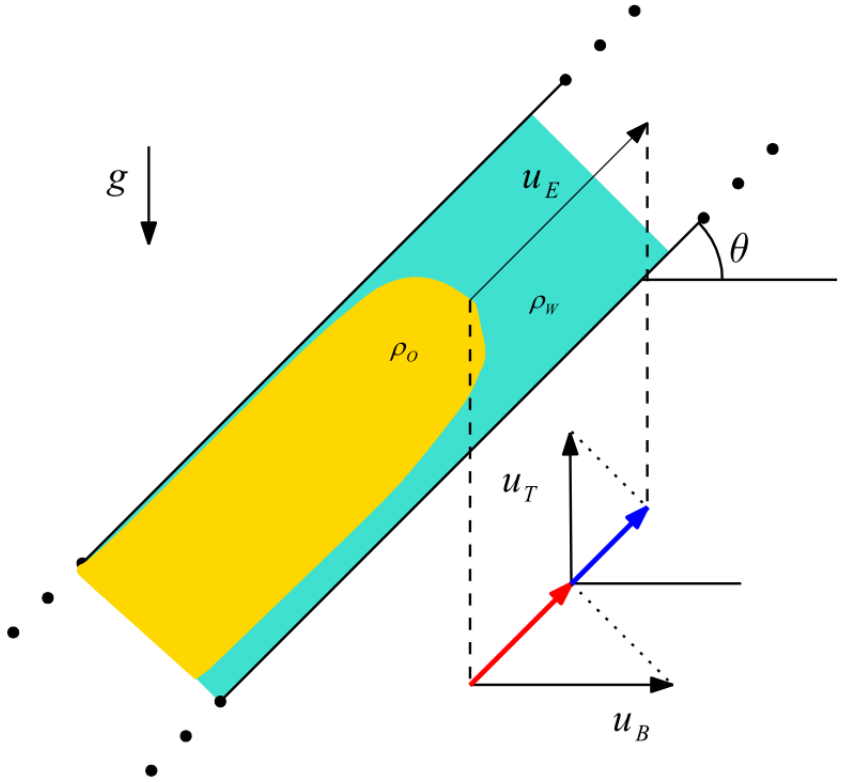

Figure 2.5: The rising of an elongated oil bubble in stagnant water in an inclined section with a positive pipe inclination angle, $\theta > 0$. This motion is created by the density difference between the oil and the water, $\rho_O < \rho_W$, under the influence of the gravitational acceleration. The effective bubble velocity is the velocity at which the front of the oil bubble propagates towards the top of the upward-inclined pipe section. The effective bubble velocity consists of the orthogonal projections of the Benjamin and Taylor bubble to the axial direction, respectively illustrated by red and blue arrow [24].

2.5. Important variables in fluid-fluid displacement

In Chapter 1, it was mentioned that many of parameters contribute to fluid-fluid displacement. Different parameters, such as the thermodynamic properties, the pipe diameter, pipe inclination and superficial velocity, have a large influence on the interactions between the fluids. The importance of physical variables with respect to other variables is demonstrated with dimensionless numbers. The relevant dimensionless numbers for fluid-fluid displacement are described later in this section. Besides the dimensionless numbers, the scaling of forces acting on the flows can illustrate which forces are important depending on the application. Firstly, the influential forces are shown.

2.5.1. Scaling of forces

As stated, depending on the type of application, some forces acting on the fluids can become more or less important than other forces. To obtain a clear insight of the importance of each force, the forces are scaled with respect to a typical length scale L. Below, an overview of the relevant (scaled) forces is given.

Inertia force f_I	$f_I \propto \rho u_s^2 L^{-1}$
Gravititional force f_G	$f_G \propto g\rho$
Buoyancy force f_B	$f_B \propto g\Delta\rho$
Viscosity force f_V	$f_V \propto \mu u_s L^{-2}$
Surface tension force f_S	$f_S \propto \sigma L^{-2}$
Pressure force f_P	$f_P \propto \Delta p L^{-1}$

The hydraulic diameter D_H can be taken as the characteristic length scale L for pipeline operations, $L = D_H$. It is directly noticed that the viscous and surface tension forces scale with D_H^{-2}. These forces are the dominant forces when the hydraulic diameter is sufficiently small. However, they are negligible for sufficiently large pipeline diameters. For large diameters, the gravitational and buoyancy forces are the most dominant forces acting on the fluids [24].

2.5.2. Dimensionless variables

A dimensional analysis is performed using all variables present in fluid-fluid displacement applications in order to obtain the relevant dimensionless numbers. The *Buckingham Pi theorem* is used to derive the dimensionless numbers. The Pi theorem states, that if a physical process involves n dimensional variables, it can be reduced to a relation between only k dimensionless variables or Πs. The reduction, $j = n - k$, equals the maximum number of variables that do not form a Π among themselves and is always less than, or equal to, the number of dimensions describing the variables [33]. The dimensions are usually given in the notation of $MLT\Theta$, which respectively represent the basic units mass, length, time and temperature. As the conservation of energy equation is not solved in the model, the Θ-dimension is not relevant in this study.

In Tab. 2.1, an overview of all dimensional variables is given. It is seen that at least twelve dimensional variables exist for fluid-fluid displacement and the reduction is equal to three, $j = 3$. Together, the variables have the dimensions of mass, length and time. This results in 9 dimensionless variables or Π, $k = n - j = 9$.

Table 2.1: Dimensional variables of a fluid-fluid displacement application

Dimensional variable	**Symbol**	**Dimensions**
Axial velocity of upper region	$u_{s,u}$	LT^{-1}
Axial velocity of lower region	$u_{s,l}$	LT^{-1}
Hydraulic diameter	D_H	L
Density of upper region	ρ_u	ML^{-3}
Density of lower region	ρ_l	ML^{-3}
Dynamic viscosity of upper region	μ_u	$ML^{-1}T^{-1}$
Dynamic viscosity of lower region	μ_l	$ML^{-1}T^{-1}$
Axial dispersion coefficient of upper region	$\mathscr{D}_{s,u}$	L^2T^{-1}
Axial dispersion coefficient of lower region	$\mathscr{D}_{s,l}$	L^2T^{-1}
gravititional acceleration	g	M^2T^{-1}
Surface tension	σ	MT^{-2}
Pressure drop	ΔP	$ML^{-1}T^{-2}$

The first four Πs are obvious. The ratios of the dimensional variables of the upper and lower region form dimensionless numbers. These dimensionless numbers are denoted with the superscript tilde, $\tilde{(\cdot)}$. It is chosen to dimensionalise these variables, using its contribution of the lower region in the denominator. Dimensionless density variables were already encountered in this study. Benjanmin [5] included the dimensionless density factor, $\Delta\rho/\rho_H$, in the Benjamin bubble velocity, to account for the density of the less dense fluid. Whereas, Henkes [15] added the factor $\rho_{\text{mix}}/\Delta\rho$ in the Froude number of equation 1.5 to account for stratification effects. This stratification Froude number is seen in the sixth Π.

$$\Pi_1 = \tilde{u_s} = \frac{u_{s,u}}{u_{s,l}}; \quad \Pi_2 = \tilde{\rho} = \frac{\rho_u}{\rho_l} \quad \text{or} \quad \Pi_2 = \tilde{\rho} = \frac{\Delta\rho}{\rho_H} \quad \text{or} \quad \Pi_2 = \tilde{\rho} = \frac{\rho_{\text{mix}}}{\Delta\rho}; \quad \Pi_3 = \tilde{\mu} = \frac{\mu_u}{\mu_l}; \quad \Pi_4 = \tilde{\mathscr{D}_s} = \frac{\mathscr{D}_{s,u}}{\mathscr{D}_{s,l}};$$

Logically, the Reynolds number is one of the dimensionless numbers found in fluid-fluid displacement applications. Here, the general Reynolds number of both regions is given. Besides, the mixture Reynolds number, found in equation (1.3), is shown. The mixture Reynolds number is the dimensionless variable, which is later used to form as empirical relation for the mass transfer between the regions.

$$\Pi_5 = Re_\beta = \frac{\rho_\beta u_{s,\beta} D_H}{\mu_\beta} \quad \text{or} \quad \Pi_5 = Re_{\text{mix}} = \frac{\rho_{\text{mix}} u_s D_H}{\mu_{\text{mix}}}$$

The Froude number is a dimensionless number to indicate the relative importance of inertia forces versus the gravity forces. The general Froude number is given for both regions. Also, the stratification Froude number of Henkes [15] and the Froude based on the effective bubble velocity, reported by Rosen Esquivel and IJzermans [24], are shown.

$$\Pi_6 = Fr_\beta = \frac{u_{s,\beta}^2}{gD_H} \quad \text{or} \quad \Pi_6 = Fr = \frac{\rho_{\text{mix}}}{\Delta\rho}\frac{u_s^2}{gD_H} \quad \text{or} \quad \Pi_6 = Fr = \frac{u_E}{\sqrt{\frac{\Delta\rho}{\rho_A}gD_H}}$$

The Schmidt number is a dimensionless number, defined as the ratio of the momentum diffusivity (kinematic viscosity) and the molecular mass diffusivity. It is similar to the Prandtl number, which is the ratio of the viscosity to the thermal diffusivity. The axial dispersion coefficient in the denominator of the Schmidt number is not equal to the molecular diffusion coefficient, as will become clear in Section 3.3.4. In fact, the presented Schmidt number might be interpreted as a turbulent Schmidt number without the eddy diffusivity.

$$\Pi_7 = Sc_\beta = \frac{\mu_\beta}{\rho_\beta \mathscr{D}_{s,\beta}}$$

The surface tension variable is seen in the Eötvös number. This dimensionless number is the ratio of the gravitational forces and the surface tension forces.

$$\Pi_8 = E\ddot{o} = \frac{g\Delta\rho D_H^2}{\sigma}$$

The Euler number is last. It is defined as the ratio of the pressure forces and the inertia forces and is used to characterise energy losses in the flow.

$$\Pi_9 = Eu = \frac{\Delta P}{\rho u_s^2}$$

Next to the just-derived dimensionless numbers, other dimensionless variables are used in the model. These dimensionless variables make it easy to compare cases and are denoted by the superscript $(.)^*$.

dimensionless time t^*	$t^* = t\sqrt{\frac{g}{D_H}}$
dimensionless axial distance s^*	$s^* = s\frac{1}{D_H}$
dimensionless superficial velocity u_s^*	$u_s^* = u_s\sqrt{\frac{1}{gD_H}}$
dimensionless interface height h^*	$h^* = h\frac{1}{D_H}$

2.6. Overview equations

Summarising the equations of conservation of mass, the multiphase transport equation and the effective bubble velocity:

$$\frac{\partial}{\partial t}\left(\alpha_\beta \rho_\beta A\right) + \frac{\partial}{\partial s}\left(u_{s,\beta}\alpha_u \rho_\beta A\right) + \Psi_{\beta_2\beta_1} P_{\beta_1,\beta_2} = 0, \tag{2.29}$$

$$\frac{\partial c_{B\beta} A_\beta}{\partial t} + \frac{\partial c_{B\beta} u_{s,\beta} A_\beta}{\partial s} - \frac{\partial}{\partial s}\left(\mathscr{D}_{s,\beta}\frac{\partial c_{B\beta}}{\partial s} A_\beta\right) + \Psi_{B,\beta_2\beta_1} P_{\beta_1,\beta 2} = 0, \tag{2.57}$$

$$u_E = u_B \cos|\theta| + u_T \sin|\theta|. \tag{2.67}$$

3

Miscible fluid-fluid model

This chapter provides additional information in order to better understand the model. As previously mentioned, the equations used in the numerical model are derived from the multiphase conservation of mass, the multiphase transport equation and the effective bubble velocity equation. In this chapter, the functions used in these equations are elaborated. These functions enable the model to find the correct physical solution in a stable way. At the end of the chapter, an overview of all assumptions that are necessary to come to this simplified model for two-phase flow is given. Also, an overview showing all the miscible fluid-fluid displacement equations is provided.

3.1. Model information

Consider the sketched configuration of Fig. 3.1 which shows a curved pipeline. In the pipeline two miscible fluids are present. The fluids have dissimilar densities, ρ_{L} and ρ_{H}. These densities represent the light and the heavy fluid. The general notation to denote the fluids is $B = \{L, H\}$ which is seen subscripts of the flow variables in Fig. 3.1. Often, the fluids are called the less dense and the denser fluid, to indicate the light and heavy fluid. An inferface between the fluids is barely recognizable and is definitely unsharp due to the miscibility character of the fluids. The light fluid is denoted by the colour red and is creeping over the heavy fluid. The denser fluid is denoted by the colour blue. The area which is not fully coloured in red or blue is defined as the mixing zone, where mass transfer takes place between the two fluids.

The curved pipe of Fig. 3.1 is described by a two-dimensional orthogonal curvilinear coordinate system. The axial axis tangential to its centreline is denoted by s and the axis perpendicular to its centreline is denoted by r. x and y represent the horizontal and vertical axis of the global coordinate system. The pipeline inclination angle along the centreline of the pipeline $\theta(s)$ is defined with respect to the x-axis and is positive in the counter-clockwise direction. The pipeline has a constant radius R and a constant cross-sectional area A.

Although the configuration is occupied with two fluids, it is assumed that a two-phase model can be used to determine the flow variables. Both fluids are treated as individual phases denoted by the subscripts $(.)_u$ and $(.)_l$, respectively indicating the upper and lower phase in the model. The general notation to denoted the phases is the subscript $\beta \in \{u, l\}$. The upper and lower phase are also called the upper and lower region, and were already introduced in Section 2.2.2. Both regions are occupied with light and heavy fluid particles. These particles contribute to the mass and volume of the regions. The subscripts $(.)_\beta$ and $(.)_B$ are used to subdivide the flow variables into the relevant region.

The ratio of the occupied cross-sectional area of a fluid and the total cross-sectional area is called the hold-up of a fluid, α. As the sum of the cross-sectional area of the regions adds up to equal the total cross-sectional area, the sum of the hold-ups does always add up to one, $\sum_\beta \alpha = 1$. The hold-up of the upper region α_u is denoted by the subscript $(.)_u$, hence it tends to float on top of the lower region. Following the opposite reasoning, the hold-up of the lower region α_l is denoted by the subscript $(.)_l$. The values of both α_u and α_l are required in the model. Therefore, two equations are necessary to solve them.

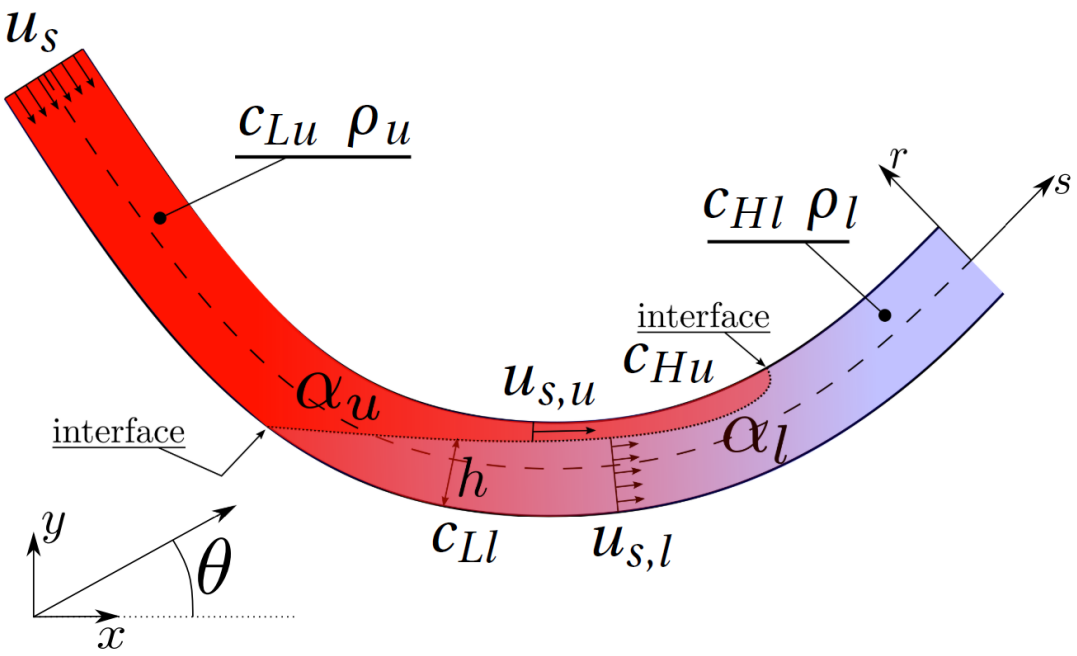

Figure 3.1: An arbitrary curved pipe section, in which two miscible fluids are present. The colour red denotes the light fluid and the colour blue denotes the heavy fluid. The area, where the colours are not 100% red or blue, is called the mixing zone, as the two fluids exchange mass and volume here [7].

Recall that no real interface can be determined between both fluids. However, an interfacial surface is assumed to exist. The corresponding interface height h is approximated with the help of the hold-ups and is denoted in Fig. 3.1 by a dashed line. This dependency of the interface height on the hold-up is explained later in Section 3.3.1. The interfacial surface height and its gradient with respect to the axial axis s are necessary in order to maintain a flat interface in an inclined pipe section. This is explained later in Section 3.3.3.

At the beginning of this arbitrary pipe section, the light fluid is entering the system at a certain velocity, being equal to the superficial velocity. The superficial velocity is denoted by u_s and is determined by the ratio of the volumetric flow rate $\dot{Q}$ and the cross-sectional area A, $u_s = \dot{Q}/A$. It is assumed that the velocity in radial direction can be neglected. The inlet velocity purely depends on the velocity in the axial direction. The axial velocity and the superficial velocity share the same notation, as they are assumed to be equivalent.

The density difference between the fluids and the pipe inclination angle results in a slip velocity between the upper and lower region. These regions move with the axial velocities $u_{s,u}$ and $u_{s,l}$, respectively. As these axial velocities often represent the velocity of an elongated bubble, they are called bubble velocities of the upper and lower region. The bubble velocities are determined by a slip relation, which is a function of the effective bubble velocity, and by an equation, which is derived from the multiphase conservation of mass, by means of the incompressibility condition (see the next Sections 3.2.2 & 3.2.3). The total velocity in axial direction is defined as $u_s = \sum_\beta \alpha_\beta u_{s,\beta} = \dot{Q}/A$. The volumetric flow rate of a region per unit area is defined as $j_\beta = \alpha_\beta u_{s,\beta}$. Another term used for the superficial velocity or total axial velocity is the mixture velocity.

To keep track of both fluids present in the upper and lower region, the volume fractions $c_{B\beta}$ were introduced in Section 2.3.2. Another term used for volume fraction is concentration. c_{Lu} is the concentration of the light fluid particles in the upper region and c_{Hu} is the concentration of the heavy fluid particles in the upper region, likewise for c_{Ll} and c_{Hl}. In Section 3.2.4 it is explained which multiphase transport equations are used to solve the four volume fraction in the model.

The densities of the regions, ρ_u and ρ_l, are found from extrapolation between both fluids by means of the volume fractions. The density of the upper region is defined as $\rho_u = c_{Lu}\rho_\mathrm{L} + c_{Hu}\rho_H$. Likewise, the density of the lower region is defined as $\rho_l = c_{Ll}\rho_L + c_{Hl}\rho_\mathrm{H}$. The dynamic viscosities per region, μ_u and μ_l, are determined in a similar way. The total mixture density is defined as $\rho = \sum_\beta \alpha_\beta \rho_\beta$.

3.2. Fluid-fluid equations

In total, eight independent variables need to be solved in this model:

- Hold-ups, α_u and α_l;
- Bubble velocities, $u_{s,u}$ and $u_{s,l}$;
- Volume fractions, c_{Lu}, c_{Hu}, c_{Ll} and c_{Hl}.

This indicates that at least eight equations are necessary to solve all the flow variables at every timestep. In this section, the fluid-fluid equations are derived to describe the miscible displacement in the model.

3.2.1. Hold-up equations

The IPCE of equation (2.29) is used as the starting point for the hold-up equation

$$\frac{\partial}{\partial t}\left(\alpha_\beta \rho_\beta A\right) + \frac{\partial}{\partial s}\left(\alpha_\beta \rho_\beta u_{s,\beta} A\right) + \Psi_{\beta_2\beta_1} P_{\beta_1,\beta_2} = 0. \tag{2.29}$$

Since the cross-sectional area is not time dependent, it is brought outside the first partial derivative. Immediately after this operation, the equation is divided by this cross-sectional area

$$\frac{\partial}{\partial t}\left(\alpha_\beta \rho_\beta\right) + \frac{1}{A}\frac{\partial}{\partial s}\left(\alpha_\beta \rho_\beta u_{s,\beta} A\right) + \frac{\Psi_{\beta_2\beta_1} P_{\beta_1,\beta_2}}{A} = 0. \tag{3.1}$$

By definition, the sum of the hold-ups always adds up to 1. By using this definition the IPCE needs to be solved for one of the fluids only. It is chosen to solve the hold-up of the light fluid present in the upper region, α_u.

Replacing the subscript $(.)_\beta$ with the subscript $(.)_u$ of the upper region, the mass transfer term $\Psi_{\beta_2\beta_1}$ with Ψ_{lu} and interface length P_{β_1,β_2} with $P_{u,l}$ in equation (3.1), obtains the hold-up equation for the upper region:

$$\frac{\partial}{\partial t}\left(\alpha_u \rho_u\right) + \frac{1}{A}\frac{\partial}{\partial s}\left(\alpha_u \rho_u u_{s,u} A\right) + \frac{\Psi_{lu} P_{u,l}}{A} = 0. \tag{3.2}$$

The equation to determine the hold-up of the lower region is defined as:

$$\alpha_l = 1 - \alpha_u. \tag{3.3}$$

3.2.2. Incompressible velocity equation

The flow is assumed to be incompressible. This indicates that the total density should be conserved in the system. The sum of the material derivative of the individual densities is zero by definition.

$$\sum_\beta \left(\frac{\mathrm{D}\rho_\beta}{\mathrm{D}t}\right) = \sum_\beta \left(\frac{\partial \rho_\beta}{\partial t} + u_{s,\beta}\frac{\partial \rho_\beta}{\partial s}\right) = 0 \tag{3.4}$$

The material derivative of the density of an individual phase is not equal to zero. This is due to mass transfer between the two regions.

$$\frac{\mathrm{D}\rho_\beta}{\mathrm{D}t} = \frac{\partial \rho_\beta}{\partial t} + u_{s,\beta}\frac{\partial \rho_\beta}{\partial s} \neq 0 \tag{3.5}$$

To determine the incompressible velocity equation, again, the IPCE of equation (2.29) serves as the starting point

$$\frac{\partial}{\partial t}\left(\alpha_\beta \rho_\beta A\right) + \frac{\partial}{\partial s}\left(\alpha_\beta \rho_\beta u_{s,\beta} A\right) + \Psi_{\beta_2\beta_1} P_{\beta_1,\beta_2} = 0. \tag{2.29}$$

Expanding the first partial derivative, to obtain two partial derivatives:

$$\alpha_\beta \frac{\partial}{\partial t}\left(\rho_\beta A\right) + \rho_\beta A\frac{\partial}{\partial t}\left(\alpha_\beta\right) + \frac{\partial}{\partial s}\left(\alpha_\beta \rho_\beta u_{s,\beta} A\right) + \Psi_{\beta_2\beta_1} P_{\beta_1,\beta_2} = 0. \tag{3.6}$$

Dividing the equation by ρ_β and taking the summation over the regions β, yields:

$$\begin{aligned} \frac{\alpha_\beta}{\rho_\beta}\frac{\partial}{\partial t}\left(\rho_\beta A\right) + A\frac{\partial}{\partial t}\left(\alpha_\beta\right) + \frac{1}{\rho_\beta}\frac{\partial}{\partial s}\left(\alpha_\beta \rho_\beta u_{s,\beta} A\right) + \frac{\Psi_{\beta_2\beta_1} P_{\beta_1,\beta_2}}{\rho_\beta} = 0, \\ \sum_\beta \left(\frac{\alpha_\beta}{\rho_\beta}\frac{\partial}{\partial t}\left(\rho_\beta A\right) + A\frac{\partial}{\partial t}\left(\alpha_\beta\right) + \frac{1}{\rho_\beta}\frac{\partial}{\partial s}\left(\alpha_\beta \rho_\beta u_{s,\beta} A\right)\right) = 0, \end{aligned} \tag{3.7}$$

where the mass exchange term $\Psi_{\beta_2\beta_1}$ has disappeared, since $\sum \Psi_{\beta_2\beta_1} = \Psi_{lu} + \Psi_{ul} = 0$. The summation of the hold-ups cannot change over time as $\sum_\beta \alpha_\beta = 1$, therefore its partial derivative with respect to time is zero.

$$A \sum_\beta \frac{\partial}{\partial t}\left(\alpha_\beta\right) = 0 \tag{3.8}$$

The equation reduces to:

$$\sum_\beta \frac{\alpha_\beta}{\rho_\beta} \frac{\partial}{\partial t}\left(\rho_\beta A\right) + \sum_\beta \frac{1}{\rho_\beta} \frac{\partial}{\partial s}\left(\alpha_\beta \rho_\beta u_{s,\beta} A\right) = 0. \tag{3.9}$$

By smartly expanding the second partial derivative and combining the first two terms, the sum of the material derivative of individual phase densities and the cross-sectional area is identified.

$$\begin{aligned} &\sum_\beta \left(\frac{\alpha_\beta}{\rho_\beta} \frac{\partial}{\partial t}\left(\rho_\beta A\right) + \frac{\alpha_\beta u_{s,\beta}}{\rho_\beta} \frac{\partial}{\partial s}\left(\rho_\beta A\right) + \frac{\rho_\beta A}{\rho_\beta} \frac{\partial}{\partial s}\left(\alpha_\beta u_{s,\beta}\right) \right) = 0 \\ &\sum_\beta \left(\frac{\alpha_\beta}{\rho_\beta} \left(\frac{\partial}{\partial t}\left(\rho_\beta A\right) + u_{s,\beta} \frac{\partial}{\partial s}\left(\rho_\beta A\right) \right) \right) + \sum_\beta \left(A \frac{\partial}{\partial s}\left(\alpha_\beta u_{s,\beta}\right) \right) = 0 \end{aligned} \tag{3.10}$$

The sum of this material derivative term is equal to zero, as is explained in equation (3.4). Due to the incompressibility condition, the IPCE is reduced to obtain the incompressible velocity equation:

$$A \sum_\beta \frac{\partial\left(\alpha_\beta u_{s,\beta}\right)}{\partial s} = 0, \tag{3.11}$$

where the cross-sectional area A is written outside the summation over the phases β, as it does not contain a space dependency.

The incompressible velocity equation is also called the divergence-free equation, as it satifiies $\nabla \cdot \mathbf{u} = 0$, due to the incompressibility condition.

3.2.3. Slip relation

The upper and lower region move at different axial velocities through the pipe. This is caused by the pipe inclination angle and the dissimiliar densities of the fluids. The fluids have the tendency to slip over each other at the assumed interface. The difference between the velocities is called the relative velocity. The second velocity equation is based on this principle. Therefore, this equation is called the slip relation.

The relative velocity between the upper and lower region is connected to the effective bubble velocity. However, they are not equal to each other. The effective bubble velocity u_E was defined in section 2.4.3 as:

$$u_E = u_B \cos|\theta| + u_T \sin|\theta| \tag{2.67}$$

where u_B and u_T are the Benjamin and Taylor bubble velocity, respectively and θ is the pipe inclination angle.

The slip relation is an artefact that corrects and matches the relative velocity to the effective bubble velocity and is defined as:

$$u_{s,u} - u_{s,l} = \mathscr{F}\mathscr{G}u_E, \tag{3.12}$$

where $\mathscr{F}$ and $\mathscr{G}$ are the functions needed for correcting and matching the slip velocity to the effective bubble velocity. These functions respectively are dependent on the hold-up of the light fluid and the gradient of the interfacial surface height with respect to the axial distance. The effective bubble velocity of equation (2.67) and (3.12) are not the same. The bubble velocity of equation (3.12) represents a function as well, of which the effective bubble velocity of equation (2.67) in theory could represent its maximum value. The functions $\mathscr{F}$, $\mathscr{G}$ and u_E are elaborated in Section 3.3.3.

3.2.4. Volume fraction equations

The general multiphase transport equation is used as the foundation for the volume fractions equations.

$$\frac{\partial c_{B\beta} A_\beta}{\partial t} + \frac{\partial c_{B\beta} u_{s,\beta} A_\beta}{\partial s} - \frac{\partial}{\partial s}\left(\mathscr{D}_{s,\beta} \frac{\partial c_{B\beta}}{\partial s} A_\beta\right) + \Psi_{B,\beta 2\beta 1} P_{\beta_1,\beta 2} = 0 \qquad (??)$$

As introducteed in Section 2.3.2, four volume fraction variables are of interest in the model; i.e. two volume fractions per fluid per region. These four volume fraction variables are:

c_{Lu}, volume fraction of the light fluid particles active in the upper region;
c_{Hu}, volume fraction of the heavy fluid particles active in the upper region;
c_{Ll}, volume fraction of the light fluid particles active in the lower region;
c_{Hl}, volume fraction of the heavy fluid particles active in the lower region.

The total volume fractions of the light and heavy fluid are defined as:

$$c_L = c_{Lu}\alpha_u + c_{Ll}\alpha_l \quad \text{and} \quad c_H = c_{Hu}\alpha_u + c_{Hl}\alpha_l \qquad (3.13)$$

By definition, the sum of the volume fractions in the upper and lower region is equal to one, as the volume of the light fluid plus the volume of the heavy fluid cannot exceed the total volume of the regions.

$$c_{Lu} + c_{Hu} = 1 \quad \text{and} \quad c_{Ll} + c_{Hl} = 1 \qquad (3.14)$$

By using this definition, only two multiphase transport equations need to be solved in the model. It is chosen to solve the volume fractions of the light fluid particles in the upper region and the heavy fluid particles present in the lower region, as these concentrations are expected to be the most dominant in the system. The four equations for solving the volume fraction variables are defined as:

$$\frac{\partial c_{Lu} A_u}{\partial t} + \frac{\partial c_{Lu} u_{s,u} A_u}{\partial s} - \frac{\partial}{\partial s}\left(\mathscr{D}_{s,u} \frac{\partial c_{Lu}}{\partial s} A_u\right) + \Psi_{L,lu} P_{u,l} = 0, \qquad (3.15)$$

$$c_{Hu} = 1 - c_{Lu}, \qquad (3.16)$$

$$\frac{\partial c_{Hl} A_l}{\partial t} + \frac{\partial c_{Hl} u_{s,l} A_l}{\partial s} - \frac{\partial}{\partial s}\left(\mathscr{D}_{s,l} \frac{\partial c_{Hl}}{\partial s} A_l\right) - \Psi_{H,ul} P_{u,l} = 0, \qquad (3.17)$$

$$c_{Ll} = 1 - c_{Hl}, \qquad (3.18)$$

where $\mathscr{D}_{s,u}$, $\mathscr{D}_{s,l}$ and $P_{u,l}$ are the axial dispersion coefficients of the upper and lower region and interface length between the regions, respectively. These variables are elaborated upon the Section 3.3.

3.3. Model functions

Functions serve as a closure for the just-derived equations. It would not be possible to generate a correct physical solution without them. This is required as the model in this study represents a simplified two-phase model. More importantly, the functions help to realise an effective and a stable solver. First, the Biberg approximation [6] is explained, as it is necessary to determine the wetted angle in a cross-sectional area filled with fluids. By using the wetted angle, the interfacial surface height, the wetted perimeters and hydraulic diameters can be calculated at any point in the pipe. The function of the wetted angle is followed by the slip relation functions: $\mathscr{F}$, $\mathscr{G}$ and u_E which are of great importance in the model and requires much attention. The axial dispersion coefficient and the transfer terms are also represented by functions, and are elaborated upon Sections 3.3.4 & 3.3.5.

3.3.1. Wetted angle

In Fig. 3.2, the cross-sectional area of an arbitrary pipe section is illustrated for a stratified flow. If the hold-ups are known, the areas occcupied by the regions can be determined; $A_u = \alpha_u A$ and $A_l = \alpha_l A$. Also, the interfacial height and the wetted perimeters play an important role in solving the velocities and volume fractions of both regions. This will become clear in the upcoming subsections 3.3.3 and 3.3.4. To determine these geometrical variables, the wetted angle γ_l has to be calculated. In Fig. 3.2, the geometrical variables and the wetted angle are visualized. The flow is idealised to have a flat surface.

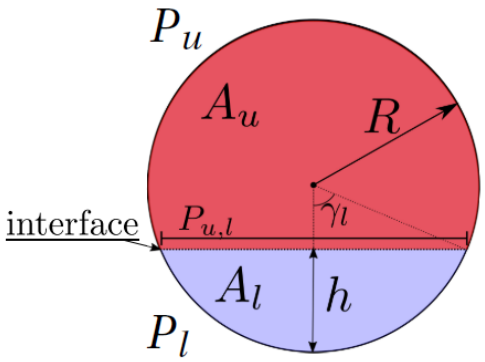

Figure 3.2: An arbitrary cross-sectional area of a pipe section, where the upper and lower regions are active. The wetted angle γ_l is used to determine all geometrical variables. [7]

The important geometrical variables can be determined with the help of trigonometry.

- the hold-up of the lower region versus the wetted angle, recall $\alpha_l = A_l / A$;

$$\alpha_l = \frac{1}{\pi}\left(\gamma_l - \frac{1}{2}\sin\left(2\gamma_l\right)\right) \tag{3.19}$$

- the interfacial height versus the wetted angle;

$$h = R\left(1 - \cos\left(\gamma_l\right)\right) \tag{3.20}$$

- the wetted interfacial perimeter versus the wetted angle;

$$P_{u,l} = 2R\sin\left(\gamma_l\right) \tag{3.21}$$

- the wetted wall perimeter of the lower region versus the wetted angle;

$$P_l = 2R\gamma_l \tag{3.22}$$

- the wetted wall perimeter of the upper region versus the wetted angle;

$$P_u = 2R\left(\pi - \gamma_l\right) \tag{3.23}$$

The wetted angle γ_l is given in [*rad*] and the pipe radius R is given in [m]. However, it is hard to derive a relation for the wetted angle as function of the hold-up of the lower region. An analytical approach exists using the Lagrange's equation, which contains a Bessel function J_n. A solution can also be found using a numerical approach. The disadvantage of these methods is that they are heavy to solve computionally. Those expressions have to be evaluated multiple times every timestep. Therefore, it is best to come up with an explicit approximation to determine the wetted angle as a function of the hold-up of the lower region. This explicit relation is called the Biberg approximation. [6]

The Biberg approximation has to match the analytic relation for the hold-up of the lower versus the wetted angle of equation (3.19). This relation is plotted in Fig. 3.3, where the wetted angle is normalized by π. Here, three points can be identified: $\gamma_l/\pi = 0$, $\frac{1}{2}$ and 1. Those points corresponds to a cross-sectional area, which is completely occupied by the light fluid, evenly occupied by both fluids and fully occupied by the heavy fluid, respectively.

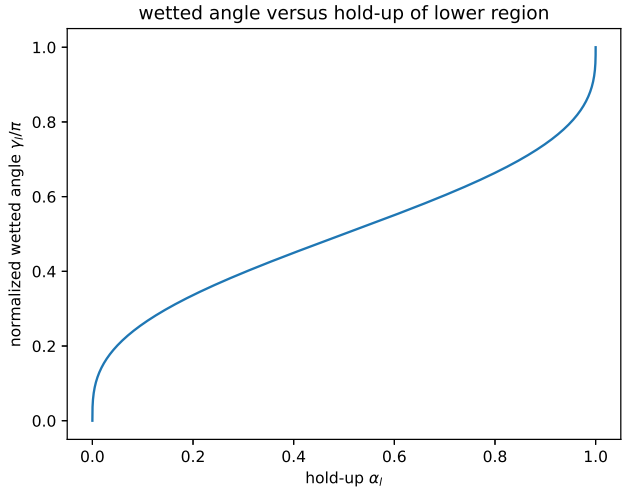

Figure 3.3: The exact solution of the wetted angle γ_l plotted against the hold-up of the lower region α_l following equation (3.19). The wetted angle is normalized by π.

Biberg approximated the wetted angle as:

$$\gamma_l = \pi\alpha_l + \left(\frac{3\pi}{2}\right)^{\frac{1}{3}} \left(1 - 2\alpha_l + \alpha_l^{\frac{1}{3}} - (1-\alpha_l)^{\frac{1}{3}}\right) + \epsilon_1, \tag{3.24}$$

where ϵ_1 is the truncation error, which is a function of the wetted angle and has a maximal magnitude of ± 0.002 [*rad*] for $0 \leq \gamma_l/\pi \leq 1$. This corresponds to inherent errors in the interfacial height and wetted perimeter, which are limited up to $\pm 0.2\%$ of the pipe diameter. Biberg has also given an approximation of higher accuracy.

$$\gamma_l = \pi\alpha_l + \left(\frac{3\pi}{2}\right)^{\frac{1}{3}} \left(1 - 2\alpha_l + \alpha_l^{\frac{1}{3}} - (1-\alpha_l)^{\frac{1}{3}}\right) - \frac{1}{200}\alpha_l(1-\alpha_l)(1-2\alpha_l)\left(1 + 4\left(\alpha_l^2 + (1-\alpha_l)^2\right)\right) + \epsilon_2 \tag{3.25}$$

Here, the truncation error ϵ_2 has a maximum value of $|\epsilon_2| \approx 0.00005$ [*rad*] for $0 \leq \gamma_l/\pi \leq 1$ and the error in the interfacial height and wetted perimeters is reduced to $\pm 0.005\%$ of the pipe's diameter. [6] The higher accuracy approximation is the preferred expression. Therefore, it is used in the model.

The geometrical variables, h, $P_{u,l}$, P_u and P_l, are all determined as the function of the wetted angle.

3.3.2. Hydraulic diameter

The hydraulic diameter is introduced to compare multiple duct flows to each other. Therefore, pipe and channel flow can be compared by means of the hydraulic diameter. The hydraulic diameter is found in the Reynolds number for all duct flow.

The hydraulic diameter is defined as four times the cross-sectional area divided by its wetted perimeter. The hydraulic diameter for pipe flow equals two times the pipe radius.

$$D_H = \frac{4A}{P} = \frac{4(A_u + A_l)}{P_u + P_l} = \frac{4\pi R^2}{2\pi R} = 2R \tag{3.26}$$

In the model, the hydraulic diameter is used to determine the Reynolds number of the upper and lower region throughout the whole system. This information is required to calculate the axial diffusion coefficients of both regions. The hydraulic diameters of the upper and lower region are denoted by $D_{H,u}$ and $D_{H,l}$ and are determined with the help of the approximated wetted angle γ_l.

$$D_{H,u} = \frac{4A_u}{P_u + P_{u,l}} \tag{3.27}$$

$$D_{H,l} = \frac{4A_l}{P_l + P_{u,l}} \tag{3.28}$$

3.3.3. Slip relation

In section 3.2.3, it was introduced that the slip relation is an artefact to match the relative slip velocity to the correct effective bubble velocity. This is achieved by the slip relation, using the functions $\mathscr{F}$, $\mathscr{G}$ and u_E.

$$u_{s,u} - u_{s,l} = \mathscr{F}\mathscr{G}u_E \tag{3.12}$$

The functions $\mathscr{F}$ and $\mathscr{G}$ are inserted in the model to take into account the effect of the hold-up of the regions and the developement of the interface between the fluids throughout the domain, respectively. To make the slip relation more stable, a function is introduced for the effective bubble velocity.

The functions $\mathscr{F}$ and $\mathscr{G}$ will be discussed first after which the function for the effective bubble velocity is explained. For the interface function $\mathscr{G}$, it will be shown that two forms exist depending on the flushing fluid.

The slip relation functions of $\mathscr{F}$ and u_E take on a special form, when the evaluated pipe section is completely horizontal, $\theta = 0$. This is discussed at the end of this section.

Hold-up function $\mathscr{F}$ The hold-up function $\mathscr{F}$ is introduced to take into account the effect of a vanishing region in the system. If a region vanishes, this indicates that only one fluid remains in the system. This effect could be measured by the magnitude of the hold-up. It is chosen to make $\mathscr{F}$ a function of the hold-up of the upper region, $\mathscr{F} = \mathscr{F}(\alpha_u)$, as this hold-up is also solved by the IPCE in the model. The choice for the hold-up does not matter, as the sum of the hold-ups is equal to one. This definition of the hold-ups indicates that

- if $\alpha_u = 0$, the upper region is removed from of the domain or the upper region has not yet entered the domain;
- if $\alpha_u = 0.5$, the upper region equals the lower region;
- if $\alpha_u = 1$, the lower region is moved out of the domain or the lower region has not yet entered the domain.

The vanishing of regions implies that one fluid is dominating the system. Only, the heavy fluid is left in the domain when $\alpha_u = 0$, likewise for the light fluid, when $\alpha_u = 1$.

A relative velocity can only exist when two fluids are present in the system. So, the hold-up function must be equal to zero when the hold-up of the upper region is equal to zero or one, $\mathscr{F}(\alpha_u = 0) = \mathscr{F}(\alpha_u = 1) = 0$.

The maximun value for the hold-up function is set at one, $\mathscr{F}(\alpha_u) = 1$. This indicates that only in the scenario that two regions are both active in the domain, the relative velocity could equal the theoretical highest magnitude of effective bubble velocity. To achieve this, the interface function $\mathscr{G}$ must be equal to one, $\mathscr{G} = 1$, and the bubble velocity function u_E has to match the maximum value of the effective bubble relation of equation (2.67). This scenario is not likely to happen.

At the moment, it is known that the hold-up function must equal $\mathscr{F}(\alpha_u) \in [0,1]$ for $0 \leq \alpha_u \leq 1$, but it is still unknown when $\mathscr{F}$ should equal its maximum value or how this value should be approached. The idea behind ranging the function between zero and one is:

- to prevent the need to use the hold-up function when only one region (fluid) is active in the domain, $\mathscr{F}(\alpha_u) = 0$ for $\alpha_u = 0$ and $\alpha_u = 1$;
- to limit the capacity of the hold-up function, when one fluid starts to enter the domain. The value of the hold-up of the upper region is less than the lower threshold value ε. Similarly, the capacity should be limited, when a fluid starts to leave the domain and α_u is greater than or equal to the upper threshold $(1-\varepsilon)$.

  The slip velocity cannot be completely equal to the effective bubble velocity in this application, as the upper region just begins to play a role or is about to give up its role in the domain,
  $\mathscr{F}(\alpha_u) \in [0,1]$ for $0 \leq \alpha_u < \varepsilon$ and $\alpha_u \geq (1-\varepsilon)$;
- to assign its maximum value to the hold-up function, when both regions (fluids) are well represented in the domain. The value of the upper hold-up satisfies both thresholds,
  $\mathscr{F}(\alpha_u) = 1$ for $\varepsilon \leq \alpha_u < (1-\varepsilon)$.

The hold-up function is no longer just a function of the hold-up of the upper region, but it is also a function of the just introduced threshold value ε, $\mathscr{F} = \mathscr{F}(\alpha_u, \varepsilon)$. A possible option for function $\mathscr{F}$ is to consider a linear relation between α_u and the upper and lower threshold values, like:

$$\mathscr{F}(\alpha_u, \varepsilon) = \begin{cases} \frac{1}{\varepsilon}\alpha_u, & \text{for } 0 \leq \alpha < \varepsilon, \\ 1, & \text{for } \varepsilon \leq \alpha_u < (1-\varepsilon), \\ -\frac{1}{\varepsilon}\alpha_u + \frac{1}{\varepsilon}, & \text{for } \alpha_u \geq (1-\varepsilon), \end{cases} \tag{3.29}$$

where the threshold value is directly connected to the slope of the function, $(1/\varepsilon)$. This option for the hold-up function is plotted in Fig. 3.4 for a threshold value of $\varepsilon = 0.3$.

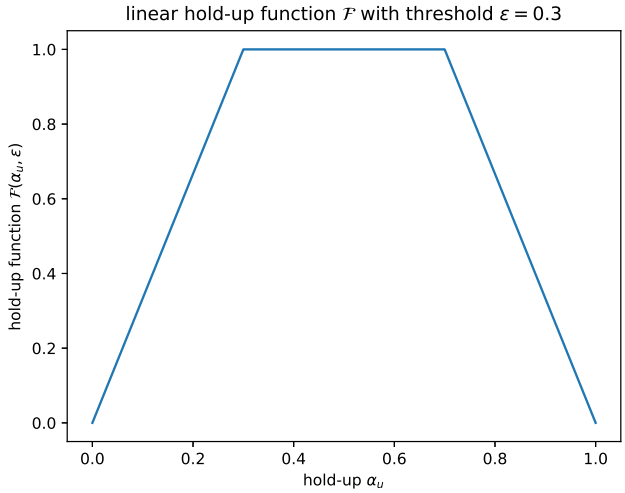

Figure 3.4: The hold-up function $\mathscr{F}$ expressed by a linear representation for a threshold value of $\varepsilon = 0.3$.

During his thesis work, Bouwhuis proved that functions which are exposed to abrupt changes in their values lead to numerical convergence problems. So, the hold-up function of equation (3.29) is not an option. Bouwhuis proposed the use of dosing relations in which the threshold values can easily be incorporated. The dosing relations decrease the function's derivative to give a more gradual approach to their minimum and maximum values [7]. The following dosing relations are used within the hold-up function:

- to gradually leave zero and to gradually approach one;

$$y(x) = -2\left(\frac{x}{\varepsilon}\right)^3 + 3\left(\frac{x}{\varepsilon}\right)^2 \tag{3.30}$$

- to gradually leave one and to gradually approach zero.

$$y(x) = 2\left(\frac{x}{\varepsilon}\right)^3 - 3\left(\frac{x}{\varepsilon}\right)^2 + 1 \tag{3.31}$$

The dosing relations are plotted in Fig. 3.5. It is illustrated how these relations achieve the decrease of the function's derivative and the gradual approach of its minimum and maximum values.

The hold-up function $\mathscr{F}$ is defined as:

$$\mathscr{F}(\alpha_u, \varepsilon) = \begin{cases} -2\left(\frac{\alpha_u}{\varepsilon}\right)^3 + 3\left(\frac{\alpha_u}{\varepsilon}\right)^2, & \text{for } 0 \leq \alpha < \varepsilon, \\ 1, & \text{for } \varepsilon \leq \alpha_u < (1-\varepsilon), \\ 2\left(\frac{\alpha_u - (1-\varepsilon)}{\varepsilon}\right)^3 - 3\left(\frac{\alpha_u - (1-\varepsilon)}{\varepsilon}\right)^2 + 1, & \text{for } \alpha_u \geq (1-\varepsilon). \end{cases} \tag{3.32}$$

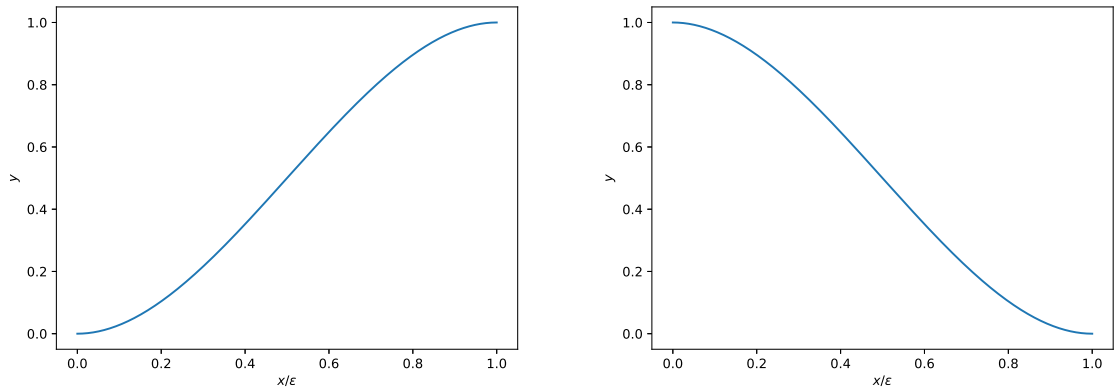

(a) equation (3.30)

(b) equation (3.31)

Figure 3.5: The dosing relations used in hold-up function $\mathscr{F}$, (a) to gradually move from zero to one and (b) to gradually move from one to zero. Note that the plotted dosing functions in (a) and (b) are normalized by the threshold value ε, which indicates that they hold for every ε.

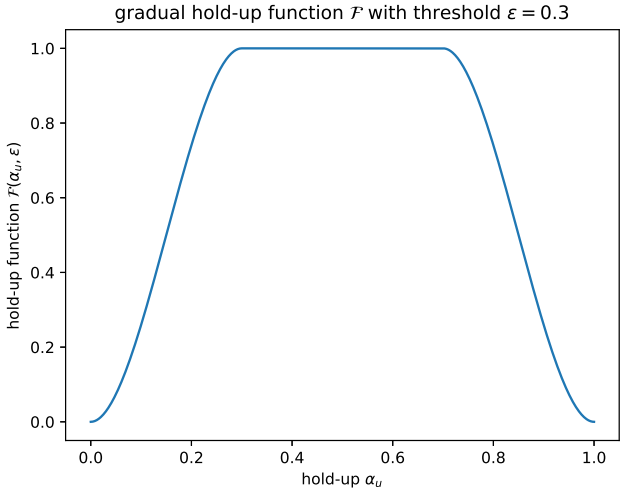

Figure 3.6: The hold-up function $\mathscr{F}$ of equation (3.32) versus the hold-up of the upper region and a threshold value ε of 0.3.

The hold-up function of equation (3.32) is plotted in Fig. 3.6 for a threshold value of $\varepsilon = 0.3$. Note that the hold-up function is easily derivated with respect to the hold-up of the upper region, which is useful for the Newton iterations. The Newton iteration is explained in Section 4.4 and elaborated upon Appendix B.

The slip relation is rewritten to:

$$u_{s,u} - u_{s,l} = \mathscr{F}(\alpha_u, \varepsilon)\, \mathscr{G}\, u_E. \tag{3.33}$$

Interface function $\mathscr{G}$ The interface function $\mathscr{G}$ is introduced to consider the effects of buoyancy on the developement of the interfacial surface in an inclined pipe section in the model. Function $\mathscr{G}$ depends on the pipe inclination angle θ, $\mathscr{G} = \mathscr{G}(\theta)$. Recall that the pipe inclination angle is positive in counter-clockwise direction with respect to the x-axis. The sections with a postive θ up to $\pi/2$ [*rad*] are referred to as *upward-inclined pipe sections* and the sections where θ is negative up to $-\pi/2$ [*rad*] are referred to as *downward-inclined pipe sections*.

Buoyancy forces arise at the interface between the two fluids, as a result of their dissimilar densities and the gravitational acceleration g. Recall that buoyancy can work in favor or against the flushing characteristics.

Two types of interfacial surfaces could be observed between the two regions, depending on the pipe inclination angle and the flow flushing characteristics. The flushing characteristics indicate whether the less dense fluid transports the denser fluid out of the system, or vice versa. The interface between the fluids is assumed to be horizontal in an inclined section, where the buoyancy forces are working against the flow direction. The interface will not be completely horizontal, as is illustrated in Fig. 1.2. A bubble interface will form inside sections where buoyancy is working in favour of the flushing fluid. Below, the four types of scenarios are summarized. Note that the mass of the upper region is locally smaller than the mass of the lower region, $\rho_u < \rho_l$. The light and heavy fluid respectively tend to be present especially in the upper and lower region.

- The less dense fluid flushes the denser fluid out of the pipe section.
  - A bubble will raise in the *upward-inclined pipe section*, as the upper region has a lower density than the lower region. The flow of the upper region is accelerated towards the end of the section. The axial velocity of the upper region exceeds the superficial velocity.
  - A horizontal interface will form between both regions in the *downward-inclined section*, as the buoyancy forces at the interfacial surface will balance each other. The interface descends in the section with approximately the total axial velocity, u_s.
- The denser fluid flushes the less dense fluid out of the pipe section.
  - A horizontal interface will form in between both regions in the *upward-inclined pipe section*, as the buoyancy forces at the interfacial surface are in equilibrium with each other. The interface moves up in the section with the superficial velocity, u_s.
  - A bubble will drop down in the *downward-inclined pipe section*, as the lower region is heavier than the upper region. The flow of the lower region is accelerated toward the end of the section and moves down at a higher velocity than the mixture velocity.

The formation of a horizontal and a bubble interface requires the interface function, in order to capture the two-phase flow phenomena. Therefore, the approach of the interface function for both phenomena is explained separately, starting with the approach for a horizontal interface.

A horizontal interfacial surface does not immediately establish in the pipe section. It needs time to develop until the buoyancy forces are in equilibrium. Therefore, a horizontal interface is called an equilibrium interface. When a (non-equilibrium) interfacial surface is moving through the pipe section, its interface angle ϕ with respect to the x-axis can be determined.

$$\tan\left(\phi\right) = \frac{\Delta h}{\Delta s}, \tag{3.34}$$

Here, Δh is the difference in interfacial surface height at the axial distance $\Delta s = s_2 - s_1$. The interface height is determined by equation (3.20) and s is the axial distance following the centreline of the pipe section. The angle is positive in counter-clockwise direction, measured from the centreline of the pipe.

The pipe inclination angle is equal to the interface angle when the interface is exactly horizontal and is sketched in Fig. 3.7a. However, the inclination and the interface angle are for all inclined pipe sections of opposite sign, $\theta = -\phi$. This must be valid over the entire length of the interfacial surface. Therefore, the equilibrium condition is given as:

$$\tan(\theta) + \left(\frac{\mathrm{d}h}{\mathrm{d}s}\right) = 0, \tag{3.35}$$

where $(\mathrm{d}h/\mathrm{d}s)$ is the gradient of the interface height with respect to the axial distance. This discrete variable is measured to track the changes of the interface angle over the relevant pipe sections where both regions are active. So, the interface function also depends on the gradient between the interfacial surface height and the axial distance, $\mathscr{G} = \mathscr{G}\left(\theta, \frac{\mathrm{d}h}{\mathrm{d}s}\right)$.

Two types of non-equilibrium interfaces can be observed. A non-equilibrium interface, where the inclination angle is smaller than the interface angle, $\theta < -\phi$, illustrated in Fig. 3.7b and a non-equilibrium, where $\theta > -\phi$. This is visualized in Fig. 3.7c. In both situations, the equilibrium interface, denoted by a dashed line, is intersected by the regions.

A front and a tail are added as extra definitions to the interfaces. The front of the interface is located above the centreline of the pipe section and the tail is located below the centreline of the pipe. The front and the tail will be used to illustrate their velocity difference. The definition of the front and the tail is not only valid in inclined section, where a horizontal interface is reproduced by the model. Also in other sections, a front and tail could be observed for either the upper or lower region. This depends on the flushing characteristics.

Note that the pipe configurations in Fig. 3.7 are solely given for a light fluid flushing a heavy fluid in a downward-inclined pipe section. From this point, all explanations in this section are solely given for this configuration. The same observations could be seen in upward-inclined pipe sections for a heavy fluid flushing out a light fluid.

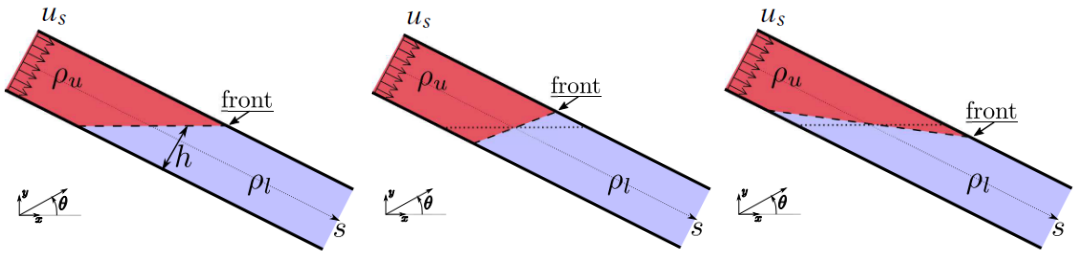

(a) Equilibrium interface, $\theta = -\phi$. (b) Non-equilibrium interface, $\theta < -\phi$. (c) Non-equilibrium interface, $\theta > -\phi$.

Figure 3.7: The type of interfaces, which could be observed in inclined sections, where a horizontal interface must be reproduced by the model. These type of interfaces are (a) the equilibrium interface, where $\theta = -\phi$, (b) a non-equilibrium interface, where $\theta < -\phi$ and (c) another non-equilibrium interface, where $\theta > -\phi$ is valid.

The purpose of the interface function G is to guide these non-equilibrium interfaces towards the equilibrium position. Now, it will be explained how the function is indeed able to achieve this for all three types of interfacial surfaces. Recall that the values of the hold-up function $\mathscr{F}$ range from zero to one. Furthermore, the values of the effective bubble velocity function u_E are always positive.

- *Equilibrium interface*, $\theta = -\phi$, corresponds with the equilibrium condition $\tan(\theta) + \left(\frac{\mathrm{d}h}{\mathrm{d}s}\right) = 0$ and is sketched in Fig. 3.7a. The equilibrium condition is satisfied along the entire interfacial surface between the two fluids. This implies that the interface is moving down towards the end of the section with the superficial velocity, u_s. The axial velocity of the upper and lower region are identical, $u_{s,u} = u_{s,l}$. The velocities at the front and the tail of the interfacial surface are the same, and the slip velocity is equal to zero. It is also possible that the equilibrium condition is only met locally along the interface.

  To incorporate this in the function, the value zero is assigned to the interface function $\mathscr{G}$ when the equilibrium condition holds entirely over the interface in the domain. It is possible that the equilibirum condition is locally validated at the interface as well. As the horizontal equilibrium position is already found, no slip velocity has to be initiated, $\mathscr{G}\left(\theta, \frac{\mathrm{d}h}{\mathrm{d}s}\right) = 0$.

- *Non-equilibrium interface*, $\theta < -\phi$, corresponds with $\tan(\theta) + \left(\frac{\mathrm{d}h}{\mathrm{d}s}\right) < 0$, sketched in Fig. 3.7b. In this scenario, the equilibrium condition is not met along the interfacial surface yet. To come to an equilibrium, two actions have to be taken.

  - The axial velocity of upper region at the front has to be accelerated, such that $u_{s,u} < u_{s,l}$ is valid locally. So, the relative velocity above the centreline is negative and needs to move towards zero. This requires the interface function to be positive, $\mathscr{G}\left(\theta, \frac{\mathrm{d}h}{\mathrm{d}s}\right) > 0$.
  - The axial velocity of the upper region at the tail of the interfacial surface has to be decelerated, as $u_{s,u} > u_{s,l}$ holds locally. Here, the slip velocity is positive and needs to move towards zero. The interface function is required to be negative, $\mathscr{G}\left(\theta, \frac{\mathrm{d}h}{\mathrm{d}s}\right) < 0$.

- *Non-equilibrium interface,* $\theta > -\phi$, corresponds with $\tan(\theta) + \left(\frac{\mathrm{d}h}{\mathrm{d}s}\right) > 0$, sketched in 3.7c. As the current interface does not satisfy the equilibrium condition, again two actions are necessary to guide the interface towards this position.
  - The axial velocity of the front of the interface moves faster than the front of the equilibrium interfacial surface and has to be decelerated. $u_{s,u} > u_{s,l}$ is satisfied here. The slip velocity is positive and has to move towards zero. This will be achieved when the interface function becomes negative, $\mathscr{G}\left(\theta, \frac{\mathrm{d}h}{\mathrm{d}s}\right) < 0$.
  - The axial velocity of the tail of the interface moves slower compared to its equal of the equilibrium interfacial surface. Therefore, the velocity has to be accelerated locally as $u_{s,u} < u_{s,l}$ is valid here. The relative velocity is negative and has to be zero for equilibrium. This is done by setting the interface function at positive values, $\mathscr{G}\left(\theta, \frac{\mathrm{d}h}{\mathrm{d}s}\right) > 0$.

Therefore, the interface function $\mathscr{G}$ must be able to assign a positive, a zero or a negative value to the slip velocity, depending on the inclination angle θ and the type of interface.

It is expected to see the effect of a positive, negative of zero interface function when reviewing the simulation results. In most specific sections, the middle of the modelled interface will satisfy the equilibrium condition and move down the pipe with the mixture velocity. The front and the tail of the interface will be transported faster or slower than the total axial velocity through the pipe section. The axial velocities of the front and tail of the region are moving faster or slower than the superficial velocity.

To prevent that the slip velocity exceeds the magnitude of the effective bubble velocity, the values of the interface function $\mathscr{G}$ range from -1 to 1, $\mathscr{G} \in \{-1, 1\}$. This is the same reasoning as used in the hold-up function $\mathscr{F}$. Bouwhuis has tried a linear relation between the minimum and maximum value of $\mathscr{G}$, but found a solution that did not converge. The velocities of the regions started to oscillate between a positive and a negative value when the equilibrium interface was approached and the equilibrium condition, corresponding with $\mathscr{G} = 0$, was never satisfied. Again, Bouwhuis proposed a dosing relation to decrease the function derivative and let $\mathscr{G}\left(\theta, \frac{\mathrm{d}h}{\mathrm{d}s}\right) = 0$ be approached gradually [7]. The dosing relation is defined as:

$$y(x) = \frac{1}{2}\left(\frac{x}{\frac{1}{2}\varepsilon}\right)^3, \tag{3.36}$$

where ε is a different threshold value than used in the hold-up function $\mathscr{F}$. The dosing relation is plotted in Fig. 3.8 for a x-axis which is normalized by ε. The plot of the dosing function is given for $\frac{x}{\varepsilon} = -\frac{1}{2}$ to $\frac{x}{\varepsilon} = \frac{1}{2}$.

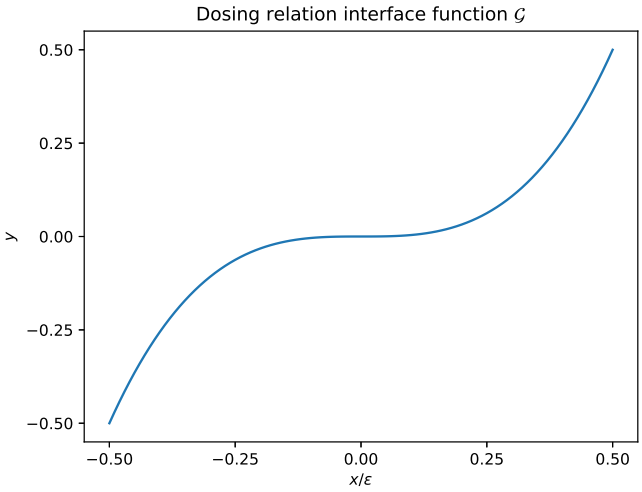

Figure 3.8: The dosing relation $y(x)$ which is defined in equation (3.36). The relation is used in interface function $\mathscr{G}$ to smoothen the area where the equilibrium condition, and the areas where the minimum and maximum values of the interface function are approached.

To avoid further confusion in the notation, the threshold value ε of the hold-up function is defined as ε_1, $\mathscr{F} = \mathscr{F}(\alpha_u, \varepsilon_1)$ and the threshold value of the interface function is defined as ε_2. The interface function also depends on this new threshold value, $\mathscr{G} = \mathscr{G}\left(\theta, \frac{\mathrm{d}h}{\mathrm{d}s}, \varepsilon_2\right)$.

In the hold-up function subsection, it was explained that functions which have abrupt changes around their minimum and maximum value are no option, as slow convergence or no convergence at all is found for the numerical model. The interface function is further smoothened to gradually approach $\mathscr{G} = -1$ and $\mathscr{G} = 1$ as well. This is also done with the help of the dosing relation proposed by Bouwhuis.

For the point $\mathscr{G} = -1$, the equation (3.36) is shifted to the left by a value of ε_2 and down by a value of -1. Similarly, the equation (3.36) is transferred to the right by a value of ε_2 and up by a value of 1. Note that the minimum and maximum value are located at $x = -\varepsilon_2$ and $x = \varepsilon_2$, respectively, and are always a distance of $2\varepsilon_2$ separated from each other, no matter the value of the threshold value ε_2. Furthermore, the point where the interface function is equal to $\mathscr{G} = 0$ is located a distance of $|\tan(\theta)|$ away from the vertical axis. Here, the equilibrium condition, $\tan(\theta) + \left(\frac{\mathrm{d}h}{\mathrm{d}s}\right) = 0$, is always satisfied.

The interface function $\mathscr{G}$ for the non-equilibrium interfaces to move towards the equilibrium position is defined as:

$$\mathscr{G}\left(\theta, \frac{\mathrm{d}h}{\mathrm{d}s}, \varepsilon_2\right) = \begin{cases} -1, & \text{for} \quad \tan(\theta) + \left(\frac{\mathrm{d}h}{\mathrm{d}s}\right) < -\varepsilon_2, \\ \frac{1}{2}\left(\frac{\tan(\theta) + \left(\frac{\mathrm{d}h}{\mathrm{d}s}\right) + \varepsilon_2}{\frac{1}{2}\varepsilon_2}\right)^3 - 1, & \text{for} \quad -\varepsilon_2 \leq \tan(\theta) + \left(\frac{\mathrm{d}h}{\mathrm{d}s}\right) < -\frac{1}{2}\varepsilon_2, \\ \frac{1}{2}\left(\frac{\tan(\theta) + \left(\frac{\mathrm{d}h}{\mathrm{d}s}\right)}{\frac{1}{2}\varepsilon_2}\right)^3, & \text{for} \quad -\frac{1}{2}\varepsilon_2 \leq \tan(\theta) + \left(\frac{\mathrm{d}h}{\mathrm{d}s}\right) < \frac{1}{2}\varepsilon_2, \\ \frac{1}{2}\left(\frac{\tan(\theta) + \left(\frac{\mathrm{d}h}{\mathrm{d}s}\right) - \varepsilon_2}{\frac{1}{2}\varepsilon_2}\right)^3 + 1, & \text{for} \quad \frac{1}{2}\varepsilon_2 \leq \tan(\theta) + \left(\frac{\mathrm{d}h}{\mathrm{d}s}\right) < \varepsilon_2, \\ 1, & \text{for} \quad \tan(\theta) + \left(\frac{\mathrm{d}h}{\mathrm{d}s}\right) > \varepsilon_2. \end{cases} \tag{3.37}$$

Note that in equation (3.37), the dependency on the flushing characteristics is not yet given. This function is visualized in Fig. 3.9 for a fixed inclination angle θ to provide a better understanding of its ability to gradually approach the values -1, 0 and 1.

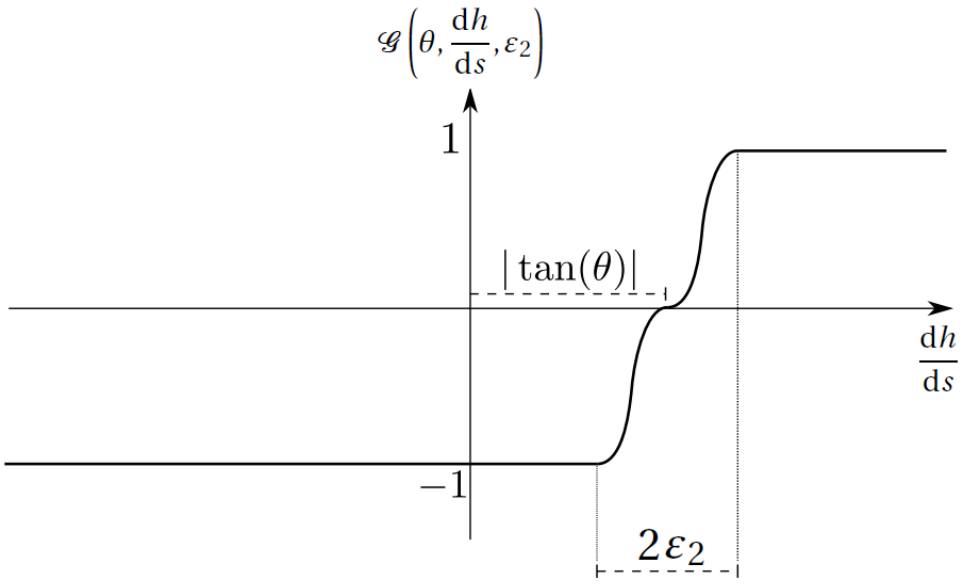

Figure 3.9: First visualization of the interface function of a horizontal interface for a fixed pipe inclination angle.

Since the formation process of the horizontal equilibrium interface is explained and incorporated in the interface function, the function is extended to integrate the formation of bubbles interface in the other pipe sections. A bubble will form in the upward-inclined section when a less dense fluid is flushing out a denser fluid from the domain. This is illustrated in Fig. 3.10a. When a denser fluid flushes out a less dense fluid on the other hand, a bubble will form in the downward-inclined sections. This is sketched in Fig. 3.10b.

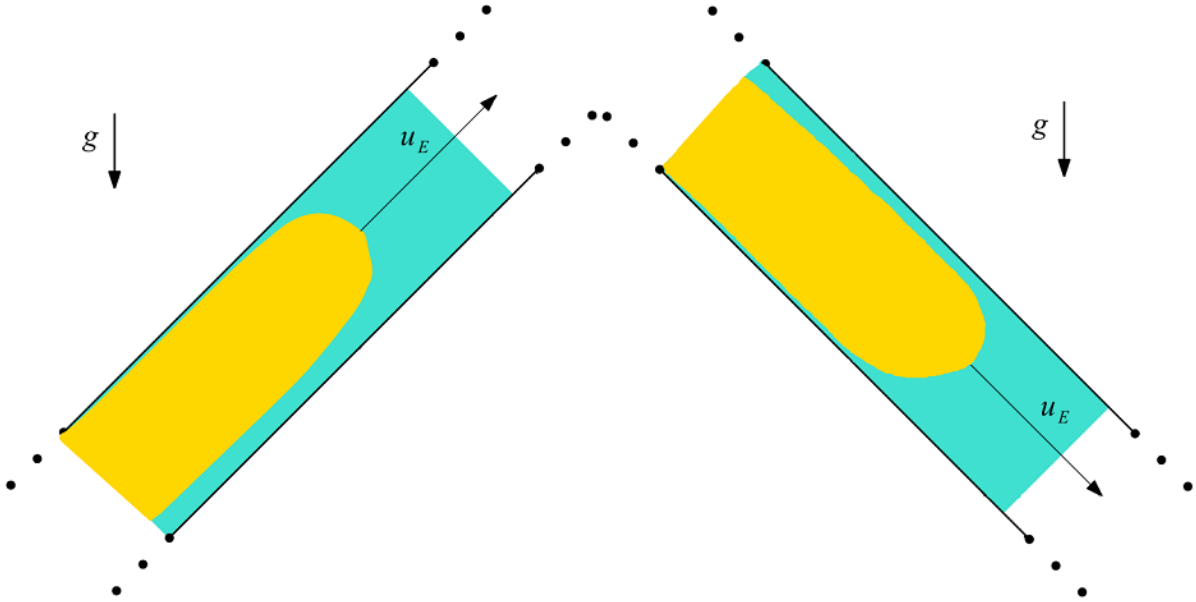

(a) Density differences result in an upward-directed buoyancy force.

(b) Buoyancy forces in favour of gravitational acceleration.

Figure 3.10: The bubble interface arises when in (a) an upward-inclined section when a light fluid flushes out a heavy fluid and (b) in a downward inclined pipe section when a heavy fluid flushes out a light fluid. [24]

The integration of the formation of bubble interfaces is easily done in the interface functions. It requires only two actions for the two different flushing characteristics.

- *Light fluid flushes out heavy fluid.* In the upward-inclined pipe section, the density difference results in buoyancy forces acting in the direction opposite to the gravitational acceleration g. The light fluid is accelerated towards the end of this section and the upper region pushes the lower region out of the domain. The axial velocity of the upper region accelerates until it dominates the section and reaches a fixed value, similar to the effective bubble velocity for this pipe inclination angle. The lower region decelerates until it is moved out the section, and its axial velocity is equal to zero. The axial velocity of the upper region is always greater than the axial velocity of the lower region in this pipe configuration, $u_{s,u} - u_{s,l} > 0$ must be valid here. To allow the axial velocity of the upper region to accelerate to the effective bubble velocity, determined by equation (2.67), the interface function for a light fluid flushing out a heavy fluid in an upward-inclined pipe section is set to one, $\mathscr{G}\left(\theta > 0, \frac{\mathrm{d}h}{\mathrm{d}s}\right), \varepsilon_2 = 1$.

- *Heavy fluid flushes out light fluid.* The dissimilar densities in the downward-inclined pipe section result in buoyancy forces acting in the same direction as the gravitational acceleration g. The heavy fluid is accelerated past the light fluid towards the end of this section. The light fluid particles descend in the section as well, but its velocity will be lower and even be decelerated. The upper region is eventually pushed out of the domain by the lower region. The axial velocity of the lower region accelerates until the heavy fluid dominates the pipe section. At that moment, the axial velocity of the lower region reaches a fixed value; i.e. the effective bubble velocity. As the velocity of the upper region is equal to zero, the relative velocity is always less than zero for this configuration, $u_{s,u} - u_{s,l} < 0$. The axial velocity of the lower region eventually becomes equal to the effective bubble velocity, calculated by equation (2.67). The interface function is assigned the value of -1 for a heavy fluid, flushing out a light fluid in a downward-inclined section, $\mathscr{G}\left(\theta < 0, \frac{\mathrm{d}h}{\mathrm{d}s}, \varepsilon_2\right) = -1$.

Therefore, the interface function $\mathscr{G}$ has two versions, for each one flushing characteristic. The interface function for a light fluid flushing a heavy fluid out of a pipe section is denoted by $\mathscr{G}_{LH}$ and is defined as:

$$\mathscr{G}_{LH}\left(\theta, \frac{\mathrm{d}h}{\mathrm{d}s}, \varepsilon_2\right) = \begin{cases} -1, & \text{for} \quad \tan(\theta) + \left(\frac{\mathrm{d}h}{\mathrm{d}s}\right) < -\varepsilon_2 \quad \text{and} \quad \theta < 0, \\ \frac{1}{2}\left(\frac{\tan(\theta) + \left(\frac{\mathrm{d}h}{\mathrm{d}s}\right) + \varepsilon_2}{\frac{1}{2}\varepsilon_2}\right)^3 - 1, & \text{for} \quad -\varepsilon_2 \leq \tan(\theta) + \left(\frac{\mathrm{d}h}{\mathrm{d}s}\right) < -\frac{1}{2}\varepsilon_2 \quad \text{and} \quad \theta < 0, \\ \frac{1}{2}\left(\frac{\tan(\theta) + \left(\frac{\mathrm{d}h}{\mathrm{d}s}\right)}{\frac{1}{2}\varepsilon_2}\right)^3, & \text{for} \quad -\frac{1}{2}\varepsilon_2 \leq \tan(\theta) + \left(\frac{\mathrm{d}h}{\mathrm{d}s}\right) < \frac{1}{2}\varepsilon_2 \quad \text{and} \quad \theta < 0, \\ \frac{1}{2}\left(\frac{\tan(\theta) + \left(\frac{\mathrm{d}h}{\mathrm{d}s}\right) - \varepsilon_2}{\frac{1}{2}\varepsilon_2}\right)^3 + 1, & \text{for} \quad \frac{1}{2}\varepsilon_2 \leq \tan(\theta) + \left(\frac{\mathrm{d}h}{\mathrm{d}s}\right) < \varepsilon_2 \quad \text{and} \quad \theta < 0, \\ 1, & \text{for} \quad \tan(\theta) + \left(\frac{\mathrm{d}h}{\mathrm{d}s}\right) > \varepsilon_2 \quad \text{and} \quad \theta < 0, \\ 1, & \text{for} \quad \theta \geq 0. \end{cases} \tag{3.38}$$

The interface function for a heavy fluid flushing out a light fluid of a pipe section, is denoted by $\mathscr{G}_{HL}$ and is defined as:

$$\mathscr{G}_{HL}\left(\theta, \frac{\mathrm{d}h}{\mathrm{d}s}, \varepsilon_2\right) = \begin{cases} -1, & \text{for} \quad \theta \leq 0, \\ -1, & \text{for} \quad \tan(\theta) + \left(\frac{\mathrm{d}h}{\mathrm{d}s}\right) < -\varepsilon_2 \quad \text{and} \quad \theta > 0, \\ \frac{1}{2}\left(\frac{\tan(\theta) + \left(\frac{\mathrm{d}h}{\mathrm{d}s}\right) + \varepsilon_2}{\frac{1}{2}\varepsilon_2}\right)^3 - 1, & \text{for} \quad -\varepsilon_2 \leq \tan(\theta) + \left(\frac{\mathrm{d}h}{\mathrm{d}s}\right) < -\frac{1}{2}\varepsilon_2 \quad \text{and} \quad \theta > 0, \\ \frac{1}{2}\left(\frac{\tan(\theta) + \left(\frac{\mathrm{d}h}{\mathrm{d}s}\right)}{\frac{1}{2}\varepsilon_2}\right)^3, & \text{for} \quad -\frac{1}{2}\varepsilon_2 \leq \tan(\theta) + \left(\frac{\mathrm{d}h}{\mathrm{d}s}\right) < \frac{1}{2}\varepsilon_2 \quad \text{and} \quad \theta > 0, \\ \frac{1}{2}\left(\frac{\tan(\theta) + \left(\frac{\mathrm{d}h}{\mathrm{d}s}\right) - \varepsilon_2}{\frac{1}{2}\varepsilon_2}\right)^3 + 1, & \text{for} \quad \frac{1}{2}\varepsilon_2 \leq \tan(\theta) + \left(\frac{\mathrm{d}h}{\mathrm{d}s}\right) < \varepsilon_2 \quad \text{and} \quad \theta > 0, \\ 1, & \text{for} \quad \tan(\theta) + \left(\frac{\mathrm{d}h}{\mathrm{d}s}\right) > \varepsilon_2 \quad \text{and} \quad \theta > 0. \end{cases} \tag{3.39}$$

Both functions are plotted in Fig. 3.11 in a three-dimensional environment for $-10 \leq \frac{\mathrm{d}}{\mathrm{d}s} \leq 10$ and $-90 \leq \theta \leq 90$. The black lines in the three-dimensional plots represent fixed pipe inclination angles. Furthermore, $y(x) = \arctan(-x)$ is plotted as a blue dashed line to visualize the position of equilibrium interface $\mathscr{G} = 0$.

The general notation for the interface function is $\mathscr{G}_{B_1B_2}$, where B_1 is the fluid that flushes out fluid B_2 of the domain, $B \in \{L, H\}$. The slip relation of equation (3.33) is extended to:

$$u_{s,u} - u_{s,l} = \mathscr{F}(\alpha_u, \varepsilon_1)\mathscr{G}_{B_1B_2}\left(\theta, \frac{\mathrm{d}h}{\mathrm{d}s}, \varepsilon_2\right) u_E. \tag{3.40}$$

Note that interface function $\mathscr{G}_{B_1B_2}$ is only defined for the postive flow direction, as the simplified model is considered in this direction alone.

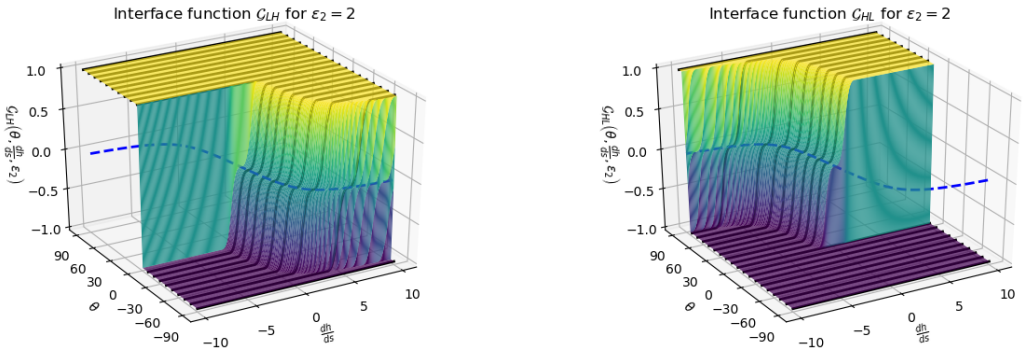

(a) equation (3.38)

(b) equation (3.39)

Figure 3.11: Three-dimensional plots for the interface functions, $\mathcal{G}_{LH}$ and $\mathcal{G}_{HL}$. The pipe inclination angle ranges from -90 to 90 [°] and the gradient of the interface height with respect to the axial distance ranges from -10 to 10.

Effective bubble velocity function u_E It was already mentioned that the effective bubble velocity in equation (3.12) represents a function of which the effective bubble velocity equation (2.67) helps to determine its magnitude. The purpose of the effective bubble velocity function is to make the slip relation more realistic for miscible flow.

The distinction between the effective bubble velocity function and the equation is the following: the equation determines the maximum value of the bubble velocity with the density of the light and heavy fluid for a specific inclination angle, whereas the function calculates the effective bubble velocity with the densities of the upper and lower region at a certain axial location. The densities of the upper and lower region are dependent on the volume fraction of the fluids per region and differ in most cases from the densities of the fluids.

The density of the upper region is determined by the following function:

$$\rho_u = \begin{cases} 0, & \text{for } \alpha_u < \varepsilon_3 \\ c_{Lu}\rho_L + c_{Hu}\rho_H, & \text{for } \varepsilon_3 \leq \alpha_u \leq 1. \end{cases} \tag{3.41}$$

The density of the lower region is solved with a similar function.

$$\rho_l = \begin{cases} 0, & \text{for } \alpha_l < \varepsilon_3 \\ c_{Ll}\rho_L + c_{Hl}\rho_H, & \text{for } \varepsilon_3 \leq \alpha_l \leq 1. \end{cases} \tag{3.42}$$

Again, ε_3 is a threshold value and is equal to $\varepsilon_3 = 0.001$. Note that the hold-ups, α_u and α_l, range between 0 and 1. The dynamic viscosities per region, μ_u and μ_l, are calculated with similar functions in the whole domain of the pipe.

The effective bubble velocity function is only active in pipe sections where the two regions are present, otherwise the function is equal to zero. The function needs a density difference between the two regions to form a bubble velocity. Furthermore, this density difference has to be less than the density of the heavy fluid minus the density of the light fluid, $\Delta\rho = \rho_H - \rho_L$. This was described as the positive density difference in Section 2.4.1.

The density difference depends on the location and is observed when one of the fluids enters the pipe section and thereby starts to flush the other fluid out of the domain. Irrespective of whether the less dense fluid flushes the denser fluid or vice versa, the same principal is observed. The flushing fluid creeps over or under the other fluid, to form an area for its own region. The just formed area is nearly totally filled by the flushing fluid and its density is nearly the density of its own fluid, likewise for the density of the other region. The density difference is close to its maximum difference. Therefore, the effective bubble velocity is almost at its peak value, when it first appears in the slip relation. The peak value of the effective bubble velocity holds until the point where one of the fluids is no longer dominant in its region.

This occurs when the flushing fluid moves further downstream in the pipe section, and the light and the heavy fluid start to mix more and more. In the front and the tail of the flushing fluid, less flushing fluid is present. Here, the fluids are able to mix quicker than in the middle region of the elongated bubble, which has its influence on the density per region at these locations; i.e. the densities of the upper and lower region will shift towards each other. This results in a magnitude of effective bubble velocity which is less for the front and the tail of the mixing zone. This magnitude gradually increases towards its peak value in the middle of the contamination zone. Thereby, the effective bubble velocity function helps the hold-up function in the gradual movement from its minimum to its maximum value. The function u_E can be seen as an extension of the hold-up function $\mathscr{F}$.

So, the effective bubble velocity depends on the densities of the upper and lower region and the pipe inclination angle. Recall that Benjamin has extended his bubble relation in a horizontal section by replacing the gravitational acceleration g for $g\Delta\rho/\rho_H$ [5]. Due the buoyancy effects between both fluids this factor is required, and therefore is adjusted in the model to $g(\rho_l-\rho_u)/\rho_l$. As only miscible fluids are considered, the effective bubble velocity changes over time. The effective bubble velocity function u_E is defined as:

$$u_E\left(\rho_u,\rho_l,\theta\right)=\begin{cases}0.767\sqrt{\dfrac{\rho_l-\rho_u}{\rho_u}gR}\cos(|\theta|)+0.496\sqrt{\dfrac{\rho_l-\rho_u}{\rho_u}gR}\sin(|\theta|), & \text{for } \rho_l-\rho_u<\rho_H-\rho_L\\ 0, & \text{Otherwise,}\end{cases} \tag{3.43}$$

All normal slip functions have been discussed and the slip relation is rewritten to:

$$u_{s,u}-u_{s,l}=\mathscr{F}\left(\alpha_u,\varepsilon_1\right)\mathscr{G}_{B_1B_2}\left(\theta,\frac{\mathrm{d}h}{\mathrm{d}s},\varepsilon_2\right)u_E\left(\rho_u,\rho_l,\theta\right). \tag{3.44}$$

The effective bubble velocity could have three possible effects on the fluid-fluid displacement, depending on the superficial velocity of the incoming flushing fluid.

1. The velocity is zero, $u_s=0\ [m/s]$. The movement of the fluid is initiated by the density differences and the fluids will move towards their equilibrium position in the pipe sections. The magnitude of the effective bubble velocity depends on the difference in thermodynamic properties of the fluid, the pipe inclination angle and the pipe radius. The magnitude of the effective bubble velocity determines at which rate the fluids find their equilibirum position.

2. The axial velocity is smaller (locally) than the effective bubble velocity, $u_s<u_E$. If the axial velocity is not large enough to overcome the effective bubble velocity for a less dense fluid flushing out denser fluid in an inclined section, this is no problem. In a downward-inclined section, buoyancy is working against the flushing mechanism and a bubble interface is seen that is assumed to be horizontal. The denser fluid is moving downward. In upward-inclined section, the buoyancy works in favor of the less dense fluid, as it accelerates in these sections. Due to the density difference, the denser fluid is pushed out rapidly, as the less dense fluid can reach velocities, which are typically in the order of the local effective bubble velocity. In the case of (nearly) horizontal sections in jumpers and tie-backs, there is trouble. As the less dense fluid arrives at such sections, it starts to creep over the denser fluid and forms a segregated flow layer. The denser fluid starts to accumulate in these sections. The denser fluid will remain in this stratified region until it gets diffused into the less dense fluid. This takes a serious amount of time, considering the fact that the molecular diffusion coefficient is responsible for the diffusion process.

3. The axial velocity is larger than the effective bubble velocity, $u_s>u_E$. The remaining denser fluid in the upward-inclined and downward-inclined pipe section is easily removed by the flushing fluid. In the horizontal section, the less dense fluid initially starts to float on top of the denser fluid, but the momentum of the less dense fluid is so high, that the stratified region is not observed long. The denser fluid does not accumulate in the low spots.

A scenario in which the axial velocity is exactly equal to the effective bubble velocity will be highly unlikely. Therefore, it is not discussed.

Special case of slip functions When the pipe inclination angle is zero, the slip relations of the hold-up function $\mathscr{F}$ and the effective bubble velocity function u_E take on a special form. The interface function G does not have to be altered for a horizontal pipe section, as its values at $\theta = 0$ [°] are equal to 1 and -1. This occurs for a less dense fluid flushing out a denser fluid or vice versa, respectively. The special form of the hold-up function is derived firstly.

In a horizontal pipe section, the model must recover stratified flow. The classical Benjamin bubble example illustrated in Fig. 1.1 (a) & (b) serves as the foundation of reproducing the stratification effects and gravity currents in the model. Another sketch of the classical Benjamin bubble is given in Fig. 3.12. It is seen, that the same functions are able to recover a segregated fluid layer in both stagnant as active flowing conditions. Here, active flow indicates that the superficial velocity of the flushing fluid is greater than zero.

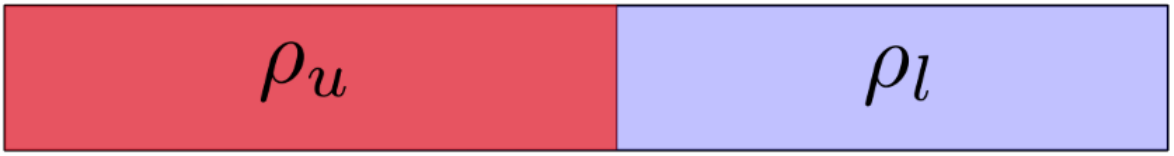

(a) Initial position of the two fluids at $t = 0$ [s], before the diaphragm is removed

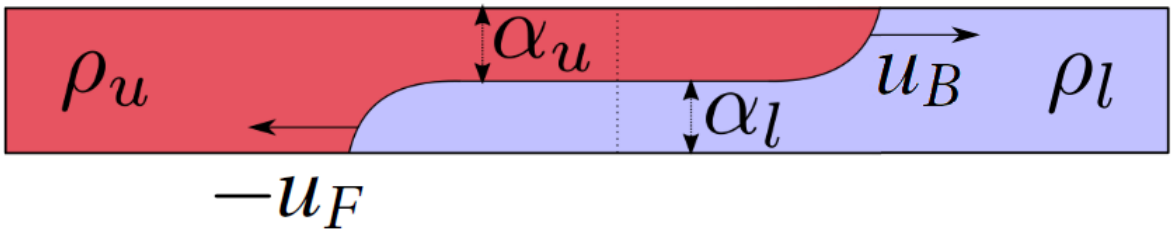

(b) Position of both fluids at $t = \Delta t$

Figure 3.12: The classic Benjamin bubble is illustrated at (a) time $t = 0$ [s] and (b) $t = \Delta t$. Initially, the light fluid is at the left hand side of the diaphragm and the heavy fluid is present at the right hand side of the diaphragm. (b) shows the movement after the diaphragm is removed, including some important flow variables [7].

In Fig. 3.12a, the initial position of the Benjamin bubble is illustrated. The less dense fluid is at the left of the diaphragm and the denser fluid on the right. When the diaphragm is broken at time $t = 0$ [s], an unbalance in the hydrostatic pressures forms at the interphasial surface. The less dense fluid starts to creep over the denser fluid, whereas the denser fluid moves below the less dense fluid. The front of the less dense fluid will move forward with the Benjamin bubble velocity of equation (2.61). Likewise, the front of the denser fluid will travel at the (water) front velocity of equation (2.62) in the opposite direction. The maximum magnitude of the effective bubble velocity is equal to the relative velocity between both regions, $u_{s,u} - u_{s,l} = u_B + u_F = u_E$.

Note that the height of the bubble is equal to $h = 1.126R$. The interface height gives a clear indication of the magnitude of the hold-up of the upper and lower region in the section of the pipe, where the Benjamin bubble is observed for fluid-fluid displacement. By using equations (3.19) & (3.20), the hold-up of the upper and lower region can be determined for the Benjamin bubble in a pipe section. This results in an equilibrium position of the Benjamin bubble for $\alpha_u \simeq 0.42$ and $\alpha_l \simeq 0.58$. As the hold-up function depends on the hold-up of the upper region, one boundary condition for the hold-up function in a horizontal pipe section is already known, $\mathscr{F}(\alpha_u \simeq 0.42) = 1$. Only for this value of the hold-up of the upper region, the hold-up function equals 1; i.e. the magnitude of the effective bubble velocity is maximum for this value. Therefore, the slip velocity is maximum for $\alpha_u \simeq 0.42$.

Two other boundary conditions for this hold-up function are the same as in the original hold-up equation, $\mathscr{F}(\alpha_u = 0) = \mathscr{F}(\alpha_u = 1) = 0$; i.e. a slip velocity must not be reproduced by the model, if one of the region is present in the pipe section.

The special form of the hold-up function is derived from the total volumetric flow rate of the regions per unit area and the slip function.

$$\alpha_u u_{s,u} + \alpha_l u_{s,l} = u_s \tag{3.45a}$$

$$u_{s,u} - u_{s,l} = \mathscr{F}\mathscr{G}_{B_1B_2} u_E \tag{3.45b}$$

equation (3.45a) must be interpreted as the added fluxes of both regions, which are equal to the total flux everywhere in the flow. As the less dense fluid is positioned on the left hand side of the diaphragm in the initial position, the current process is considered as a flushing process where the less dense fluid is flushing out the denser fluid, although the fluids are stagnant. Interface function G_{LH} is equal to 1 for this application, $\mathscr{G}_{B_1B_2} = G_{LH} = 1$. The maximum value of the effective bubble velocity is equal to the Benjamin velocity plus the front bubble velocity as stated earlier. The values of these functions are inserted into equation (3.45b) and equation (3.45a) is written in a matrix and vector formulation.

$$\begin{bmatrix} \alpha_u & \alpha_l \\ 1 & -1 \end{bmatrix} \begin{pmatrix} u_{s,u} \\ u_{s,l} \end{pmatrix} = \begin{pmatrix} u_s \\ \mathscr{F}(u_B + u_F) \end{pmatrix} \tag{3.46}$$

Rewriting the formulation to the solution of the velocity vector, yields:

$$\begin{pmatrix} u_{s,u} \\ u_{s,l} \end{pmatrix} = \frac{-1}{\alpha_u + \alpha_l} \begin{bmatrix} -1 & -\alpha_l \\ -1 & \alpha_u \end{bmatrix} \begin{pmatrix} u_s \\ \mathscr{F}(u_B + u_F) \end{pmatrix} \tag{3.47}$$

Knowing that $\sum_\beta \alpha_\beta = 1$, the equation is transformed into an equation notation, reads:

$$u_{s,u} = u_s + (1 - \alpha_u)\mathscr{F}(u_B + u_F) \tag{3.48a}$$

$$u_{s,l} = u_s - \alpha_u \mathscr{F}(u_B + u_F) \tag{3.48b}$$

Substituting $u_s = 0$, $u_{s,u} = u_B$ and $u_{s,l} = -u_F$, results in:

$$u_B = (1 - \alpha_u)\mathscr{F}(u_B + u_F) \tag{3.49a}$$

$$-u_F = -\alpha_u \mathscr{F}(u_B + u_F) \tag{3.49b}$$

If the superficial velocity is not equal zero, the velocity of the upper and lower region will take the values of $u_{s,u} = u_B + u_s$ and $u_{s,l} = -u_F + u_s$ and the observed equation (3.49) will be exactly the same. Solving equation (3.49) results in two solutions for the hold-up function in a horizontal pipe section.

$$\mathscr{F}(\alpha_u) = \frac{1}{(1 + u_F/u_B)(1 - \alpha_u)} \tag{3.50a}$$

$$\mathscr{F}(\alpha_u) = \frac{u_F/u_B}{(1 + u_F/u_B)\alpha_u} \tag{3.50b}$$

Both results are valid to be implemented for different areas of the hold-up of the upper region. For $\alpha_u < 0.42$, equation (3.50a) is employed and for $\alpha_u \geq 0.42$, equation (3.50b) is used. Summarized:

$$\mathscr{F}(\alpha_u) = \begin{cases} \dfrac{1}{(1 + u_F/u_B)(1 - \alpha_u)}, & \text{for } 0 \leq \alpha_u < 0.42, \\ \dfrac{u_F/u_B}{(1 + u_F/u_B)\alpha_u}, & \text{for } 0.42 \leq \alpha_u \leq 1. \end{cases} \tag{3.51}$$

equation (3.51) is plotted in Fig. 3.13. It is seen that only the boundary condition $\mathscr{F}(\alpha_u = 0.42) = 1$ is satisfied, whereas $\mathscr{F}(\alpha_u = 0) = 0$ and $\mathscr{F}(\alpha_u = 1) = 0$ are not. To meet the remaining two boundary conditions, the dosing relations which were introduced in equations (3.30) & (3.31) and respectively, as shown in Fig. 3.5a & 3.5b, are imployed. The threshold value ε_1 is used again. The updated hold-up function $\mathscr{F}$ becomes:

$$\mathscr{F}(\alpha_u, \varepsilon_1) = \begin{cases} \dfrac{-2\left(\frac{\alpha_u}{\varepsilon_1}\right)^3 + 3\left(\frac{\alpha_u}{\varepsilon_1}\right)^2}{(1 + u_F/u_B)(1 - \alpha_u)}, & \text{for } 0 \leq \alpha_u < \varepsilon_1, \\ \dfrac{1}{(1 + u_F/u_B)(1 - \alpha_u)}, & \text{for } \varepsilon_1 \leq \alpha_u < 0.42, \\ \dfrac{u_F/u_B}{(1 + u_F/u_B)\alpha_u}, & \text{for } 0.42 \leq \alpha_u < (1 - \varepsilon_1), \\ \dfrac{\left(\frac{u_F}{u_B}\right)\left(2\left(\frac{\alpha_u - (1-\varepsilon_1)}{\varepsilon_1}\right)^3 - 3\left(\frac{\alpha_u - (1-\varepsilon_1)}{\varepsilon_1}\right)^2 + 1\right)}{(1 + u_F/u_B)\alpha_u}, & \text{for } (1 - \varepsilon_1) \leq \alpha_u \leq 1. \end{cases} \tag{3.52}$$

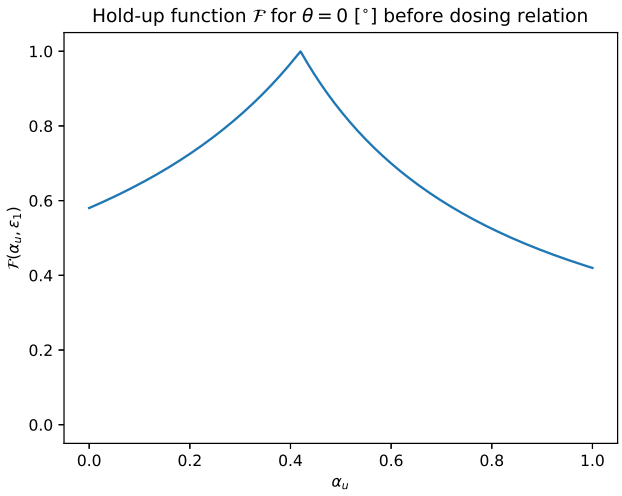

Figure 3.13: The hold-up function of equation (3.51) in a horizontal pipe section. The dosing relations are not implemented yet and the boundary conditions at $\alpha_u = 0$ and $\alpha_u = 1$ are not met.

equation(3.52) is plotted in Fig. 3.14 and clearly satisfies all three boundary conditions. The opposite initial condition, where the heavy fluid is on the left hand side of the diaphragm and the heavy fluid is assumed to flush out the light fluid, results in exactly the same solution for hold-up function $\mathscr{F}(\alpha_u, \varepsilon_1)$. This derivation is not shown here. For the hold-up function it is irrelevant which fluid is the flushing fluid, unlike for the interface function $\mathscr{G}$ and the effective bubble velocity function u_E.

The hold-up function no longer depends solely on the hold-up of the upper region α_u and the threshold value ε_1, but it also depends on the pipe inclination angle θ. Now, the hold-up function is defined as:

$$\mathscr{F}(\alpha_u, \theta, \varepsilon_1) = \begin{cases} \mathscr{F}_{\theta=0}, & \text{for } \theta = 0, \\ \mathscr{F}_{\theta\neq 0}, & \text{for } \theta \neq 0, \end{cases} \tag{3.53}$$

where $\mathscr{F}_{\theta=0}$ is equal to the hold-up function just derived in equation (3.52), and $\mathscr{F}_{\theta\neq 0}$ is the hold-up function derived earlier in equation 3.32.

The maximum value of the effective bubble velocity is equal to the Benjamin bubble velocity plus the front bubble velocity, which is valid in applications of active flow as well. In the current implementation of the effective bubble velocity function the calculated effective bubble velocity for a pipe inclination angle of zero corresponds to one time the Benjamin bubble velocity. To incorporate the effect of the formation of stratified flow and gravity currents in the model, the effective bubble velocity has to be multiplied with the factor $(1 + u_F/u_B)$, which will give the correct bubble movement in a horizontal pipe section. The updated function of the effective bubble velocity becomes:

$$u_E(\rho_u, \rho_l, \theta) = \begin{cases} 0.767\sqrt{\dfrac{\rho_l - \rho_u}{\rho_l} gR}\cos(|\theta|) + 0.496\sqrt{\dfrac{\rho_l - \rho_u}{\rho_l} gR}\sin(|\theta|), & \text{for } \rho_l - \rho_u < \rho_H - \rho_L \quad \& \quad \theta \neq 0, \\ (1 + u_F/u_B)u_E, & \text{for } \theta = 0, \\ 0, & \text{Otherwise,} \end{cases} \tag{3.54}$$

where the value of $(1+u_F/u_B)u_E$ given for $\theta = 0$ is not simply equal to $u_B + u_F$, which was defined in equations (2.61) & (2.62). Only the factor $(1 + u_F/u_B)$ is calculated using these equations. This is caused by the changing densities of the regions due to the miscibility character of the fluids.

The updated and final form of the slip relation is defined in the model as:

$$u_{s,u} - u_{s,l} = \mathscr{F}(\alpha_u, \theta, \varepsilon_1)\mathscr{G}_{B_1B_2}\left(\theta, \frac{\mathrm{d}h}{\mathrm{d}s}, \varepsilon_2\right) u_E(\rho_u, \rho_l, \theta). \tag{3.55}$$

As the magntiude of the front bubble velocity is always smaller than the Benjamin bubble velocity for fluid-fluid displacements, asymmetric movement of a stagnant Benjamin bubble is observed in a pipe. For channel flow, this movement is symmetric, which is shown later in Appendix B.

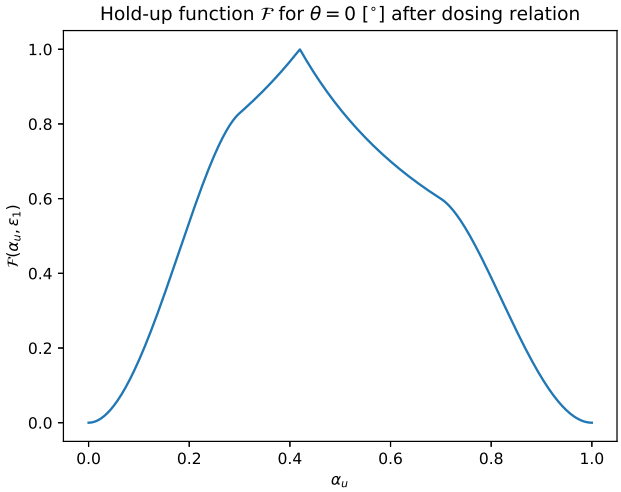

Figure 3.14: The hold-up function $\mathscr{F}(\alpha_u, \varepsilon_1)$ of equation (3.52) in a horizontal pipe section. The dosing relations are implemented and the threshold value is $\varepsilon_1 = 0.3$.

Furthermore, the front bubble velocity is always associated with the velocity of the denser fluid. Therefore, the axial velocity of the lower region will approach $\pm u_F$ in stagnant flow and $\pm u_F + u_s$ in active flow. Whereas the Benjamin bubble velocity is associated with the velocity of the less dense fluid; i.e. the axial velocity of the upper region will approach $\pm u_B$ or $\pm u_B + u_s$. Here, the plus minus sign is given to indicate the flushing direction. Note that the superficial velocity is always positive, as only this flow direction is considered in this study.

In Section 1.2 it was mentioned that a longer stratification length is observed for a less dense fluid displacing a denser fluid, than the other way around. This is caused by the fact that the absolute value of axial velocity of the upper region is by definition larger than the equivalent value of the axial velocity of the lower region in horizontal sections.

3.3.4. Axial dispersion coefficient function

The axial dispersion coefficient $\mathscr{D}_s$ is used in the multiphase transport equations to respectively solve the volume fractions of the light and heavy fluid in the upper and lower region. As mentioned earlier, these coefficients depend on the axial location and time. However, it was not yet elaborated how the magnitudes of the axial dispersion coefficient are determined along the pipeline. At first, a more theoretical background is given for the axial dispersion coefficient. Afterwards, the empirical relation used in the function of the model to determine the coefficients of the regions, $\mathscr{D}_{s,u}$ and $\mathscr{D}_{s,l}$, is given.

Axial dispersion is often used to describe the spread of a solute in a flow relative to the axial flow direction. A pulse of solute is injected in the flow and does not remain concentrated; i.e. it is axially dispersed. This dispersion is not only caused by axial diffusion, the advection of fluid particles play a role as well. In fact, advection plays the major role in the axial dispersion of particles and the contribution of axial diffusion is very small for turbulent flow. Axial dispersion is a function of the Reynolds number of the flow [12].

To better understand how the magnitude of axial dispersion is influenced by the Reynolds number in a pipe, the term fully developed flow is introduced. When a flow enters a pipe, a boundary layer starts to develop over the entire pipe surface. The flow influenced by the boundary layer is decelerated, whereas the flow in the centre of the pipe is accelerated. The boundary layer grows until the point where the entire pipe is filled with the boundary layer. Shortly after this point, the flow no longer has a dependence on flow disturbances at the inlet of the pipe and the cross-sectional velocity profile remains constant. Now, the flow has become fully developed [32].

In short, the turbulent velocity profile could be described by the use of three layers:

- A laminar-like part close to the pipe surface with large velocity gradients in the radial direction, called the viscous sublayer.
- A relative uniform part in the centre of the pipe called the core region, where the velocity gradients in the radial direction are close to zero.
- A buffer layer closing the gap between the viscous sublayer and the core region with moderate velocity gradients in the radial direction.

An almost uniform velocity profile in the core region indicates that the relative movement of fluid particles is minimal and most fluid particles are moving with a homogeneous velocity in the axial direction. Compared to the core region, the relative movement of fluid particles is higher in the buffer layer and much higher in the viscous sublayer [22].

Although the viscous sublayer is thin in turbulent flow, the layer can hold up a considerable amount of solute. It was mentioned in Section 1.2 that the residence time in the viscous sublayer can be significant. This increases the axial dispersion, as the solute is more distibuted over the pipe. The lower the Reynolds number, the higher the contribution of the viscous sublayer to the axial dispersion coefficient is. This remains valid for $Re < 20,000$. Above this Reynolds number, the core region becomes such large that piston-like flow is approached and the axial dispersion is reduced gradually [12].

Taylor constructed a virtual coefficient of dispersion K_* for turbulent flow, which is dimensionless and constant, $K_* = 10.1$. It primarily consists of a contribution of the advection of fluid particles. The rate of the transfer of particles due to turbulent diffusion plays a minor role in the dimensionless dispersion coefficient. K_* is defined as the axial dispersion coefficient divided by the pipe radius and the friction velocity [30].

$$K_* = \frac{\mathscr{D}_s}{u_* R} = 10.1 \tag{3.56}$$

The friction velocity u_* is defined as the square root of the wall shear divided by the density and can be related to the coefficient of friction in a pipe. The explicit Churchill correlation is used to determine the Fanning friction factor f in the model [32].

Taylor performed experiments where salt was injected in a flow of water to validate the theoretical value of the virtual coefficient of dispersion. He measured the temporal conductivity variations in a 16.5 $[m]$ long pipe at the downstream locations 3.22 and 16.3 $[m]$. The experiments were executed for the Reynolds numbers, $Re = 11,800$ and $19,000$. He observed that the latter almost reproduces the theoretical value of the virtual coeffcient of dispersion at the second measurement point, whereas the value of the former exceeds the theoretical value everywhere. The smaller the Reynolds number, the larger the dimensionless axial dispersion coefficient. This is expected because of the viscous sublayer, which contains more solute for a smaller Reynolds number. Furthermore, he noticed a lack in symmetry in the concentration-time curves at the measurement point due to the influence of the viscous sublayer. However, this asymmetry is resolved when the typical length as a result of the advection of fluid particles $x = u_s t$ is much larger than the typical length of diffused fluid particles $x = \sqrt{4\mathscr{D}_s t}$ [30].

Krantz and Wasan [17] have proposed to non-dimensionalise the axial dispersion coefficient with the superficial velocity and the hydraulic diameter, instead of to non-dimensionalise it with the friction velocity and the pipe radius.

$$\bar{K} = \frac{\mathscr{D}_s}{\bar{u} D_H} = K_* \left(\frac{u_*}{2\bar{u}} \right) \tag{3.57}$$

As stated, it is assumed that the superficial velocity is equal to the total axial velocity in the model, $\bar{u} \approx u_s$.

The notation of Krantz and Wasan is used by Hart to describe his empirical relation of the axial dispersion coefficient. Hart has performed experiments in which he injected dye into a flow of water to measure the axial dispersion coefficient for a variety of Reynolds numbers. These Reynolds numbers ranged from $Re = 2,000$ to $50,000$. The dye was injected into the flow after 3.5 $[m]$, as measured from the inlet of the pipe. The pipe has a total length of 16.56 $[m]$ and a radius of 0.012 $[m]$. The flow at the injection point is assumed to be fully developed. The experimental data are fitted to obtain his empirical relation of the dimensionless axial dispersion coefficient. The empirical relation is valid for $3,000 < Re < 50,000$ and includes both critical and fully-turbulent flow. [12]

$$\bar{K} = \frac{\mathscr{D}_s}{u_s D_H} = 1.17 \cdot 10^9 Re^{-\left(\frac{5}{2}\right)} + 0.41 \tag{3.58}$$

Both Taylor and Hart argue that the dimensionless axial dispersion coefficient can also be used for the case in which one fluid is flushing another fluid out of a pipe. The coefficient can be used provided that both fluids are miscible and that their densities and viscosities do not differ greatly. The concentration-time curve at a fixed point in the pipe will look like a curve for piston-like flow with some axial mixing. Taylor suggested that the curve can be approximated by a Gaussian impulse response function. This is confirmed by the experiments of Hart [12][30]. The Gaussian impulse response function is defined at axial location $s = s_1$ in the pipe as:

$$c(s,t) = \frac{1}{2} - \frac{1}{2} erf\left(\frac{s - s_1}{\sqrt{4\mathscr{D}_s t}}\right) \tag{3.59}$$

where c is the volume fraction of one of the fluids, which depends on the axial location and time and erf is the error function, $erf(s) = \frac{2}{\sqrt{\pi}} \int_0^s e^{\zeta^2} \mathrm{d}\zeta$.

The relations of Taylor and Hart are compared for the set-up of Hart. The results of the (dimensionless) axial diffusion coefficients versus the Reynolds number are given in Fig. 3.15 for $3,000 < Re < 50,000$. It is noticed that the experimental results for the dimensionless axial dispersion coefficient are about twice as large for $Re > 20,000$ than the values predicted by the relation of Taylor. This is seen in Fig. 3.15a. Hart's experiments are more recent and correctly predict the friction coefficient in the transition from laminar to turbulent flow in the pipe. Therefore, the empirical relation of Hart is chosen to predict for the axial dispersion coefficient in the model, despite the large differences between the results.

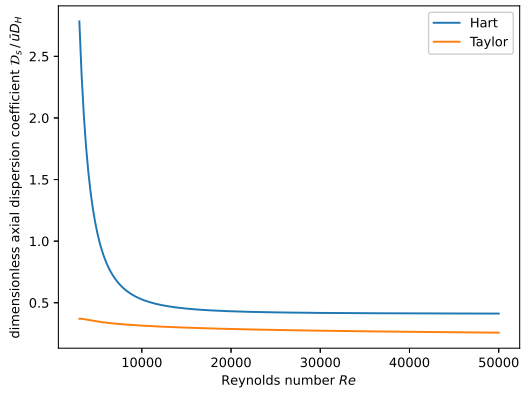

(a) $\bar{K} = \frac{\mathscr{D}_S}{u_S D_H}$.

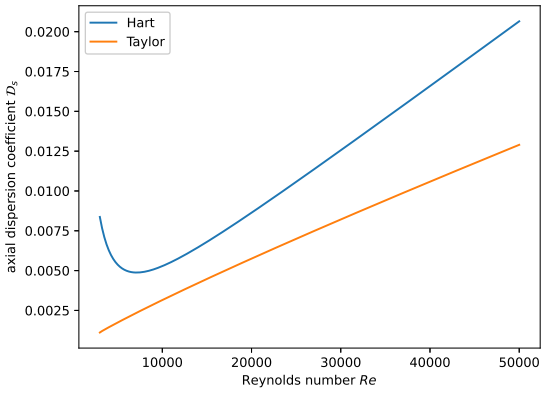

(b) $\mathscr{D}_s$

Figure 3.15: The relations of Hart and Taylor, plotted for the experimental set-up of Hart. In (a) the dimensionless dispersion coefficients are plotted and in (b) the axial dispersion coefficients are drawn.

The relation of Hart as plotted in Fig. 3.15a perfectly shows the theory of the virtual axial dispersion coefficient, as is explained in this section. The influence of the viscous sublayer is of such influence for the critical flow, that the magnitude of the dimensionless axial dispersion coefficient is large as well. As the flow becomes fully turbulent, the uniform region of the cross-sectional velocity will become more and more dominant. The motion relative to the axial flow direction is minimal. The dimensionless axial dispersion coefficient approaches the asymptotic value of 0.41 for $Re > 20,000$.

The plot of the axial dispersion coefficient determined by the empirical relation of Hart in Fig. 3.15b clearly shows the contribution to the dispersion coefficient of both the axial diffusion and the advection of the fluid particles. The axial diffusion is dominant for $Re = 3,000$ and very quickly loses its dominance to the advection of fluid particles when the flow moves from critical to turbulent flow. As the flow accelerates, the advection of fluid particles takes places at a higher rate; the contribution of advection is dominant for $Re > 20,000$. The axial dispersion coefficient almost increases linearly from this point.

The axial dispersion coefficients for the upper and lower, $\mathscr{D}_{s,u}$ and $\mathscr{D}_{s,l}$, are defined as:

$$\mathscr{D}_{s,u} = u_{s,u} D_{H,u} \bar{K}_u = u_{s,u} D_{H,u} \cdot \left(1.17 \cdot 10^9 \left(\frac{\rho_u u_{s,u} D_{H,u}}{\mu_u}\right)^{-2.5} + 0.41\right) \tag{3.60}$$

$$\mathscr{D}_{s,l} = u_{s,l} D_{H,l} \bar{K}_l = u_{s,l} D_{H,l} \cdot \left(1.17 \cdot 10^9 \left(\frac{\rho_l u_{s,l} D_{H,l}}{\mu_l}\right)^{-2.5} + 0.41\right) \tag{3.61}$$

It should be noted that axial dispersion is always present in the model as long as a region is active in the domain and has an axial velocity.

The magnitude of the axial dispersion coefficient differs per region, which could have a couple of reasons. Each region has its own thermodynamic properties. This results in a Reynolds number per region that is by definition dissimilar. This indicates that even in the case of a horizontal equilibrium interface, when both regions move with the same velocity through the pipe, the axial dispersion coefficient is different per region. The difference is enlarged in pipe sections where one of the regions is more active, as a larger hydraulic diameter is obtained for the more active region. Therefore, the pipe inclination angle and the density difference can also result in sufficiently large differences in the axial dispersion coefficient per region.

3.3.5. Transfer term function

In the multiphase continuity and transport equation of equation (2.29) and (2.57), two kind of transfer terms were introduced, $\Psi_{\beta_2\beta_1}$ and $\Psi_{B,\beta_2\beta_1}$. Both terms are cross-sectionally averaged. The former is a mass transfer rate per unit area from region β_2 to β_1 in the units $\left[\frac{kg}{m^2 s}\right]$. While the latter is a volumetric flow rate per unit area of fluid B from β_2 to β_1 in the units $\left[\frac{m}{s}\right]$. Both rates transfer their mass or volume through the interfacial surface that is assumed to exist. To obtain the correct units in the multiphase continuity and transport equation, the transfer terms are multiplied with the wetted interface length $P_{u,l}$.

In section 2.2.2, it was already explained that the transfer taking place from the lower region to the upper region is regarded as positive, as the positive y-direction is directed in this way. So, the transfer that takes place from the upper to the lower region is by definition negative.

Until Section 3.2.2, nothing was mentioned about the weight of the transfer terms. However, one important key feature of the transfer terms was illustrated in this section. Both transfer rates from region to region are equal to each other, however they differ in sign. In other words, the sum of the transfer terms is equal to zero. No mass or no volume is added or removed in the domain. A fluid does only enter the system at the inlet and leaves at the outlet of the pipe.

$$\sum \Psi_{\beta_2\beta_1} = \Psi_{lu} - \Psi_{ul} = 0 \tag{3.62}$$

$$\sum \Psi_{B,\beta_2\beta_1} = \Psi_{L,lu} - \Psi_{L,ul} = 0 \tag{3.63}$$

$$\sum \Psi_{B,\beta_2\beta_1} = \Psi_{H,lu} - \Psi_{H,ul} = 0 \tag{3.64}$$

By looking at the units of the mass and volumetric transfer term, it is obvious that they differ by a density term. The mass transfer term is created by multiplying the volumetric transfer term of the light and heavy fluid by the density of the light and heavy fluid, respectively.

$$\Psi_{lu} = \Psi_{L,lu}\rho_L + \Psi_{H,lu}\rho_H \quad \text{and} \quad \Psi_{ul} = \Psi_{L,ul}\rho_L + \Psi_{H,ul}\rho_H \tag{3.65}$$

It is clear that the sum of the mass transfer terms, Ψ_{lu} and Ψ_{ul}, is equal to zero for this definition.

However, the magnitude of the volumetric transfer rates is unknown. Literature also does not provide a decent empirical relation, as the empirical relation of Hart does for the axial dispersion coeffcient. Therefore, an attempt is made to provide such a relation in this research. The volumetric transfer rate of the light and heavy fluid are assumed to be equal to each other and are consant in the domain. Various values for the volumetric transfer terms are tried in cases with different Reynolds numbers. Their numerical solutions are compared with experimental and CFD research and the values that result in a match are saved.

The goal is to plot these matches versus the Reynolds number of the flow and fit an empirical relation, as a function of the mixture Reynolds number of equation (1.3) for the transfer terms. To do so, the volumetric transfer term has to be non-dimensionalised. This could be done with the superficial velocity.

$$\Psi^*_{L,lu} = \frac{\Psi_{L,lu}}{u_s} = a \cdot Re^b_{\text{mix}} + c \tag{3.66}$$

Here, a, b and c are fitting parameters. Note, that only one empirical relation is needed, as the volumetric transfer terms of both fluids are assumed to be equal to each other.

Similar to the effective bubble velocity, the transfer terms are only present when the upper and lower regions are both active in a pipe section. This is achieved, when the hold-ups of the upper and lower region are greater than ε_3. The transfer term function is defined as:

$$\Psi(u_E) = \begin{cases} \Psi_{L,lu} = \Psi_{H,lu} = \Psi_c \quad \text{and} \quad \Psi_{lu} = \Psi_{L,lu}\rho_L + \Psi_{H,lu}\rho_H, & \text{for } \alpha_u > \varepsilon_3 \,\&\, \alpha_u > \varepsilon_3, \\ \Psi_{L,lu} = \Psi_{H,lu} = \Psi_{lu} = 0, & \text{elsewhere,} \end{cases} \tag{3.67}$$

where Ψ_c represents the constant value, which will to be varied in the simulations to find the correct match for the volumetric transfer terms.

The transfer terms are important variables to obtain a physical solution for the miscible model, as they describe the mixing process in the domain. Too much or too little mixing would result in unphysical results, whereas no mixing at all would result in immiscible behaviour in the domain. Ideally, the transfer terms would fluctuate from location to location, as the axial dispersion coefficient. Whereas the $\Psi^*_{L,lu}$ term of equation (3.66) is the same in all locations where two fluids are present. Nonetheless, this relation is a good first estimation of the magnitude of the volumetric transfer terms.

3.4. Overview of model assumptions

The assumptions to come to the desired simplified two-fluid model are given in the following overview.

- **Two-fluid model**; Two fluids are present in the system, each divided over its own region: the upper region and the lower region. The two fluids are denoted as a light and a heavy fluid. The regions are treated as if they were two distinct phases. This could be extended to any number of fluids / phases.
- **One-dimensional flow**; As the simplified model uses cross-sectional averaged equations and quantities, the flow is one-dimensional and the information about the flow pattern is lost. The flow cannot be assumed to be fully developed, as the model is not capable of handling a velocity gradient in the radial direction. Piston-like flow is assumed for both regions.
- **Stratified flow**; Density differences between fluids are important and cannot be neglected. The pipe inclination angle $\theta(s)$ and the dissimilar densities result in the formation of bubbles. These buoyancy effects and gravity currents are taken into account via the slip relation. The gravity currents indicate that back flow will be shown in the model.
- **Miscible flow**; Mass and volume transfer takes place between the regions.The transfer terms from region to region are equal in magnitude, but of opposite sign. Their sum is equal to zero. In the domain, no sources of sinks are present, indicating that no mass or volume is added to or removed from the flow.
- **Incompressible flow**; The total density in the system is constant for incompressible flow. This flow functionality is used to derive a velocity equation in subsection 3.2.2.
- **Isobaric flow**; the flow is assumed to be isobaric, no hydraulic gradients are present in the flow [25]. The conservation of momentum equation is not solved in the model, as earlier research has proven that it is hard to obtain the correct bubble velocities with the momentum equations [26], whereas Bouwhuis has proven the effectiveness of the bubble relations in his master thesis [7].
- **Isothermal flow**; The flow is assumed to be isothermal. The conservation of energy equation is not solved in the simplifed model, as it is suspected that the temperature gradients play a minor role in the flow.
- **Constant cross-sectional area**; The cross-sectional area $A(s)$ is constant over time along the centreline of the pipe section. A possible effect of the curvature in the pipe sections can be neglected in the equations.

- **Axial velocity dominant**; The velocity in the radial and circumferential direction of the flow are assumed to play no role in the model and are neglected. The velocity in the axial direction of the flow u_s is dominant in the system. The flow is assumed to be positive in the axial direction from left to right.
- **Interfacial surface**; An interfacial surface is assumed to be active between the upper and lower region, although the fluids are miscible. Furthermore, the interface is assumed to be perfectly horizontal, for calculating the geometrical variables in the cross-sectional area, as is explained in Section 3.3.1.
- **Axial dispersion dominant**; The time scale of axial advection is much larger than the time scale of radial diffusion due to the turbulent flow. Axial dispersion is dominant in the model and its coefficient, needed in the multiphase transport equation, is determined by the empirical relation of Hart.
- **Minimal turbulent effects**; The effect of turbulent flow is only encountered in the axial dispersion coefficient, as the empirical relation of Hart is a function of the Reynolds number. Effects of a turbulent velocity profile are neglected and the model solves no turbulence model.
- **No viscosity effects**; Viscosity effects play a role at the fluid-fluid displacement at the interface and the wall. They could be encountered in the slip relation or in the possible friction relations. However, the viscosity effects are neglected in the model. They are only used to determine the Reynolds number, needed for the axial dispersion coefficient.
- **No interfacial friction**; The pressure forces on the interface and between the light and heavy fluid particles are neglected.
- **Linear extrapolation of density and viscosity**; It is assumed, that both values of the density and the viscosity per region can be linearly extrapolated using the volume fractions.

3.5. Overview equations

All miscible fluid-fluid displacement equations are given in the following overview.

$$\frac{\partial}{\partial t}\left(\alpha_u \rho_u\right) + \frac{1}{A}\frac{\partial}{\partial s}\left(\alpha_u \rho_u u_{s,u} A\right) + \frac{\Psi_{lu} P_{u,l}}{A} = 0 \tag{3.68a}$$

$$\alpha_l = 1 - \alpha_u \tag{3.68b}$$

$$A\sum_{\beta}\frac{\partial\left(\alpha_\beta u_{s,\beta}\right)}{\partial s} = 0 \tag{3.68c}$$

$$u_{s,u} - u_{s,l} = \mathscr{F}\left(\alpha_u, \theta, \varepsilon_1\right)\mathscr{G}_{B_1B_2}\left(\theta, \frac{\mathrm{d}h}{\mathrm{d}s}, \varepsilon_2\right) u_{E,B_1B_2}\left(\rho_u, \rho_l, \theta\right) \tag{3.68d}$$

$$\frac{\partial c_{Lu} A_u}{\partial t} + \frac{\partial c_{Lu} u_{s,u} A_u}{\partial s} - \frac{\partial}{\partial s}\left(\mathscr{D}_{s,u}\frac{\partial c_{Lu}}{\partial s} A_u\right) + \Psi_{L,lu} P_{u,l} = 0 \tag{3.68e}$$

$$c_{Hu} = 1 - c_{Lu} \tag{3.68f}$$

$$\frac{\partial c_{Hl} A_l}{\partial t} + \frac{\partial c_{Hl} u_{s,l} A_l}{\partial s} - \frac{\partial}{\partial s}\left(\mathscr{D}_{s,l}\frac{\partial c_{Hl}}{\partial s} A_l\right) - \Psi_{H,ul} P_{u,l} = 0 \tag{3.68g}$$

$$c_{Ll} = 1 - c_{Hl} \tag{3.68h}$$

Although all averaging-brackets are omitted, it must be noted that all variables should be interpreted as cross-sectional averages.

4

Numerical discretisation of a one-dimensional fluid-fluid displacement model

The miscible set of equations are discretised following the finite volume method on a staggered grid layout in this chapter. It is discussed what the options are to discretise the equations in time and in space and how those equations are treated in the coupled solver with the correct boundary conditions. Furthermore, the consistency is checked for a simpler model, which is validated by the analytical solution diffusion equation.

4.1. Grid layout

To solve a flow application, a domain is divided into volumes called cells. Together, all cells form a grid. In Fig. 4.1, the grid layout which is used in this study is presented. The domain in which the fluids are present is called the interior. The volumes outside the domain are called the exterior. The set of equations is solved for the interior cells only.

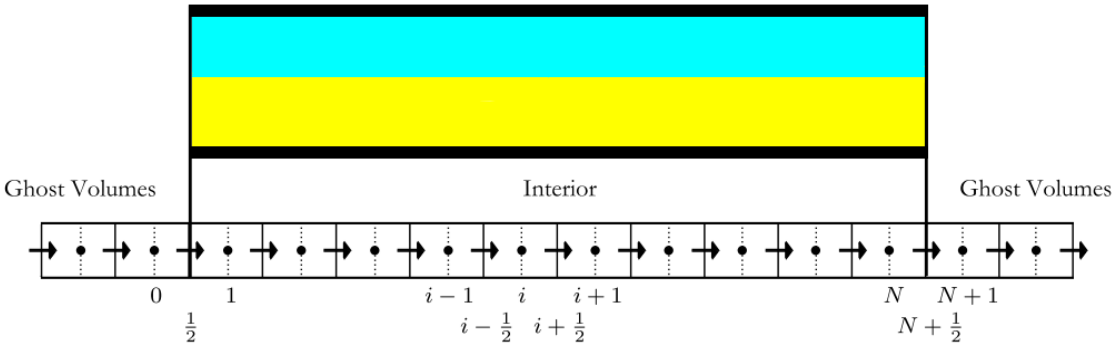

Figure 4.1: A representation of the grid used in the present model. The staggered grid layout places the scalar quantities in the cell centres, which are denoted by i and represented by a dot in the figure, and the vectorial quantities at the cell boundaries, denoted by $i-\frac{1}{2}$ and $i+\frac{1}{2}$ and represented by an arrow. The interior is divided into N cells and lasts from cell boundary $\frac{1}{2}$ until $N+\frac{1}{2}$. The ghost cells are needed to assign boundary conditions to the interior and to determine the discretisation of spatial terms for the set of equations [26].

The interior is divided into N uniform cells of length Δs. All cells are ordered in a so-called staggered configuration. The scalar quantities like the hold-ups, the volume fractions, the pipe inclination angle and the densities are located in the nodes denoted by i for a staggered arrangement. Whereas the vectorial quantities, such as velocities and diffusive fluxes, are located at the successive mid nodes $i-\frac{1}{2}$ and $i+\frac{1}{2}$. In other words, the scalar quantities are defined in the cell centres represented by a dot, and the vectorial quantities are defined on the cell boundaries represented by an arrow in Fig. 4.1 [23].

The flow solution needs the information of the flow variables defined in the exterior. The exterior consists of extra cells, the so-called ghost cells. The required number of ghost cells depends on the numerical scheme that is used to discretise the spatial terms in the set of the equations of (3.68). Especially, it depends on the advective terms of the Individual Phase Continuity Equation (IPCE) and the multiphase transport equation. This will be explained in Section 4.5. The ghost cells are also used to assign boundary conditions to the domain. The type of boundary conditions used in the model are explained in Section 4.6 [26].

Originally, the staggered grid is designed to provide a strong coupling between the pressure and velocity variables in a CFD-model. In a numerical pressure-correction method, like Semi-Implicit Method for Pressure Linked Equations (SIMPLE), staggered grids are preferred over collocated grids, in which both scalar and vectorial quantities are located in the same nodes. These collocated grids often lead to spurious spatial oscillations. The staggered grid arrangement prevents this instability and is a very robust method [23].

The pressure variable is not solved in the current set of equations. As a result, arising spatial oscillations due to a collocated grid are not an issue in the model. Nonetheless, a staggered configuration is chosen. This makes it possible to integrate pressure variables and to include friction effects into the model in a later study. Also, Shell's inhouse dynamic simulation tool, COMPAS, uses this type of grid layout [7].

4.2. Finite Volume Method

In Section 2.2, the Finite Volume Method (FVM) was already mentioned. The FVM is used in this study to discretise the set of equations of (3.68). The FVM is based on the integral form of the conservation laws, rather than directly from the differential equations which are used in another discretisation method: the Finite Difference Method (FDM). Recall that the IPCE and the multiphase transport equation are also derived from the integral form of their conservation law. Therefore, these differential equations can directly be discretised following a FVM.

Where the FDM is known to break down near discontinuities in the solution, the FVM is known for its handling of discontinuities in the computational domain. Moreover, FVMs are capable to deal with local grid adaptions and complex geometries. FVMs are closely related to FDMs, as often FVMs can be interpreted as finite difference approximations. This is done in the numerical analysis for FVMs, as a lot of research has been conducted for the stability, consistency and convergence of FDMs. This is in contrast to the amount of research done for FVMs related to these topics [18][21]. The conditions for the convergence of a FVM are given in Section 4.7

4.3. Time discretisation methods

To discretise the partial derivative terms with respect to the time variable t in the miscible set of equations of (3.68), various methods exist.

Consider an Ordinary Differential Equation (ODE) for the scalar quantity Q which is to be discretised in time. At the start, a clear choice has to be made between an explicit and an implicit time discretisation method. In an explicit time method, the solution of Q on the next time step solely depends on the solution of Q for the previous (current) time step. The time step is denoted by the parameter n. The next time step is denoted by $n+1$, while the current time step is denoted by n. An example of an explicit time discretisation method is the explicit Euler method.

$$\begin{aligned} \frac{\mathbf{Q}^{n+1}-\mathbf{Q}^{n}}{\Delta t} &= \mathbf{R}\left(\mathbf{Q}^{n}\right) \\ \mathbf{Q}^{n+1} &= \mathbf{Q}^{n}+\Delta t\mathbf{R}\left(\mathbf{Q}^{n}\right) \end{aligned} \tag{4.1}$$

Here, Δt is the time step and $\mathbf{R}$ represents the right hand side of the ODE. $\mathbf{Q}$ and $\mathbf{R}$ are denoted by a bold character to indicate they represent a vector of length N; i.e. the number of cells of the interior. If the initial condition $\mathbf{Q}^0$ is known, the solution can be found for the next time step. However, a disadvantage of the explicit Euler method is that the time step has to be chosen at relatively small values, as the explicit method has small stability domain. Furthermore, the method is only first-order accurate. The truncation error for an advection-diffusion equation discretised by the explicit Euler method is worked out in Section 4.7.1 to demonstrate the impact of numerical diffusion.

In an implicit method, the solution of Q on $n+1$ is determined by the solution of Q at $n+1$. The easiest implicit method is the implicit Euler method.

$$\begin{aligned} \frac{\mathbf{Q}^{n+1}-\mathbf{Q}^{n}}{\Delta t} &= \mathbf{R}\left(\mathbf{Q}^{n+1}\right) \\ \mathbf{Q}^{n+1}-\Delta t\mathbf{R}\left(\mathbf{Q}^{n+1}\right) &= \mathbf{Q}^{n} \end{aligned} \tag{4.2}$$

To obtain a solution using an implicit method, the relation of equation (4.2) has to be rewritten to a diagonal linear system; i.e. $\mathbf{A}\mathbf{Q}^{n+1} = \mathbf{b}^{n}$. $\mathbf{A}$ is a diagonal dominant matrix and is nonsingular; i.e. its determinant is nonzero. Multiple iterative algorithms exist to solve this linear relation, for example the Jacobian method and the Gauss-Seidel method. Implicit methods are computationally more heavy than explicit methods as a result of their iterative solving procedures.

The implicit Euler method is unconditionally stable. However it is only first-order accurate in time, like its explicit brother. To get second-order accuracy in time, the ODE can be solved by the trapezoidal rule method. This implicit method is called the Crank-Nicolson method.

$$\begin{aligned} \frac{\mathbf{Q}^{n+1}-\mathbf{Q}^{n}}{\Delta t} &= \frac{1}{2}\left(\mathbf{R}\left(\mathbf{Q}^{n+1}\right)+\mathbf{R}\left(\mathbf{Q}^{n}\right)\right) \\ \mathbf{Q}^{n+1}-\frac{1}{2}\Delta t\mathbf{R}\left(\mathbf{Q}^{n+1}\right) &= \mathbf{Q}^{n}+\frac{1}{2}\Delta t\mathbf{R}\left(\mathbf{Q}^{n}\right) \end{aligned} \tag{4.3}$$

The Crank-Nicolson method is unconditionally stable as well and is the preferred time discretisation method used in this FVM model. The Backward Differential Formula 2 (BDF2) method is another second-order accurate method and a multi time step method. Its stability domain is larger than for the Crank-Nicolson method, but its implementation is more difficult [21].

To gain a better understanding of the nodes and time parametres that play a role in the different time discretisation methods, the stencils of the explicit Euler, the implicit Euler and the Crank-Nicolson methods are given in Fig. 4.2. The stencils are given for a diffusion equation.

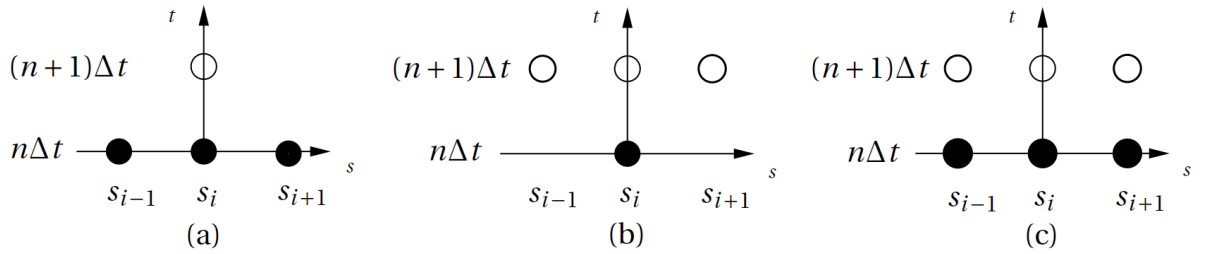

Figure 4.2: The stencils of the time discretisation methods are given for (a) explicit Euler method, (b) implicit Euler method and (c) Crank-Nicolson method [21].

4.4. Discretisation of miscible set of equations

As the staggered grid, the FVM and the time discretisation methods are introduced, the miscible set of equations can be discretised. During the discretisation of the equations, some extra definitions needed in the discretised FVM model are explained. The discretisation of the advective terms of the IPCE and transport equation are given in Section 4.5, as the discretisation of those terms require more attention to obtain a good second-order accuracy in space than the diffusive terms.

4.4.1. Individual Phase Continuity Equation

The discretisation of the IPCE of equation (3.2) starts at its differential form. Recall that the IPCE is used to solve the hold-up of the upper region.

$$\frac{\partial}{\partial t}\left(\alpha_u\rho_u\right)+\frac{1}{A}\frac{\partial}{\partial s}\left(\alpha_u\rho_u u_{s,u}A\right)+\frac{\Psi_{lu}P_{u,l}}{A}=0 \tag{3.2}$$

Integrating equation (3.2) over the volume occupied by the upper region in the i^{th} cell and dividing by the cell length Δs, yields:

$$\frac{\mathrm{d}}{\mathrm{d}t}\left(\alpha_{u_i}\rho_{u_i}\right)+\frac{1}{A_i\Delta s}\left(\left(\alpha_u\rho_u A\right)_{i+\frac{1}{2}}u_{s,u_{i+\frac{1}{2}}}-\left(\alpha_u\rho_u A\right)_{i-\frac{1}{2}}u_{s,u_{i-\frac{1}{2}}}\right)+\frac{\Psi_{lu_i}P_{u,l_i}}{A_i}=0. \tag{4.4}$$

The hold-ups, densities, areas, the mass transfer term and the wetted perimeter are defined in the cell centre on the i^{th} locations, whereas the velocity variable is defined at the cell boundaries on the $i+\frac{1}{2}^{\text{th}}$. Information on the terms $(\alpha_u \rho_u A)_{i-\frac{1}{2}}$ and $(\alpha_u \rho_u A)_{i+\frac{1}{2}}$ of the advective term of equation (4.4) is also required on the cell boundaries. How those terms are discretised is shown in Section 4.5. For now, these are denoted by a $\hat{(\cdot)}$. All relevant variables for the IPCE are illustrated in Fig. 4.3.

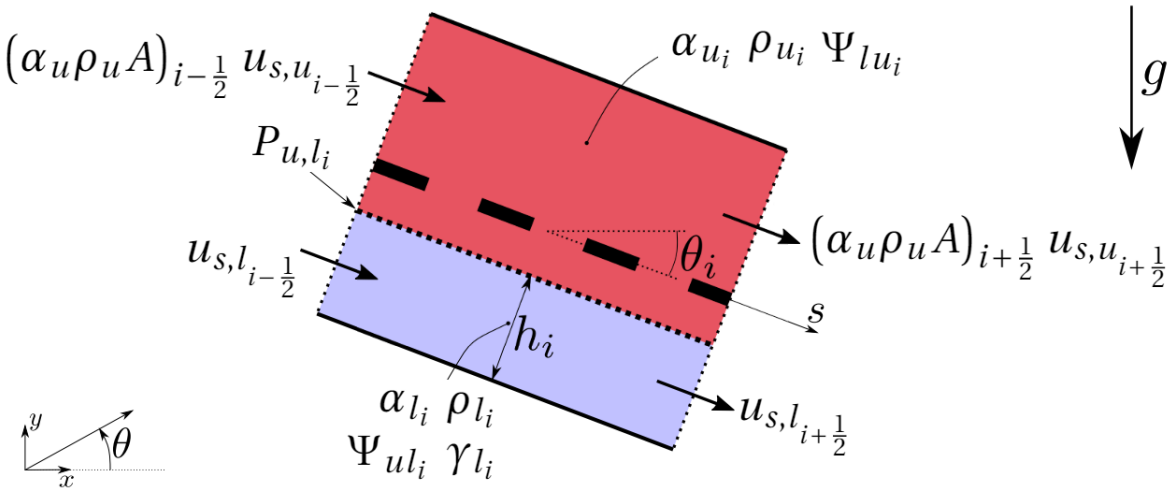

Figure 4.3: The relevant flow variables needed for discretising the IPCE are visualised around the cell i. Note that the advective fluxes are included as well. [7]

Applying the Crank-Nicolson method to the semi-discretised equation (4.4), results into:

$$\begin{aligned}\frac{\alpha_{u_i}^{n+1}\rho_{u_i}^{n+1}-\alpha_{u_i}^{n}\rho_{u_i}^{n}}{\Delta t} &+\frac{1}{2}\frac{\hat{\alpha}_{u_{i+\frac{1}{2}}}^{n+1}\hat{\rho}_{u_{i+\frac{1}{2}}}^{n+1}\hat{A}_{i+\frac{1}{2}}^{n+1}u_{s,u_{i+\frac{1}{2}}}^{n+1}-\hat{\alpha}_{u_{i-\frac{1}{2}}}^{n+1}\hat{\rho}_{u_{i-\frac{1}{2}}}^{n+1}\hat{A}_{i-\frac{1}{2}}^{n+1}u_{s,u_{i-\frac{1}{2}}}^{n+1}}{A_i^{n+1}\Delta s_i^{n+1}} &&+\frac{1}{2}\frac{\Psi_{lu_i}^{n+1}P_{u,l_i}^{n+1}}{A_i^{n+1}}\cdots\\ &+\frac{1}{2}\frac{\hat{\alpha}_{u_{i+\frac{1}{2}}}^{n}\hat{\rho}_{u_{i+\frac{1}{2}}}^{n}\hat{A}_{i+\frac{1}{2}}^{n}u_{s,u_{i+\frac{1}{2}}}^{n}-\hat{\alpha}_{u_{i-\frac{1}{2}}}^{n}\hat{\rho}_{u_{i-\frac{1}{2}}}^{n}\hat{A}_{i-\frac{1}{2}}^{n}u_{s,u_{i-\frac{1}{2}}}^{n}}{A_i^{n}\Delta s_i^{n}} &&+\frac{1}{2}\frac{\Psi_{lu_i}^{n}P_{u,l_i}^{n}}{A_i^{n}}=0.\end{aligned} \tag{4.5}$$

The incremental-iterative formulation is used in the model. It is a useful tool to determine the increment between the time steps and iteration steps. First, the formulation of the incremental method is shown for the hold-up of the upper region with respect to the time step.

$$\alpha_{u_i}^{n+1}=\alpha_{u_i}^{n}+\Delta\alpha_{u_i}^{n+1} \tag{4.6}$$

Here, $\alpha_{u_i}^{n+1}$ is the hold-up at the next time step, $\alpha_{u_i}^{n}$ is the hold-up at the previous time step and $\Delta\alpha_{u_i}^{n+1}$ is the increment between the hold-up at the two time steps. It is illustrated how this incremental formulation evolves, starting from the initial solution of the hold-up of the upper region at time step $n=0$ (time $t=0$ [s]).

$$\begin{aligned}n=0 \quad & \alpha_{u_i}^{1}=\alpha_{u_i}^{0}+\Delta\alpha_{u_i}^{1}\\ n=1 \quad & \alpha_{u_i}^{2}=\alpha_{u_i}^{1}+\Delta\alpha_{u_i}^{2}\\ n=n \quad & \alpha_{u_i}^{n+1}=\alpha_{u_i}^{n}+\Delta\alpha_{u_i}^{n+1}\end{aligned}$$

An iterative procedure has to be performed to determine the solution of the hold-up at the new time step. Analogous to the notation of the time step n, the iteration step is denoted by the parameter m. The iterative incremental formulation of the hold-up is defined by:

$$\alpha_{u_i}^{m+1}=\alpha_{u_i}^{m}+\Delta\alpha_{u_i}^{m+1}, \tag{4.7}$$

where the time step parameter n is not simply replaced.

When the iteration step begins at $m = 0$, the iterative procedure already calculates the value of the new time step after the first iteration step. To gain a better understanding of this process, it is illustrated as well.

$$\begin{aligned} m = 0 \quad & \alpha_{u_i}^{n+1,(1)} = \alpha_{u_i}^{n+1,(0)} + \Delta\alpha_{u_i}^{n+1,(1)} \\ m = 1 \quad & \alpha_{u_i}^{n+1,(2)} = \alpha_{u_i}^{n+1,(1)} + \Delta\alpha_{u_i}^{n+1,(2)} \\ m = m \quad & \alpha_{u_i}^{n+1,(m+1)} = \alpha_{u_i}^{n+1,(m)} + \Delta\alpha_{u_i}^{n+1,(m+1)} \Longleftrightarrow \alpha_{u_i}^{m+1} = \alpha_{u_i}^{m} + \Delta\alpha_{u_i}^{m+1} \end{aligned}$$

Here, $\alpha_{u_i}^{n+1,(0)}$ should be interpreted as $\alpha_{u_i}^{n}$. Replacing the terms with $(.)^{n+1}$ by $(.)^{m+1}$ in equation (4.5) yields:

$$\begin{aligned} \frac{\alpha_{u_i}^{m+1}\rho_{u_i}^{m+1} - \alpha_{u_i}^{n}\rho_{u_i}^{n}}{\Delta t} \quad & + \frac{1}{2}\frac{\hat{\alpha}_{u_{i+\frac{1}{2}}}^{m+1}\hat{\rho}_{u_{i+\frac{1}{2}}}^{m+1}\hat{A}_{i+\frac{1}{2}}^{m+1}u_{s,u_{i+\frac{1}{2}}}^{m+1} - \hat{\alpha}_{u_{i-\frac{1}{2}}}^{m+1}\hat{\rho}_{u_{i-\frac{1}{2}}}^{m+1}\hat{A}_{i-\frac{1}{2}}^{m+1}u_{s,u_{i-\frac{1}{2}}}^{m+1}}{A_i^{m+1}\Delta s_i^{m+1}} + \frac{1}{2}\frac{\Psi_{lu_i}^{m+1}P_{u,l_i}^{m+1}}{A_i^{m+1}} \cdots \\ & + \frac{1}{2}\frac{\hat{\alpha}_{u_{i+\frac{1}{2}}}^{n}\hat{\rho}_{u_{i+\frac{1}{2}}}^{n}\hat{A}_{i+\frac{1}{2}}^{n}u_{s,u_{i+\frac{1}{2}}}^{n} - \hat{\alpha}_{u_{i-\frac{1}{2}}}^{n}\hat{\rho}_{u_{i-\frac{1}{2}}}^{n}\hat{A}_{i-\frac{1}{2}}^{n}u_{s,u_{i-\frac{1}{2}}}^{n}}{A_i^{n}\Delta s_i^{n}} + \frac{1}{2}\frac{\Psi_{lu_i}^{n}P_{u,l_i}^{n}}{A_i^{n}} = 0. \end{aligned} \tag{4.8}$$

It is observed that many terms in equation (4.8) that need to be determined on the next iteration step are multiplied by each other. No information is available on those terms yet, therefore they have to be approximated. The implicit time discretisation methods are known for producing these nonlinear terms.

Before it is explained how these nonlinear terms are handled in the model, equation (4.8) is simplified. The density and the mass transfer variables are already determined by the data of the model on the previous time step n, and are constant in the iteration procedure. The reason to make the density and the mass transfer variables constants in the iteration procedure is elaborated in Section 4.8. The cross-sectional area of the pipe A is constant in time and space, as A is specified upfront by the hydraulic diameter of the pipe which is constant along the pipe. Therefore, it is neither an iteration nor a time dependent variable and the notations $(.)^{m+1}$ and $(.)^{n}$ are dropped. The notation $\hat{(.)}$ is dropped as well for A. Though, the nodal notation of the cross-sectional area is included, as A could have an altering cross-sectional area along the axial axis in future studies. Furthermore, the wetted perimeter is determined using the data of the previous iteration step m. Alternating these simplifications in equation (4.8), results into:

$$\begin{aligned} \frac{\alpha_{u_i}^{m+1}\rho_{u_i}^{n} - \alpha_{u_i}^{n}\rho_{u_i}^{n}}{\Delta t} & + \frac{1}{2}\frac{\hat{\alpha}_{u_{i+\frac{1}{2}}}^{m+1}\hat{\rho}_{u_{i+\frac{1}{2}}}^{n}A_{i+\frac{1}{2}}u_{s,u_{i+\frac{1}{2}}}^{m+1} - \hat{\alpha}_{u_{i-\frac{1}{2}}}^{m+1}\hat{\rho}_{u_{i-\frac{1}{2}}}^{n}A_{i-\frac{1}{2}}u_{s,u_{i-\frac{1}{2}}}^{m+1}}{A_i\Delta s} + \frac{1}{2}\frac{\Psi_{lu_i}^{n}P_{u,l_i}^{m}}{A_i} \cdots \\ & + \frac{1}{2}\frac{\hat{\alpha}_{u_{i+\frac{1}{2}}}^{n}\hat{\rho}_{u_{i+\frac{1}{2}}}^{n}A_{i+\frac{1}{2}}u_{s,u_{i+\frac{1}{2}}}^{n} - \hat{\alpha}_{u_{i-\frac{1}{2}}}^{n}\hat{\rho}_{u_{i-\frac{1}{2}}}^{n}A_{i-\frac{1}{2}}u_{s,u_{i-\frac{1}{2}}}^{n}}{A_i\Delta s} + \frac{1}{2}\frac{\Psi_{lu_i}^{n}P_{u,l_i}^{n}}{A_i} = 0, \end{aligned} \tag{4.9}$$

in which $\hat{\alpha}_{u_{i-\frac{1}{2}}}^{m+1}u_{s,u_{i-\frac{1}{2}}}^{m+1}$ and $\hat{\alpha}_{u_{i-\frac{1}{2}}}^{m+1}u_{s,u_{i-\frac{1}{2}}}^{m+1}$ are the nonlinear terms of the discretised IPCE. The solution of the hold-up of the upper region at $m+1$ depends on the solution of the velocity of the upper region at the new iteration level. It is difficult and computationally time consuming to deal with this nonlinearity. Two common procedures are the Newton-Raphson method and the Picard method. The Newton linearisation approximates these terms as:

$$\begin{aligned} \hat{\alpha}_{u_{i-\frac{1}{2}}}^{m+1}u_{s,u_{i-\frac{1}{2}}}^{m+1} \simeq \hat{\alpha}_{u_{i-\frac{1}{2}}}^{m+1}u_{s,u_{i-\frac{1}{2}}}^{m} + \hat{\alpha}_{u_{i-\frac{1}{2}}}^{m}u_{s,u_{i-\frac{1}{2}}}^{m+1} - \hat{\alpha}_{u_{i-\frac{1}{2}}}^{m}u_{s,u_{i-\frac{1}{2}}}^{m} \quad \text{and} \\ \hat{\alpha}_{u_{i+\frac{1}{2}}}^{m+1}u_{s,u_{i+\frac{1}{2}}}^{m+1} \simeq \hat{\alpha}_{u_{i+\frac{1}{2}}}^{m+1}u_{s,u_{i+\frac{1}{2}}}^{m} + \hat{\alpha}_{u_{i+\frac{1}{2}}}^{m}u_{s,u_{i+\frac{1}{2}}}^{m+1} - \hat{\alpha}_{u_{i+\frac{1}{2}}}^{m}u_{s,u_{i+\frac{1}{2}}}^{m}, \end{aligned} \tag{4.10}$$

while the Picard linearisation approximates the terms as:

$$\hat{\alpha}_{u_{i-\frac{1}{2}}}^{m+1}u_{s,u_{i-\frac{1}{2}}}^{m+1} \simeq \hat{\alpha}_{u_{i-\frac{1}{2}}}^{m+1}u_{s,u_{i-\frac{1}{2}}}^{m} \quad \text{and} \quad \hat{\alpha}_{u_{i+\frac{1}{2}}}^{m+1}u_{s,u_{i+\frac{1}{2}}}^{m+1} \simeq \hat{\alpha}_{u_{i+\frac{1}{2}}}^{m+1}u_{s,u_{i+\frac{1}{2}}}^{m}, \tag{4.11}$$

where $\hat{\alpha}_{u_{i-\frac{1}{2}}}^{m+1}u_{s,u_{i-\frac{1}{2}}}^{m}$ and $\hat{\alpha}_{u_{i+\frac{1}{2}}}^{m+1}u_{s,u_{i+\frac{1}{2}}}^{m}$ are preferred over $\hat{\alpha}_{u_{i-\frac{1}{2}}}^{m}u_{s,u_{i-\frac{1}{2}}}^{m+1}$ and $\hat{\alpha}_{u_{i+\frac{1}{2}}}^{m}u_{s,u_{i+\frac{1}{2}}}^{m+1}$, as the IPCE is used to solve the hold-up of the upper region. [23]

An advantage of Newton's method is that it can reach an exponential convergence rate when it is correctly applied, while Picard's method is only capable of achieving a linear convergence rate. However, a single Newton iteration is computationally more demanding than a single Picard iteration, and the exponential convergence of the Newton method requires a sufficiently good initial estimate.

It is chosen to approximate the nonlinear terms by Picard's method in the current FVM model, as it simplifies the discretisation and is possibly even faster than Newton's method. Nonetheless, research is done on the possibilities of implementing Newton's method. This is elaborated in Appendix B. Applying Picard's method, and thereby setting the axial velocity variables of the upper region back to the current iteration level m, yields:

$$\begin{aligned}\frac{\alpha_{u_i}^{m+1}\rho_{u_i}^{n}-\alpha_{u_i}^{n}\rho_{u_i}^{n}}{\Delta t}+\frac{1}{2}\frac{\hat{\alpha}_{u_{i+\frac{1}{2}}}^{m+1}\hat{\rho}_{u_{i+\frac{1}{2}}}^{n}A_{i+\frac{1}{2}}u_{s,u_{i+\frac{1}{2}}}^{m}-\hat{\alpha}_{u_{i-\frac{1}{2}}}^{m+1}\hat{\rho}_{u_{i-\frac{1}{2}}}^{n}A_{i-\frac{1}{2}}u_{s,u_{i-\frac{1}{2}}}^{m}}{A_i\Delta s}+\frac{1}{2}\frac{\Psi_{lu_i}^{n}P_{u,l_i}^{m}}{A_i}\cdots\\ +\frac{1}{2}\frac{\hat{\alpha}_{u_{i+\frac{1}{2}}}^{n}\hat{\rho}_{u_{i+\frac{1}{2}}}^{n}A_{i+\frac{1}{2}}u_{s,u_{i+\frac{1}{2}}}^{n}-\hat{\alpha}_{u_{i-\frac{1}{2}}}^{n}\hat{\rho}_{u_{i-\frac{1}{2}}}^{n}A_{i-\frac{1}{2}}u_{s,u_{i-\frac{1}{2}}}^{n}}{A_i\Delta s}+\frac{1}{2}\frac{\Psi_{lu_i}^{n}P_{u,l_i}^{n}}{A_i}=0\end{aligned} \tag{4.12}$$

The last step is to implement the iterative incremental formulation of the hold-up of the upper region of Eqn (4.7) in the previous equation (4.12), to obtain the fully discretised IPCE in the incremental formulation.

$$\begin{aligned}&\frac{\Delta\alpha_{u_i}^{m+1}\rho_{u_i}^{n}}{\Delta t}&&+\frac{1}{2}\frac{\Delta\hat{\alpha}_{u_{i+\frac{1}{2}}}^{m+1}\hat{\rho}_{u_{i+\frac{1}{2}}}^{n}A_{i+\frac{1}{2}}u_{s,u_{i+\frac{1}{2}}}^{m}-\Delta\hat{\alpha}_{u_{i-\frac{1}{2}}}^{m+1}\hat{\rho}_{u_{i-\frac{1}{2}}}^{n}A_{i-\frac{1}{2}}u_{s,u_{i-\frac{1}{2}}}^{m}}{A_i\Delta s}&&+\frac{1}{2}\frac{\Psi_{lu_i}^{n}P_{u,l_i}^{m}}{A_i}=\cdots\\ &-\frac{\alpha_{u_i}^{m}\rho_{u_i}^{n}-\alpha_{u_i}^{n}\rho_{u_i}^{n}}{\Delta t}&&-\frac{1}{2}\frac{\hat{\alpha}_{u_{i+\frac{1}{2}}}^{m}\hat{\rho}_{u_{i+\frac{1}{2}}}^{n}A_{i+\frac{1}{2}}u_{s,u_{i+\frac{1}{2}}}^{m}-\hat{\alpha}_{u_{i-\frac{1}{2}}}^{m}\hat{\rho}_{u_{i-\frac{1}{2}}}^{n}A_{i-\frac{1}{2}}u_{s,u_{i-\frac{1}{2}}}^{m}}{A_i\Delta s}&&-\frac{1}{2}\frac{\Psi_{lu_i}^{n}P_{u,l_i}^{m}}{A_i}\cdots\\ &&&-\frac{1}{2}\frac{\hat{\alpha}_{u_{i+\frac{1}{2}}}^{n}\hat{\rho}_{u_{i+\frac{1}{2}}}^{n}A_{i+\frac{1}{2}}u_{s,u_{i+\frac{1}{2}}}^{n}-\hat{\alpha}_{u_{i-\frac{1}{2}}}^{n}\hat{\rho}_{u_{i-\frac{1}{2}}}^{n}A_{i-\frac{1}{2}}u_{s,u_{i-\frac{1}{2}}}^{n}}{A_i\Delta s}&&-\frac{1}{2}\frac{\Psi_{lu_i}^{n}P_{u,l_i}^{n}}{A_i}.\end{aligned} \tag{4.13}$$

Together with the other discretised incremental equations equation (4.13) is solved in the iteration procedure of a coupled solver. The coupled solver is explained in section 4.8. Note that the increments of the hold-up of the upper region are all brought to the left hand side in equation (4.13). On the right hand side of this equation, the original discretised of equation (4.5) is observed minus the time dependencies at the new time level. The right hand side must always contain the original discretised equation for the incremental-iterative formulation. This is considered as the biggest advantage of this method and must always be checked.

The hold-up of the lower region is determined directly after the iteration procedure of the coupled solver by:

$$\alpha_{l_i}^{m+1}=1-\alpha_{u_i}^{m+1}. \tag{4.14}$$

4.4.2. Incompressible velocity equation

The sum of the incompressible velocity equation of equation (3.11) is taken over the upper and lower region, $\beta\in(u,l)$.

$$A\sum_{\beta}\frac{\partial\left(\alpha_\beta u_{s,\beta}\right)}{\partial s}=A\frac{\partial\left(\alpha_u u_{s,u}+\alpha_l u_{s,l}\right)}{\partial s}=0 \tag{3.11}$$

Integrating equation (3.11) over the volume occupied in the i^{th} cell and dividing by the cell length Δs yields:

$$\frac{A_i}{\Delta s}\left(\hat{\alpha}_{u_{i+\frac{1}{2}}}u_{s,u_{i+\frac{1}{2}}}+\hat{\alpha}_{l_{i+\frac{1}{2}}}u_{s,l_{i+\frac{1}{2}}}-\hat{\alpha}_{u_{i-\frac{1}{2}}}u_{s,u_{i-\frac{1}{2}}}-\hat{\alpha}_{l_{i-\frac{1}{2}}}u_{s,l_{i-\frac{1}{2}}}\right)=0 \tag{4.15}$$

Dividing by $A_i/\Delta s$, and setting all variables at the new time step (implicit method), results into:

$$\hat{\alpha}_{u_{i+\frac{1}{2}}}^{n+1}u_{s,u_{i+\frac{1}{2}}}^{n+1}+\hat{\alpha}_{l_{i+\frac{1}{2}}}^{n+1}u_{s,l_{i+\frac{1}{2}}}^{n+1}-\hat{\alpha}_{u_{i-\frac{1}{2}}}^{n+1}u_{s,u_{i-\frac{1}{2}}}^{n+1}-\hat{\alpha}_{l_{i-\frac{1}{2}}}^{n+1}u_{s,l_{i-\frac{1}{2}}}^{n+1}=0, \tag{4.16}$$

where all four terms are nonlinear terms. The incremental formulation for the velocity variables is similar to the notation of the hold-ups.

$$u_{s,u_{i+\frac{1}{2}}}^{m+1}=u_{s,u_{i+\frac{1}{2}}}^{m}+\Delta u_{s,u_{i+\frac{1}{2}}}^{m+1}\quad\text{and}\quad u_{s,l_{i+\frac{1}{2}}}^{m+1}=u_{s,l_{i+\frac{1}{2}}}^{m}+\Delta u_{s,l_{i+\frac{1}{2}}}^{m+1} \tag{4.17}$$

Using the Picard method to approximate the nonlinear terms of equation (4.16) and implementing the incremental formuation of the velocity variables yields:

$$\begin{aligned}&\hat{\alpha}_{u_{i+\frac{1}{2}}}^{m}\Delta u_{s,u_{i+\frac{1}{2}}}^{m+1}+\hat{\alpha}_{l_{i+\frac{1}{2}}}^{m}\Delta u_{s,l_{i+\frac{1}{2}}}^{m+1}&&-\hat{\alpha}_{u_{i-\frac{1}{2}}}^{m}\Delta u_{s,u_{i-\frac{1}{2}}}^{m+1}-\hat{\alpha}_{l_{i-\frac{1}{2}}}^{m}\Delta u_{s,l_{i-\frac{1}{2}}}^{m+1}=\cdots\\ &-\hat{\alpha}_{u_{i+\frac{1}{2}}}^{m}u_{s,u_{i+\frac{1}{2}}}^{m}-\hat{\alpha}_{l_{i+\frac{1}{2}}}^{m}u_{s,l_{i+\frac{1}{2}}}^{m}&&+\hat{\alpha}_{u_{i-\frac{1}{2}}}^{m}u_{s,u_{i-\frac{1}{2}}}^{m}+\hat{\alpha}_{l_{i-\frac{1}{2}}}^{m}u_{s,l_{i-\frac{1}{2}}}^{m}.\end{aligned} \tag{4.18}$$

equation (4.18) is the fully discretised incompressible velocity equation in incremental formulation.

4.4.3. Slip relation

The final slip relation of equation (3.55) is considered.

$$u_{s,u} - u_{s,l} = \mathscr{F}(\alpha_u, \theta, \varepsilon_1)\mathscr{G}_{B_1B_2}\left(\theta, \frac{\mathrm{d}h}{\mathrm{d}s}, \varepsilon_2\right) u_E(\rho_u, \rho_l, \theta) \tag{3.55}$$

As the slip relation does not contain any partial derivatives with respect to time and space, the discretisation process is simplified. Evaluating the slip relation directly at cell edge $i-\frac{1}{2}$ and time level $n+1$ and omitting the dependencies of the Slip functions yields:

$$u^{n+1}_{s,u_{i-\frac{1}{2}}} - u^{n+1}_{s,l_{i-\frac{1}{2}}} = \mathscr{F}^{n+1}_{i-\frac{1}{2}}\mathscr{G}^{n+1}_{B_1B_2{}_{i-\frac{1}{2}}}\, u^{n+1}_{E_{i-\frac{1}{2}}}. \tag{4.19}$$

The slip relation is discretised for the $i-\frac{1}{2}{}^{\text{th}}$ node, as this is the first cell edge in the staggered grid arrangement.

The three slip relations $\mathscr{F}$, $\mathscr{G}_{B_1B_2}$, and u_E are the nonlinear terms of the discretised slip relation. The hold-up and interface function respectively depend on the hold-up of the upper and lower region. The effective bubble velocity function is a function of the densities of both regions, which depend on the volume fraction of the fluids in the regions. Recall that these variables are all defined in the i^{th} node, while their information is needed at the $i\pm\frac{1}{2}{}^{\text{th}}$ nodes.

The slip relation is not derived from the integral form of a conservation law and is an artefact to couple the slip velocity to the correct effective bubble velocity via the functions. The relation does not include a partial derivative with respect to the axial distance, and therefore is its discretised form not able to handle to the fluxes as a FVM. To approximate the fluxes of the variables at the cell edges the central scheme is used as it averages the values variables of the two sequent cells. The central scheme is denoted by the superscript $\bar{(\cdot)}$ and elaborated in Section 4.5. In Fig. 4.4 the variables which have to be approximated around the node $i-\frac{1}{2}$ are visualised.

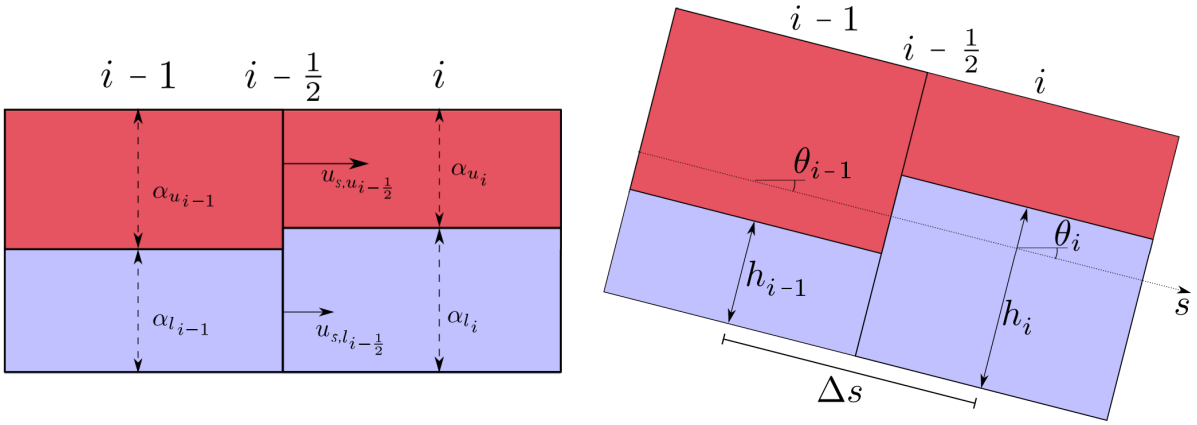

Figure 4.4: The variables which have to be approximated at a cell edge for the slip relation are illustrated. The values of the variables at $i-\frac{1}{2}$ are determined by the central scheme and thereby use the information of these variables at the cell centres $i-1$ and i. Note that the density variables are not included in the figures, however the central scheme is also adopted to determine their values at the cell edges, as the effective bubble velocity function requires those as input. [7]

The functions do not depend on the axial velocities of the upper and lower regions, and as the slip relation is an equation used to solve the velocity variables, no linearisation process is needed to apply Picard's method. When Newton's method is applied, increments of the hold-ups and volume fractions would be present in the discretised slip relation.

The hold-up and interface function are determined at the previous iteration level m and the effective bubble velocity function is calculated at the previous time step n, as it depends on the densities terms which are determined at this time level as well.

Implementing the incremental formulation of the velocity variables of equation (4.17), setting the correct time and iterative dependency levels and taking into account the dependencies of the Slip functions yields:

$$\begin{aligned}\Delta u^{m+1}_{s,u_{i-\frac{1}{2}}} - \Delta u^{m+1}_{s,l_{i-\frac{1}{2}}} = \dots \\ \mathscr{F}^{m}_{i-\frac{1}{2}}\left(\tilde{\alpha}^{m}_{u_{i-\frac{1}{2}}}, \tilde{\theta}_{i-\frac{1}{2}}, \varepsilon_1\right)\mathscr{G}^{m}_{B_1B_2{}_{i-\frac{1}{2}}}\left(\tilde{\theta}_{i-\frac{1}{2}}, \frac{\mathrm{d}\tilde{h}}{\mathrm{d}s}^{m}_{i-\frac{1}{2}}, \varepsilon_2\right)u^{n}_{E_{i-\frac{1}{2}}}\left(\tilde{\rho}^{n}_{u_{i-\frac{1}{2}}}, \tilde{\rho}^{n}_{u_{i-\frac{1}{2}}}, \tilde{\theta}_{i-\frac{1}{2}}\right) - u^{m}_{s,u_{i-\frac{1}{2}}} + u^{m}_{s,l_{i-\frac{1}{2}}}.\end{aligned} \tag{4.20}$$

equation (4.20) is the fully discretised Slip relation in the incremental-iterative formulation used in the coupled solver.

4.4.4. Multiphase transport equation

The discretisation of the multiphase transport equations of equations (3.15) & (3.17) is only shown for equation (3.15), as the same discretising procedure must be followed for both equations.

$$\frac{\partial c_{Lu}A_u}{\partial t} + \frac{\partial c_{Lu}u_{s,u}A_u}{\partial s} - \frac{\partial}{\partial s}\left(\mathscr{D}_{s,u}\frac{\partial c_{Lu}}{\partial s}A_u\right) + \Psi_{L,lu}P_{u,l} = 0 \tag{3.15}$$

Integrating equation (3.15) over the volume of the upper region of the i^{th} node, dividing by Δs, yields:

$$\begin{aligned}\frac{\mathrm{d}}{\mathrm{d}t}\left(c_{Lu_i}A_{u_i}\right) + \frac{1}{\Delta s}\left(\left(c_{Lu}A_u\right)_{i+\frac{1}{2}}u_{s,u_{i+\frac{1}{2}}} - \left(c_{Lu}A_u\right)_{i-\frac{1}{2}}u_{s,u_{i-\frac{1}{2}}}\right)\dots \\ - \frac{1}{\Delta s}\left(\left(\mathscr{D}_{s,u}\left(\frac{\partial c_{Lu}}{\partial s}\right)A_u\right)_{i+\frac{1}{2}} - \left(\mathscr{D}_{s,u}\left(\frac{\partial c_{Lu}}{\partial s}\right)A_u\right)_{i-\frac{1}{2}}\right) + \Psi_{L,lu_i}P_{u,l_i} = 0.\end{aligned} \tag{4.21}$$

The FVM of the equation (4.21) is similar to the semi-discretised equation as observed in equation (4.4). Here an extra diffusve term is seen. The volume fraction, area, axial dispersion coefficient, volumetric transfer term and wetted perimeter variables are in the cell centre and the velocity variables at the cell egdes. Both advective and diffusive fluxes need to be determined at the cell boundaries, but require another type of discretisation. Again, the contribution to the advective fluxes of the volume fraction and the area is explained in Section 4.5, and their variables at the $i \pm \frac{1}{2}^{th}$ nodes are denoted by the superscript $(\tilde{.})$. All relevant flow variables needed in the discretisation process of the multiphase transport equations are visualised in Fig. 4.5.

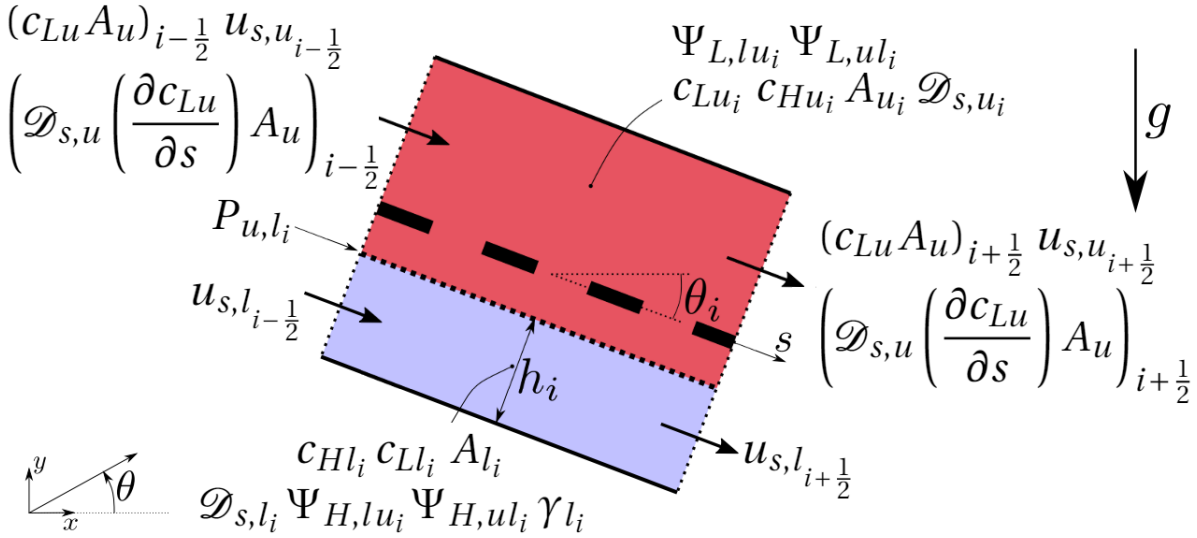

Figure 4.5: The relevant flow variables needed for discretising the multiphase transport equation are visualised around the cell i. Note that the advective and diffusive fluxes for of equation (4.21) are added as well. [7]

The discretisation method of the diffusive fluxes is already explained here, as it is less complicated and gives less complications to the numerical solution. The diffusive flux can be approximated by a central discretisation, which is obtained by expanding a Taylor series around $i \pm \frac{1}{2}$. [23]

$$\left(\mathscr{D}_{s,u}\left(\frac{\partial c_{Lu}}{\partial s}\right)A_u\right)_{i+\frac{1}{2}} = \tilde{\mathscr{D}}_{s,u_{i+\frac{1}{2}}}\frac{c_{Lu_{i+1}} - c_{Lu_i}}{\Delta s}\tilde{A}_{u_{i+\frac{1}{2}}}\left(+\mathscr{O}\left(\Delta s^2\right)\right) \tag{4.22a}$$

$$\left(\mathscr{D}_{s,u}\left(\frac{\partial c_{Lu}}{\partial s}\right)A_u\right)_{i-\frac{1}{2}} = \tilde{\mathscr{D}}_{s,u_{i-\frac{1}{2}}}\frac{c_{Lu_i} - c_{Lu_{i-1}}}{\Delta s}\tilde{A}_{u_{i-\frac{1}{2}}}\left(+\mathscr{O}\left(\Delta x^2\right)\right) \tag{4.22b}$$

Here, the axial dispersion coefficient and area variables are defined as:

$$\tilde{\mathscr{D}}_{s,u_{i+\frac{1}{2}}} = \frac{\mathscr{D}_{s,u_{i+1}} + \mathscr{D}_{s,u_i}}{2}; \qquad \text{and} \qquad \tilde{\mathscr{D}}_{s,u_{i-\frac{1}{2}}} = \frac{\mathscr{D}_{s,u_i} + \mathscr{D}_{s,u_{i-1}}}{2}; \tag{4.23a}$$

$$\tilde{A}_{u_{i+\frac{1}{2}}} = \frac{A_{u_{i+1}} + A_{u_i}}{2}; \qquad \text{and} \qquad \tilde{A}_{u_{i-\frac{1}{2}}} = \frac{A_{u_i} + A_{u_{i-1}}}{2}. \tag{4.23b}$$

This method is called the central scheme and is explained in Section 4.5.

As can be seen in equation (4.22), the central discretisation is second-order accurate. This holds for a uniform grid, however on a non-smooth grid the consistency might be lost. [21] The consistency of a numerical method is explained in Section 4.7.

Implementing the Crank-Nicolson time discretisation method into equation (4.21) and taking into account the new notations of the advective and diffusive fluxes, results in:

$$\begin{aligned}
&\frac{c^{n+1}_{Lu_i}A^{n+1}_{u_i} - c^{n}_{Lu_i}A^{n}_{u_i}}{\Delta t} + \frac{1}{2}\frac{\hat{c}^{n+1}_{Lu_{i+\frac{1}{2}}}\hat{A}^{n+1}_{u_{i+\frac{1}{2}}}u^{n+1}_{s,u_{i+\frac{1}{2}}} - \hat{c}^{n+1}_{Lu_{i-\frac{1}{2}}}\hat{A}^{n+1}_{u_{i-\frac{1}{2}}}u^{n+1}_{s,u_{i-\frac{1}{2}}}}{\Delta s}\cdots \\
&\qquad - \frac{1}{2\Delta s}\left(\tilde{\mathscr{D}}^{n+1}_{s,u_{i+\frac{1}{2}}}\frac{c^{n+1}_{Lu_{i+1}} - c^{n+1}_{Lu_i}}{\Delta s}\tilde{A}^{n+1}_{u_{i+\frac{1}{2}}} - \tilde{\mathscr{D}}^{n+1}_{s,u_{i-\frac{1}{2}}}\frac{c^{n+1}_{Lu_i} - c^{n+1}_{Lu_{i-1}}}{\Delta s}\tilde{A}^{n+1}_{u_{i-\frac{1}{2}}}\right)\cdots \\
&\qquad + \frac{1}{2}\Psi^{n+1}_{L,lu_i}P^{n+1}_{u,l_i}\cdots \\
&\qquad + \frac{1}{2}\frac{\hat{c}^{n}_{Lu_{i+\frac{1}{2}}}\hat{A}^{n}_{u_{i+\frac{1}{2}}}u^{n}_{s,u_{i+\frac{1}{2}}} - \hat{c}^{n}_{Lu_{i-\frac{1}{2}}}\hat{A}^{n}_{u_{i-\frac{1}{2}}}u^{n}_{s,u_{i-\frac{1}{2}}}}{\Delta s}\cdots \\
&\qquad - \frac{1}{2\Delta s}\left(\tilde{\mathscr{D}}^{n}_{s,u_{i+\frac{1}{2}}}\frac{c^{n}_{Lu_{i+1}} - c^{n}_{Lu_i}}{\Delta s}\tilde{A}^{n}_{u_{i+\frac{1}{2}}} - \tilde{\mathscr{D}}^{n}_{s,u_{i-\frac{1}{2}}}\frac{c^{n}_{Lu_i} - c^{n}_{Lu_{i-1}}}{\Delta s}\tilde{A}^{n}_{u_{i-\frac{1}{2}}}\right)\cdots \\
&\qquad + \frac{1}{2}\Psi^{n}_{L,lu_i}P^{n}_{u,l_i} = 0.
\end{aligned} \tag{4.24}$$

In equation (4.24), only nonlinear terms are observed at the new time level $n+1$; eight in total. Therefore, Newton's method would require much effort to linearise this equation. Note that the area of the upper region can actually be written as the hold-up of the upper region multiplied by the total cross-sectional area of the pipe; $A_u = \alpha_u A$.

The incremental formulation for the volume fraction of the light fluid particles in the upper region is defined as:

$$c^{m+1}_{Lu_i} = c^{m}_{Lu_i} + \Delta c^{m+1}_{Lu_i}. \tag{4.25}$$

In Picard's linearisation method, only the volume fraction variables at the new iteration level $m+1$ are considered, as the multiphase transport equation is used to solve the concentrations. Furthermore, the axial dispersion coefficient and the volumetric transfer term are determined at the previous time step level n and are constants in the fully discretised equation.

Implementing the incremental formulation of the volume fractions and considering the time and iterative dependencies of the variables yields:

$$\begin{aligned}
&\frac{\Delta c^{m+1}_{Lu_i} A^m_{u_i}}{\Delta t} + \frac{1}{2}\frac{\Delta \hat{c}^{m+1}_{Lu_{i+\frac{1}{2}}} \hat{A}^m_{u_{i+\frac{1}{2}}} u^m_{s,u_{i+\frac{1}{2}}} - \Delta \hat{c}^{m+1}_{Lu_{i-\frac{1}{2}}} \hat{A}^m_{u_{i-\frac{1}{2}}} u^m_{s,u_{i-\frac{1}{2}}}}{\Delta s} \cdots \\
&\quad - \frac{1}{2\Delta s}\left(\tilde{\mathscr{D}}^n_{s,u_{i+\frac{1}{2}}} \frac{\Delta c^{m+1}_{Lu_{i+1}} - \Delta c^{m+1}_{Lu_i}}{\Delta s} \tilde{A}^m_{u_{i+\frac{1}{2}}} - \tilde{\mathscr{D}}^n_{s,u_{i-\frac{1}{2}}} \frac{\Delta c^{m+1}_{Lu_i} - \Delta c^{m+1}_{Lu_{i-1}}}{\Delta s} \tilde{A}^m_{u_{i-\frac{1}{2}}} \right) = \dots \\
&- \frac{c^m_{Lu_i} A^m_{u_i} - c^n_{Lu_i} A^n_{u_i}}{\Delta t} - \frac{1}{2}\frac{\hat{c}^m_{Lu_{i+\frac{1}{2}}} \hat{A}^m_{u_{i+\frac{1}{2}}} u^m_{s,u_{i+\frac{1}{2}}} - \hat{c}^m_{Lu_{i-\frac{1}{2}}} \hat{A}^m_{u_{i-\frac{1}{2}}} u^m_{s,u_{i-\frac{1}{2}}}}{\Delta s} - \frac{1}{2}\Psi^n_{L,lu_i} P^m_{u,l_i} \cdots \\
&\quad + \frac{1}{2\Delta s}\left(\tilde{\mathscr{D}}^n_{s,u_{i+\frac{1}{2}}} \frac{c^m_{Lu_{i+1}} - c^m_{Lu_i}}{\Delta s} \tilde{A}^m_{u_{i+\frac{1}{2}}} - \tilde{\mathscr{D}}^n_{s,u_{i-\frac{1}{2}}} \frac{c^m_{Lu_i} - c^m_{Lu_{i-1}}}{\Delta s} \tilde{A}^m_{u_{i-\frac{1}{2}}} \right) \cdots \\
&\quad - \frac{1}{2}\frac{\hat{c}^n_{Lu_{i+\frac{1}{2}}} \hat{A}^n_{u_{i+\frac{1}{2}}} u^n_{s,u_{i+\frac{1}{2}}} - \hat{c}^n_{Lu_{i-\frac{1}{2}}} \hat{A}^n_{u_{i-\frac{1}{2}}} u^n_{s,u_{i-\frac{1}{2}}}}{\Delta s} - \frac{1}{2}\Psi^n_{L,lu_i} P^n_{u,l_i} \cdots \\
&\quad + \frac{1}{2\Delta s}\left(\tilde{\mathscr{D}}^n_{s,u_{i+\frac{1}{2}}} \frac{c^n_{Lu_{i+1}} - c^n_{Lu_i}}{\Delta s} \tilde{A}^n_{u_{i+\frac{1}{2}}} - \tilde{\mathscr{D}}^n_{s,u_{i-\frac{1}{2}}} \frac{c^n_{Lu_i} - c^n_{Lu_{i-1}}}{\Delta s} \tilde{A}^n_{u_{i-\frac{1}{2}}} \right).
\end{aligned} \tag{4.26}$$

equation (4.26) is the fully discretised multiphase transport equation of volume fraction variable c_{Lu}. Note that only the increments of this variable are on the left hand side. The right hand side displays the original Crank-Nicolson formulation of the equation given in equation (4.24).

The volume fraction of the heavy fluid particles in the upper region is determined directly after the iteration procedure of the coupled solver by:

$$c^{m+1}_{Hu} = 1 - c^{m+1}_{Lu}. \tag{4.27}$$

The fully discretised multiphase transport equation of volume fraction variable c_{Hl} is defined as:

$$\begin{aligned}
&\frac{\Delta c^{m+1}_{Hl_i} A^m_{l_i}}{\Delta t} + \frac{1}{2}\frac{\Delta \hat{c}^{m+1}_{Hl_{i+\frac{1}{2}}} \hat{A}^m_{l_{i+\frac{1}{2}}} u^m_{s,l_{i+\frac{1}{2}}} - \Delta \hat{c}^{m+1}_{Hl_{i-\frac{1}{2}}} \hat{A}^m_{l_{i-\frac{1}{2}}} u^m_{s,l_{i-\frac{1}{2}}}}{\Delta s} \cdots \\
&\quad - \frac{1}{2\Delta s}\left(\tilde{\mathscr{D}}^n_{s,l_{i+\frac{1}{2}}} \frac{\Delta c^{m+1}_{Hl_{i+1}} - \Delta c^{m+1}_{Hl_i}}{\Delta s} \tilde{A}^m_{l_{i+\frac{1}{2}}} - \tilde{\mathscr{D}}^n_{s,l_{i-\frac{1}{2}}} \frac{\Delta c^{m+1}_{Hl_i} - \Delta c^{m+1}_{Hl_{i-1}}}{\Delta s} \tilde{A}^m_{l_{i-\frac{1}{2}}} \right) = \dots \\
&- \frac{c^m_{Hl_i} A^m_{l_i} - c^n_{Hl_i} A^n_{l_i}}{\Delta t} - \frac{1}{2}\frac{\hat{c}^m_{Hl_{i+\frac{1}{2}}} \hat{A}^m_{l_{i+\frac{1}{2}}} u^m_{s,l_{i+\frac{1}{2}}} - \hat{c}^m_{Hl_{i-\frac{1}{2}}} \hat{A}^m_{l_{i-\frac{1}{2}}} u^m_{s,l_{i-\frac{1}{2}}}}{\Delta s} + \frac{1}{2}\Psi^n_{H,ul_i} P^m_{l,l_i} \cdots \\
&\quad + \frac{1}{2\Delta s}\left(\tilde{\mathscr{D}}^n_{s,l_{i+\frac{1}{2}}} \frac{c^m_{Hl_{i+1}} - c^m_{Hl_i}}{\Delta s} \tilde{A}^m_{l_{i+\frac{1}{2}}} - \tilde{\mathscr{D}}^n_{s,l_{i-\frac{1}{2}}} \frac{c^m_{Hl_i} - c^m_{Hl_{i-1}}}{\Delta s} \tilde{A}^m_{l_{i-\frac{1}{2}}} \right) \cdots \\
&\quad - \frac{1}{2}\frac{\hat{c}^n_{Hl_{i+\frac{1}{2}}} \hat{A}^n_{l_{i+\frac{1}{2}}} u^n_{s,l_{i+\frac{1}{2}}} - \hat{c}^n_{Hl_{i-\frac{1}{2}}} \hat{A}^n_{l_{i-\frac{1}{2}}} u^n_{s,l_{i-\frac{1}{2}}}}{\Delta s} + \frac{1}{2}\Psi^n_{H,ul_i} P^n_{l,l_i} \cdots \\
&\quad + \frac{1}{2\Delta s}\left(\tilde{\mathscr{D}}^n_{s,l_{i+\frac{1}{2}}} \frac{c^n_{Hl_{i+1}} - c^n_{Hl_i}}{\Delta s} \tilde{A}^n_{l_{i+\frac{1}{2}}} - \tilde{\mathscr{D}}^n_{s,l_{i-\frac{1}{2}}} \frac{c^n_{Hl_i} - c^n_{Hl_{i-1}}}{\Delta s} \tilde{A}^n_{l_{i-\frac{1}{2}}} \right).
\end{aligned} \tag{4.28}$$

This is the second multiphase transport equation in the coupled solver which solves the volume fraction of the heavy fluid particles of the lower region. The volume fraction of the light fluid particles of the lower region are directly determined at the end of the iteration procedure by:

$$c^{m+1}_{Ll} = 1 - c^{m+1}_{Hl}. \tag{4.29}$$

4.5. Discretisation of advective terms

It was mentioned earlier that finding a reliable higher-order accurate scheme for the advective term is challenging. The advective terms of equations (4.13), (4.26) & (4.28) were already denoted by the superscript $\dot{(\cdot)}$, but the terms were not discretised yet. In this section, the method for obtaining a solution of high numerical accuracy from the advective terms is described.

This section could also be interpreted as an explanation of how variables defined in the i^{th} node could be determined at the $i \pm \frac{1}{2}^{\text{th}}$ nodes. To better visualise this process, an illustration of a series of cells is given in Fig. 4.6.

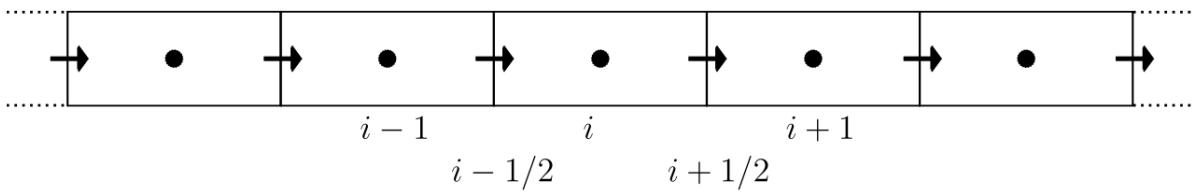

Figure 4.6: A series of cells with nodal notation. The dots represent the scalar quantities defined in the i^{th}, and the arrows represent the vectorial quantities defined at the $i \pm \frac{1}{2}^{\text{th}}$ nodes. [26]

The scalar quantity Q, introduced in Section 4.3, is used throughout this section to visualise the discretisation implementation of the different schemes.

4.5.1. Central scheme

The central scheme was already mentioned in Section 4.4.3 & 4.4.4 to determine the flow variables inside the slip relations and the axial dispersion coefficient and area of the upper region at the cell boundaries for the diffusive flux. Variables discretised by the central scheme are denoted by the superscript $\bar{(\cdot)}$.

The central scheme approximates the quantity Q at a cell edge by taking the average of the neighbouring cells. It is often considered as a basic example for approximating a cell centred variable at a cell boundary.

$$Q_{i-\frac{1}{2}} = \frac{1}{2}\left(Q_i + Q_{i-1}\right) \tag{4.30a}$$

$$Q_{i+\frac{1}{2}} = \frac{1}{2}\left(Q_{i+1} + Q_i\right) \tag{4.30b}$$

The advective terms are rarely discretised using this scheme, although the method is second-order accurate in space. The central scheme will introduce oscillations into the solution near steep gradients. These oscillations can result in unphysical values above 1 and below zero for the hold-up and volume fraction variables [23]. Regions with steep gradients are also known as discontinuities and will be encoutered many times in the cases of Chapter 5. The overshoots and undershoots at the discontinuities caused by the oscillations are called the Gibbs'phenomenon. Moreover, a dispersive error is seen in the solution despite the second-order accuracy of the scheme. This dispersive error might also cause a slight shift of the solution near large gradients called a phase error [18]. So, the central scheme has its disadvantages, but discretising the advective terms by the central scheme is nonetheless the preferred choice when the flow solution is expected to be smooth [21].

The central scheme provides a good solution to discretise the variables in the diffusive fluxes seen in equation (4.22). Oscillations will not be encountered by implementing this scheme due to the already diffusive character of the term.

Not only the scalar quantities of the diffusive terms are approximated at the cell edges by the central scheme, the velocity variables are approximated by this scheme as well to determine the axial velocities of the regions in the cell centres.

$$\bar{u}_{s,u_i} = \frac{1}{2}\left(u_{s,u_{i-\frac{1}{2}}} + u_{s,u_{i+\frac{1}{2}}}\right) \tag{4.31a}$$

$$\bar{u}_{s,l_i} = \frac{1}{2}\left(u_{s,l_{i-\frac{1}{2}}} + u_{s,l_{i+\frac{1}{2}}}\right) \tag{4.31b}$$

In the numerical model this is used to obtain a first idea of the sign of the velocity variables in the cell centres. Thereafter, a more accurate approximation of the velocity variables is made by a high-resolution scheme, explained in 4.5.3.

As shown in Subsection 4.5.3, the Lax-Wendroff scheme results in the central scheme for the chosen approach to discretise the advective terms. Besides, this scheme lacks the same weaknesses as the central scheme. However, the accuracy of the Lax-Wendroff scheme is wanted for a smooth flow solution, as will become clear.

The variables discretised by the central scheme are denoted by the superscript $\breve{(.)}$, as the central scheme is only used for variables seen in the diffusive terms of the model. These variables are easily distinquished by this notation from the discretised advective terms denoted by $\hat{(.)}$.

4.5.2. Upwind scheme

The upwind method approximates the value of the scalar quantity Q at the cell edges by considering the direction (sign) of the relevant velocity variable at those cell boundaries. The sign of the local axial velocity of the region determines the upwind direction. The value left of the cell boundary is taken if the velocity is positive (or equal to zero), and the value on the right of the cell boundary is chosen when the velocity is negative in magnitude. The scalar quantity at the $i-\frac{1}{2}^{\text{th}}$ is defined by the upwind scheme as,

$$\hat{Q}_{i-\frac{1}{2}} = \begin{cases} Q_{i-1}, & \text{for } u_{s,\beta_{i-\frac{1}{2}}} \geq 0, \\ Q_i, & \text{for } u_{s,\beta_{i-\frac{1}{2}}} < 0, \end{cases} \tag{4.32}$$

and at the $i+\frac{1}{2}^{\text{th}}$ as,

$$\hat{Q}_{i+\frac{1}{2}} = \begin{cases} Q_i, & \text{for } u_{s,\beta_{i+\frac{1}{2}}} \geq 0, \\ Q_{i+1}, & \text{for } u_{s,\beta_{i+\frac{1}{2}}} < 0, \end{cases} \tag{4.33}$$

The upwind scheme is widely used, as it is easily implemented in a numerical model. Its robustness and ability to compute discontinuities without introducing oscillations is seen as an advantage of this method. In other words, the scheme keeps the flow solution monotonic when this is needed. However, the disadvantage of the upwind scheme is that it causes an extra diffusive term into the model, which leads to smeared solutions and poor accuracies [18]. The derivation of this extra diffusive term, known as the numerical diffusion, is given in Section 4.7.1. A Taylor series expansion of the upwind scheme is given there as well, in order to visualise the scheme's first-order accuracy in space.

4.5.3. High-resolution schemes

The perfect scheme for the discretisation of the advective terms would be capable of predicting of a smooth flow solution at second-order accuracy, and of handling discontinuities in the flow without the introduction of oscillations. The obtained solution of discontinuities should also be of higher-order accuracy. Schemes which satisfy these criteria are called high-resolution schemes. So, the high-resolution schemes are designed to combine the best features of the Lax-Wendroff and upwind schemes.

The high-resolution schemes can be described using the definition of *Total Variation Diminishing* (TVD), a concept introduced by Harten [13]. This concept is a way to measure the oscillations in the solution, and to check whether the total variation of these oscillations do not increase over time. Therefore, the concept was introduced by Harten as Total Variation Non-Increasing (TVNI). The total variation of a set of data q^n (at time level n) is defined as:

$$\text{TV}\left(q^n\right) = \sum_{i=-\infty}^{\infty} \left|q_i - q_{i-1}\right|. \tag{4.34}$$

A scheme is called TVD, if for any set of data q^n, the values q^{n+1} computed by the method satisfy:

$$\text{TV}\left(q^{n+1}\right) \leq \text{TV}\left(q^n\right). \tag{4.35}$$

To guarantee that the TVD condition of equation (4.35) is satisfied, a high-resolution scheme makes use of a so-called limiter function. The idea behind the limiter function is that the scheme is altered over time and space to solve the different flow solutions present in the domain. If the solution is smooth, the high-resolution scheme should be equal to the Lax-Wendroff scheme, and when a discontinuity is seen in the flow solution, the scheme should behave like an upwind scheme. [18]

The magnitude of the limiter function is determined by the slope of the scalar quantities between three successive nodes (this is the reason that the chosen staggered grid contains two ghosts cells at both sides of the interior). The notation introduced by Leonard & Mokhtari [19] is used in this study and is illustrated in Fig. 4.7 to determine $Q_{i+\frac{1}{2}}$ for $u_{s,\beta} \geq 0$. Here, u indicates the upstream node, c represents the current node and d is the downstream node. The Leonard & Mokhtari notation depends on the sign of the velocity variable, just like the upwind scheme.

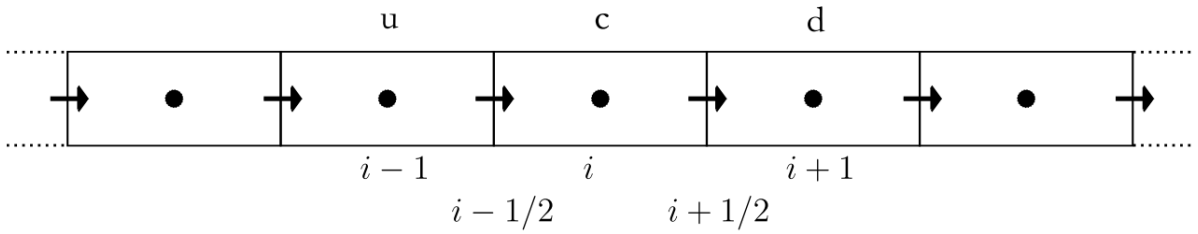

Figure 4.7: The series of cells with nodal notation as illustrated in Fig. 4.6, plus the notations u, c and d introduced by Leonard & Mokhtari. Here, the notations are used to determine the scalar quantity Q at the $i+\frac{1}{2}^{\text{th}}$ node for $u_{s,\beta} \geq 0$. [26]

The u-c-d-notation for Q at the $i-\frac{1}{2}^{\text{th}}$ node is represented by:

$$\hat{Q}_{i-\frac{1}{2}} = \begin{cases} Q_u = Q_{i-2}, \\ Q_c = Q_{i-1}, \\ Q_d = Q_i, \end{cases} \text{for } u_{s,\beta_{i-\frac{1}{2}}} \geq 0; \quad \text{and} \quad \hat{Q}_{i-\frac{1}{2}} = \begin{cases} Q_u = Q_{i+1}, \\ Q_c = Q_i, \\ Q_d = Q_{i-1}, \end{cases} \text{for } u_{s,\beta_{i-\frac{1}{2}}} < 0; \tag{4.36}$$

and the notation for Q at the $i+\frac{1}{2}^{\text{th}}$ node is defined as:

$$\hat{Q}_{i+\frac{1}{2}} = \begin{cases} Q_u = Q_{i-1}, \\ Q_c = Q_i, \\ Q_d = Q_{i+1}, \end{cases} \text{for } u_{s,\beta_{i+\frac{1}{2}}} \geq 0; \quad \text{and} \quad \hat{Q}_{i+\frac{1}{2}} = \begin{cases} Q_u = Q_{i+2}, \\ Q_c = Q_{i+1}, \\ Q_d = Q_i, \end{cases} \text{for } u_{s,\beta_{i+\frac{1}{2}}} < 0. \tag{4.37}$$

The large advantage of the notation by Leonard & Mokhtari is that it covers both signs of the velocity variables at the same time; i.e. $u_{s,\beta_{i\pm\frac{1}{2}}} \geq 0$ and $u_{s,\beta_{i\pm\frac{1}{2}}} < 0$. The slope between the upstream, current and downstream node is denoted by λ and is defined for a scalar quantity Q as:

$$\lambda_{i\pm\frac{1}{2}} = \frac{Q_c - Q_u}{Q_d - Q_c}. \tag{4.38}$$

$\lambda_{i\pm\frac{1}{2}}$ is also called the *smoothness gradient* as it determines the magnitude of the local gradient, which is equal to one for a smooth flow solution. Furthermore, it can be shown by a Taylor series expansion that $\lambda_{i\pm\frac{1}{2}}$ is second-order accurate in space for a smooth flow solution; i.e. $\mathcal{O}\left(\Delta s^2\right)$ [23].

The scalar quantity Q is approximated at the $i\pm\frac{1}{2}^{\text{th}}$ node by:

$$\begin{aligned} Q_{i\pm\frac{1}{2}} &= Q_c + \frac{1}{2}\mathscr{L}\left(\lambda_{i\pm\frac{1}{2}}\right)(Q_d - Q_c), \\ &= \left(1 - \frac{1}{2}\mathscr{L}\left(\lambda_{i\pm\frac{1}{2}}\right)\right)Q_c + \frac{1}{2}\mathscr{L}\left(\lambda_{i\pm\frac{1}{2}}\right)Q_d, \end{aligned} \tag{4.39}$$

in which $\mathscr{L}\left(\lambda_{i\pm\frac{1}{2}}\right)$ is the limiter function. Various limiter functions exist. Some are more suitable for predicting a particular type of flow solution, but all depend on the smoothness gradient. When the Leonard & Mokhtari notation is taken into account for equation (4.39), it is evident to see that when $\mathscr{L}\left(\lambda_{i\pm\frac{1}{2}} = 0\right) = 0$, the high-resolution schemes reduces to the upwind method, and that when $\mathscr{L}\left(\lambda_{i\pm\frac{1}{2}} = 1\right) = 1$, the high-resolution scheme is exactly the same as the Lax-Wendroff scheme (central scheme) [23].

The magnitude of the limiter function and the smoothness gradient form a domain in which the high-resolution schemes are said to be TVD. This domain is formed by the minmod and superbee limiter functions. Besides it is known that all high-resolution schemes must satisfy the points $\mathscr{L}\left(\lambda_{i\pm\frac{1}{2}}\right) = 0$ and 1, which represent the upwind and Lax-Wendroff scheme, respectively. So, the upwind scheme is a TVD-scheme as well. However it is a TVD-method of poor accuracy, and the Lax-Wendroff is only a TVD-scheme for a smooth flow solution.

The requirements for a high-resolution scheme to be TVD are summarised by LaVeque as:

$$0 \leq \frac{\mathscr{L}(\lambda)}{\lambda} \leq 2 \quad \text{and} \quad 0 \leq \mathscr{L}(\lambda) \leq 2. \tag{4.40}$$

Also, LaVeque states that the limiter function should be equal to zero, when the smoothness gradient is less than zero. For $\lambda < 0$, the flow solution is near a local extremum with steep gradients. Here, the limiter functions are assigned the value of zero, and represent the upwind method locally, until the smoothness gradient is greater than zero again, and the limiter function determines its own output. Therefore, a TVD-scheme is never completely second-order accurate in space at a discontinuity, as the upwind method is needed locally to smear to flow solution. Only for a smoothness gradient of one, the flow solution is smooth. Above or below $\lambda = 1$, the flow solution is full of local maxima and minima.

The second-order TVD-domain is plotted in Fig. 4.8. The domain is formed by the intersections of the black lines, which represent the minmod and superbee limiter functions [21].

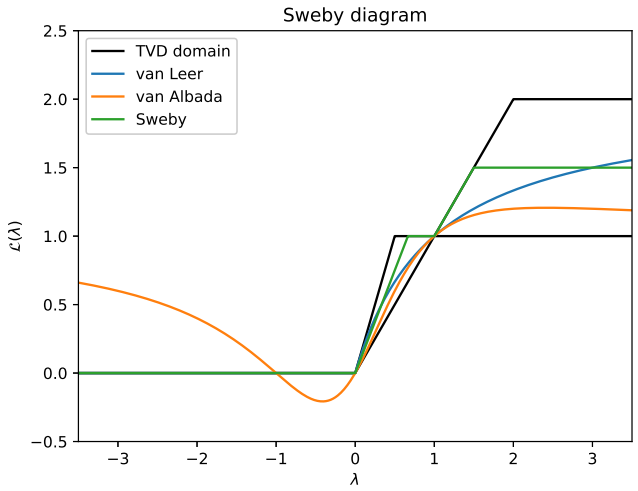

Figure 4.8: Sweby diagram to visualise the TVD domain and the magnitude of the limiter functions versus the smoothness gradient.

The plot is called the Sweby diagram, and it contains three limiter functions of intermediate behaviour: the van Leer, van Albada and Sweby limiter functions. These functions are tested in the numerical model. Their intermediate behaviour is seen for $\lambda > 1$, as the magnitude of these functions is approximately between the values of the minmod and superbee limiter functions. The minmod limiter function is known to be too dispersive near a discontinuity and the superbee method is known to be too steepening near large gradients. Therefore, these two limiters are not used in the numerical model. An overview of the mathematical relation of the (high-resolution) schemes which are used in the numerical model is given in Tab. 4.1.

Table 4.1: The limiter functions used in the numerical model which (locally) satisfy the TVD condition of equation (4.35).

Method	**Slope limiter function**
1st order upwind	$\mathscr{L}(\lambda) = 0$
Lax-Wendroff	$\mathscr{L}(\lambda) = 1$
Van Leer	$\mathscr{L}(\lambda) = (\lambda + \lvert\lambda\rvert)/(1 + \lvert\lambda\rvert)$
Albada	$\mathscr{L}(\lambda) = (\lambda^2 + \lambda)/(\lambda^2 + 1)$
Sweby	$\mathscr{L}(\lambda) = \max\left[0, \min\left(\beta\lambda, 1\right), \min\left(r, \beta\right)\right]$ where $1 \leq \beta \leq 2$

Due to their intermediate flux-limiting character, the van Leer, van Albada and Sweby limiter function show similar performance when tested in the case presented in Section 4.9. However, the Sweby limiter with $\beta = 1.5$ converges faster, while showing less dispersive behaviour. Therefore, the Sweby limiter function is the preferred limiter function used in the numerical model. This is not shown in Section 4.9.

Nonetheless, the van Leer and van Albada limiter function have an important advantage as well. The methods are continuously differentiable, which is required when Newton's method is applied to solve the nonlinear terms of the model at each time step.

4.6. Boundary conditions

As stated in Section 4.1, the ghost cells outside the interior are used to assign boundary conditions to the flow variables. These Boundary Conditions (BC) are crucial for obtaining a correct solution from the numerical model and only have to be assigned to the flow variables which are solved in the iteration procedure. The values of these variables in the ghost cell are also used to determine the smoothness gradient at the border of the interior $i = \frac{1}{2}$ and $i = N + \frac{1}{2}$.

Typically, three types of boundary conditions are seen in the numerical model:

- Neumann BC; the Neumann BC specifies the value of the gradient of the flow variable with respect to the axial distance. This gradient is equal to zero for a solid wall. This type of boundary condition is useful to simulate the Benjamin bubble in a pipe, presented in Section 5.1.
- Dirichlet BC; the Dirichlet BC assigns a constant value to flow variable in the ghost cells. In the numerical model, it is used to prescribe inflow variables of a pipe.
- Specified flux BC; the specified flux BC specifies the advective or diffusive flux normal to the edges of the interior in the ghost cells. A no-flux boundary is also possible, where the advective and diffusive fluxes are in balance.

A boundary condition can be specified at both cell centres and cell edges. Before the results are presented, it is first mentioned which boundary conditions are used to simulate a particular case.

The fully discretised miscible set of equations presented in Section 4.4 is not complete; it misses one equation. The discretised IPCE and multiphase transport equations each consist of N equations, as for all interior cells the hold-ups and volume fractions must be determined. The number of cell edges of the interior is $N+1$, therefore $2(N+1)$ equations must exist to determine all velocity variables. The slip relation consists of $N+1$ equations; however, the incompressible velocity equation exists of N equations. As the incompressible velocity equation starts with the nodes $i = \frac{1}{2}$ and $i = \frac{3}{2}$, one last relation is needed for the node $i = N + \frac{1}{2}$. This relation should be interpreted as a boundary condition at the right border of the interior.

The boundary condition relation at the node $i = N + \frac{1}{2}$ is equal to the total velocity in the axial direction.

$$u_s = \sum_{\beta} \alpha_\beta u_{s,\beta} = \alpha_u u_{s,u} + \alpha_l u_{s,l} \tag{4.41}$$

Evaluating equation (4.41) at the $N + \frac{1}{2}^{\text{th}}$ node, and setting the variables to the new time level $n+1$ yields:

$$\hat{\alpha}^{n+1}_{u_{N+\frac{1}{2}}} u^{n+1}_{s,u_{N+\frac{1}{2}}} + \hat{\alpha}^{n+1}_{l_{N+\frac{1}{2}}} u^{n+1}_{s,l_{N+\frac{1}{2}}} = u_s. \tag{4.42}$$

Implementing the incremental formulation for the velocity variables in equation (4.42) and applying Picard's method with respect to the velocity variables, results in:

$$\hat{\alpha}^{m}_{u_{N+\frac{1}{2}}} \Delta u^{m+1}_{s,u_{N+\frac{1}{2}}} + \hat{\alpha}^{m}_{l_{N+\frac{1}{2}}} \Delta u^{m+1}_{s,l_{N+\frac{1}{2}}} = u_s - \hat{\alpha}^{m}_{u_{N+\frac{1}{2}}} u^{m}_{s,u_{N+\frac{1}{2}}} - \hat{\alpha}^{m}_{l_{N+\frac{1}{2}}} u^{m}_{s,l_{N+\frac{1}{2}}}. \tag{4.43}$$

By adding equation (4.43) to the fully discretised miscible set of equations the numerical model is completed.

Note that the boundary conditions for the velocity variables only have to be given at each iteration of the coupled solver to update the flow variables which have to be determined by the high-resolution scheme.

4.7. Numerical analysis

To analyse whether the FVM is suitable to approximate a real flow problem correctly, one would like to know the accuracy of the numerical method. However, the real flow solution is unknown for the pipeline operations described in Chapter 1. Therefore, the accuracy of the numerical method is often quantified by determining the error between the method and a simpler flow configuration, of which the analytical solution can be calculated. Furthermore, the accuracy of the numerical method can be validated by comparing its results with an experimental dataset [18].

The accuracy of a numerical method can also be determined by a mathematical approach. By means of numerical analysis, the consistency, stability and convergence of a FVM can be verified.

4.7.1. Consistency

For a FVM to be consistent, the Partial Differential Equation (PDE) should be reproduced exactly when the temporal step and the spatial step are going to zero; $\Delta t, \Delta s \rightarrow 0$. This can be determined by the truncation error. The truncation error for a numerical solution is defined as the difference between the truncated value of the approximated numerical model and the actual value of the solution. [21] In other words, it illustrates the magnitude of the local error in the solution for all time steps. The total error due to the numerical approximation of a solution grows over time. In general, the numerical solution depends on the chosen numerical schemes, the temporal and spatial step size, the flow variables and thermodynamic variables.

The local truncation error is relatively easy to investigate. It can be well-approximated by a Taylor series expansion for a smooth flow solution. [18] A truncation error example is worked out in this section. However, the focus lays on formulating the created dissipation error which is caused by the numerical discretisation of the temporal and spatial partial derivatives. This dissipation error is also called numerical diffusion due to its diffusive character on the solution. The goal of this example is to show the conditions which are needed for the physical dispersion coefficient to dominate in the numerical solution (instead of the numerical dispersion term).

The effects of numerical diffusion are shown for the IPCE of equation (2.29) and the multiphase volume fraction equation of equation (2.57). The continuity equation represents an advection equation and does not contain a diffusive term. The volume fraction equation is an advection-diffusion equation and already contains a diffusive term. Here, the physical dispersion in a turbulent domain is represented by the axial dispersion coefficient. Numerical discretisation introduces diffusion for the former, whereas it adds an extra diffusion parameter to the model for the latter. A simplified form of equations (2.29) & (2.57) is wanted for which the numerical diffusion effects are easily shown. This is done by excluding flow variables from the equations, as these variables are irrelevant for showing the numerical diffusion effects. The excluded variable of equation (2.29) is the density and the excluded variables of equation (2.57) is the cross-sectional area. The exchange terms are excluded from the present analysis as well, as these terms do not require discretisation. This results in:

$$\frac{\partial \alpha}{\partial t} + u_s \frac{\partial \alpha}{\partial s} = 0 \tag{4.44}$$

$$\frac{\partial c}{\partial t} + u_s \frac{\partial c}{\partial s} - \mathscr{D}_s \frac{\partial^2 c}{\partial s^2} = 0 \tag{4.45}$$

Note that the axial velocity u_s and the axial dispersion coefficient $\mathscr{D}_s$ are positive and constant in these equations. These variables do not depend on temporal and spatial locations. So, they can be placed outside the advective and diffusive partial derivatives. Furthermore, the density is constant as single-phase flow is assumed here. The cross-sectional area of the pipe is assumed to be constant over time and space. Therefore, they do not contribute to the numerical diffusion.

The equations are discretised by the explicit Euler time method. The advective terms are discretised using the upwind scheme and the diffusive term is discretised by a central approximation method.

$$\frac{\partial \alpha}{\partial t} \approx \frac{\alpha_i^{n+1} - \alpha_i^n}{\Delta t} \tag{4.46}$$

$$u_s \frac{\partial \alpha}{\partial s} \approx u_s \frac{\alpha_i^n - \alpha_{i-1}^n}{\Delta s} \tag{4.47}$$

$$\frac{\partial c}{\partial t} \approx \frac{c_i^{n+1} - c_i^n}{\Delta t} \tag{4.48}$$

$$u_s \frac{\partial c}{\partial s} \approx u_s \frac{c_i^n - c_{i-1}^n}{\Delta s} \tag{4.49}$$

$$\mathscr{D}_s \frac{\partial^2 c}{\partial s^2} \approx \mathscr{D}_s \frac{c_{i+1}^n - 2c_i^n + c_{i-1}^n}{\Delta s^2} \tag{4.50}$$

The exact basic equations of equations (4.44) and (4.45) are numerically approximated by:

$$\frac{\alpha_i^{n+1} - \alpha_i^n}{\Delta t} + u_s \frac{\alpha_i^n - \alpha_{i-1}^n}{\Delta s} = 0, \tag{4.51}$$

$$\frac{c_i^{n+1} - c_i^n}{\Delta t} + u_s \frac{c_i^n - c_{i-1}^n}{\Delta s} - \mathscr{D}_s \frac{c_{i+1}^n - 2c_i^n + c_{i-1}^n}{\Delta s^2} = 0. \tag{4.52}$$

To examine the numerical diffusion of these discretisation methods, Taylor series expansions of α_i^{n+1} around α_i^n and of α_{i-1} around α_i are given for the hold-up variable. For the volume fraction variable, Taylor series expansions of c_i^{n+1} around c_i^n and of $c_{i\pm1}^n$ around c_i^n are derived, which read:

$$\alpha_i^{n+1} = \alpha_i^n + \Delta t \frac{\partial \alpha}{\partial t} + \frac{\Delta t^2}{2} \frac{\partial^2 \alpha}{\partial t^2} + \mathscr{O}\left(\Delta t^3\right), \tag{4.53}$$

$$\alpha_{i-1}^n = \alpha_i^n - \Delta s \frac{\partial \alpha}{\partial s} + \frac{\Delta s^2}{2} \frac{\partial^2 \alpha}{\partial s^2} + \mathscr{O}\left(\Delta s^3\right), \tag{4.54}$$

$$c_i^{n+1} = c_i^n + \Delta t \frac{\partial c}{\partial t} + \frac{\Delta t^2}{2} \frac{\partial^2 c}{\partial t^2} + \mathscr{O}\left(\Delta t^3\right), \tag{4.55}$$

$$c_{i\pm1} = c_i \pm \frac{\partial c}{\partial s} \Delta s + \frac{1}{2} \frac{\partial^2 c}{\partial s^2} \Delta s^2 \pm \frac{1}{6} \frac{\partial^3 c}{\partial s^3} \Delta s^3 + \frac{1}{24} \frac{\partial^4 c}{\partial s^4} \Delta s^4 \pm \frac{1}{120} \frac{\partial^5 c}{\partial s^5} \Delta s^5 + \mathscr{O}\left(\Delta s^6\right), \tag{4.56}$$

where $\mathscr{O}(\Delta t^{(.)})$ and $\mathscr{O}(\Delta s^{(.)})$ describe up to which order the Taylor series of the variables are derived. Substituting the Taylor expansions into the discretised equations, yields:

$$\frac{\partial \alpha}{\partial t} + \frac{\Delta t}{2} \frac{\partial^2 \alpha}{\partial t^2} + \mathscr{O}\left(\Delta t^2\right) + u_s \left(\frac{\partial \alpha}{\partial s} - \frac{\Delta s}{2} \frac{\partial^2 \alpha}{\partial s^2} + \mathscr{O}\left(\Delta s^2\right) \right) = 0; \tag{4.57}$$

$$\frac{\partial c}{\partial t} + \frac{\Delta t}{2} \frac{\partial^2 c}{\partial t^2} + \mathscr{O}\left(\Delta t^2\right) + u_s \left(\frac{\partial c}{\partial s} - \frac{\Delta s}{2} + \mathscr{O}\left(\Delta s^2\right) \right) - \mathscr{D}_s \left(\frac{\partial^2 c}{\partial s^2} + \frac{\Delta s^2}{12} \frac{\partial^4 c}{\partial s^4} + \mathscr{O}\left(\Delta s^4\right) \right) = 0 \tag{4.58}$$

The second derivatives of the hold-up and the volume fraction with respect to time also have an contribution to numerical diffusion. This contribution can be obtained by taking the time derivative of equations (4.44) & (4.45) [14], which read:

$$\frac{\partial^2 \alpha}{\partial t^2} + u_s \frac{\partial}{\partial s} \left(\frac{\partial \alpha}{\partial t} \right) = 0, \tag{4.59}$$

$$\frac{\partial^2 c}{\partial t^2} + u_s \frac{\partial}{\partial s} \left(\frac{\partial c}{\partial t} \right) - \mathscr{D}_s \frac{\partial^2}{\partial s^2} \left(\frac{\partial c}{\partial t} \right) = 0. \tag{4.60}$$

Substituting for $\partial \alpha / \partial t$ and $\partial c / \partial t$ from equations (4.44) & (4.45), results into:

$$\frac{\partial^2 \alpha}{\partial t^2} = u_s^2 \frac{\partial^2 \alpha}{\partial s^2}, \tag{4.61}$$

$$\frac{\partial^2 c}{\partial t^2} = u_s^2 \frac{\partial^2 c}{\partial s^2} - 2u_s \mathscr{D}_s \frac{\partial^3 c}{\partial s^3} + \mathscr{D}_s^2 \frac{\partial^4 c}{\partial s^4}. \tag{4.62}$$

Neglecting the higher order derivatives $\partial^3 c/\partial s^3$ and $\partial^4 c/\partial s^4$ yields:

$$\frac{\partial^2 \alpha}{\partial t^2} \approx u_s^2 \frac{\partial^2 \alpha}{\partial s^2}, \tag{4.63}$$

$$\frac{\partial^2 c}{\partial t^2} \approx u_s^2 \frac{\partial^2 c}{\partial s^2}. \tag{4.64}$$

Implementing these second time derivatives into equations (4.57) & (4.58) and rearranging these equations up to an error of $\mathcal{O}\left(\Delta t^2\right)$ and $\mathcal{O}\left(\Delta s^2\right)$ gives the following result:

$$\frac{\partial \alpha}{\partial t} + u_s \frac{\partial \alpha}{\partial s} - \left(\frac{u_s \Delta s}{2} - \frac{u_s^2 \Delta t}{2}\right) \frac{\partial^2 \alpha}{\partial s^2} = \mathcal{O}\left(\Delta t^2\right) + \mathcal{O}\left(\Delta s^2\right), \tag{4.65}$$

$$\frac{\partial c}{\partial t} + u_s \frac{\partial c}{\partial s} - \left(\mathscr{D}_s + \frac{u_s \Delta s}{2} - \frac{u_s^2 \Delta t}{2} + \frac{\mathscr{D}_s \Delta s^2}{12} \frac{\partial^2}{\partial s^2}\right) \frac{\partial^2 c}{\partial s^2} = \mathcal{O}\left(\Delta t^2\right) + \mathcal{O}\left(\Delta s^2\right). \tag{4.66}$$

Note that inside the brackets all terms share the same units, which are similar to a kinematic viscosity (inertial diffusivity), mass diffusivity or thermal diffusivity term. The discretised term from the partial derivative with respect to time tries to decrease the magnitude of the numerical diffusion, whereas discretised terms originating from the advective and diffusive terms contribute to a new or extra dispersion coefficient.

Both the single-phase continuity equation as the single-phase volume fraction equation produce the same numerical diffusive term out of their discretised advective terms. It is denoted by $\mathscr{D}_{N,\text{adv}}$ and is known as the lowest order error of the advective term.

$$\mathscr{D}_{N,\text{adv}} = \frac{u_s \Delta s}{2} \tag{4.67}$$

The ratio of the advective transport and the diffusive transport is a dimensionless number called the Péclet number, *Pe*. This physical dimensionless number also has its numerical equivalent. The numerical Péclet number is defined in this model as:

$$Pe = \frac{u_s \Delta s}{\mathscr{D}_s}. \tag{4.68}$$

The numerical diffusion caused by discretising the advective term is unimportant in the model, if:

$$\frac{u_s \Delta s}{2\mathscr{D}_s} \ll 1. \tag{4.69}$$

Note that high-resolution schemes are used in the model instead of the upwind scheme. These schemes are second-order accurate in space for smooth solutions, but near discontinuities these schemes make use of the upwind scheme before entering the second-order TVD domain. Overall, the contribution of advective terms to the numerical diffusion magnitude is higher for the upwind scheme compared to the high resolution schemes for the same spatial step size. The condition presented in equation (4.69) is the worst case scenario of numerical diffusion due to the advective term happening in the model.

The numerical diffusive term caused by the diffusive term in the single-phase volume fraction equation is denoted by $\mathscr{D}_{N,\text{dif}}$.

$$\mathscr{D}_{N,\text{dif}} = \frac{\mathscr{D}_s \Delta s^2}{12} \frac{\partial^2 c}{\partial s^2} \tag{4.70}$$

$\mathscr{D}_{N,\text{dif}}$ is known as the lowest order error of the discretised diffusive term. Typically, the contribution to the numerical diffusion of the advective term is much larger than the input of the diffusive term. Therefore, the lowest order term introduced by the discretisation of the diffusive term is irrelevant in the numerical model, which is satisfied if:

$$\begin{aligned} \frac{\mathscr{D}_s \Delta s^2}{12} \frac{\partial^4 c}{\partial s^4} &\ll \frac{u_s \Delta s}{2} \frac{\partial^2 c}{\partial s^2}, \\ \frac{\mathscr{D}_s \Delta s}{6 s_0^2} &\ll u_s, \end{aligned} \tag{4.71}$$

where s_0 is a characteristic length. In the model, this length is equivalent to the hydraulic diameter D_H. The contribution of the diffusive term is unimportant in the model if the following condition is validated:

$$\frac{\mathscr{D}_s \Delta s}{6 D_H^2 u_s} \ll 1. \tag{4.72}$$

The contribution of the time derivatives to the numerical diffusion is denoted by $\mathscr{D}_{N,\mathrm{t}}$.

$$\mathscr{D}_{N,\mathrm{t}} = \frac{u_s^2 \Delta t}{2} \tag{4.73}$$

Generally, this contribution to the numerical diffusion is always less than the contribution of the discretised advective terms, which results in:

$$\begin{aligned} \frac{u_s^2 \Delta t}{2} &< \frac{u_s \Delta s}{2} \\ \frac{u_s \Delta t}{\Delta s} &< 1 \end{aligned} \tag{4.74}$$

The ratio $u_s \Delta t / \Delta s$ is known as the Courant number Co and is elaborated in next Subsection 4.7.2. The first three terms between brackets of equation (4.66) can be rewritten, to obtain:

$$\mathscr{D}_s \left(1 + \frac{u_s \Delta s}{2\mathscr{D}_s} - \frac{u_s^2 \Delta t}{2\mathscr{D}_s} \right) = \mathscr{D}_s \left(1 + \frac{Pe(1 - Co)}{2} \right). \tag{4.75}$$

Therefore, the numerical diffusion for an advection-diffusion equation is a function of both the numerical Péclet and Courant number [14].

4.7.2. Stability

For the numerical method to be affective, the method must be stable in some appropriate sense. This means that small errors made in each time step do not grow too fast in later time steps and corrupt the numerical solution. [18]

To analyse the stability of a FDM, three main approaches can be performed:

- a Fourier analysis, also called a von Neumann stability analysis;
- energy method;
- normal mode analysis, also called Gustafsson-Kreis-Sundström (GKS) analysis.

The energy method and the normal mode analysis are the more general techniques. To perform a Fourier analysis, one is restricted to a linear FDM with constant coefficients for periodic problems [21]. Stability is of key importance in the model and the Courant number is used as a stability condition.

This stability condition is known as the Courant-Friedrichs-Lewy (CFL) condition, and is defined as:

$$\textbf{CFL condition}: \quad |Co| \leq 1. \tag{4.76}$$

The CFL condition needs to be satisfied for a TVD method to remain stable. [18]. After the spatial step size is set, it is used to determine the temporal step size. Note that the ratio between the temporal and spatial step sizes is coupled in the Courant number; $\Delta t / \Delta s$ = constant. When the spatial step size is altered, the temporal step size automatically adapts as well for a specific case. In the fluid-fluid displacement model, the Courant number is defined as:

$$Co = \frac{u_g \Delta t}{\Delta s}, \tag{4.77}$$

where $u_g = \sqrt{g D_H}$ is the gravitational velocity; i.e. the largest (bubble) velocity that could be observed in the flow domain.

The total variation also provides a stability definition for TVD methods for nonlinear problems. High-resolution schemes are always nonlinear, as the limiter function depends on the smoothness gradient. The definition states: *a numerical method is total variation bounded (TVB), if for any data* q^0 *(with* $TV(q^0) < \infty$ *and time* t*, there is a constant* $R > 0$ *and an initial value* $\Delta t_0 > 0$*, such that* $TV(q^0) \leq R$ *for all* $n\Delta t$ *whenever* $\Delta t < \Delta t_0$. When $R = TV(q^0)$ for any t, a TVD method is certainly TVB, as long as the CFL condition is satisfied. When no spurious oscillations arise in the flow solution, the stability of a TVD method is guaranteed [18].

4.7.3. Convergence

An FDM is called convergent, if the FDM solution converges to the exact solution when the temporal and spatial step size are going to zero, $\Delta t, \Delta s \rightarrow 0$ and for $s_i \rightarrow s$ and $t^n \rightarrow t$. It is hard to prove convergence, nonetheless the *Lax equivalence theorem* offers a solution: *A consistent FDM for a well-posed linear initial value problem is convergent, if and only if it is stable.* [21]

So, the key for a convergent numerical method is to guarantee that the method is both consistent and stable. It is assumed that the current numerical method satisfies both requirements, provided that the CFL condition is met for stability. The term well-posedness indicates that the eigenvalues of the systems' Jacobian matrix must be real and distinct. In other words, a solution to the problem must exist that is unique and changes when the initial conditions are altered. To determine the well-posedness of the miscible set of equations is not within the scope of this research. Therefore, it is assumed that the miscible set of equations of equation (3.68) is well-posed [18][26].

4.8. Coupled solver

To solve the fully discretised miscible set of equations, two main approaches exist: a coupled and a segregated solver. The segregated approach solves all equations sequentially in segregated matrices, whereas the coupled approach bundles all equations in one matrix and solves those simultaneously. For this numerical model, the segregated solver would include 3 matrices of size NxN to solve for the hold-ups and volume fraction and 2 matrices of size $(N+1)$x$(N+1)$ to solve for the velocity variables. Matrix **A** of the coupled solver has the size $(2(N+1)+3N)$x$(2(N+1)+3N)$, when Picard's method is applied. The size of matrix **A** can become very large when the number of cells is increased. Typically, this results in a longer computational time for the coupled solver than for the segregated solver for the same flow configuration, as the coupled approach is more heavy to solve computationally. A coupled approach is also known as a monolithic approach.

Typically, a segregated approach is suitable to model processes of slow transients and phenomena in long pipelines (as it is less computationally heavy than a coupled approach). However, the transient solution of a pipeline is expected to change rapidly, as the interaction among the miscible fluid is strong and undulations are seen in the terrain. It is preferable to solve such problems in an approach in which the equations are more tightly coupled. [23] Furthermore, research has been done in simulating a similar case by both the segregated and coupled approach in this study. For a classic Benjamin bubble case, the coupled approach is able to obtain an equilibrium position in which the light fluid is on top of the heavy fluid for a sufficient time t. The segregated approach failed to realize an equilibrium position, as an instability got into the solution at the left boundary, despite applying the same wall boundary conditions as for the coupled approach. Details on this comparison are not given in this report. As the coupled approach has proven to be more robust, it is the chosen approach in the present study.

The fully discretised miscible set of equations is given in an incremental-iterative formulation. This indicates that incremental variables are only found on the left hand side of each equation. The right hand side of the equations contain the variables, which were determined in the previous time or iteration step. The right hand side of the equation is also known as the residual side.

The numerical model can be represented by the diagonal linear system; $\mathbf{A}\Delta = \mathbf{r}$. **A** multiplied by Δ results on the left hand side of the discretised miscible equations and **r** is a vector containing all $(2(N+1)+3N)$ equations of the model. The solver **A** contains all incremental variables to determine the solution at the new iteration level. **A** is a diagonal matrix which is made sparse at each iteration step m. The matrix has to be non-singular, which means that the inverse of matrix **A** exists and that its determinant is nonzero. In a sparse matrix only the nodes which have a value are saved. This requires less storage. In Fig. 4.9, an example of a diagonal sparse matrix **A** is given for the Benjamin bubble case with a number of cells of $N = 50$ (if the number of cells is increased, Fig. 4.9 would become unreadable). The blue squares in the matrix represent the active increments in the solver. It is observed that in the middle of the matrix more squares are present after a number of time steps of $nt = 100$, as the fluids are both active in the domain here.

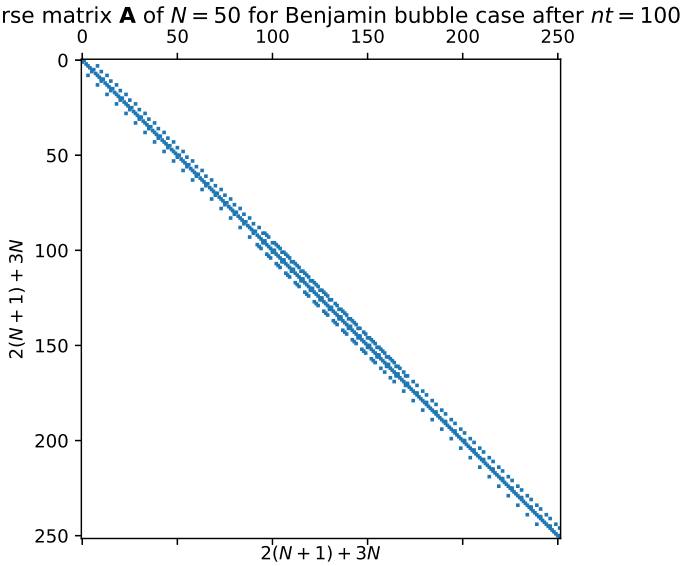

Figure 4.9: The sparse matrix **A** is visualised for a Benjamin bubble case. The sparse matrix is presented after the number time step $N_t = 100$ and the number of cells is equal to $N = 50$.

The solver matrix **A**, the increment vector Δ, and the residual vector **r** are defined as:

$$\mathbf{A} = \begin{bmatrix} \cdot & & & & & & \\ & \ddots & & & & & \\ & & \ddots & & & & \\ & & & \ddots & & & \\ & & & & \ddots & & \\ & & & & & \cdot \end{bmatrix}; \quad \Delta = \begin{bmatrix} \Delta u_{s,u_{\frac{1}{2}}} \\ \Delta u_{s,l_{\frac{1}{2}}} \\ \Delta \alpha_{u_1} \\ \Delta c_{Lu_1} \\ \Delta c_{Hl_1} \\ \vdots \end{bmatrix}; \quad \mathbf{r} = \begin{bmatrix} r_{u,slip_{\frac{1}{2}}} \\ r_{u,imcom_{\frac{1}{2}}} \\ r_{\alpha_1} \\ r_{cLu_1} \\ r_{cHl_1} \\ \vdots \end{bmatrix}, \tag{4.78}$$

where the increments and residuals are given for the first cell only. The notation to indicate the iteration and time level dependencies is omitted here. To indicate the difference between the two velocity equations, the slip relation is denoted by $r_{u,\text{slip}}$ and the incompressible velocity equation is denoted by $r_{u,\text{incom}}$. Note that the velocity variables start at the node $i = \frac{1}{2}$ and the variables defined in the cell centre start at $i = 1$.

To determine the flow solution at the new iteration step $m+1$, the diagonal linear system is solved by:

$$\Delta = \mathbf{A}^{-1}\mathbf{r}. \tag{4.79}$$

When the iteration procedure of equation (4.79) has finished at iteration level m, the new flow solution at iteration level $m+1$ is determined. The flow solution at $m+1$ is defined as the flow solution at m plus the incremental values at $m+1$ multiplied by a relaxation factor ζ. A relaxation factor helps to increase the convergence rate of the iteration procedure. The relaxation factor is said to be over-relaxed when its value is above one, and to be under-relaxed when its value is below one. The relaxation factors introduced by Bouwhuis are used in the numerical model. The relaxation factor for the velocity and hold-up variables is equal to $\zeta_1 = 0.8$ and the relaxation factor for the volume fraction variables is equal to $\zeta_2 = 0.7$ [7].

The right hand side of the fully discretised miscible equations describes the residual terms. During each iteration step, the maxima of the residual values of the velocity, hold-up and volume fraction equations are separately measured and checked. The magnitude of these maximum values of the residuals is supposed to become smaller and smaller when more iterations have been made. This implies that the flow variables move towards a iteration step where their solution does not change anymore. When this has happened, convergence has been reached for the flow variables and the iteration procedure is stopped. The flow variables at the last iteration step $m+1$ are set equal to the new time step $n+1$.

The system has reached convergence within a time step, when the residuals of the velocity, the hold-up and the volume fraction variables have all become smaller than the desired tolerance level during the iteration procedure. This tolerance level should be interpreted as another threshold value and is denoted by ε_4. The desired tolerance level is set at ε_4 = 1e-10. When the maximum of the values of the residuals do not meet the desired tolerance as the iteration procedure has reached the maximum iteration step $m_{\max}$, the coupled solver is stopped; no converge is found for this particular time step.

A schematic overview of the coupled solver used in the numerical model is given in Fig. 4.10. The coupled solver itself is displayed inside a dotted square.

4.8.1. Remarks on coupled solver

The employed coupled approach in the numerical model is in fact more a semi-coupled approach, as Picard's method is applied to linearise the nonlinear terms. Furthermore, the density, axial dispersion coefficient, transfer term and the effective bubble velocity function variables are all determined inside the time loop instead of the iteration loop and are constant throughout the iteration procedure. All these variables directly (or indirectly) depend on the threshold value ε_3. This threshold value regulates whether a region has arrived in a particular cell or not, when it has arrived the cell is activated, and the density and other variables are calculated for this cell; $\alpha_u > \varepsilon_3$ or $\alpha_l > \varepsilon_3$. The threshold value is set at ε_3 = 1e-03. If the magnitude of a hold-up variable is in subsequent iteration steps above and below ε_3, a flipflopping process is observed activating and deactivating variables for a particular cell. When this flipflopping process is continued, no convergence is found for the current time step, as the residuals of the equations are not able to reduce their values below the desired tolerance.

In addition, to determine the smoothness gradient of the hold-ups and volume fraction variables, the velocity variables of the previous time step are used, as again a flipflopping process would cause an issue. At certain locations the velocity variables can flipflop between a positive value for the current iteration step and a negative value for the next iteration step (and so on). When the velocity variables which are determined in the iteration step are used to calculate the new smoothness gradients, the gradient changes sign per iteration step. This could lead to no convergence for the current time step and may lead to oscillations in the flow solution.

In the incremental vector Δ, all velocity variables are defined at the cell edges. The hold-up and the volume fraction variables are defined at the cell centres. However, the advective terms of equations (4.13), (4.26) & (4.28) still contain the incremental variables at the nodes $i-\frac{1}{2}$ and $i+\frac{1}{2}$. These advective terms have to be rewritten using equation (4.39) to a form in which the variables only contain dependencies at the cell centres nodes. This is elaborated in Appendix A

When Newton's method is applied, a segregated approach would not even be possible. Newton's method requires the set of equations to be fully coupled and therefore needs to be solved by the coupled solver. As the linearisation process of Newton's method could involve all miscible variables which are actively used in the numerical model, the hold-up of the lower region variable needs to be added to the solver matrix. Matrix **A** grows in size by NxN cells. The volume fraction of the light fluid particles in the lower region and of the heavy fluid particles in the upper region are not required in the solver matrix, as no variable or function in the miscible model depends on these concentration variables. As a start for future research to optimise the current numerical model, an attempt to apply Newton's method is made for an immiscible model. This is elaborated in Appendix B.

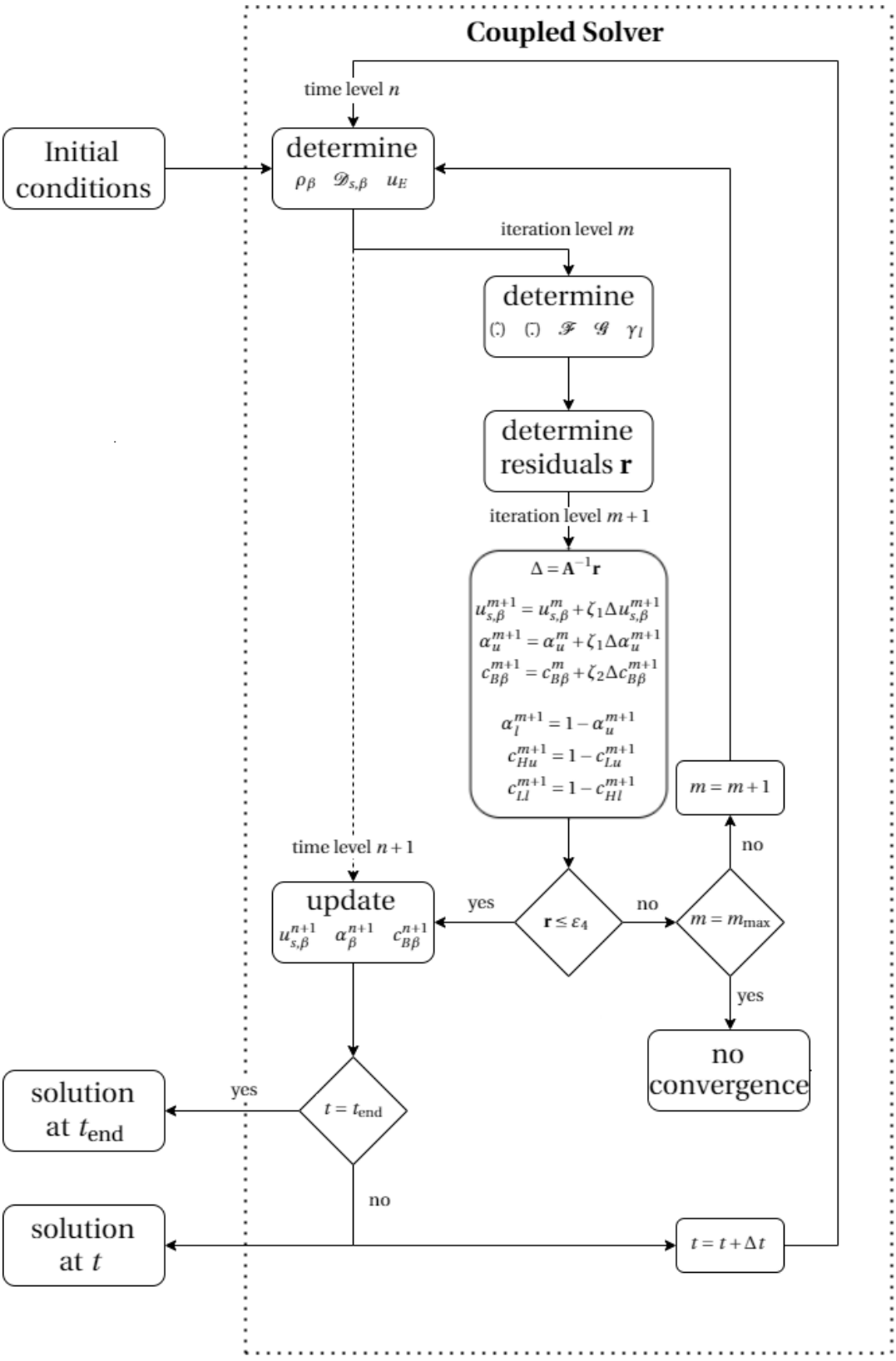

Figure 4.10: A schematic overview of the coupled solver is presented to visualise the steps taken inside the solver.

4.9. Model validation

To prove the capabilities of a numerical model, the flow solution of the model can be compared with a simple case for which an analytical solution exists, as described in Section 4.7. The analytical solution of a turbulent diffusion equation is considered, and the model is validated for the single-phase transport equation of equation (2.39). Together with the validation, grid sensitivity experiments in time and space are performed to investigate the impact of the numerical diffusion on the flow solution. The validation is performed on the geometry used by Hart to find his empirical relation of equation (3.58). [12] At the end of this section, Hart's experiments are simulated to compare the numerical model with experimental data.

4.9.1. Analytical solution

The single-phase transport equation of (2.39) is reduced following the same steps as described in Section 4.7.1. However, no analytical solution exists of the remaining advection-diffusion equation. Nonetheless, the equation can be approximated by a turbulent diffusion equation for which an analytical solution exists. The diffusion equation is simply translated in space by the constant axial velocity u_s to compare its solution to the solution of the single-phase transport equation.

$$\frac{\partial c}{\partial t} + u_s \frac{\partial c}{\partial s} = \mathscr{D}_s \frac{\partial^2 c}{\partial s^2} \longleftrightarrow \frac{\partial \bar{c}}{\partial t} = \mathscr{D}_s \frac{\partial^2 \bar{c}}{\partial s^2} \tag{4.80}$$

Here, $\bar{c}$ indicates the translated solution of the diffusion equation; i.e. $c(s,t) \approx \bar{c}(s-ut,t)$. The solution of both equations can be compared only if they share the same initial solution; i.e. $c(s,t_0) = \bar{c}(s,t_0)$. The initial solution for which an analytical solution exists for the turbulent diffusion equation is a step function defined as:

$$\bar{c}(s,t_0) = \begin{cases} 1, & \text{for } -\dfrac{\Phi}{2} < s < \dfrac{\Phi}{2}, \\ 0, & \text{Otherwise,} \end{cases} \tag{4.81}$$

where $\pm\frac{\Phi}{2}$ indicates that the step function is evenly distributed around the point $s_0 = s = 0\ [m]$. The analytical solution for an unbounded initial condition of $\bar{c}$ is created by the superposition of two Gaussian impulse response functions defined in equation (3.59).

$$\bar{c}(s,t) = \frac{1}{2}\left[erf\left(\frac{s+\frac{\Phi}{2}}{\sqrt{4\mathscr{D}_s t}} \right) - erf\left(\frac{s-\frac{\Phi}{2}}{\sqrt{4\mathscr{D}_s t}} \right) \right] \tag{4.82}$$

The peak value of the diffusion equation will always be located at s_0, as the equation does not contain an advective term. The peak value of the diffusion equation is determined by:

$$\bar{c}(s_0,t) = \frac{1}{2}\left[erf\left(\frac{\frac{\Phi}{2}}{\sqrt{4\mathscr{D}_s t}} \right) - erf\left(\frac{-\frac{\Phi}{2}}{\sqrt{4\mathscr{D}_s t}} \right) \right], \tag{4.83}$$

where $\sqrt{4\mathscr{D}_s t}$ is the estimated diffusion length after diffusion time t.

4.9.2. Grid sensitivity in time and space

An analytical solution of the single-phase transport equation is desired, because the empirical relation of Hart is added to include a turbulent axial dispersion coefficient in the model. Hart's experiments include three cases that fall under the turbulent domain: $Re = 5990$, 20500 and 50890. These cases will be used to validate the single-phase transport equation in the model by the analytical solution of the (turbulent) diffusion equation of equation (4.83). Hart's geometry is illustrated in Fig. 4.11.

Recall that Hart injects a dye into a flow solution during one second to measure the axial dispersion coefficient at various Reynolds numbers. Hart's geometry is 16.56 metres long and consist of six volume fraction measurement points of the dye. The dye is injected after 3.5 metres. The distance upstream of the injection point is used by Hart to fully develop the flow inside the pipe in which the pipe radius is $R = 0.012\ [m]$. The flow variables for the considered turbulent experimental cases of Hart are summarised in Tab. 4.2. The flow variables are constant for the different experiments. Therefore, it is possible to solve the single-phase transport equation in a solver which only solves the volume fraction of the dye in its diagonal matrix **A**. As a result, the grid could be further refined and the computational time is decreased drastically.

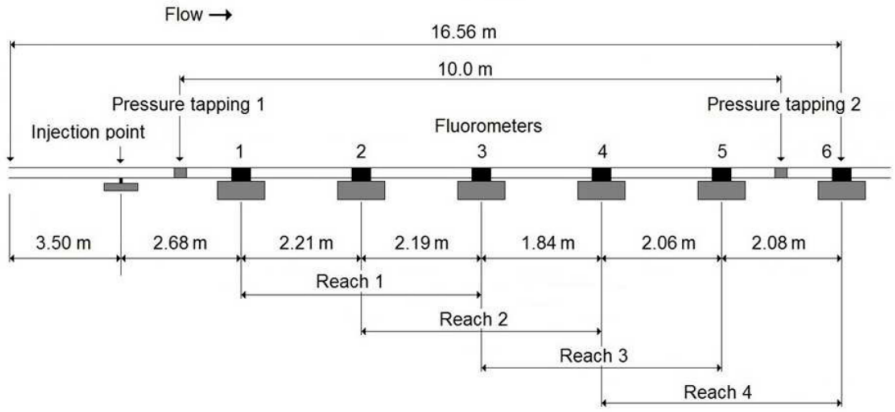

Figure 4.11: The geometry used by Hart in his experiments. [12]

Table 4.2: An overview of the flow variables of Hart's three turbulent experiments is given. The overview includes the Reynolds number, the (virtual) axial dispersion coefficients and the approximated time to reach the first measurement point.

Reynolds number	**Axial velocity**	**Virtual axial diffusion coefficient**	**Axial diffusion coefficient**	**Time to reach first measurment point**
$Re = 5990$	$u_s = 0.250161\ [m/s]$	$\bar{K} = 0.831326\ [-]$	$\mathscr{D}_s = 0.0049912\ \left[m^2/s\right]$	$t \approx 10.71\ [s]$
$Re = 20500$	$u_s = 0.856143\ [m/s]$	$\bar{K} = 0.429445\ [-]$	$\mathscr{D}_s = 0.008824\ \left[m^2/s\right]$	$t \approx 3.130\ [s]$
$Re = 50890$	$u_s = 2.125324\ [m/s]$	$\bar{K} = 0.412003\ [-]$	$\mathscr{D}_s = 0.02102\ \left[m^2/s\right]$	$t \approx 1.261\ [s]$

As all dye is injected during one second, the width of the three initial step functions of the experimental cases simply equals its superficial velocity given in Tab. 4.2. In Fig. 4.12 the initial step functions of the turbulent cases are illustrated around the point s_0.

The numerical validation of the single-phase transport equation is only considered up to the first measurement point of Hart, as for this point the error of the numerical method is already shown. A similar error is still present in the subsequent measurement points. It is even enlarged as the flow is advected further down the pipe. Besides, the evaluation of the the validation up to other measurement points would even increase the simulation time.

To underline the importance of a second-order accurate numerical method with respect to the numerical diffusion present in the flow solution, the validation is shown for three different combinations of numerical discretisation methods:

- implicit Euler to discretise the equation in time and upwind scheme for the advective terms,
- implicit Euler to discretise the equation in time and high-resolution scheme for the advective terms,
- Crank-Nicolson to discretise the equation in time and high-resolution scheme for the advective terms.

Note that the diffusive terms are always discretised using a central approximation method.

The 3.5 metres long pipe section upstream of the injection point are omitted from the interior for the validation. This distance is not necessary in the numerical model for the flow to become fully-developed, as the model itself is one-dimensional and piston-like flow is assumed in the model. As the exact width of initial step functions cannot be modelled, four different grids are considered to approximate this width: $\Delta s = 0.01, 0.005, 0.0025$ and $0.00125\ [m]$. These spatial step sizes all result in the same initial step block for most cases and therefore can be compared with each other. Note that a spatial step size of $\Delta s = 0.02\ [m]$ or larger would definitely result in another width for the step functions.

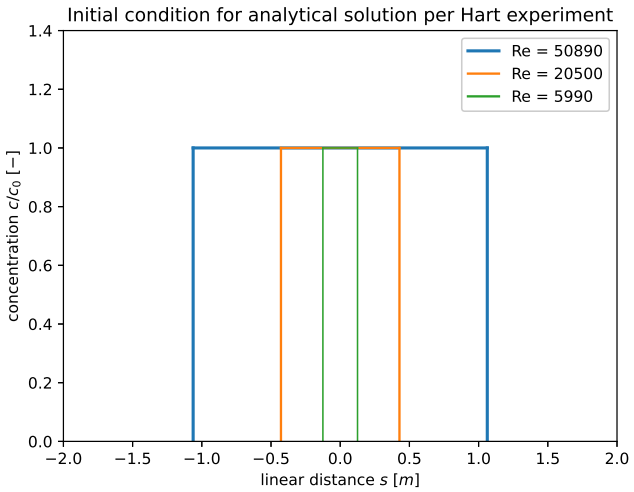

Figure 4.12: The initial step functions of analytical simulations are visualised around the point s_0

In Fig. 4.11 it is shown that the first measurement point is located 2.68 metres away from the injection point. However, the interior of geometry is 3 metres long for the validation case in the numerical model, as the flux boundary condition is applied at the end at the node $N+\frac{1}{2}$ for the volume fraction of the dye. A flux boundary condition is required for the numerical model to find quick convergence when the dye is flowing through the outlet. However it is known to give a wrong flow solution near the boundary. To solve this, the rule of thumb is to add around 10 times the hydraulic diameter as an extra length to the pipe's geometry. As the pipe radius is 0.012 $[m]$, a new interior length of 3 $[m]$ should definitely be sufficient to obtain a correct physical flow solution at the first measurement point. The flux boundary condition at $N+\frac{1}{2}$ is estimated by the axial dispersion coefficient and the axial velocity.

The interior is extended again to include the initial step functions of the three turbulent experimental cases, as the step functions are considered to be evenly distributed around s_0. For $Re = 5990$, this length is only 0.125 $[m]$. However this length is already more than 1 $[m]$ for $Re = 50,890$.

As the superficial velocity is the highest velocity observed in the validation cases, the Courant number is defined as:

$$Co = \frac{u_s \Delta t}{\Delta s}. \tag{4.84}$$

The Courant number is set at 1 to compare the different types of numerical schemes with each other; i.e. grid sensitivity experiment cases in space. When the numerical model is analysed for its grid sensitivity in time, the Courant number is varied from $Co = 1, 0.5, 0.25$ and 0.125 for a spatial grid size $\Delta s = 0.01$ $[m]$. The grid sensitivity in time is investigated with the Crank-Nicolson method and the Sweby limiter function only.

Validation of $Re = 5,990$ case In Tab. 4.3, the peak values at the first measurement point are illustrated to compare the results of the grid sensitivity simulations in time and space with the analytical solution for $Re = 5,990$. The widths of the initial step functions are all equal to $\Phi = 0.25$ $[m]$, therefore the simulations share the same analytical solution, making a comparison of the results very valuable. The relative error is within 10% of the analytical solution for all simulations discretised by the Crank-Nicolson (CN) method in time, whereas the simulations discretised by the implicit Euler method show larger deviations from the analytical solution.

This is also shown in Fig. 4.13a, where the relative error at the coarsest grid of the CN method is approximately as low as the relative errors at the finest grid for the Euler methods. However, the slope at which the relative error is reduced is larger for the Euler methods than for the CN method. In Fig. 4.13b it is visualised that time step independence is almost reached for the coarsest grid, as the plot clearly shows that the the peak value moves towards a time independent result.

Nonetheless, a better accuracy was expected for the numerical simulations for $Re = 5,990$. The reason of the error might be that the numerical diffusion is hindering the model to converge towards the analytical solution. In Fig. 4.14 the profiles of the peak values are plotted for the grid sensitivity simulations in time and space for the CN method. Its results seem to stagnate and to converge towards a value that is different from the analytical solution, while mesh size and time step independence seem to have been reached. As the Reynolds number is low, the axial dispersion coefficient is low as well. The dispersion coefficient is not able to overcome the remaining numerical diffusion in the system for this Reynolds number. It is suspected that the higher Reynolds numbers, the better the model handles numerical diffusion.

Validation of $Re = 20,500$ case In Tab. 4.4, the peak values at the first measurement point are illustrated to compare the results of the grid sensitivity simulations in time and space with the analytical solution for $Re = 20,500$. The widths of the initial step functions are all equal to $\Phi = 0.855$ $[m]$, except for the width for the coarsest grid: $\Phi = 0.86$ $[m]$. Therefore, only the relative error results of the three finest grids can be compared with each other, as they share the same analytical solution. As a consequence, the results of the relative error of the coarsest grid are left out of the relative error plot of Fig. 4.15a. The value of the analytical solution of the coarsest grid is somewhat larger than the analytical solution of the other grids, as shown in Tab. 4.4.

The relative errors are within 10% of the analytical solution for all simulations except of the experiment of the Euler-upwind method on the coarsest grid. The results of the relative error of the CN-Sweby method show even better results and are within 0.4% of the analytical solution for the grid sensitivity simulations in space. The CN-Sweby method also performs very well for the grid sensitivity simulations in time, as for the coarsest grid time step independence is almost reached. This is illustrated in Fig. 4.15b.

Despite the good results for the CN-Sweby method, numerical diffusion is still noticed in the system. Again, the profiles of the peak values illustrated for the grid sensitivity tests in time and space in Fig. 4.16 show that the results seem to converge towards a value distinct from the analytical solution. Nonetheless, this value is very close to the value of the analytical solution.

Validation of $Re = 50,890$ case In Tab. 4.5, the peak values at the first measurement point are illustrated to compare the results of the grid sensitivity simulations in time and space with the analytical solution for $Re = 50,890$. The widths of the initial step functions are equal to $\Phi = 2.125$ $[m]$, except the width for the coarsest grid: $\Phi = 2.13$ $[m]$. Therefore the results of the relative error of the three finest grids can be compared with each other, as they share the same analytical solution. The results of the relative error of the coarsest grid are left out of the relative error plot of Fig. 4.15a. The value of the analytical solution of the coarsest grid is somewhat larger than the analytical solution of the other grids, as shown in Tab. 4.5.

The simulations performed by the Euler methods are in very good agreement with the analytical solution. For the simulations performed on the two coarsest grids by the CN method something unlogical occurs. The relative error of spatial step size $\Delta s = 0.005$ $[m]$ is less than the relative error of the two finest grids and therefore is not included in Fig. 4.15a. The relative error of the experiment of coarsest grid is even negative. This indicates that a larger value is obtained at the peak value in the experiment compared to the analytical solution which is unphysical. The grid sensitivity in the time simulations also shows this unphysical behaviour of the numerical model for the coarsest spatial step size. The behaviour of the two coarsest grids is visualised is Fig. 4.18. As the relative errors of the grid sensitivity simulations in time are all negative compared to the analytical solution, this relative error plot cannot be given.

Apparently, numerical diffusion is no longer in the system, as even the results of the relative error of the Euler methods are in such a close agreement with the analytical solution. However, the fact that the peak value of a simulation with the CN method is larger than the analytical solution is alarming, as this unphysical result should never occur. Furtermore, the results of the grid sensitivity tests in time do not converge towards a specific value, tabulated in Tab. 4.5. A possible explanation for this phenomenon might be that contribution to the numerical diffusion of the time derivatives dominates for the two coarsest grid steps. This results in a value for the (numerical) axial dispersion coefficient that is below the calculated axial dispersion coefficient tabulated for $Re = 50,890$ in Tab. 4.2.

Table 4.3: The peak values at the first measurement point are given and compared to the analytical solution for $Re = 5,990$.

Grid sensitivity in space	**'Analytical' solution**	$\Delta s = 0.00125$ $[m]$ $\Delta t = 0.004997$ $[s]$	$\Delta s = 0.0025$ $[m]$ $\Delta t = 0.00994$ $[s]$	$\Delta s = 0.005$ $[m]$ $\Delta t = 0.01999$ $[s]$	$\Delta s = 0.01$ $[m]$ $\Delta t = 0.03997$ $[s]$
Euler - upwind	0.297625	0.267528	0.258823	0.243238	0.217787
Relative	-	0.030197	0.038802	0.054387	0.079838
Relative %	-	10.15%	13.04%	18.27%	26.83%
Euler - Sweby	0.297625	0.272032	0.267284	0.258266	0.241966
Relative	-	0.025593	0.030341	0.039359	0.055659
Relative %	-	8.599%	10.19%	13.22%	18.70%
CN - Sweby	0.297625	0.276099	0.275143	0.273047	0.268777
Relative	-	0.021526	0.022482	0.024578	0.028848
Relative %	-	7.233%	7.554%	8.258%	9.692%
Grid sensitivity in time	**'Analytical' solution**	$Co = 0.125$ $\Delta t = 0.00146$ $[s]$	$Co = 0.25$ $\Delta t = 0.00292$ $[s]$	$Co = 0.5$ $\Delta t = 0.00584$ $[s]$	$Co = 1$ $\Delta t = 0.01168$ $[s]$
CN - Sweby	0.297625	0.270007	0.269983	0.269832	0.268777
Relative	-	0.027618	0.027642	0.027793	0.028848
Relative %	-	9.279%	9.286%	9.338%	9.692%

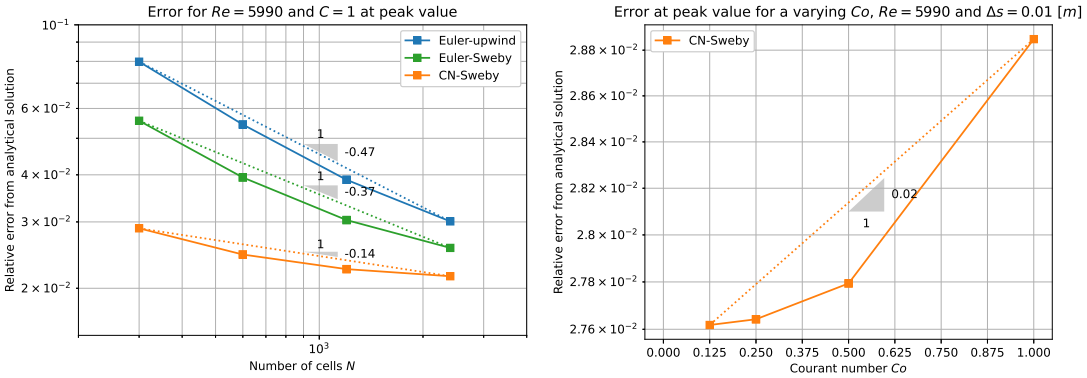

(a) Relative error results for grid refinement in space

(b) Relative error results for grid refinement in time

Figure 4.13: The relative error with respect to the analytical solution is visualised for the grid sensitivity in (a) space and (b) time for $Re = 5,990$.

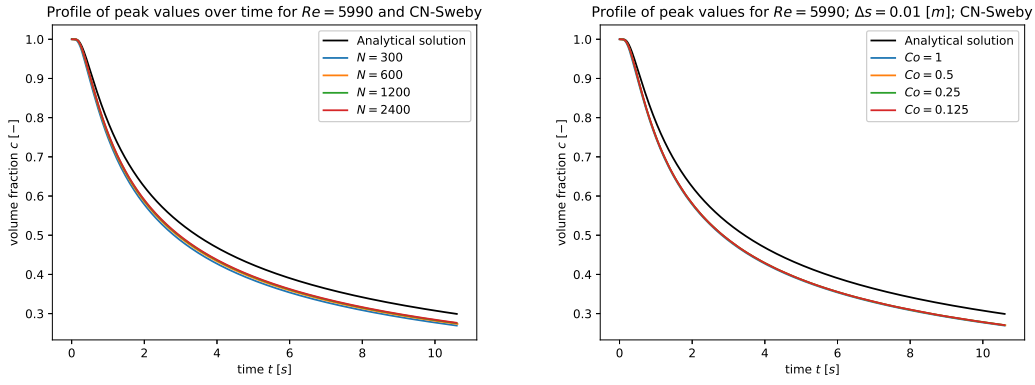

(a) Profile of peak values for grid refinement in space

(b) Profile of peak values for grid refinement in time

Figure 4.14: The profiles of the peak values over time of the advective volume are visualised for the grid sensitivity in (a) space and (b) time for $Re = 5,990$.

Table 4.4: The peak values at the first measurement point are given and compared to the analytical solution for $Re = 20{,}500$.

Grid sensitivity in space	**'Analytical' solution**	$\Delta s = 0.00125$ $[m]$ $\Delta t = 0.00146$ $[s]$	$\Delta s = 0.0025$ $[m]$ $\Delta t = 0.00292$ $[s]$	$\Delta s = 0.005$ $[m]$ $\Delta t = 0.00584$ $[s]$	$\Delta s = 0.01$ $[m]$ $\Delta t = 0.01168$ $[s]$
Euler - upwind	0.931486	0.911315	0.893205	0.858561	0.797778
Relative	-	0.020171	0.038281	0.072925	0.133708
Relative %	-	2.165%	4.110%	7.829%	14.35%
Euler - Sweby	0.931486	0.920147	0.910934	0.893314	0.861113
Relative	-	0.011339	0.020552	0.038172	0.070373
Relative %	-	1.212%	2.206%	4.098%	7.555%
CN - Sweby	0.931486	0.928722	0.928156	0.927834	0.929523
Relative	-	0.002764	0.00333	0.003652	0.001963
Relative %	-	0.2967%	0.3575%	0.3921%	0.2107%
Grid sensitivity in time	**'Analytical' solution**	$Co = 0.125$ $\Delta t = 0.00146$ $[s]$	$Co = 0.25$ $\Delta t = 0.00292$ $[s]$	$Co = 0.5$ $\Delta t = 0.00584$ $[s]$	$Co = 1$ $\Delta t = 0.01168$ $[s]$
CN - Sweby	0.933285	0.929926	0.929922	0.929879	0.929523
Relative	-	0.003359	0.003363	0.003406	0.003762
Relative %	-	0.3599%	0.3603%	0.3649%	0.4031%

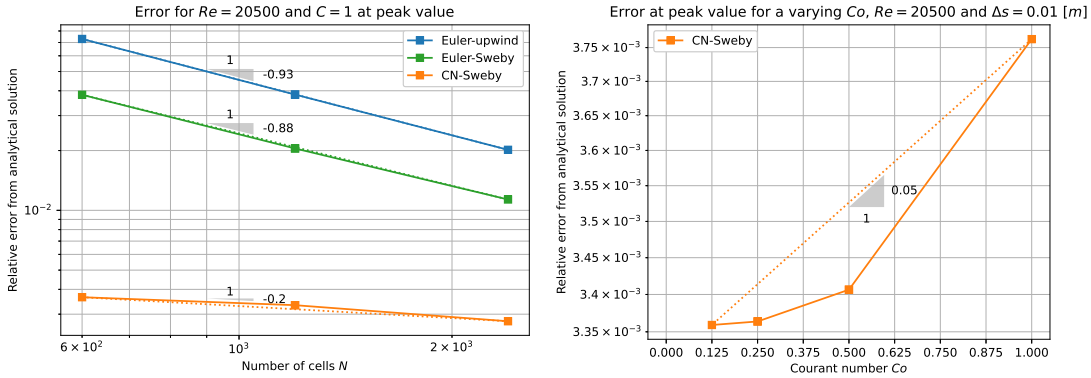

(a) Relative error results for grid refinement in space

(b) Relative error results for grid refinement in time

Figure 4.15: The relative error with respect to the analytical solution is visualised for the grid sensitivity in (a) space and (b) time for $Re = 20{,}500$.

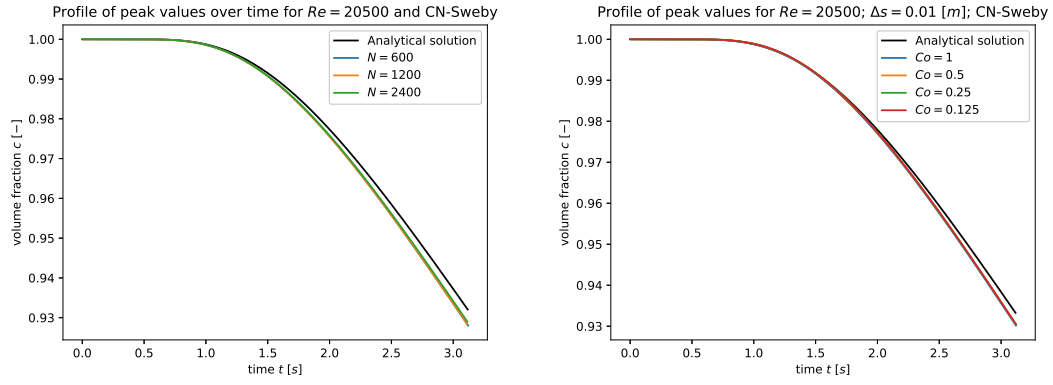

(a) Profile of peak values for grid refinement in space

(b) Profile of peak values for grid refinement in time

Figure 4.16: The profiles of the peak values over time of the advective volume are visualised for the grid sensitivity in (a) space and (b) time for $Re = 20{,}500$.

Table 4.5: The peak values at the first measurement point are given and compared to the analytical solution for $Re = 50,890$.

Grid sensitivity in space	**'Analytical' solution**	$\Delta s = 0.00125$ $[m]$ $\Delta t = 0.004997$ $[s]$	$\Delta s = 0.0025$ $[m]$ $\Delta t = 0.00994$ $[s]$	$\Delta s = 0.005$ $[m]$ $\Delta t = 0.01999$ $[s]$	$\Delta s = 0.01$ $[m]$ $\Delta t = 0.03997$ $[m]$
Euler - upwind	0.99999607	0.999985	0.999961	0.999828	0.998812
Relative	-	1.107e-05	3.507e-05	1.6807e-04	0.001184
Relative %	-	1.107e-03%	3.507e-03%	0.016807%	0.1184%
Euler - Sweby	0.99999607	0.9999918	0.9999857	0.999965	0.999860
Relative	-	4.27e-06	1.037e-05	3.107e-05	1.3607e-04
Relative %	-	4.27e-04%	1.037e-03%	3.107e-03%	0.013607%
CN - Sweby	0.99999607	0.9999955	0.99999529	0.9999958	0.9999968
Relative	-	5.7e-07	7.8e-07	2.7e-07	-7.1e-07
Relative %	-	5.7e-05%	7.8e-05%	2.7e-05%	-7.1e-05%
Grid sensitivity in time	**'Analytical' solution**	$Co = 0.125$ $\Delta t = 0.00146$ $[s]$	$Co = 0.25$ $\Delta t = 0.00292$ $[s]$	$Co = 0.5$ $\Delta t = 0.00584$ $[s]$	$Co = 1$ $\Delta t = 0.01168$ $[s]$
CN - Sweby	0.99999627	0.9999972	0.9999969	0.9999972	0.9999968
Relative	-	-1.13e-06	-8.3e-07	-1.13e-06	-7.1e-07
Relative %	-	-1.13e-04%	-8.3e-05%	-1.13e-04%	-7.1e-05%

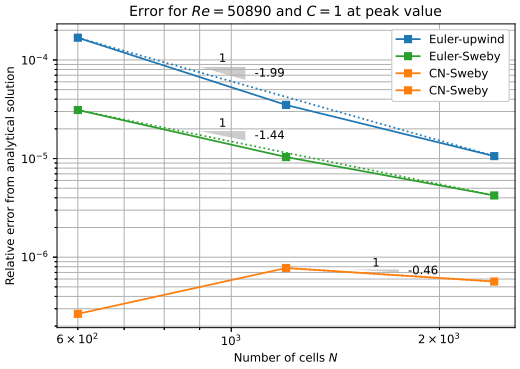

Figure 4.17: The relative error with respect to the analytical solution is visualised for the grid sensitivity in space for $Re = 50,890$.

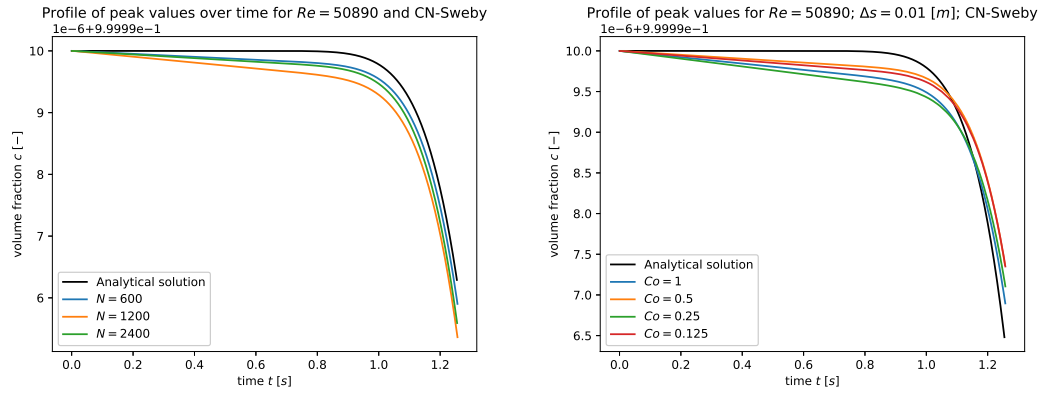

(a) Profile of peak values for grid refinement in space

(b) Profile of peak values for grid refinement in time

Figure 4.18: The profiles of the peak values over time of the advective volume are visualised for the grid sensitivity in (a) space and (b) time for $Re = 50,890$.

4.9.3. Experiments of Hart

The three turbulent experimental cases of Hart are used as reference cases to validate the numerical model by an analytical solution of the diffusion equation. The difference with Hart's experimental cases is that initial step functions are used as an input to the numerical model for the validation cases, whereas Hart injects all dye during one second into the flow solution.

The numerical model is also capable of modelling the three turbulent experimental cases of Hart. By constructing a Neumann boundary condition which is equal to one during the injection time and equal to zero after the injection time, the actual experiments of Hart could be numerically approximated. The flux boundary condition at the exit still remains. The injection rate of Hart's turbulent experiments is illustrated in Fig. 4.19.

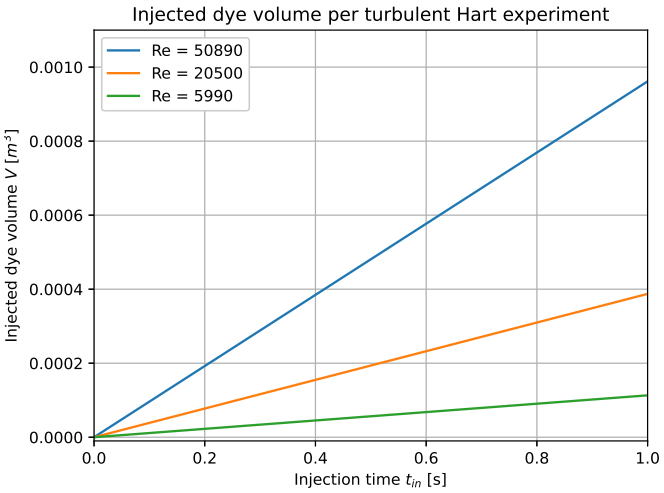

Figure 4.19: The injection rate of dye is visualised per turbulent experiment of Hart.

In his article Hart reports the volume fraction of the dye at the first and sixth (last) measurement point. The last measurement point is located 13.06 $[m]$ from the inlet point. Due to the flux BC at the outlet, the interior grid is extended from 3 to 13.5 $[m]$. As the interior has increased in size, the solver matrix $\mathbf{A}$ will become extremely large if the finest grid of the validation case is used. This could result in a very long simulation time. As the coarsest grid gives good results compared to the analytical solution for the Crank-Nicolson method combined with the Sweby limiter function, the spatial step size of $\Delta s = 0.01$ $[m]$ is the finest grid in modelling Hart's experiments. The numerical simulations are performed with a Courant number of $Co = 0.5$.

As in Section 5.4 interiors are observed which are longer than Hart's geometry and require the solving of all miscible variables, these simulations are performed for coarser spatial step size $\Delta s = 0.02$ and $\Delta s = 0.04$ $[m]$. Therefore, the current numerical simulations also serve as grid sensitivity simulations in space for later numerical cases.

Tabs. 4.6, 4.4 & 4.10 respectively provide the numerical results of the peak values for $Re = 5,990$, $Re = 20,500$ and $Re = 50,890$ for the first and the last measurement point. The time of arrival of the peak values at these measurement points is also tabulated. As Hart reports the peak values normalised by the peak values of the first measurement point in his article, in this study normalised peak values are provided as well. These normalised results are given in Tabs. 4.7, 4.9 & 4.11. The normalised peak values of all turbulent simulations are plotted in Figs. 4.20, 4.21 & 4.22. The time axis is normalised as well. The peak values are translated towards the origin by their time of arrival at the particular measurement point, and subsequently divided by the time of arrival at the first measurement point of the Reynolds number case $Re = 50,890$. The three different case can be compared with each other using this normalised time axis.

Hart's experimental results are also illustrated in Figs. 4.20, 4.21 & 4.22. The normalised peak values at the last measurement point reported by Hart are approximately 0.52, 0.69 and 0.91 for $Re = 5,990$, $Re = 20,500$ and $Re = 50,890$, respectively. The numerical results are in close agreement with each other, but they deviate from the mentioned experimental values. For $Re = 5,990$ and $Re = 20,500$, the numerical solutions deviate from Hart's experiment relatively by approximately 12% and 6%. This is probably due to numerical diffusion which still remains in the flow solution for these Reynolds numbers, as is seen in the validation case. The normalised peak value of the last measurement point is overestimated by approximately 6% by the numerical model compared to Hart's experimental results for $Re = 50,890$, as presumably the axial dispersion coefficient is again underestimated for this Reynolds number.

The plots in Figs. 4.20, 4.21 & 4.22 show an asymmetrical behaviour predicted by the numerical model, although this asymmetry is less compared to the results reported by Hart. The asymmetry arises as the dye is injected for 1 second into the flow solution. The dye which is injected first is longer exposed to the physical axial dispersion coefficient within the interior. This results in the right side of the peak which is more diffused than the left side of the peak. Therefore, the predicted asymmetrical behaviour is a good feature of the numerical model. In the grid sensitivity simulations with the analytical solution this asymmetry is not observed, as the initial conditions result in beautiful symmetrical behaviours throughout the interior.

The normalised peak values at the first and last measurement points show great similarities for the three different grids. The profiles of the peaks almost entirely overlap in Figs. 4.20, 4.21 & 4.22. Therefore, it is shown that mesh step independence has been reached for the numerical simulations of Hart, and that the interior of pipelines can perfectly be approximated with a coarse spatial step size of $\Delta s = 0.04$ $[m]$ as long as the Crank-Nicolson method combined with the Sweby limiter function is used in the model.

4.9.4. Conclusions on model validation

Numerical simulations have been performed to compare the results of the model with an analytical solution and experimental data of Hart. Grid sensitivity tests in space are completed for both sets of simulations which show very good agreement with each other for the Crank-Nicolson method combined with the Sweby limiter function. The grid sensitivity tests in time show a beautiful converging trend to the analytical solution simulations.

In both sets of simulations, numerical diffusion plays a role for the Reynolds number $Re = 5,990$ and $Re = 20,500$. However, numerical diffusion becomes of less importance when the Reynolds number increases. For $Re = 50,890$, the analytical solution is almost entirely approached by the Euler methods, whereas the CN method overestimates the analytical solution for particular simulations. Anyhow, this overestimation of the analytical solution is very small; there is a relative difference in the order of 1e-06 or lower. The CN method overestimates the peak values of Hart's experiments for $Re = 50,890$ as well. As stated, it is suspected that the physical axial dispersion is underestimated for this method in both sets of simulations.

Overall, it is concluded that the numerical model performs well in approximating the analytical solution of a turbulent diffusion equation and in approximating Hart's experiments. The numerical model is valid.

Table 4.6: The results of the simulations of Hart's experiment $Re = 5,990$ are given for the first and the last measurement points.

$Re = 5,990$	**peak value at first measurement point**	**time of arrival of peak value at first measurement point** $[s]$	**peak value at last measurement point**	**time of arrival of peak value at last measurement point** $[s]$
$\Delta s = 0.01$ $[m]$ $\Delta t \approx 0.02$ $[s]$	0.303011	11.0537	0.138203	52.4900
$\Delta s = 0.02$ $[m]$ $\Delta t \approx 0.04$ $[s]$	0.304978	11.0737	0.138911	52.4900
$\Delta s \approx 0.04$ $[m]$ $\Delta t \approx 0.08$ $[s]$	0.295406	11.1327	0.135454	52.4600

Table 4.7: The normalised results of the simulations of Hart's experiment $Re = 5,990$ are given for the first and the last measurement points.

$Re = 5,990$	**Normalised volume fraction of first measurement point**	**Normalised volume fraction of last measurement point**
$\Delta s = 0.01$ $[m]$	1	0.456099
$\Delta s = 0.02$ $[m]$	1	0.455479
$\Delta s \approx 0.04$ $[m]$	1	0.458535

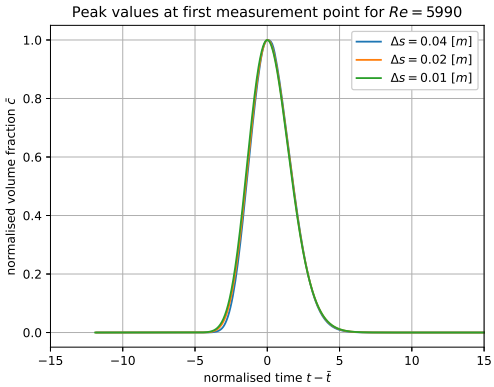

(a) Normalised peak values at first measurement point

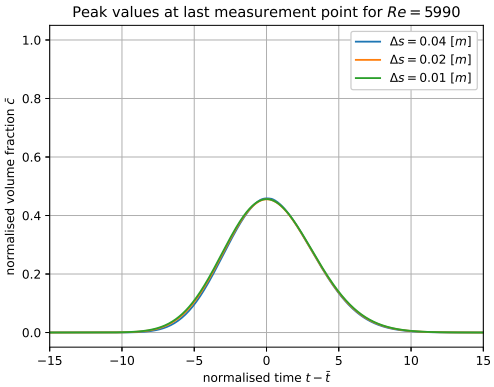

(b) Normalised peak values at last measurement point

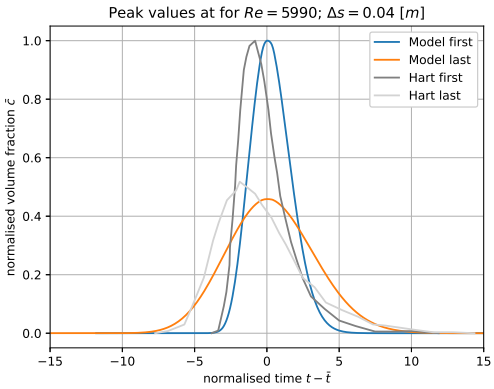

(c) Normalised peak values at first and last measurement points for $\Delta s = 0.04$ $[m]$ including data of Hart [12]

Figure 4.20: The normalised peak values are visualised for $Re = 5,990$ of (a) the first measurement point for all grids, (b) the last measurement point for all grids, (c) the first and last measurement point for $\Delta s = 0.04$ $[m]$.

Table 4.8: The results of the simulations of Hart's experiment $Re = 20,500$ are given for the first and the last measurement points.

$Re = 20,500$	**peak value at first measurement point**	**time of arrival of peak value at first measurement point** $[s]$	**peak value at last measurement point**	**time of arrival of peak value at last measurement point** $[s]$
$\Delta s = 0.01$ $[m]$ $\Delta t \approx 0.006$ $[s]$	0.934972	3.65070	0.592819	15.7301
$\Delta s = 0.02$ $[m]$ $\Delta t \approx 0.01$ $[s]$	0.938742	3.66822	0.594801	15.7243
$\Delta s \approx 0.04$ $[m]$ $\Delta t \approx 0.02$ $[s]$	0.938395	3.70023	0.598842	15.7377

Table 4.9: The normalised results of the simulations of Hart's experiment $Re = 20,500$ are given for the first and the last measurement points.

$Re = 20,500$	**Normalised volume fraction of first measurement point**	**Normalised volume fraction of last measurement point**
$\Delta s = 0.01$ $[m]$	1	0.634050
$\Delta s = 0.02$ $[m]$	1	0.633615
$\Delta s \approx 0.04$ $[m]$	1	0.637137

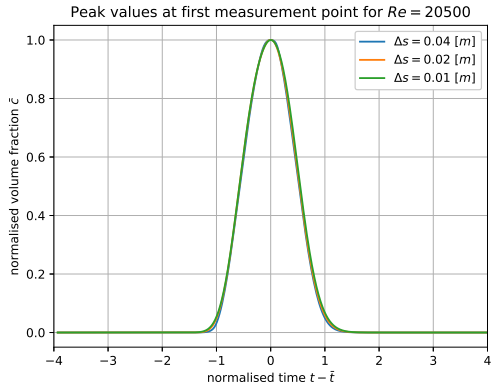

(a) Normalised peak values at first measurement point

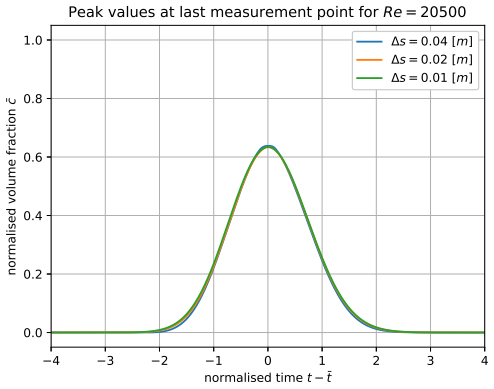

(b) Normalised peak values at last measurement point

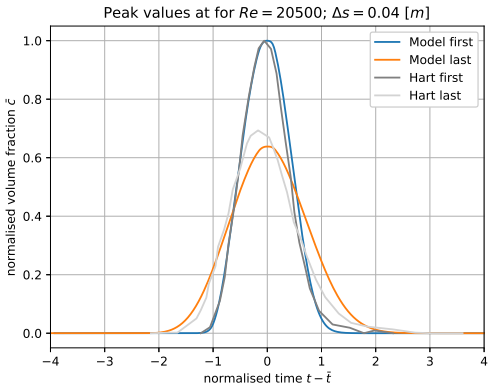

(c) Normalised peak values at first and last measurement points for $\Delta s = 0.04$ $[m]$ including data of Hart [12]

Figure 4.21: The normalised peak values are visualised for $Re = 20,500$ of (a) the first measurement point for all grids, (b) the last measurement point for all grids, (c) the first and last measurement point for $\Delta s = 0.04$ $[m]$.

Table 4.10: The results of the simulations of Hart's experiment $Re = 50,890$ are given for the first and the last measurement points.

$Re = 50,890$	**peak value at first measurement point**	**time of arrival of peak value at first measurement point** $[s]$	**peak value at last measurement point**	**time of arrival of peak value at last measurement point** $[s]$
$\Delta s = 0.01$ $[m]$ $\Delta t \approx 0.002$ $[s]$	0.9999970	1.85647	0.964741	6.65412
$\Delta s = 0.02$ $[m]$ $\Delta t \approx 0.005$ $[s]$	0.9999989	1.86823	0.967244	6.65412
$\Delta s \approx 0.04$ $[m]$ $\Delta t \approx 0.009$ $[s]$	0.9999962	1.88500	0.975936	6.63500

Table 4.11: The normalised results of the simulations of Hart's experiment $Re = 50,890$ are given for the first and the last measurement points.

$Re = 50,890$	**Normalised volume fraction of first measurement point**	**Normalised volume fraction of last measurement point**
$\Delta s = 0.01$ $[m]$	1	0.964734
$\Delta s = 0.02$ $[m]$	1	0.967245
$\Delta s \approx 0.04$ $[m]$	1	0.975940

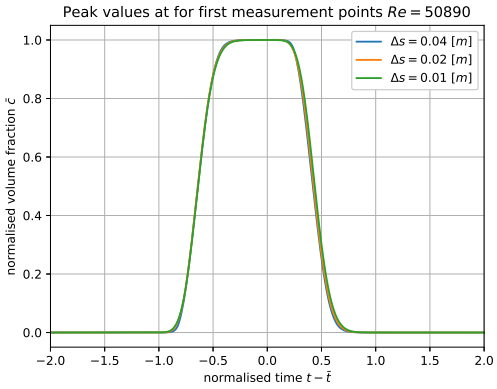

(a) Normalised peak values at first measurement point

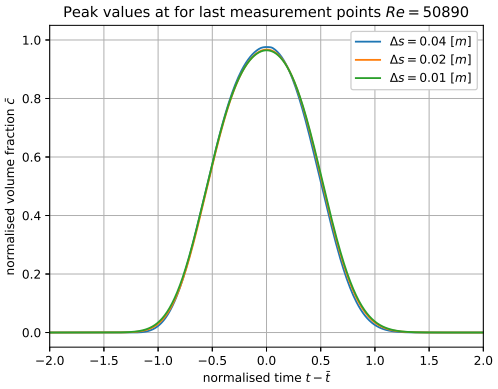

(b) Normalised peak values at last measurement point

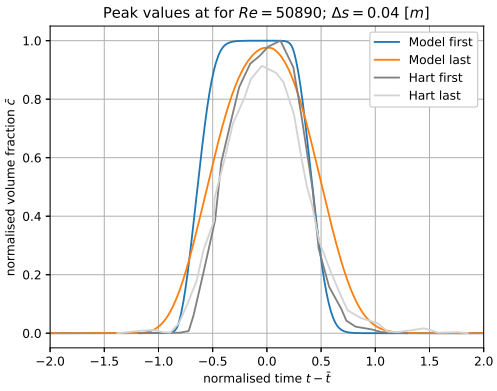

(c) Normalised peak values at first and last measurement points for $\Delta s = 0.04$ $[m]$ including data of Hart [12]

Figure 4.22: The normalised peak values are visualised for $Re = 50,890$ of (a) the first measurement point for all grids, (b) the last measurement point for all grids, (c) the first and last measurement point for $\Delta s = 0.04$ $[m]$.

5

Results of fluid-fluid displacement cases

The miscible set of equations of (3.68) is discretised in Chapter 4. This numerical model will be tested for its capabilities by simulating four different miscible fluid-fluid displacement cases in this chapter. The first three cases are simulated without knowing the right volumetric transfer terms upfront. In Section 5.4 the results of the numerical model are matched with Dellecase's experimental results [10] and CFD results of the Dellecase experiment in order to derive an empirical relation for the volumetric transfer term. In Section 5.5 the Froude number case and the W-shaped pipe cases are resimulated with a volumetric transfer terms of the derived empirical relation.

5.1. Benjamin bubble

In this section the classic Benjamin bubble example of Fig. 1.1 (a) & (b) is tested. To reproduce the bubble formation in a pipe, the model makes use of the special form of the hold-up function $\mathscr{F}$ which is described in Section 3.3.3.

The Benjamin bubble formation is modelled for two different initial conditions:

1. the light fluid is located at the left side of the diaphragm and the heavy fluid is located at the right side at $t_0 = t = 0$ $[s]$;
2. the heavy fluid is located at the left side of the diaphragm and the light fluid is located at the right side at t_0.

Initial condition 1 and its bubble formation were already visualised in Fig. 3.12, as this condition was used to derive the hold-up function and effective bubble velocity function at $\theta = 0$. The initial condition 2 and its bubble formation are exactly the opposite of scenario 1 and are illustrated in Fig. 5.1. Note that $\rho_u = \rho_L$ and $\rho_l = \rho_H$ at t_0.

It is expected that the fluid-fluid displacement behaviour of the two scenarios are exactly opposite. Recall that the Benjamin bubble velocity is always larger than water front velocity for horizontal pipe flow; i.e. $u_B > u_F$. As a result, the upper region will reach the wall sooner than the lower region for all simulations.

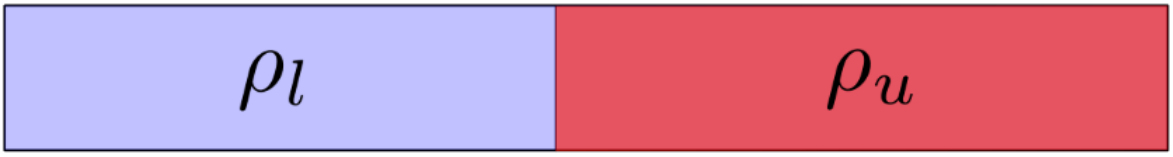

(a) Initial position 2 of the two fluids before the diaphragm is removed

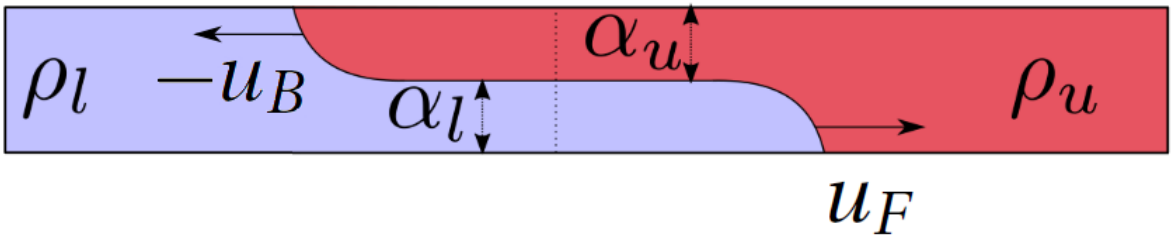

(b) Position of both fluids at $t = \Delta t$ for scenario 2

Figure 5.1: The classic Benjamin bubble is illustrated at (a) time t_0 and (b) $t = \Delta t$. Initially, the heavy fluid is at the left side of the diaphragm and the light fluid is present at the right side of the diaphragm. Figure (b) shows the movement after the diaphragm is removed, including some important flow variables [7].

The simulation input parameters are summarised in the following overview:

- The selected light fluid is methanol and the selected heavy fluid is fresh water. Their thermodynamic properties denoted in the subscript $B \in \{L, H\}$ at 20 degrees Celsius are:

$$\rho_L = 791.7 \left[\frac{kg}{m^3}\right] \quad \text{and} \quad \mu_L = 0.593\text{e-}03 \left[\frac{kg}{ms}\right]$$
$$\rho_H = 998.2 \left[\frac{kg}{m^3}\right] \quad \text{and} \quad \mu_H = 1.0005\text{e-}03 \left[\frac{kg}{ms}\right]$$

- The pipe radius is $R = 0.1$ $[m]$ which results in a hydraulic diameter of $D_H = 0.2$ $[m]$;
- The length of the pipe is $s_{\text{total}} = 4$ $[m]$; i.e. $s^* = \frac{4}{D_H} = 20$;
- The pipe inclination angle is $\theta = 0$ $[°]$; i.e. the pipe is horizontal;
- The total number of cells is $N = 100$, this yields $\Delta s = 0.04$ $[m]$; $\Delta s^* = 0.2$;
- The Courant number is set at $Co = 0.25$, this generates a time step of $\Delta t = 0.007139$ $[s]$; $\Delta t^* \approx 0.050$;
- The total simulation time is $t = 30$ $[s]$; i.e. $t^* = 30\sqrt{\frac{g}{D_H}} \approx 210$;
- The flow is initially stagnant; i.e. the superficial velocity is $u_s = 0$ $\left[\frac{m}{s}\right]$;
- The magnitudes of the Benjamin and water front velocities within the geometry are:

$$u_B = 0.3455 \left[\frac{m}{s}\right], \quad u_F = 0.2500 \left[\frac{m}{s}\right];$$

- The initial conditions for scenario 1 are defined as:

$$\alpha_u(s, t_0) = c_{Lu}(s, t_0) = \begin{cases} 1, & \text{for } 0 \le s < 2, \\ 0, & \text{for } 2 \le s \le 4, \end{cases} \quad \text{and} \quad \alpha_l(s, t_0) = c_{Hl}(s, t_0) = \begin{cases} 0, & \text{for } 0 \le s < 2, \\ 1, & \text{for } 2 \le s \le 4, \end{cases}$$

- The initial conditions for scenario 2 are defined as:

$$\alpha_u(s, t_0) = c_{Lu}(s, t_0) = \begin{cases} 0, & \text{for } 0 \le s < 2, \\ 1, & \text{for } 2 \le s \le 4, \end{cases} \quad \text{and} \quad \alpha_l(s, t_0) = c_{Hl}(s, t_0) = \begin{cases} 1, & \text{for } 0 \le s < 2, \\ 0, & \text{for } 2 \le s \le 4, \end{cases}$$

- Neumann boundary conditions are assigned at the left and right wall of domain, as no flow is allowed to pass through the walls;

$$
\begin{aligned}
&u_{s,\beta_{-\frac{3}{2}}} = u_{s,\beta_{-\frac{1}{2}}} = u_{s,\beta_{\frac{1}{2}}} && \text{and} \quad u_{s,\beta_{N+\frac{5}{2}}} = u_{s,\beta_{N+\frac{3}{2}}} = u_{s,\beta_{N+\frac{1}{2}}} \\
&\alpha_{u_{-1}} = \alpha_{u_0} = \alpha_{u_1} && \text{and} \quad \alpha_{u_{N+2}} = \alpha_{u_{N+1}} = \alpha_{u_N} \\
&c_{B\beta_{-1}} = c_{B\beta_0} = c_{B\beta_1} && \text{and} \quad c_{B\beta_{N+2}} = c_{B\beta_{N+1}} = c_{B\beta_N}
\end{aligned}
$$

- The volumetric transfer terms are set at $\Psi_{L,lu} = \Psi_{H,lu} = 5\text{e-}04 \left[\frac{m}{s}\right]$;
- $\mathscr{G}_{LH}$ is required for initial condition 1 and $\mathscr{G}_{HL}$ is required for initial condition 2;
- The threshold values used in the slip functions $\mathscr{F}$ and $\mathscr{G}_{B_1B_2}$ are $\varepsilon_1 = 0.3$ and $\varepsilon_2 = 2$ [7].

As the empirical relation of the transfer terms in the form described in equation (3.66) is derived in Section 5.4, the value of the volumetric transfer terms is still unknown. The selected value is high to show the fluid-fluid mixing on this relative short time frame. Furthermore, the mass transfer terms are set to zero in this cases; $\Psi_{\beta_1\beta_2} = 0 \left[\frac{kg}{m^2 s}\right]$, as it influences the magnitude of the hold-up variables in the horizontal pipe section. It is wanted that the area of regions remains constant after the equilibrium postion of the hold-up distrbution has been reached in which the exchange of fluids is allowed. Therefore, an exchange between the regions is observed due to the volumetric transfer terms only.

In Figs. 5.3, 5.4, 5.5 & 5.6 the results of the hold-up, velocity and volume fraction distributions for the Benjamin bubble cases are presented. It is observed that the Benjamin bubble is recovered for both initial conditions by the model. The figures are divided into two columns: (1) the left column is denoted by *LH*, as it represents initial condition 1 and (2) the right column is denoted by *HL* as it illustrates initial condition 2. The distributions of the flow variables are visualised at five different time steps. The specific dimensionless time is found on the left of each plot.

The hold-up distribution shows the expected behaviour. Directly after the diaphragm has been removed the upper region creeps over the lower region and moves towards the wall in a separated layer. In Fig. 5.3 it is seen that the correct height of this separate layer is reproduced by the model, corresponding to $\alpha_u \approx 0.42$. This height is somewhat larger at the front of the upper region which implies that the bubble is being formed.

In the separated layer regions where the hold-up of the upper region equals 0.42, the hold-up function $\mathscr{F}$ allows the slip velocity between the region to be equal to the effective bubble velocity; $\mathscr{F}(\alpha_u = 0.42) = 1$. The signs of the axial velocities per region for the two scenarios are exactly opposite. For initial condition 1, the upper region moves towards the right wall. The axial velocity of the upper region is postive, whereas the axial velocity of the upper region is negative for scenario 2. At the front and the tail of the bubble the velocities deviate slightly from the magnitude of the velocities in the separated layers. Again, this is due to the formation of the bubble. The spikes, showing peak values of the effective bubble velocity, are seen due to the discretisation of the densities by the central scheme. They are limited so that they do not exceed the maximum value of the effective bubble velocity in a horizontal pipe section.

The volume fraction variables show symmetrical behaviour as well. c_{Lu} and c_{Hl} are plotted together with the total volume fraction of the light fluid c_L and the heavy fluid c_H, respectively. The volume fraction of the fluid particles in the regions are less than one due to dispersion and mass transfer. The local spikes which are seen for the volume fraction of the heavy fluid particles in the lower region are coupled to the small spikes observed for the axial velocity of the lower region. The volume fraction of the fluid particles in the regions reduce in magnitude as a result of the mass transfer. When $c_{Lu} \approx 0.5$ and $c_{Hl} = 0.5$, the fluids would be mixed completely. The total volume fraction of the fluids remain constant as no mass is added to or removed from the domain. After the equilibrium position has been reached the hold-up distribution does not change either. This is due to the same reason.

The averaged number of iterations per time step is approximately equal to 20 for both initial conditions. The evolution of the number of iterations per time step is plotted for *LH* in Fig 5.2a. The residuals of the flow variabels at $t^* = 7.0$ are plotted in Fig. 5.2b for *LH* as well. All slopes of the residuals are approximately equal to one which corresponds to Picard's method.

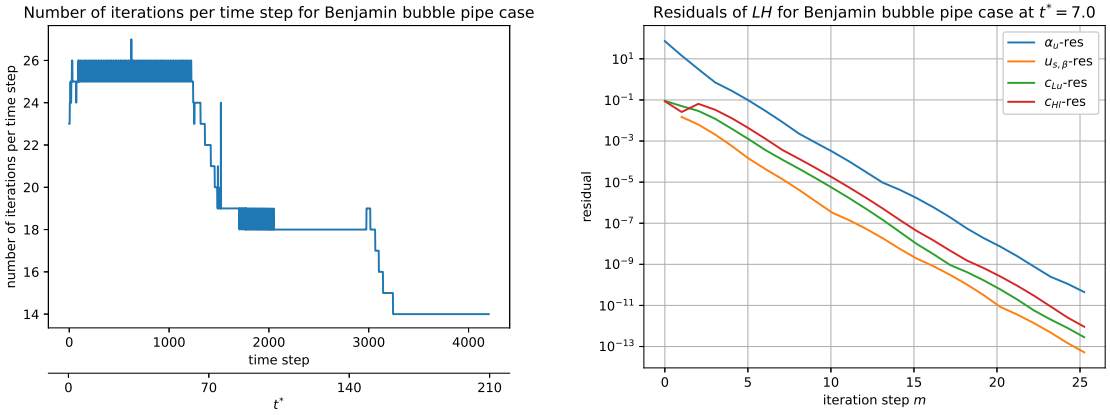

(a) The number of iterations per time step for Benjamin bubble pipe case *LH* (b) Residuals for Benjamin bubble pipe case *LH* at $t^* = 7.0$

Figure 5.2: The number of iterations per time step is visualised in (a) and the residuals of the flow variables solved in the coupled matrix **A** are visualised in (b) for the Benjamin bubble pipe case *LH*.

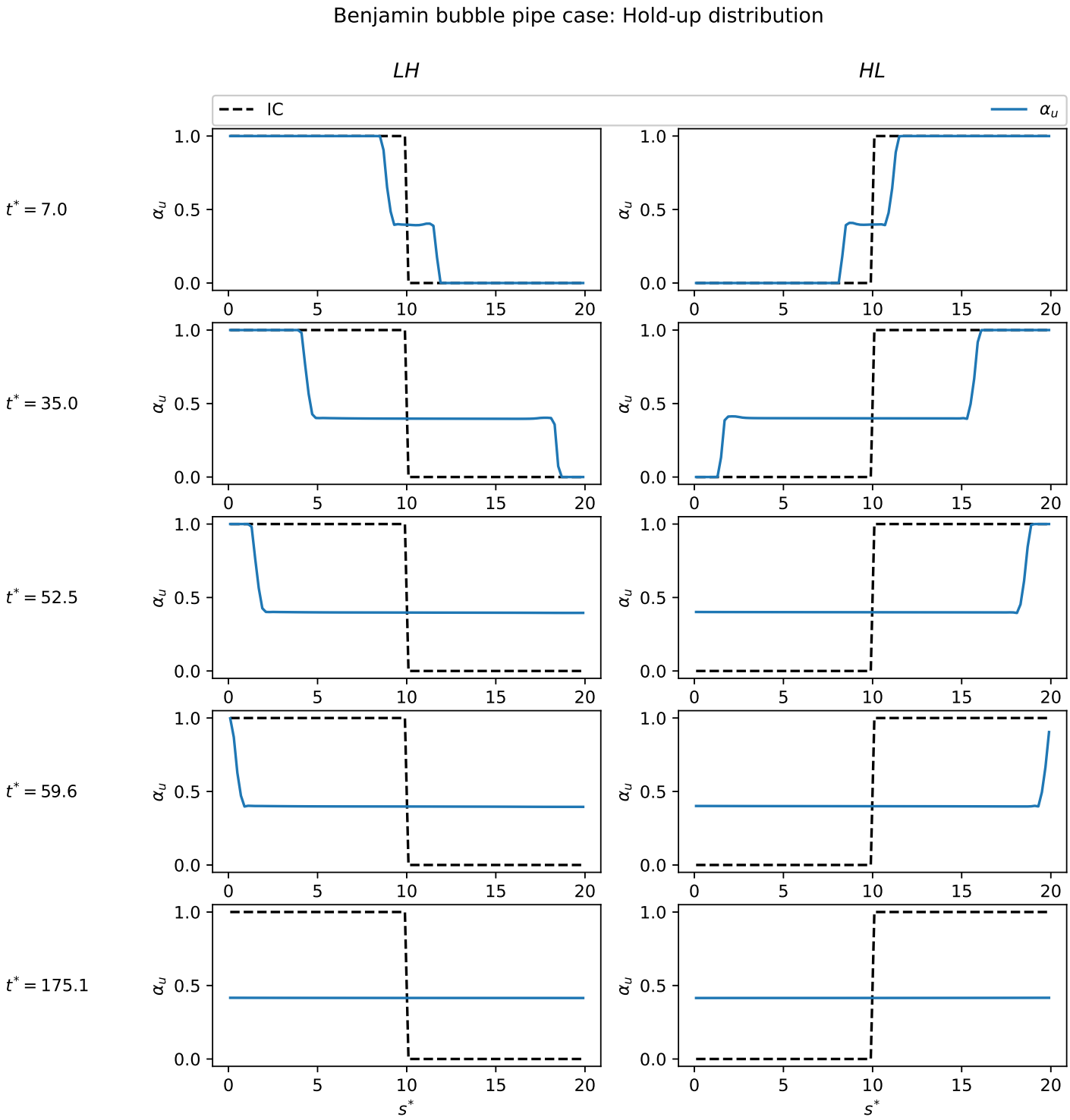

Figure 5.3: The distribution of the hold-up variables is visualised for two Benjamin bubble pipe cases: *LH* and *HL*, The distributions of α_u are given at five different time steps.

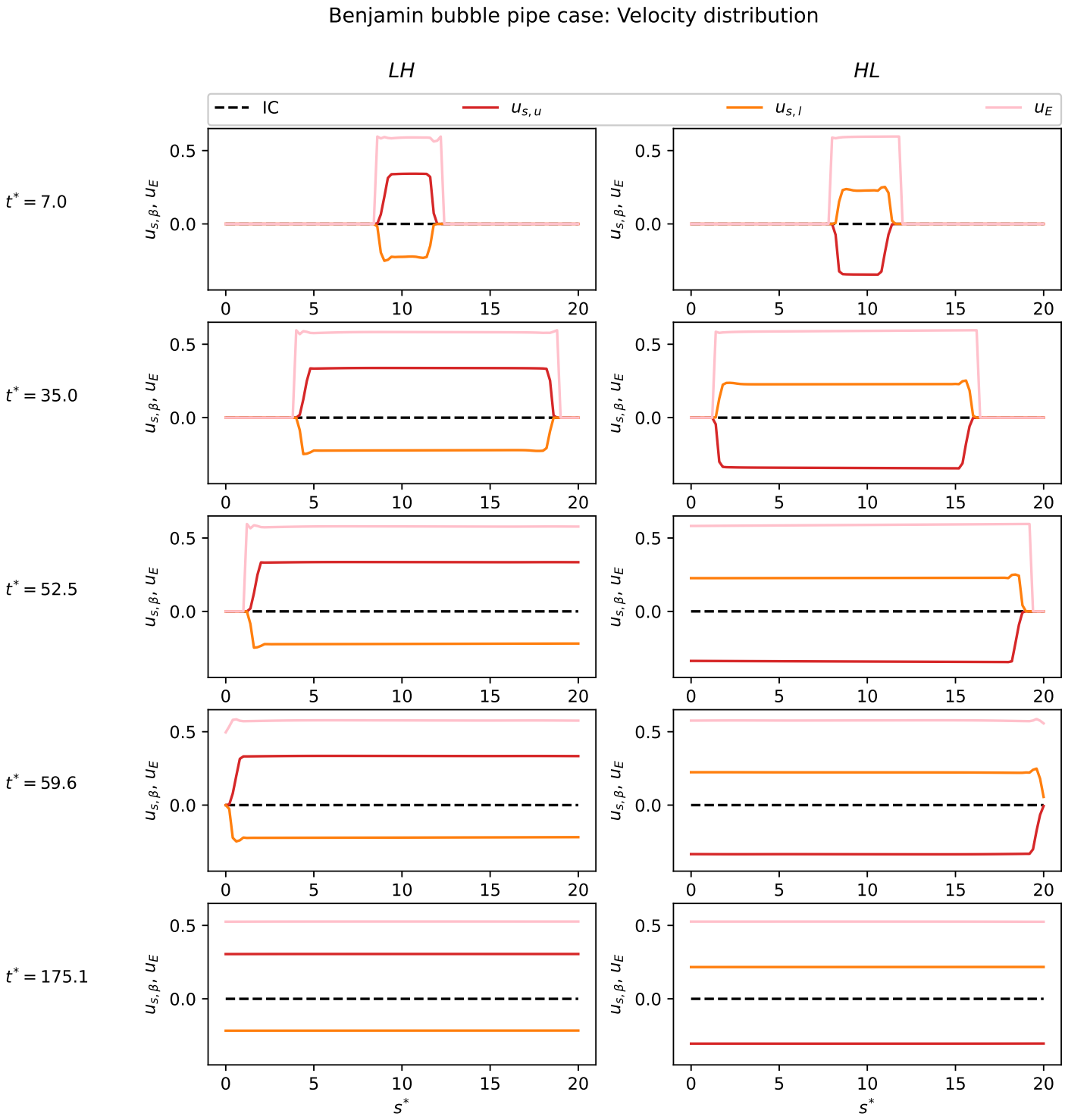

Figure 5.4: The distribution of the velocity variables is visualised for two Benjamin bubble pipe cases: *LH* and *HL*, The distributions of $u_{s,u}$, $u_{s,l}$ and u_E are given at five different time steps.

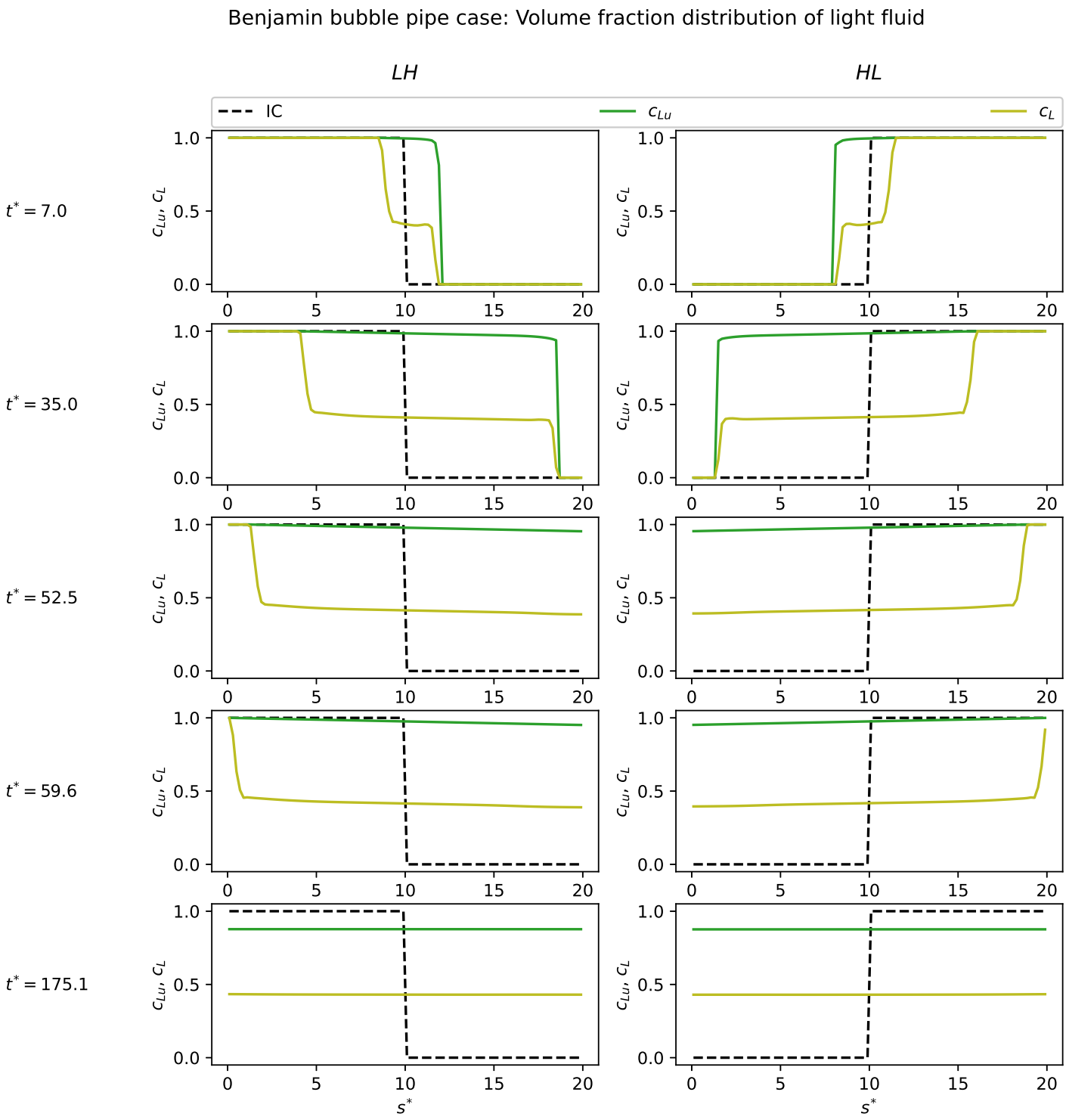

Figure 5.5: The distribution of the volume fraction variables of the light fluid is visualised for two Benjamin bubble pipe cases: *LH* and *HL*, The distributions of c_{Lu} and c_L are given at five different time steps.

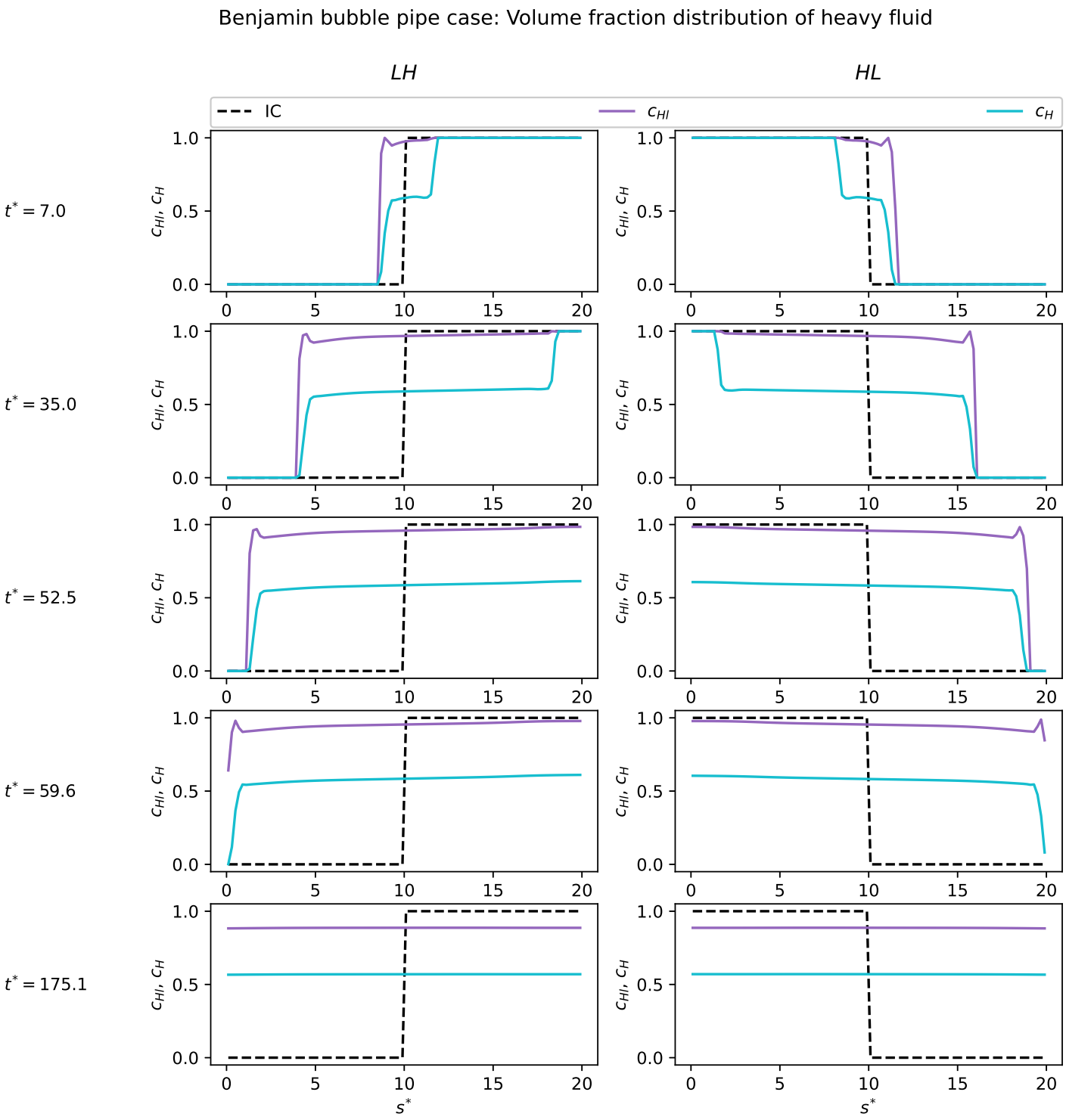

Figure 5.6: The distribution of the volume fraction variables of the heavy fluid is visualised for two Benjamin bubble pipe cases: *LH* and *HL*, The distributions of c_{Hl} and c_H are given at five different time steps.

5.2. Froude number

The model has proven that it is able to reproduce a Benjamin bubble in a pipe, where the upper region is moving at the Benjamin bubble velocity and the lower region at the water front velocity. When the flow is not stagnant in a horizontal pipe, the model must reproduce these bubbles velocities within the regions relative to the superficial velocity as well. Due to this velocity difference per region, the flushing characteristic where a light fluid flushes out a heavy fluid of a pipe section is reported in the literature to result in a longer mixing length than the opposite flushing characteristic [15].

Furthermore, Henkes [15] reported that stratification effects are no longer observed for multiphase flow in horizontal pipe sections for a modified Froude number above 15. The Froude number is modified to include the effect of a density difference within the flow and was given in Chapter 1.

$$Fr = \frac{\rho_{\text{mix}}}{\Delta\rho} \frac{u_s^2}{gD_H} \tag{1.5}$$

The model is tested for a series of Froude numbers starting at $Fr = 0.125$ which is doubled until $Fr = 16$ is reached. These simulations are performed for the flushing characteristics *LH* and *HL* of which the notations were already introduced in Section 5.1. It is investigated whether the model is able to predict a longer mixing length for *LH* than for *HL* and whether stratification effects are still predicted by the model for large Froude numbers for both flushing characteristics or not. Note that a model which is one-dimensional is normally not able to capture stratified flow. However, the hold-up function $\mathscr{F}$ has been constructed to mimic stratification effects in a horizontal pipe section. Therefore, it is assumed that stratification effects are seen in the model when the hold-up of the upper region is approximately equal to 0.42 over some axial distance.

The initial conditions *LH* and *HL* are illustrated in Fig. 5.7. The pipe is 15 metres long and the flushing fluid is initially only present in the first metre of the pipe. Note that $\rho_u = \rho_L$ and $\rho_l = \rho_H$ at t_0.

(a) Initial condition 1: *LH*

(b) Initial condition 2: *HL*

Figure 5.7: The initial conditions for the Froude number cases are visualised. In (a) flushing characteristic *LH* is shown and flushing characteristic *HL* is illustrated in (b) [7].

The simulation input parameters are summarised in the following overview:

- the selected light fluid is methanol (CH_3OH) and the selected heavy fluid is fresh water. Their thermodynamic properties denoted in the subscript $B \in \{L, H\}$ at 20 degrees Celsius are:

$$\rho_L = 791.7 \left[\frac{kg}{m^3}\right] \quad \text{and} \quad \mu_L = 0.593\text{e-}03 \left[\frac{kg}{ms}\right]$$
$$\rho_L = 998.2 \left[\frac{kg}{m^3}\right] \quad \text{and} \quad \mu_L = 1.0005\text{e-}03 \left[\frac{kg}{ms}\right]$$

- The pipe radius is $R = 0.02$ $[m]$ which results in a hydraulic diameter of $D_H = 0.04$ $[m]$;
- The length of the pipe is $s_{\text{total}} = 15$ $[m]$; i.e. $s^* = \frac{15}{D_H} = 375$;
- The pipe inclination angle distribution is $\theta = 0$; the pipe is horizontal;
- The total number of cells is $N = 375$, this yields $\Delta s = 0.04$ $[m]$; $\Delta s = 1$;
- The Courant number is set at $Co = 0.25$. The generated time steps are different per Froude number case and are tabulated in Tab. 5.1;

- The total simulation time is $t = 10\ [s]$; i.e. $t^* = 10\sqrt{\frac{g}{D_H}} \approx 156.6$;
- The superficial velocity per Froude number case is tabulated in Tab 5.1;
- The magnitudes of the Benjamin and water front velocities within the geometry are:

$$u_B = 0.1545\left[\frac{m}{s}\right], \quad u_F = 0.1118\left[\frac{m}{s}\right];$$

- The initial conditions for scenario 1 are defined as:

$$\alpha_u(s,t_0) = c_{Lu}(s,t_0) = \begin{cases} 1, & \text{for } 0 \le s < 1, \\ 0, & \text{for } 1 \le s \le 15, \end{cases} \quad \text{and} \quad \alpha_l(s,t_0) = c_{Hl}(s,t_0) = \begin{cases} 0, & \text{for } 0 \le s < 1, \\ 1, & \text{for } 1 \le s \le 15, \end{cases}$$

- The initial conditions for scenario 2 are defined as:

$$\alpha_u(s,t_0) = c_{Lu}(s,t_0) = \begin{cases} 0, & \text{for } 0 \le s < 1, \\ 1, & \text{for } 1 \le s \le 15, \end{cases} \quad \text{and} \quad \alpha_l(s,t_0) = c_{Hl}(s,t_0) = \begin{cases} 1, & \text{for } 0 \le s < 1, \\ 0, & \text{for } 1 \le s \le 15, \end{cases}$$

- Dirichlet boundary conditions are assigned at the inlet of the pipe to give the flow variables its initial value at every time step. At the outlet the values of the flow variables in the ghost cells are approximated by its two predecessor cells. The BCs are given for the first ghost next to the interior only;

$$\begin{aligned} u_{s,\beta_{-\frac{1}{2}}} &= u_{s,\beta_{-\frac{1}{2}}}(t_0) && \text{and} \quad u_{s,\beta_{N+\frac{3}{2}}} = 2u_{s,\beta_{N+\frac{1}{2}}} - u_{s,\beta_{N-\frac{1}{2}}} \\ \alpha_{u_0} &= \alpha_{u_0}(t_0) && \text{and} \quad \alpha_{u_{N+1}} = 2\alpha_{u_N} - \alpha_{u_{N-1}} \\ c_{B\beta_0} &= c_{B\beta_0}(t_0) && \text{and} \quad c_{B\beta_{N+1}} = 2c_{B\beta_N} - c_{B\beta_{N-1}} \end{aligned}$$

  The pipe length and the initial position is chosen such that the inlet and outlet of the pipe is not reached by the flushing fluid for all Froude number cases;
- The volumetric transfer terms are set at $\Psi_{L,lu} = \Psi_{H,lu} = 0\ \left[\frac{m}{s}\right]$;
- $\mathscr{G}_{LH}$ is required for initial condition 1 and $\mathscr{G}_{HL}$ is required for initial condition 2;
- The threshold values used in the slip functions $\mathscr{F}$ and $\mathscr{G}_{B_1B_2}$ are $\varepsilon_1 = 0.3$ and $\varepsilon_2 = 2$ [7].

Table 5.1: The superficial velocity, the mixture Reynolds number and the dimensionless temporal step size are tabulated per Froude number cases.

Froude number Fr	**Superficial velocity** $u_s\ [m/s]$	**Mixture Reynolds number** Re_{mix}	**Dimensionless temporal step size** Δt^*
0.125	0.1064	4779.7	0.2500
0.25	0.1504	6759.6	0.2500
0.5	0.2128	9559.5	0.2500
1	0.3009	13519.2	0.2500
2	0.4255	19119.0	0.2500
4	0.6017	27038.3	0.2500
8	0.8510	38238.0	0.1840
16	1.2036	54076.7	0.1301

The hydraulic diameter of the pipe is chosen such that the mixture Reynolds numbers, which are tabulated in 5.1, are within the range for Hart's empirical relation for the axial dispersion coefficient [12], except for $Fr = 16$ which is slightly above $Re_{\text{mix}} = 50,000$.

The magnitude of volumetric transfer terms is expected to depend on the mixture Reynolds number. As an empirical relation of the volumetric transfer term as a function of the mixture Reynolds number is not known yet, the volumetric transfer terms are set at zero for all eight Froude number cases. The only diffusion which will be seen during the simulations is induced by the axial dispersion coefficient. The magnitude of the axial dispersion coefficient will grow per increasing mixture Reynolds number as explained in Section 3.3.4.

The hold-up distributions are divided into two plots: Fig. 5.10 includes the Froude numbers $Fr = [0.125, 0.25, 0.5, 1]$ which are plotted until $s^* = 200$ and Fig. 5.11 contains the Froude numbers $Fr = [2, 4, 8, 16]$ which are plotted until $s^* = 375$. Again, the flushing characteristic *LH* is visualised in the left column and *HL* is featured in the right column to show the distinctions between both cases. Only the distributions of the hold-up of the upper regions are given for the Froude number case, as they will show whether the stratification effects are encountered by the model. The specific dimensionless time is found on the left of each plot.

In Tab. 5.2 the axial distances travelled by the front and the tail of the bubble per Froude number cases are tabulated for *LH* and *HL*. The distance travelled by the front is determined by measuring when $\alpha_u = 0.95$ for *LH* and $\alpha_u = 0.05$ for *HL* at each simulation time. To determine the distance travelled by the tail of the bubble, the exact opposite procedure is required. The relative axial distances between the front and the tail of the bubbles are given as well.

The Benjamin bubble velocity and the water front velocity for the selected hydraulic diameter are $u_B = 0.1545$ and $u_F = 0.1118$ $\left[\frac{m}{s}\right]$, which play an important role in the fluid-fluid displacement in a horizontal pipe as explained in Section 3.3.3. Especially, the displacement results of the Froude numbers $Fr = 0.125$ and $Fr = 0.25$ are interesting as their superficial velocities are close to the given bubble velocities. For *LH* it is seen for $Fr = 0.125$ that the location of the tail remains around its initial position as the relative velocity difference between the water front velocity and the specific superficial velocity is very small. For *HL* a similar fluid-fluid behaviour is observed for $Fr = 0.25$; here the relative velocity of the Benjamin bubble velocity and the superficial velocity are in close agreement. For $Fr = 0.125$ even backflow is encountered in the pipe section, as the Benjamin bubble velocity is larger than the superficial velocity.

The hold-up distributions plotted in Fig. 5.10 show many similarities for both flushing characteristics; stratified layers are reproduced by the model of which the relative mixing length between the front and the tail of the bubble is somewhat larger for *LH* than for *HL*. For *LH* the front of the bubble is always located further downstream.

The deviations between the hold-up distributions for the flushing characteristics are seen in Fig. 5.11. For *HL* it is observed that stratified layers of fluid are still reproduced for $Fr = 2$ and in some extent for $Fr = 4$. However the hold-up distributions for $Fr = 8$ and $Fr = 16$ do not show stratification effects, the model reproduces a trend which behaves more like a Gaussian impulse response function given in equation (3.59). The results of the hold-up distributions for *LH* show a similar trend to the results depicted in Fig. 5.10.

The reason for these deviations is found by analysing the results of all flow variables, for the Froude numbers. The differences between the results for the high Froude numbers are caused by the treatment of the tail of the bubbles for *LH* and *HL* in the model. For *HL* the tail is associated with the upper region. In the upper region, the Reynolds number is larger than in the lower region due to the thermodynamic properties, which results in a larger axial dispersion coefficient for the upper region compared to the lower region. Therefore, the volume fraction of the light particles in the upper region are more dispersed for *HL* in comparison to the volume fraction of the heavy fluid in the lower region for *LH*. As a consequence the density of the upper region in the tail reduces rapidly and the local magnitude of the effective bubble velocity becomes smaller than $u_B + u_F$. This is needed to produce stratified layers within a horizontal pipe section, and the hold-up distribution takes the form as presented for $Fr = 4, 8, 16$. The plots of the velocity and volume fraction distributions are not added in this report.

In Tab. 5.2, it is found that the typical relative axial distance reproduced by the model is indeed larger for *LH* compared to *HL*. The model still predicts stratified flow for high Froude numbers and by looking at the hold-up distributions associated with these Froude numbers for *LH*, it is concluded that the axial dispersion coefficient is underestimated in the tail of the bubble. However, recall that the mass transfer term is set to zero for these simulations. Therefore, another explanation is that the axial dispersion within the upper region for *HL* is overestimated within the model, and that mass transfer is needed for the stratification effects to vanish at high Froude numbers for *LH*.

The averaged number of iterations per time step is less for the low Froude numbers than for the high Froude numbers; the coupled solver requires more effort to reduce the residuals of the flow variables when the superficial velocity increases. The averaged number of iterations per time step is less for *LH* than for *HL*. The evolutions of the number of iterations are plotted for $Fr = 0.125$ and $Fr = 16$ and both flushing characteristics in Fig. 5.8. The residuals of these four cases are plotted in Fig. 5.9. For the low Froude numbers the slopes of the residuals of all flow variables are somewhat above one, and the slopes of the residuals for the high Froude number are slightly below one.

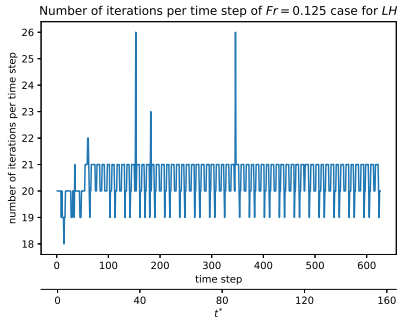

(a) Number of iterations per time step for $Fr = 0.125$ for LH

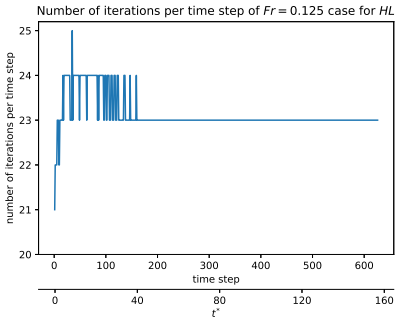

(b) Number of iterations per time step for $Fr = 0.125$ for HL

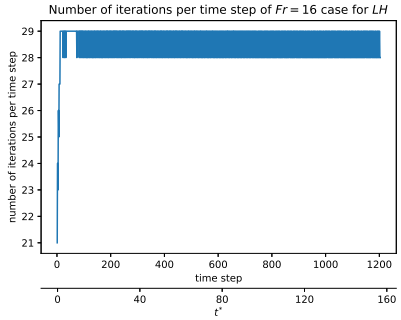

(c) Number of iterations per time step for $Fr = 16$ for LH

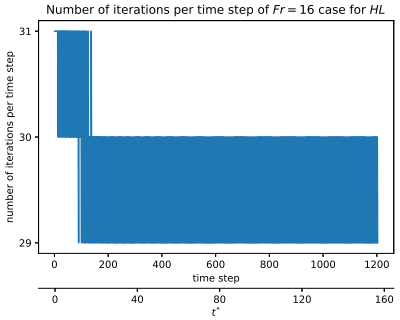

(d) Number of iterations per time step for $Fr = 16$ for HL

Figure 5.8: The iterations per time step are visualised for LH (a) $Fr = 0.125$ and (c) $Fr = 16$ and for HL (b) $Fr = 0.125$ and (d) $Fr = 16$.

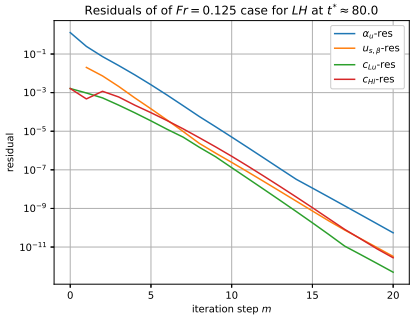

(a) Residuals of $Fr = 0.125$ for LH at $t^* \approx 80.0$

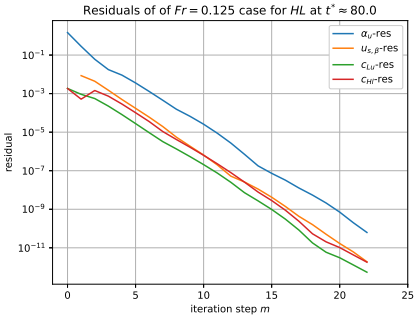

(b) Residuals of $Fr = 0.125$ for HL at $t^* \approx 80.0$

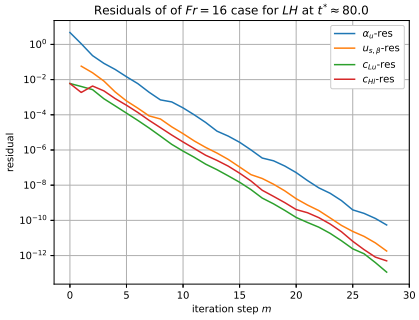

(c) Residuals of $Fr = 16$ for LH at $t^* \approx 80.0$

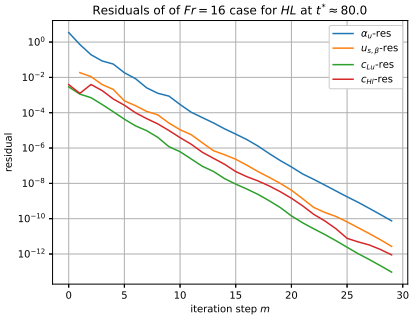

(d) Residuals of $Fr = 16$ for HL at $t^* \approx 80.0$

Figure 5.9: Residuals are visualised for LH (a) $Fr = 0.125$ and (c) $Fr = 16$ and for HL (b) $Fr = 0.125$ and (d) $Fr = 16$ at $t^* \approx 80.0$.

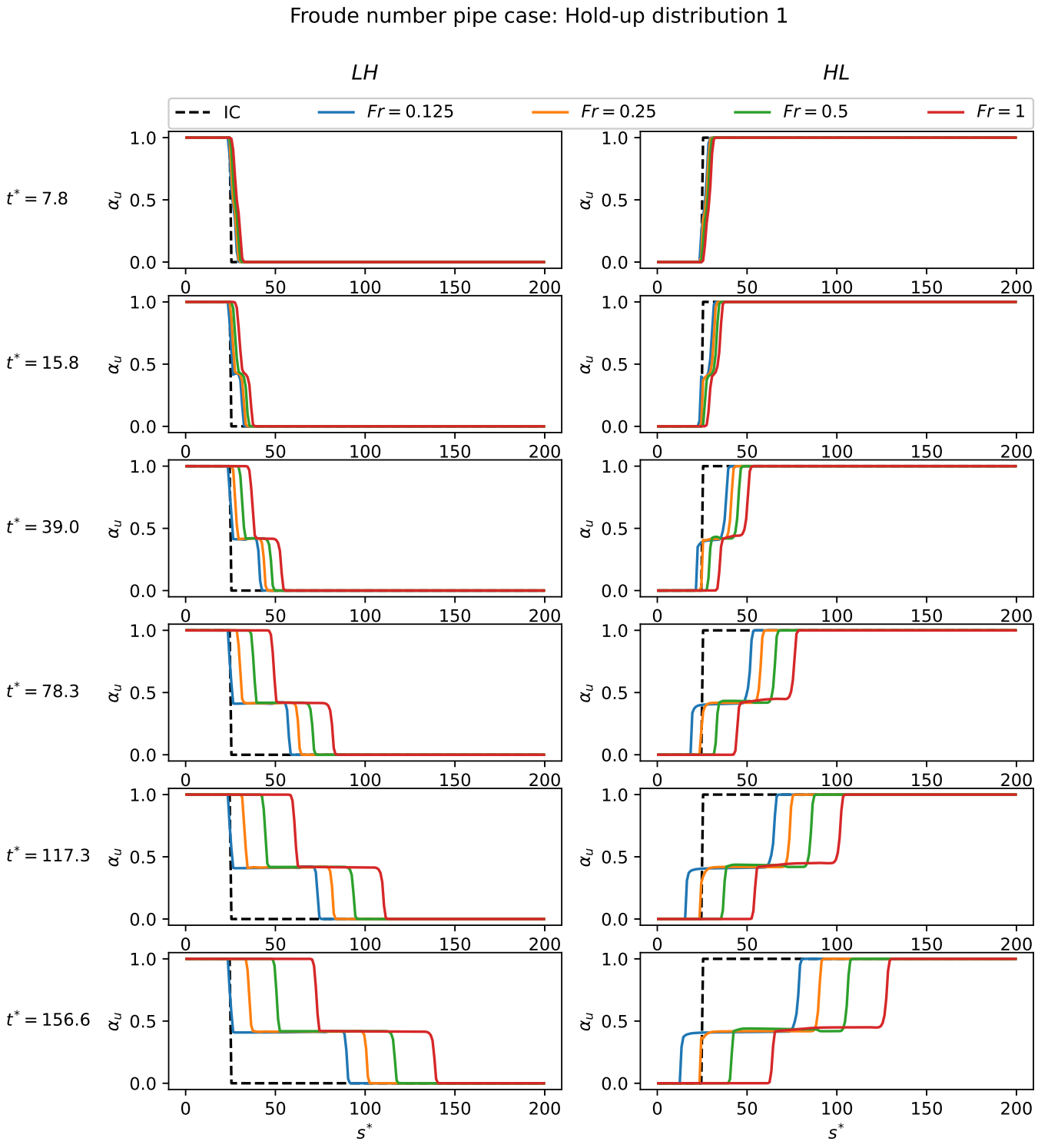

Figure 5.10: The hold-up distributions of $Fr = [0.125, 0.25, 0.5, 1]$ are visualised for *LH* and *HL*.

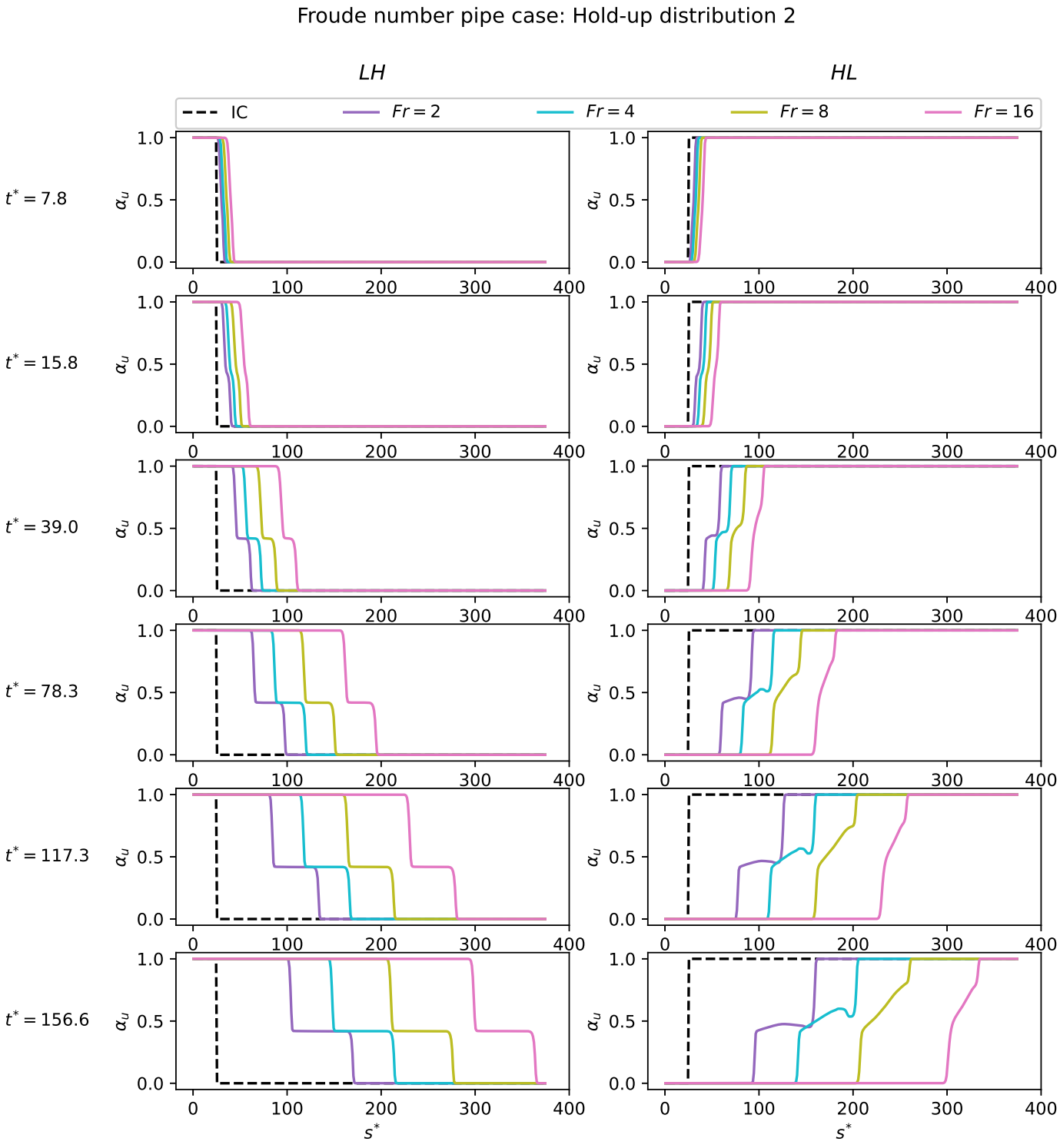

Figure 5.11: The hold-up distributions of $Fr = [2, 4, 8, 16]$ are visualised for *LH* and *HL*.

Table 5.2: The axial distance travelled by the front and the tail of the bubble is tabulated per Froude number for *LH* and *HL*. The axial distances are given at the dimensionless simulation times $t^* = [39.0, 78.3, 117.3, 156.6]$ and the relative distance between the front and the tail is given as well.

LH	**Distance tail s^* at** $t^* \approx 39.0$	**Distance front s^* at** $t^* \approx 39.0$	Δs^* **at** $t^* \approx 39.0$	**Distance tail s^* at** $t^* \approx 78.3$	**Distance front s^* at** $t^* \approx 78.3$	Δs^* **at** $t^* \approx 78.3$	**Distance tail s^* at** $t^* \approx 117.3$	**Distance front s^* at** $t^* \approx 117.3$	Δs^* **at** $t^* \approx 117.3$	**Distance tail s^* at** $t^* \approx 156.6$	**Distance front s^* at** $t^* \approx 156.6$	Δs^* **at** $t^* \approx 156.6$
$Fr = 0.125$	23.5	41.5	18.0	23.5	58.5	35.0	23.5	74.5	51.0	23.5	90.5	67.0
$Fr = 0.25$	26.5	44.4	18.0	28.5	63.5	35.0	31.5	82.5	51.0	34.5	101.5	67.0
$Fr = 0.5$	30.5	48.5	18.0	36.5	71.5	35.0	42.5	94.5	52.0	49.5	117.5	68.0
$Fr = 1$	35.5	54.5	19.0	47.5	82.5	35.0	59.5	111.5	52.0	71.5	139.5	68.0
$Fr = 2$	43.5	62.5	19.0	62.5	98.5	36.0	82.5	134.5	52.0	102.5	170.5	68.0
$Fr = 4$	53.5	73.5	20.0	84.5	120.5	36.0	115.5	167.5	52.0	146.5	214.5	68
$Fr = 8$	69.5	88.5	19.0	115.5	151.5	36.0	162.5	214.5	52.0	207.5	275.5	68.0
$Fr = 16$	91.5	110.5	19.0	159.5	195.5	36.0	227.5	280.5	53.0	296.5	364.5	68.0
HL	**Distance tail s^* at** $t^* \approx 39.0$	**Distance front s^* at** $t^* \approx 39.0$	Δs^* **at** $t^* \approx 39.0$	**Distance tail s^* at** $t^* \approx 78.3$	**Distance front s^* at** $t^* \approx 78.3$	Δs^* **at** $t^* \approx 78.3$	**Distance tail s^* at** $t^* \approx 117.3$	**Distance front s^* at** $t^* \approx 117.3$	Δs^* **at** $t^* \approx 117.3$	**Distance tail s^* at** $t^* \approx 156.6$	**Distance front s^* at** $t^* \approx 156.6$	Δs^* **at** $t^* \approx 156.6$
$Fr = 0.125$	21.5	39.5	18.0	18.5	52.5	34.0	16.5	66.5	50.0	13.5	79.5	66.0
$Fr = 0.25$	24.5	42.5	18.0	24.5	58.5	34.0	24.5	75.5	51.0	24.5	91.5	67.0
$Fr = 0.5$	27.5	46.5	19.0	32.5	66.5	34.0	36.5	86.5	50.0	40.5	107.5	67.0
$Fr = 1$	33.5	51.5	18.0	43.5	77.5	34.0	53.5	103.5	50.0	62.5	129.5	67.0
$Fr = 2$	41.5	59.5	18.0	58.5	93.5	35.0	76.5	126.5	50.0	94.5	160.5	66.0
$Fr = 4$	51.5	70.5	19.0	80.5	115.5	35.0	110.5	160.5	50.0	140.5	204.5	64.0
$Fr = 8$	67.5	85.5	18.0	112.5	144.5	32.0	159.5	203.5	44.0	205.5	260.5	55.0
$Fr = 16$	89.5	105.5	16.0	158.5	181.5	23.0	228.5	257.5	29.0	299.5	333.5	34.0

5.3. W-shaped pipe

The former two cases have showed the capabilities of the model on horizontal pipe sections. As the terrain for the pipelines is never completely flat, the model has to be tested for inclined sections as well. It is chosen to test the model with a W-shaped pipe geometry, illustrated in Fig. 5.12. Here, the W-shaped pipe is filled with a heavy fluid which has to be flushed out of the pipe section by a light fluid.

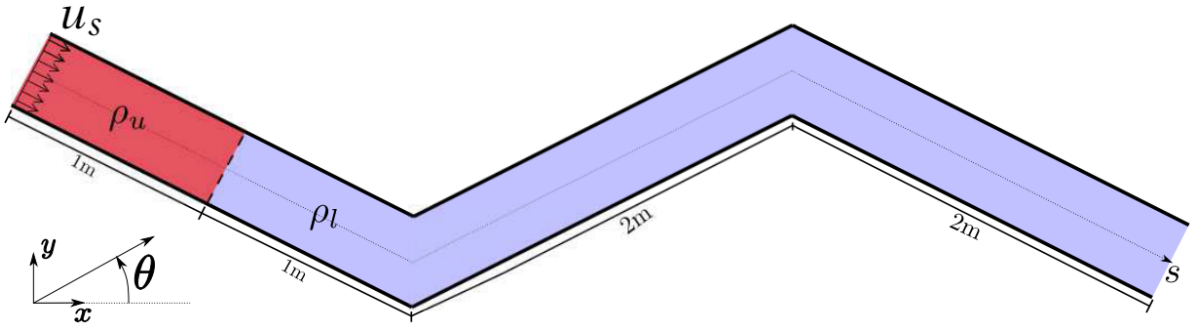

Figure 5.12: The geometry of the W-shaped pipe is visualised. The geometry has an axial length of 6 metres of which each third part has an opposite pipe inclination angle of $\theta = \pm 40$. [7]

The W-shaped pipe is 6 metres long and consists of three sections of 2 metres. These sections alternately have a pipe inclination angle of -40 and 40 degrees. Again, two different initial conditions are simulated: the initial condition of Fig. 5.12 and the initial condition where the pipe is full of a light fluid which has to be flushed by a heavy fluid. Initial condition 2 is not illustrated. Again, a light fluid flushing a heavy fluid is denoted by *LH* and a heavy fluid flushing a light fluid is denoted by *HL*.

As explained in Section 3.3.3, the flushing characteristic is very important for the model, as it determines which type of interface is observed in an inclined section. By simulating the same geometry for both initial conditions the opposite physical phenomenon should be observed in the inclined pipe sections.

The simulation input parameters are summarised in the following overview:

- The selected light fluid is methanol (CH_3OH) and the selected heavy fluid is fresh water. Their thermodynamic properties denoted in the subscript $B \in \{L, H\}$ at 20 degrees Celsius are:

$$\rho_L = 791.7 \left[\frac{kg}{m^3}\right] \quad \text{and} \quad \mu_L = 0.593\text{e-}03 \left[\frac{kg}{ms}\right]$$
$$\rho_H = 998.2 \left[\frac{kg}{m^3}\right] \quad \text{and} \quad \mu_H = 1.0005\text{e-}03 \left[\frac{kg}{ms}\right]$$

- The pipe radius is $R = 0.1\ [m]$ which results in a hydraulic diameter of $D_H = 0.2\ [m]$;
- The length of the pipe is $s_{\text{total}} = 6\ [m]$; i.e. $s^* = \frac{6}{D_H} = 30$;
- The pipe consists of inclined sections only. The pipe inclination angle distribution is:

$$\theta = \begin{cases} -40\,[^\circ], & \text{for } 0 \le s < 2, \\ 40\,[^\circ], & \text{for } 2 \le s < 4, \\ -40\,[^\circ], & \text{for } 4 \le s \le 6, \end{cases}$$

  the pipe inclination angle distribution is plotted together with the pipe elevation y in Fig. 5.13 to clarify the implementation of the W-shaped pipe in the model.

- The total number of cells is $N = 150$, this yields $\Delta s = 0.04\ [m]$; $\Delta s^* = 0.2$;
- The Courant number is set at $Co = 0.25$, this generates a time step of $\Delta t = 0.007139\ [s]$; $\Delta t^* \approx 0.050$;
- The total simulation time is $t = 50\ [s]$; i.e. $t^* = 30\sqrt{\frac{g}{D_H}} \approx 350$;
- The superficial velocity is $u_s = 0.1\ \left[\frac{m}{s}\right]$, this yields $Re_{\text{mix}} = 22402$;

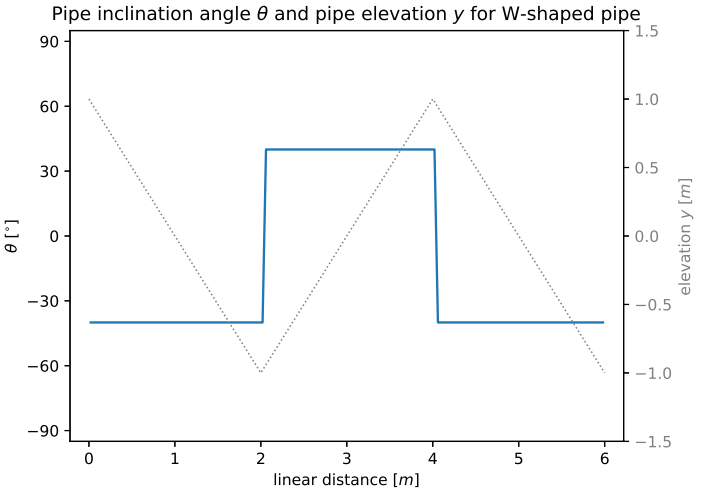

Figure 5.13: The pipe inclination angle distribution θ is visualised together with the elevation y for W-shaped pipe case.

- The magnitudes of the Benjamin, Taylor and water front velocities within the geometry are:

$$u_B = 0.3455\left[\frac{m}{s}\right], \quad u_T = 0.2234\left[\frac{m}{s}\right], \quad u_F = 0.2500\left[\frac{m}{s}\right];$$

- The initial conditions for scenario 1 are defined as:

$$\alpha_u(s,t_0) = c_{Lu}(s,t_0) = \begin{cases} 1, & \text{for } 0 \le s < 1, \\ 0, & \text{for } 1 \le s \le 6, \end{cases} \quad \text{and} \quad \alpha_l(s,t_0) = c_{Hl}(s,t_0) = \begin{cases} 0, & \text{for } 0 \le s < 1, \\ 1, & \text{for } 1 \le s \le 6, \end{cases}$$

- The initial conditions for scenario 2 are defined as:

$$\alpha_u(s,t_0) = c_{Lu}(s,t_0) = \begin{cases} 0, & \text{for } 0 \le s < 1, \\ 1, & \text{for } 1 \le s \le 6, \end{cases} \quad \text{and} \quad \alpha_l(s,t_0) = c_{Hl}(s,t_0) = \begin{cases} 1, & \text{for } 0 \le s < 1, \\ 0, & \text{for } 1 \le s \le 6, \end{cases}$$

- Dirichlet boundary conditions are assigned at the inlet of the pipe to give the flow variables its initial value at every time step. At the outlet the values of the flow variables in the ghost cells are approximated by its two predecessor cells. The BCs are only given for the first ghost next to the interior here;

$$\begin{aligned} u_{s,\beta_{-\frac{1}{2}}} &= u_{s,\beta_{-\frac{1}{2}}}(t_0) && \text{and} \quad u_{s,\beta_{N+\frac{3}{2}}} = 2u_{s,\beta_{N+\frac{1}{2}}} - u_{s,\beta_{N-\frac{1}{2}}} \\ \alpha_{u_0} &= \alpha_{u_0}(t_0) && \text{and} \quad \alpha_{u_{N+1}} = 2\alpha_{u_N} - \alpha_{u_{N-1}} \\ c_{B\beta_0} &= c_{B\beta_0}(t_0) && \text{and} \quad c_{B\beta_{N+1}} = 2c_{B\beta_N} - c_{B\beta_{N-1}} \end{aligned}$$

- The volumetric transfer terms are set at $\Psi_{L,lu} = \Psi_{H,lu} = 1\text{e-}05\left[\frac{m}{s}\right]$;
- $\mathscr{G}_{LH}$ is required for initial condition 1 and $\mathscr{G}_{HL}$ is required for initial condition 2;
- The threshold values used in the slip functions $\mathscr{F}$ and $\mathscr{G}_{B_1B_2}$ are $\varepsilon_1 = 0.3$ and $\varepsilon_2 = 2$ [7].

In Figs. 5.16, 5.17, 5.18 & 5.19 the results of the hold-up, velocity and volume fraction distributions for the two W-shaped pipe cases are presented. The figures are divided into two columns: (1) the left column is denoted by *LH*, as it represents initial condition 1 and (2) the right column is denoted by *HL* as it illustrates initial condition 2. The distributions of the flow variables are visualised at eight different time steps. The specific dimensionless time is found on the left of each plot. Note that the magnitude of the effective bubble velocity defined in equation (2.67) is the same for the upward- and downward-inclined sections.

The effective bubble velocity is filtered and set to zero in the regions where only one fluid is observed. The spikes of the effective bubble velocity function, which are seen in Fig. 5.17, are caused by the approximation of the densities at the cell edges by the central scheme. Typically, the densities will behave differently in upward- and downward-inclined sections, due to the flushing characteristics, causing the effective bubble velocity to change locally.

The volumetric transfer rate is set relatively low to better visualise the observed phenomena in the pipe section for the different flushing characteristics. As the phenomena are different for *LH* and *HL* in the inclined pipe section, their results are discussed separately, starting with the initial case *LH*.

5.3.1. Light fluid flushing a Heavy fluid - *LH*

The light fluid is positioned halfway of the first downward-inclined pipe section for initial condition 1. When the diaphragm is removed at t_0 the interface between the fluids will move towards its horizontal equilibrium position. As the buoyancy forces are working against the flushing characteristic, the heavy fluid is pushed out of the downward-inclined section with approximately the superficial velocity. When the upward-inclined section is reached, the upper region forms a bubble interface and the region is accelerated towards the top of the upward-inclined section, where the upper region accumulates until it is able to form an equilibrium interface and flushes out the lower region of the second downward-inclined section.

In the upward-inclined pipe section the superficial velocity is not able to conquer the effective bubble velocity and the lower region creates a separate region for itself in the section, as is explained and illustrated in the V-shaped section of Fig. 1.2 (a). The stagnant separate layer is visualised in Fig. 5.17, as the axial velocity of the lower region over this layer has become completely zero at $t^* = 175.1$. The light fluid, which is still flowing through the inlet arrives at the upward-inclined section and is instantly accelerated over the area of the lower region, as this stagnant layer reduces the total cross-sectional area of the pipe. Eventually, the separated layer of heavy fluid is removed from the upward-inclined section by diffusion and mass transfer. However, this has not happened during the total simulation time yet.

As the equilibrium interface moves down the pipe sections at approximately the superficial velocity, a slip velocity is barely seen at the downward-inclined sections. The equilibrium interface slowly descends in the second downward-inclined pipe for the last three time steps. At the last time step $t^* = 560.3$ the interface has reached the outlet and the hold-up of the upper region has become 1 over almost the entire section. In the part of the section where the hold-up has become entirely equal to one, the effective bubble velocity is zero, as an effective bubble velocity cannot exist in a region where only one fluid is active.

5.3.2. Heavy fluid flushing a Light fluid - *HL*

The heavy fluid is positioned halfway the first downward-inclined pipe section for initial condition 2. After the diaphragm has been removed, a bubble forms in the section. As the superficial velocity is not able to overcome the effective bubble velocity, back flow is observed; the upper region creates a separate layer inside the downward-inclined section and moves towards the inlet. The lower region is headed towards the bottom of the downward-inclined pipe section. When this section is reached, the lower region accumulates until it is able to push the light fluid out of the upward-inclined section; an equilibrium interface is formed which moves towards the top of this section with the superficial velocity.

Meanwhile, the upper region has reached the inlet and forms a separate region in the first downward-inclined section, where it is exposed to diffusion and mass transfer. As a consequence the density of the upper region becomes higher and the local effective bubble velocity does not exceed the superficial velocity anymore. As a result, the upper region is totally flushed out of the first downward-inclined and the upward-inclined sections.

The lower region has already arrived at the top of the upward-inclined pipe section in the meantime and directly forms a bubble interface with the available heavy fluid. As the superficial velocity is not able to overcome the effective bubble velocity in this section, the upper region remains in this part of the pipe. This layer is eventually diffused out of the section, but this is not observed within the current simulation time. Another phenomenon which is recognised at this separate layer, is the formation of small waves. This is visualised at the last time step $t^* = 560.3$ in the plots of Figs. 5.16, 5.17, 5.18 & 5.19.

It is not clear whether these waves (oscillations) are a physical or a numerical phenomenon. Nonetheless, the waves might provide a different mechanism for displacing the fluids, as they basically look like a Kelvin-Helmholtz instability, which is known to enhance mixing in a region. It would be remarkable if it is only a numerical phenomenon as the high resolution scheme is chosen to provide sufficient numerical accuracy. The scheme is known to prevent oscillations into regions where discontinuities are seen in the flow solution. To clarify this has to be investigated in physical experiments in a test facility.

5.3.3. Iterations

The averaged number of iterations per time step is approximately 19 for initial condition 1 and approximately 23 for initial condition 2. The evolution of the number of iterations per time step is plotted in Fig. 5.14 for both cases, and the residual of *LH* and *HL* are plotted in Fig. 5.15 at $t^* \approx 70.0$. The slopes of the residuals for *LH* are somewhat below one and do not achieve a linear convergence rate locally at $t^* = 70.0$. The slopes of the residuals of the hold-up and velocity variables are around 1.35 for *HL*, and its slopes of the residuals of the volume fraction variables are slightly above one at $t^* = 70.0$. The model exceeds a linear convergence rate and overachieves for Picard's method locally for *HL*.

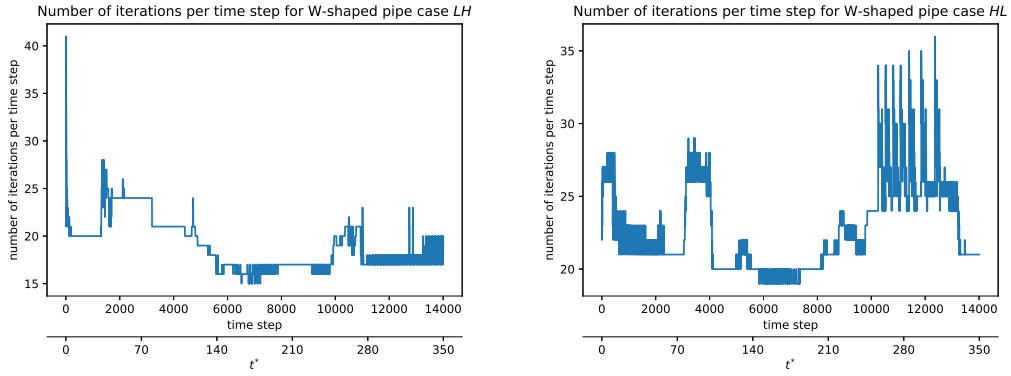

(a) The number of iterations per time step for case *LH*

(b) The number of iterations per time step for case *HL*

Figure 5.14: The number of iterations per time step is visualised in (a) and the residuals of the flow variables solved in the coupled matrix **A** are visualised in (b) for the Benjamin bubble pipe case *LH*.

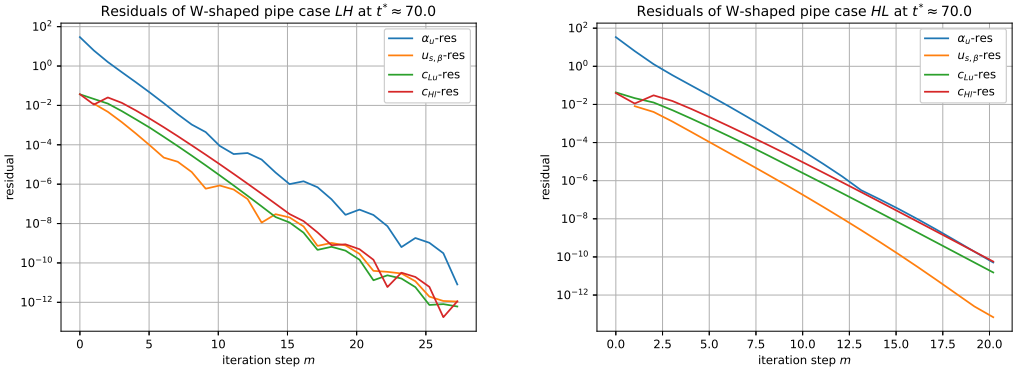

(a) Residuals for W-shaped pipe case *LH* at $t^* = 70.0$

(b) Residuals for W-shaped pipe case *HL* at $t^* = 70.0$

Figure 5.15: The residuals of the flow variables solved in the coupled matrix **A** for the W-shaped pipe case (a) *LH* and (b) *HL* at $t^* \approx 70.0$.

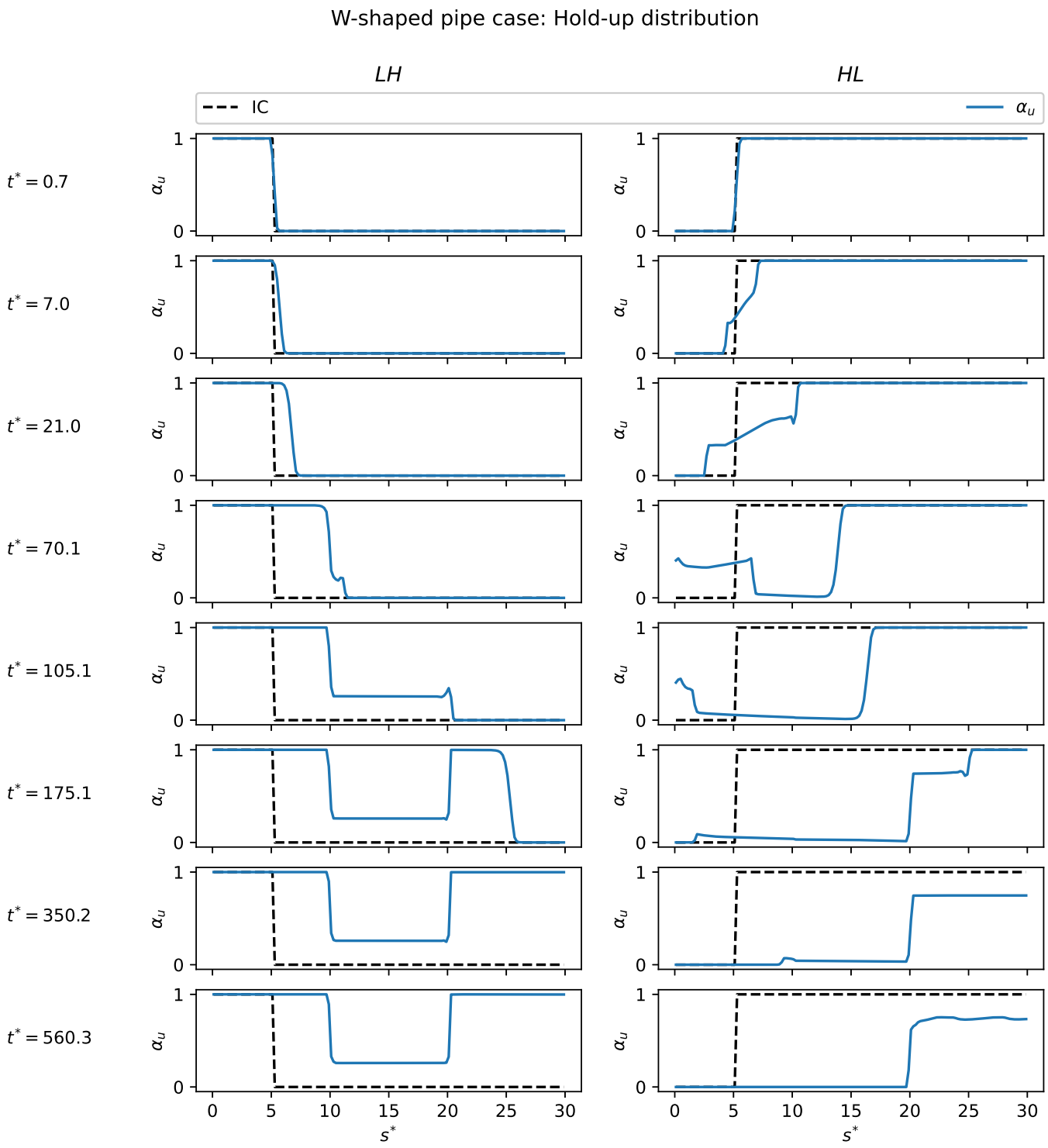

Figure 5.16: The distribution of the hold-up variables is visualised for two W-shaped pipe cases: *LH* and *HL*, The distributions of α_u are given at eight different time steps.

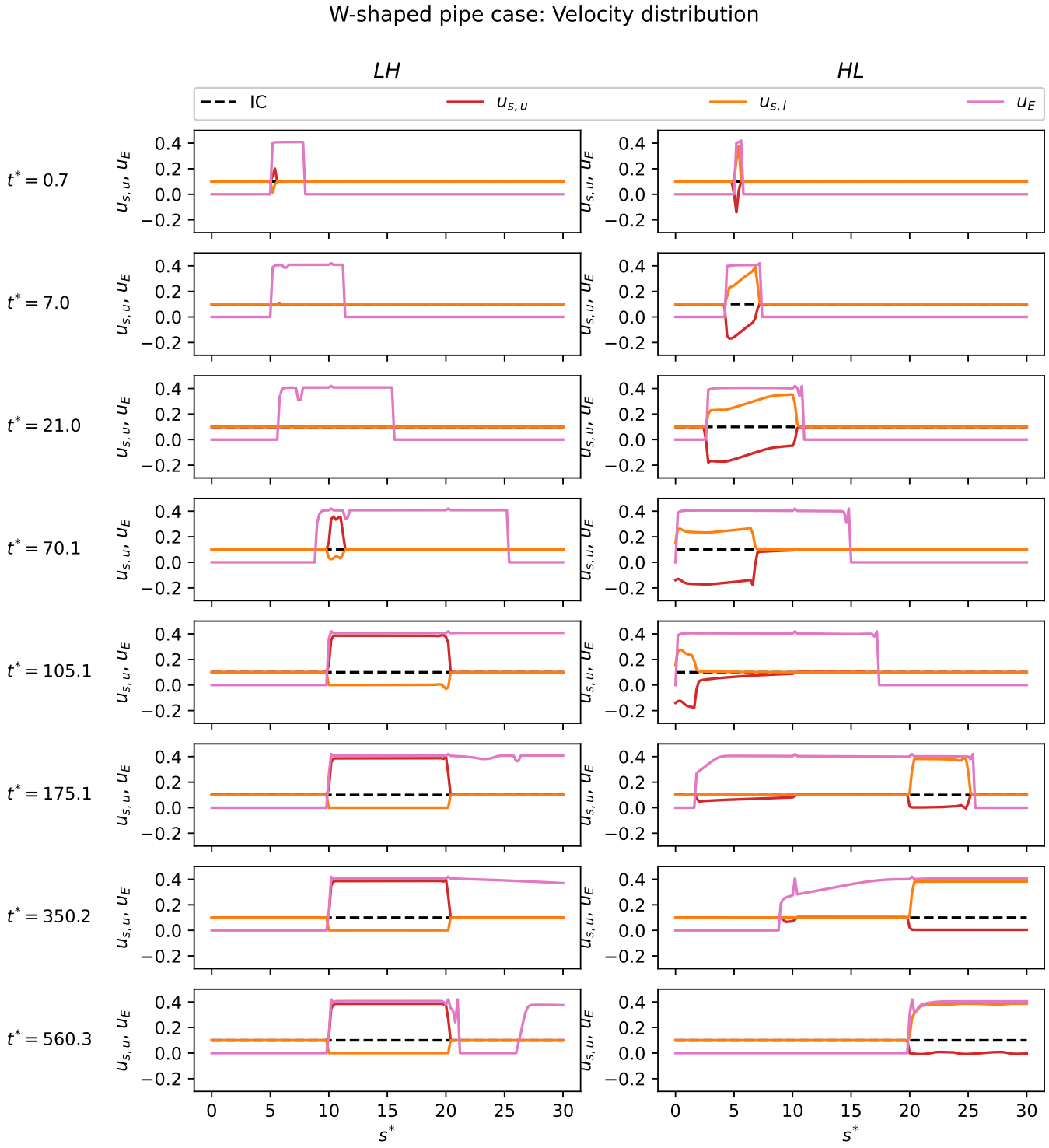

Figure 5.17: The distribution of the velocity variables is visualised for two W-shaped pipe cases: *LH* and *HL*, The distributions of $u_{s,u}$, $u_{s,l}$ and u_E are given at eight different time steps.

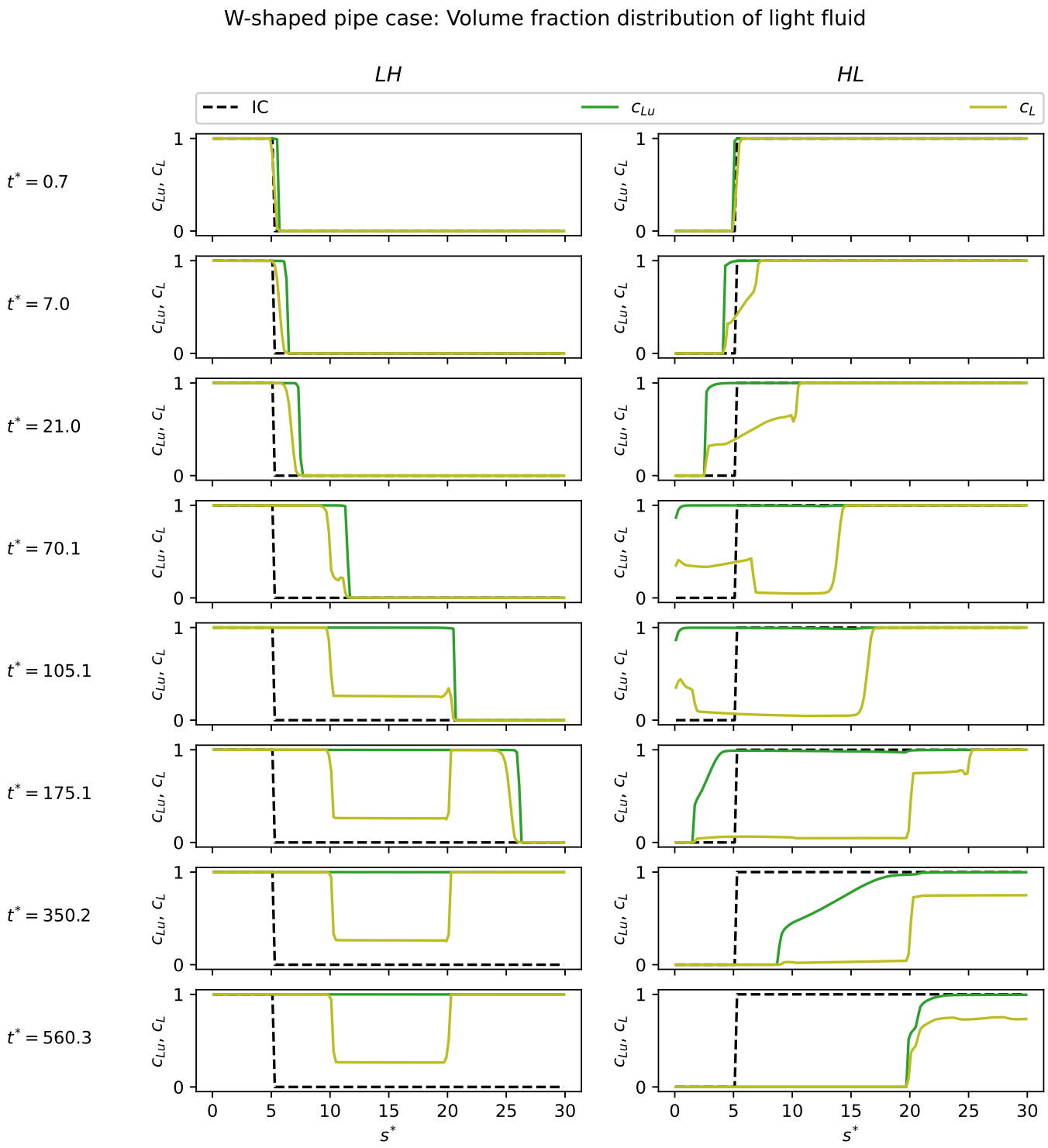

Figure 5.18: The distribution of the volume fraction variables of the light fluid is visualised for two W-shaped pipe cases: *LH* and *HL*, The distributions of c_{Lu} and c_L are given at eight different time steps.

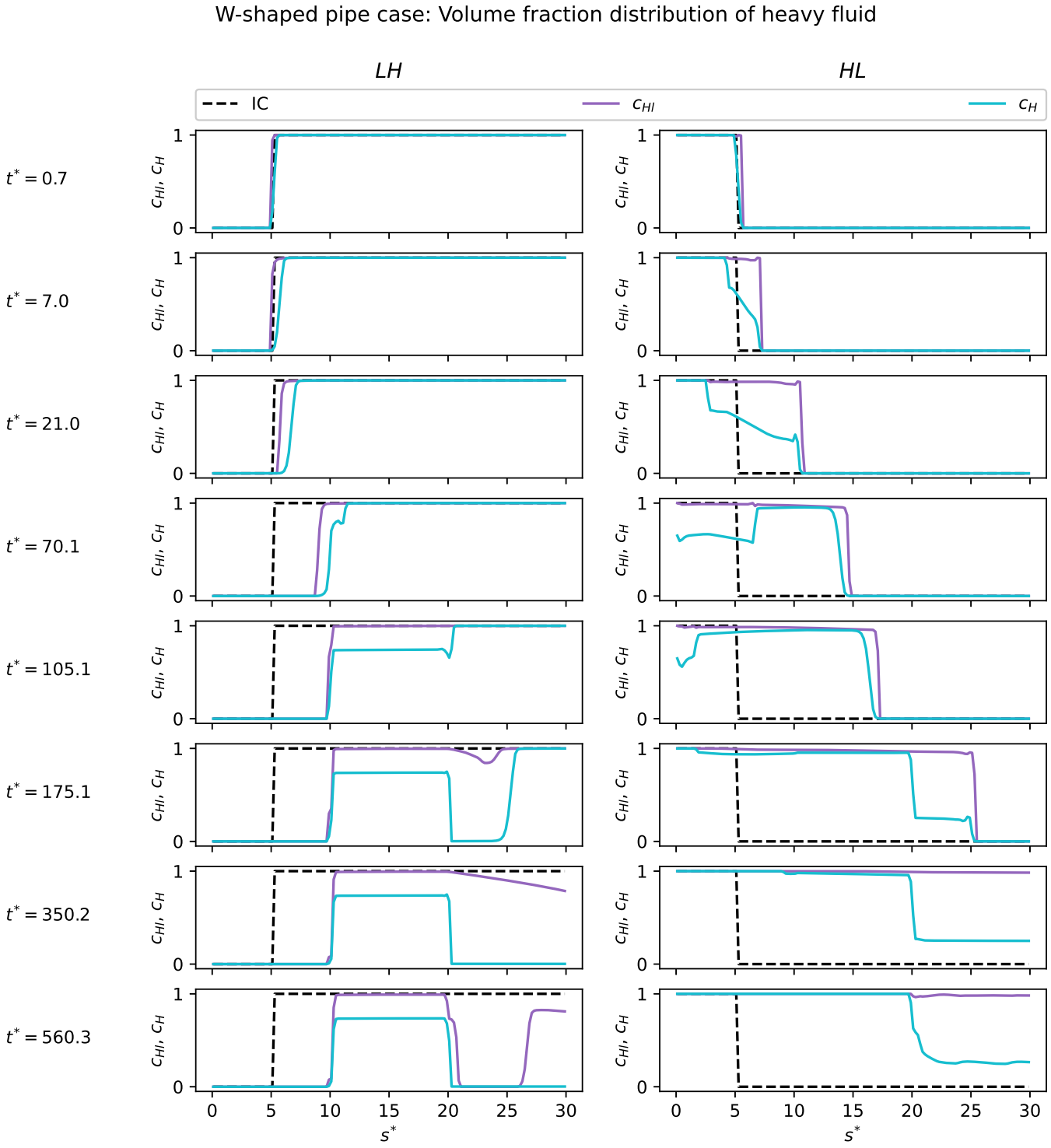

Figure 5.19: The distribution of the volume fraction variables of the light fluid is visualised for two W-shaped pipe cases: *LH* and *HL*, The distributions of c_{Hl} and c_H are given at eight different time steps.

5.4. Dellecase study

Dellecase performed experiments flushing fresh and salt water out of a jumper-like geometry with methanol [10]. The jumper-like geometry was illustrated in Fig. 1.6. The goal of this section is to use the Dellecase experiments to derive an empirical relation for the transfer terms $\Psi_{B,\beta_1\beta_2}$ of equation 3.66. To derive this relation, Dellecase's experimental results are required to match with the results of the numerical model in which the volumetric transfer terms are estimated upfront.

Dellecase presented his results by showing the volume fraction of methanol in the jumper-like geometry, after one jumper volume of methanol had been inserted at the inlet. One jumper volume of methanol is approximately equal to 34 gallons, i.e. $V \approx 0.1287\ [m^3]$. The superficial velocities of Dellecase's experiments are $u_s \approx 0.02, 0.06, 0.15$ and $0.30\ [\frac{m}{s}]$, of which the last three velocities are simulated by the numerical model. The case $u_s = 0.02\ [\frac{m}{s}]$ falls into the laminar flow domain and the model does not include a relation for a laminar axial dispersion coefficient. Therefore, the $u_s = 0.02\ [\frac{m}{s}]$ is excluded from the present analysis.

The jumper-like geometry has a total axial length of approximately 30 metres. However, simulating the whole Dellecase's jumper geometry would require too much computational power. Therefore, only half of the geometry is considered in this study. This corresponds with point 7 in Fig. 1.6, and with an axial length of approximately 15 metres. In Fig. 5.20 the half jumper-like geometry used within the model is plotted. For the exact lengths of all horizontal and vertical pipe sections within Dellecase's jumper-like geometry, the reader is referred to Dellecase [10].

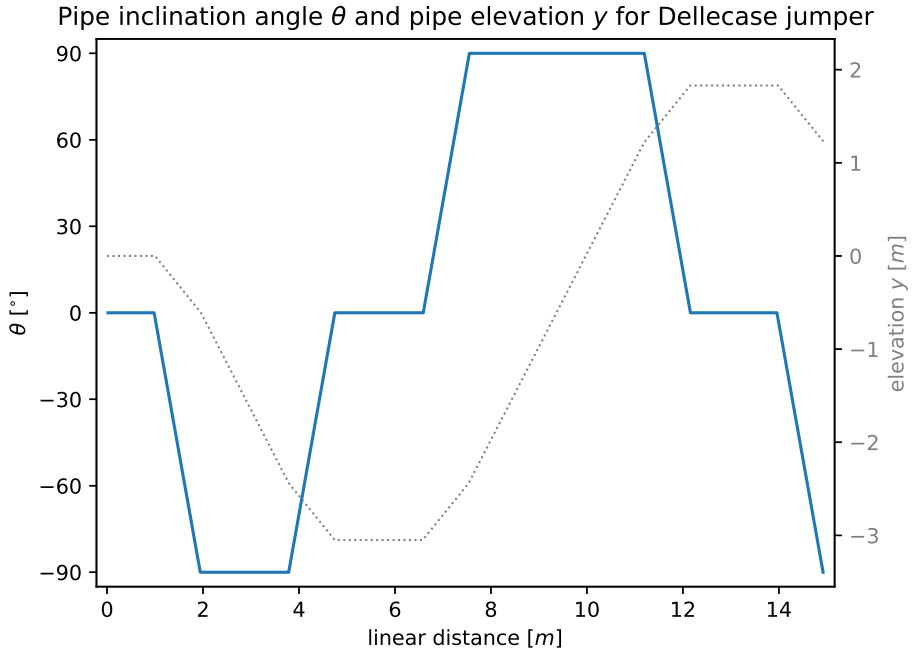

Figure 5.20: The pipe inclination angle θ and pipe elevation y are visualised for Dellecase's half jumper-like geometry used within the model.

5.4.1. Smoothening of slip relation functions

In Figs. 1.6 & 5.20 it is seen that the jumper geometry consists of so-called elbow corners. Within an elbow corner the flow is deflected from a horizontal orientation to a vertical orientation or vice versa; i.e. the pipe inclination angle moves from $\theta = 0 \longrightarrow \theta = -90$, $\theta = -90 \longrightarrow \theta = 0$, $\theta = 0 \longrightarrow \theta = 90$ or $\theta = 90 \longrightarrow \theta = 0$. The radius of the curvature at the elbow corner is $r = 0.61\ [m]$ in the jumper geometry which corresponds to an axial length of the elbow corner of $s_{\text{elbow}} \approx 0.958\ [m]$.

A limitation of the current model is that it has been derived for purely horizontal or purely inclined pipe geometries. No smooth transition exists in elbow corners where horizontal pipe sections are connected to inclined pipe geometries.

The slip relation functions change when the pipe inclination angle goes from $\theta = 0$ to $\theta \neq 0$:

- the hold-up function function $\mathscr{F}$ jumps from $\mathscr{F}_{\theta=0}$ to $\mathscr{F}_{\theta\neq 0}$;
- the interface function $\mathscr{G}_{LH}$ is equal to 1 for $\theta \geq 0$ and moves directly for $\theta < 0$ to its form illustrated in Fig. 3.9;
- the magnitude of the effective bubble velocity function u_E equals $u_B + u_F$ at $\theta = 0$. When $\theta \neq 0$, the magnitude of the effective bubble velocity is directly determined by the first condition of equation (3.54).

The simulation results of the current model showed sharp gradients of the flow variables when the elbow corners were entered or left by the flow solution. Moreover, the current implementation of the model showed slow convergence rates when the fluids are active in these transition geometries. These simulation results are not presented in this report.

To smoothen the flow solution when the fluids are entering or leaving the elbow corner and other slip relation functions are activated, the dosing relation of equation (3.30) is used. The dosing relation is introduced to gradually change the form of the slip relation functions at $\theta = 0$ to their form at $\theta \neq 0$ after a certain pipe inclination angle. This pipe inclination angle is defined as θ_{smooth}. It was investigated which θ_{smooth} resulted in the best convergence rates, and thereby helped the flow solution to reduce the sharp gradients observed at the elbow corners. It is found that a smoothening pipe inclination angle of $\theta_{\text{smooth}} = 15$ [°] gives the best results. The comparison between different smoothening angles is not given in this report. In Fig. 5.21 the modified slip relation functions are plotted between $\theta = 0$ and θ_{smooth}. Note that $\theta_{\text{smooth}} = \pm 15$ [°] is required for the slip relation functions $\mathscr{F}$ and u_E and that $\theta_{\text{smooth}} = -15$ [°] is sufficient for the interface function $\mathscr{G}_{LH}$.

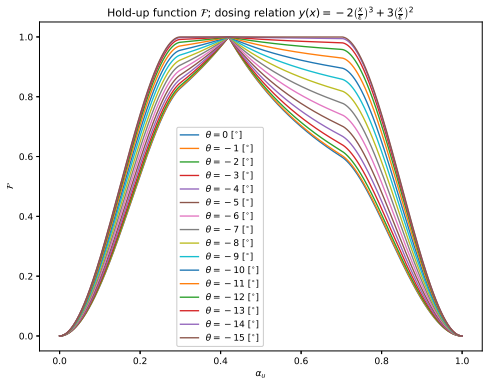

(a) Modified hold-up function $\mathscr{F}$

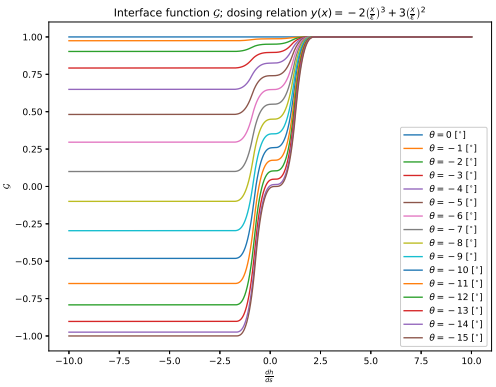

(b) Modified hold-up function $\mathscr{G}$

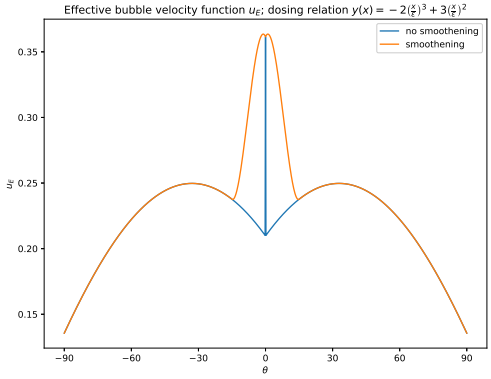

(c) Modified effective bubble velocity function u_E

Figure 5.21: The modified slip relation functions are visualised. In (a) the hold-up function $\mathscr{F}$ is illustrated for $\theta = [-15, 0]$, (b) the interface function $\mathscr{G}$ is illustrated between $\theta = [-15, 0]$, as well and (c) the effective bubble velocity function is presented for $\theta = [-90, 90]$

The simulation input parameters are summarised in the following overview:

- The thermodynamic properties of methanol denoted $(.)_L$ and fresh water denoted by $(.)_H$ at 20 degrees Celsius are:
$$\rho_L = 791.7 \left[\frac{kg}{m^3}\right] \quad \text{and} \quad \mu_L = 0.593\text{e-}03 \left[\frac{kg}{ms}\right]$$
$$\rho_H = 998.2 \left[\frac{kg}{m^3}\right] \quad \text{and} \quad \mu_H = 1.0005\text{e-}03 \left[\frac{kg}{ms}\right];$$
- The pipe radius is $R = 0.0381\ [m]$ which results in a hydraulic diameter of $D_H = 0.0762\ [m]$;
- The length of the pipe is $s_{\text{total}} \approx 14.94\ [m]$;
- The pipe inclination angle distribution is:
$$\theta = \begin{cases} 0\,[^\circ], & \text{for } 0 \le s < 1, \\ 0 \rightarrow -90\,[^\circ], & \text{for } 1 \le s < 1.958, \\ -90\,[^\circ], & \text{for } 1.958 \le s < 3.788, \\ -90 \rightarrow 0\,[^\circ], & \text{for } 3.788 \le s < 4.746, \\ 0\,[^\circ], & \text{for } 4.746 \le s < 6.576, \\ 0 \rightarrow 90\,[^\circ], & \text{for } 6.576 \le s < 7.535, \\ 90\,[^\circ], & \text{for } 7.535 \le s < 11.19, \\ 90 \rightarrow 0\,[^\circ], & \text{for } 11.19 \le s < 12.15, \\ 0\,[^\circ], & \text{for } 12.15 \le s < 13.98, \\ 0 \rightarrow -90\,[^\circ], & \text{for } 13.98 \le s \le 14.94, \end{cases}$$
this pipe inclination angle distribution results in the distribution which is plotted in Fig. 5.20;
- The total number of cells is $N = 374$, this yields $\Delta s \approx 0.04\ [m]$;
- The Courant number is set at $Co = 0.5$, instead of $Co = 0.5$ to reduce the simulation length. This generates a time step of $\Delta t = 0.02317\ [s]$; the time step is the same for all three cases, as their superficial velcotity is below the gravitational velocity; $u_s < u_g$;
- The total simulation time differs per case and depends on the specific volumetric flow rate, the cross-sectional area and the total volume of the displacement flushing fluid. The total simulation time per case is given here:
$$u_s = 0.06 \left[\frac{m}{s}\right];\ Re_{\text{mix}} = 5135.5; \quad \rightarrow \quad t = 449.4\,[s],$$
$$u_s = 0.15 \left[\frac{m}{s}\right];\ Re_{\text{mix}} = 12839; \quad \rightarrow \quad t = 179.7\,[s],$$
$$u_s = 0.30 \left[\frac{m}{s}\right];\ Re_{\text{mix}} = 25677; \quad \rightarrow \quad t = 89.88\,[s];$$
- The magnitudes of the Benjamin, Taylor and water front velocities within the geometry are:
$$u_B = 0.2133 \left[\frac{m}{s}\right], \quad u_T = 0.1379 \left[\frac{m}{s}\right], \quad u_F = 0.1543 \left[\frac{m}{s}\right];$$
- The initial conditions are defined as:
$$\alpha_u(s, t_0) = c_{Lu}(s, t_0) = 0, \text{ for entire interior} \quad \text{and} \quad \alpha_l(s, t_0) = c_{Hl}(s, t_0) = 1, \text{ for entire interior};$$
the entire volume of Dellecase's half jumper-like geometry is filled with fresh water;
- Dirichlet boundary conditions are assigned at the inlet of the pipe to give the flow variables its initial value at every time step. At the outlet the values of the flow variables in the ghost cells are approximated by its two predecessor cells. The BCs are only given for the first ghost next to the interior here;
$$u_{s,\beta_{-\frac{1}{2}}} = u_{s,\beta_{-\frac{1}{2}}}(t_0) \quad \text{and} \quad u_{s,\beta_{N+\frac{3}{2}}} = 2u_{s,\beta_{N+\frac{1}{2}}} - u_{s,\beta_{N-\frac{1}{2}}}$$
$$\alpha_{u_0} = \alpha_{u_0}(t_0) \quad \text{and} \quad \alpha_{u_{N+1}} = 2\alpha_{u_N} - \alpha_{u_{N-1}}$$
$$c_{B\beta_0} = c_{B\beta_0}(t_0) \quad \text{and} \quad c_{B\beta_{N+1}} = 2c_{B\beta_N} - c_{B\beta_{N-1}};$$

- The volumetric transfer terms are matched to the Dellecase's experimental results and are given per case;
- $\mathscr{G}_{LH}$ is required in the simulations;
- The threshold values used in the slip functions $\mathscr{F}$ and $\mathscr{G}_{B_1B_2}$ are $\varepsilon_1 = 0.3$ and $\varepsilon_2 = 2$ [7].

Note that the dimensionless time t^* and axial distance s^* are not used for the Dellecase study, as the simulation results of the numerical model are directly compared with Dellecase experimental results. However, a new dimensionless time is introduced to compare the three different cases with each other. The dimensionless time τ is defined as the simulation time of the cases divided by its total simulation time; i.e. an equivalent τ implies that the relative amount of inserted methanol is equal for the three volumetric flow cases and $\tau = 1$ corresponds to one jumper volume of methanol which is inserted into the system.

5.4.2. Volumetric transfer term Ψ

The averaged methanol concentration is the only available quantity in the Dellecase experiments at $\tau = 1$ at the numbered locations illustrated in Fig. 1.6. This makes it hard to match the simulation results to Dellecase's experimental results. Ideally, transient data are needed to see the behaviour of the methanol concentration at these fixed points. Therefore, the transient data of the methanol concentration in Dellecase's jumper-like geometry has been reproduced by a CFD model as a part of this study. A more detailed description of how this CFD model is built up is given together with an overview of the CFD simulation results in Appendix C.

In this section, the numerical model is matched to the Dellecase experimental results and to the CFD results making a comparison in the middle the first low spot. This corresponds to the axial distance $s \approx 5.66$ $[m]$ from the inlet of the half jumper geometry, which is point 2 in Fig. 1.6.

Superficial velocity case: $u_s = 0.06 \left[\frac{m}{s}\right]$ In Fig. 5.23 the transient methanol concentration is given for the CFD simulations and the numerical model simulations at the first low spot until $\tau = 1$. The Dellecase experimental point is given as well. This superficial velocity case $u_s = 0.06 \left[\frac{m}{s}\right]$ has proven to be the only case where a match is found for both the CFD results and the Dellecase experimental results with the numerical model. Three different Ψ values plotted in Fig. 5.23 are $\Psi = 0$, $\Psi =$ 8e-06 and $\Psi =$ 9e-06 $\left[\frac{m}{s}\right]$. Here, Ψ denotes the volumetric transfer term $\Psi_{B,\beta_1\beta_2}$ which is not used for readability. Ψ is initiated in the model and is active in the pipe sections where both fluids are present.

$\Psi = 0 \left[\frac{m}{s}\right]$ is the reference case of the numerical model in which only turbulent dispersion is responsible for the mixing of the fluids. It is observed that the numerical model reproduces a stratified layer for this reference case. This layer remains in the first low spot even after one full jumper volume of methanol has been displaced in the geometry. $\Psi =$ 8e-06 $\left[\frac{m}{s}\right]$ perfectly matches the data point of the Dellecase experiments and $\Psi =$ 9e-06 $\left[\frac{m}{s}\right]$ is in line with the CFD results at $\tau = 1$ when the stratified layer has totally disappeared in the low spot. These results are also in line with the conclusions made for the CFD simulations; the CFD model slightly overpredicts the mass transfer and turbulent dispersion in the simulations.

Superficial velocity case: $u_s = 0.15 \left[\frac{m}{s}\right]$ In Fig. 5.24 the transient methanol concentration is given for the CFD simulations and the numerical model simulations at the first low spot until $\tau = 1$. The experimental data point of Dellecase is given in this figure as well. It is shown that the reference case of the numerical model $\Psi = 0 \left[\frac{m}{s}\right]$ predicts a stratified layer in the first low spot, which has disappeared before τ has reached a value of one. It is found that $\Psi =$ 8e-05 $\left[\frac{m}{s}\right]$ matches the CFD results at a methanol concentration of one.

Superficial velocity case: $u_s = 0.30 \left[\frac{m}{s}\right]$ In Fig. 5.25 the transient methanol concentration is given for the CFD simulations and the numerical model simulations at the first low spot until $\tau = 1$ together with the experimental data point of Dellecase. It is observed that the numerical model predictions are already in line with the CFD results for $\Psi = 0 \left[\frac{m}{s}\right]$. Therefore, a clear match for a Ψ greater than zero cannot be made for this superficial velocity case.

Unfortunately, at least three matched Ψ values are required to derive the intended empirical relation of equation (3.66). Therefore, it is decided to derive a linear relation for Ψ based on the two matched Ψ values of the superficial velocity cases $u_s = 0.06$ and $u_s = 0.15 \left[\frac{m}{s}\right]$. In this relation the Ψ term is non-dimensionalised by the superficial velocity and is a function of the mixture Reynolds number.

The linear relation of the non-dimensionalised volumetric transfer term Ψ^* is defined as:

$$\Psi^* = \frac{\Psi}{u_s} = 4.976\text{e-}08 \cdot Re_{\text{mix}} - 1.055\text{e-}04. \tag{5.1}$$

This linear empirical relation of the Ψ term is plotted in Fig. 5.22. In this plot the matched Ψ terms are also included. Using the relation, the estimated volumetric transfer term for the superficial velocity case $u_s = 0.30$ $\left[\frac{m}{s}\right]$ is Ψ = 3.516e-04 $\left[\frac{m}{s}\right]$ and is included in Fig. 5.25. It is shown that this high transfer term results in smoothening of the methanol concentration and does not allow a stratified layer to form at the low spot.

Note that the empirical relation slightly overestimates the volumetric transfer term, as it is based on the CFD results of the Dellecase experiments. However, the linear empirical relation provides a first good estimation to predict the volumetric transfer term of a methanol - fresh water mixture as a function of the mixture Reynolds number. Nonetheless, it is expected that Ψ would show nonlinear behaviour for an increasing Re_{mix}. To derive such a nonlinear empirical relation for Ψ a new miscible fluid-fluid displacement case is required for which transient data is available.

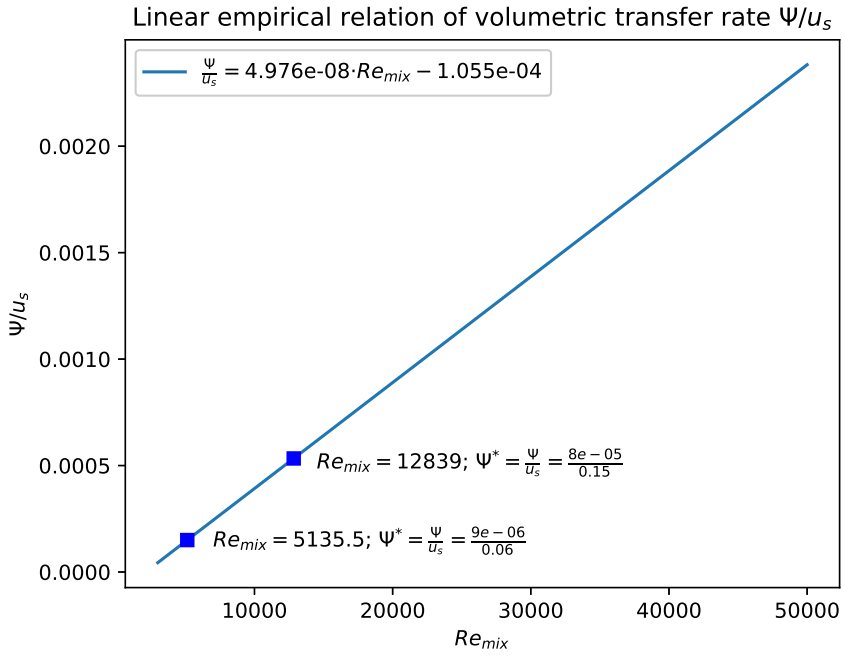

Figure 5.22: The derived linear empirical relation of the volumetric transfer term is visualised between $Re_{\text{mix}} = 3,000$ and $Re_{\text{mix}} = 50,000$. The volumetric transfer term Ψ are non-dimensionalised by the superficial velocity u_s.

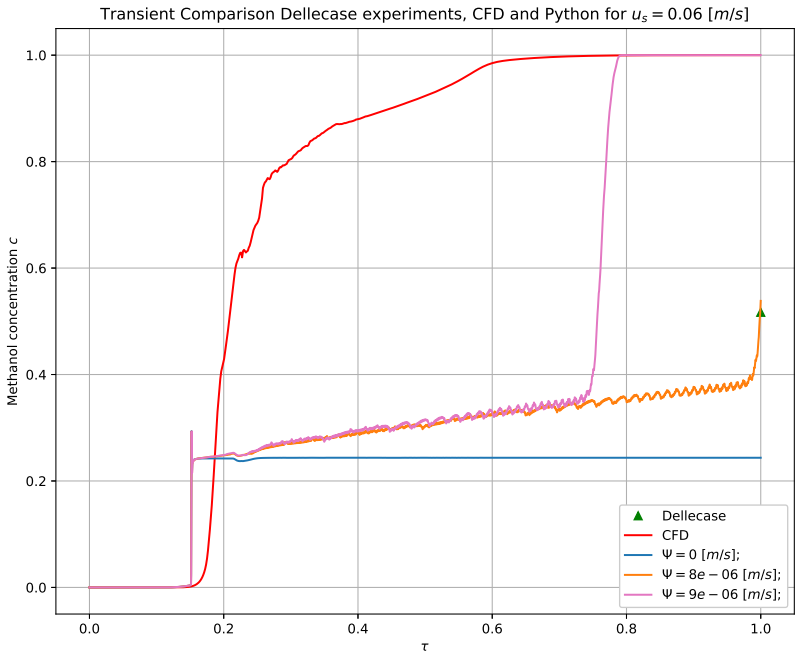

Figure 5.23: The transient methanol concentration profile for the CFD and numerical model are presented for the superficial velocity case $u_s = 0.06$ $\left[\frac{m}{s}\right]$ at the middle of the first low spot of the jumper geometry. At $\tau = 1$ the experimental results of Dellecase are added.

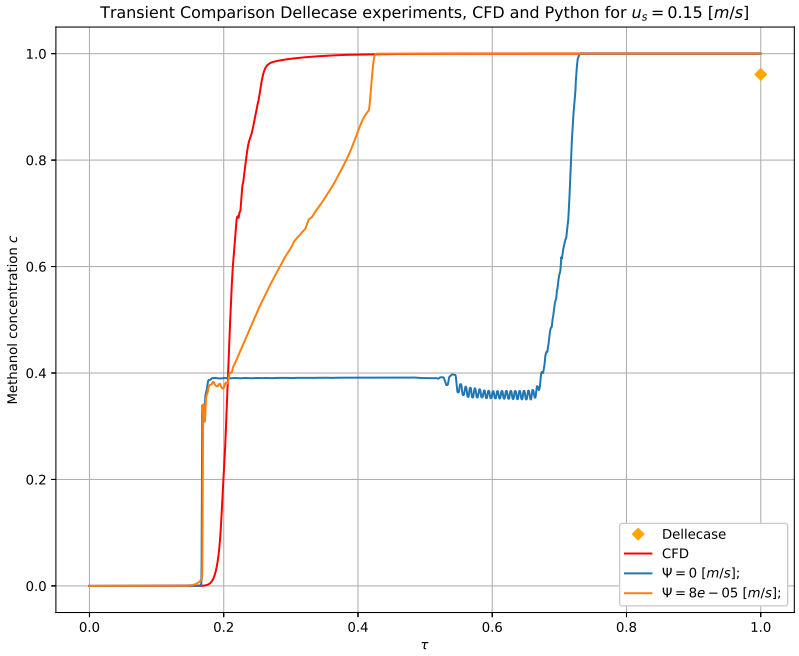

Figure 5.24: The transient methanol concentration profile for the CFD and numerical model are presented for the superficial velocity case $u_s = 0.15$ $\left[\frac{m}{s}\right]$ at the middle of the first low spot of the jumper geometry. At $\tau = 1$ the experimental results of Dellecase are added.

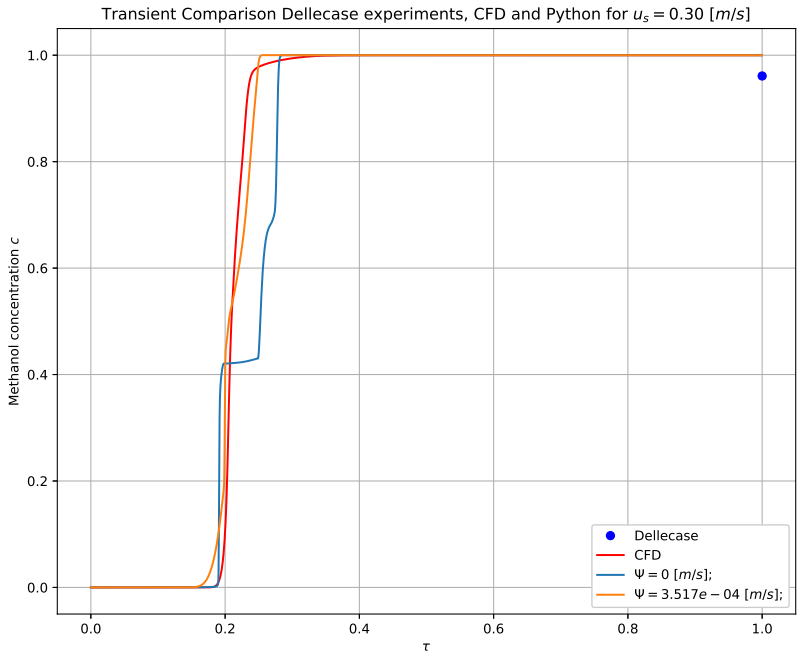

Figure 5.25: The transient methanol concentration profile for the CFD and numerical model are presented for the superficial velocity case $u_s = 0.30 \left[\frac{m}{s}\right]$ at the middle of the first low spot of the jumper geometry. At $\tau = 1$ the experimental results of Dellecase are added.

5.4.3. Flow variable distributions

In Figs. 5.28, 5.30 & 5.32 the hold-up and velocity distribution are plotted for all Dellecase simulations. To underline the difference between the zero Ψ and the nonzero Ψ terms, the hold-up distribution is given for the zero volumetric transfer terms and nonzero terms. This resulted in a match with the CFD results. These data are only plotted for the hold-up variables. For the $u_s = 0.06 \left[\frac{m}{s}\right]$ case the hold-up distribution of the match between the numerical model and the Dellecase experiments is visualised as well. In the legend of the figures it is indicated which hold-up distribution corresponds to which Ψ term. The velocity distribution corresponds to the volumetric transfer terms which are reported in the title of the figure.

In Figs. 5.29, 5.31 & 5.33 the volume fraction distribution of the light and heavy fluid are plotted for all Dellecase simulations. These volume fraction variables are only illustrated for the Ψ term which is reported in the title of the figure. The distribution of the three Dellecase simulations are given at different dimensionless times τ are compared to each other, as the cases show other flow phenomena at different time steps.

Superficial velocity case: $u_s = 0.06 \left[\frac{m}{s}\right]$ The hold-up distributions of the $u_s = 0.06 \left[\frac{m}{s}\right]$ case of the three different Ψ terms coincide with each other up to $\tau \approx 0.4$. After the methanol has reached the outlet and has created separated layers of methanol and fresh water, the mass and volumetric transfer between regions become important in the jumper geometry. At $\tau = 0.7$ and $\tau = 1$ the deviations in the hold-up distribution of the nonzero Ψ term with the zero Ψ term are clearly shown. Surface waves are seen in the stratified layers, like in the W-shaped pipe case of Section 5.3. For Ψ = 9e-06 $\left[\frac{m}{s}\right]$ the methanol has just flushed out the fresh water of the low spot and its subsequent elbow corner at $\tau = 1$.

At $\tau = 0.02$ the methanol has just reached the first elbow corner which directs the flow to a downward vertical pipe section. The methanol accumulates at the beginning of the elbow, and as the water front velocity is higher than the superficial velocity, a gravity current is moving from the elbow corner towards the inlet. This gravity current pushes out the fresh water of the stratified layer at the first horizontal level. Gravity current is illustrated by a negative axial velocity of the lower region in the velocity distribution at $\tau = 0.02$ and $\tau = 0.04$.

The behaviour of the velocity variables in the downward vertical pipe section is opposite to its behaviour in the horizontal and upward vertical pipe sections. As buoyancy works against the flushing characteristic, the heavy fluid wants to move upwards. As a consequence, the axial velocity of the lower region is locally larger than the axial velocity of the upper region. The axial velocity of the upper region can even become negative at specific locations. This behaviour is seen in the velocity distributions at $\tau = 0.04$ and $\tau = 0.1$.

In between $\tau = 0.1$ and $\tau = 0.4$ stratified layers have formed from the low spot until the last elbow corner. In the last elbow corner the methanol re-accumulates and pushes out the fresh water. In the stratified layers the mass transfer will take place. It is seen at $\tau = 0.7$ that the volume fraction of the light heavy fluid particles in the lower region is decreasing in the segregated flow area. Due to the decreasing volume fraction, the magnitude of density of the lower region becomes less and the effective bubble velocity becomes less as well. Eventually, the superficial velocity is able to locally overcome the effective bubble velocity and the stratified layer is broken up. Simultaneously, the total volume fraction of the light fluid increases, whereas the total volume fraction of heavy fluid decreases.

Superficial velocity case: $u_s = 0.15 \left[\frac{m}{s}\right]$ The hold-up distributions of the $u_s = 0.15 \left[\frac{m}{s}\right]$ case only coincide at $\tau = 0.02$. After the methanol has accumulated at the first elbow corner, the hold-up of the upper region shows different flow phenomena for the case of $\Psi = 0 \left[\frac{m}{s}\right]$ and the case of $\Psi =$ 8e-05. A gravity current of fresh water is observed for the case of $\Psi = 0 \left[\frac{m}{s}\right]$ which slowly moves towards the inlet. Here, the water front velocity is associated with lower region is somewhat higher than the superficial velocity. This causes the slow backflow movement of the water bubble. The case of $\Psi =$ 8e-05 $\left[\frac{m}{s}\right]$ does not show that behaviour. The mass transfer causes an immediate decrease in the magnitude of the effective bubble velocity in the stratifed layer of the first horizontal pipe section. The surface waves are observed again and the methanol is able to flush out the fresh water directly from the inlet.

At $\tau = 0.1$, the methanol is in the downward vertical pipe section and the same behaviour is observed as in the $u_s = 0.06 \left[\frac{m}{s}\right]$ case. The axial velocity of the upper region becomes smaller than the axial velocity of the lower region, and can even become negative. The fresh water is flushed out of the pipe section with the superficial velocity.

It is seen in the hold-up distribution at $\tau = 0.2$ and $\tau = 0.4$ that the magnitude of the hold-up of the upper region for the nonzero Ψ case is less than for the zero case. This causes the magnitude of the effective bubble velocity to be less as well. Combined with the low value of volume fraction of the heavy fluid particles in the lower region, the stratified layer is quickly flushed out of the low spot. Again the surface waves are spotted in the stratified layer before it is removed out of this pipe section for both Ψ cases.

The local values of the effective bubble velocity decrease even further as the methanol has continued its way to the upward vertical pipe section and the attached elbow corners under the influence of the volume fraction of the heavy fluid particles. The stratified layers get flushed out quickly of these pipe sections at $\tau = 0.6$ and $\tau = 0.8$. Eventually, the fresh water has been removed totally from the jumper geometry at $\tau = 1$ resulting in a jumper full of methanol.

Superficial velocity case: $u_s = 0.30 \left[\frac{m}{s}\right]$ The hold-up distributions of both Ψ terms for the $u_s = 0.15 \left[\frac{m}{s}\right]$ case show similar behaviour up to the time when the first low spot is reached by the methanol. Here, the high volumetric transfer term does not allow a stratified layer to develop as shortly as for the case of $\Psi = 0 \left[\frac{m}{s}\right]$ case which is seen at $\tau = 0.2$.

The volume fraction of heavy fluid particles of the lower region needs less time to get dispersed over the pipe sections for the high volumetric transfer terms case than for the zero Ψ case. As a consequence, the magnitude of the effective bubble velocity is lowered over these pipe sections and the fresh water is rapidly flushed out of the pipe sections for the $\Psi =$ 3.516e-04 $\left[\frac{m}{s}\right]$. At $\tau = 0.6$ the fresh water has been removed almost entirely from the jumper geometry and only methanol remains in the pipe sections at $\tau = 1$.

5.4.4. Iterations

In Fig. 5.26 the number of iterations per time step is visualised for the three simulated Dellecase cases. Remarkably, the $u_s = 0.06$ $\left[\frac{m}{s}\right]$ case results in three time steps in which no convergence was found by the solver for all Ψ terms. This is illustrated by the peaks in Fig. 5.26a. It was investigated what caused the failing convergence for these time steps. Unfortunately, no explanation was found. The case was simulated with $Co = 0.25$ to see if halving the time step would solve this issue, but it also included some time steps in which no convergence was found. As no instabilities are seen in the flow solution which grow in time, the simulated $u_s = 0.06$ $\left[\frac{m}{s}\right]$ case is assumed to be valid. In the $u_s = 0.15$ and $u_s = 0.30$ $\left[\frac{m}{s}\right]$ cases, convergence is found in all time steps.

The residuals of the flow variables of the Dellecase simulations are given at $\tau = 0.5$ in Fig. 5.27. The slopes of the residuals are all close to a value of one which corresponds to Picard's method.

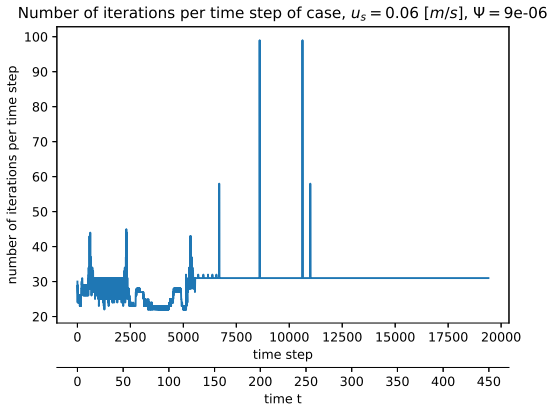

(a) Number of iterations per time step of case $u_s = 0.06$ $\left[\frac{m}{s}\right]$ and $\Psi = 9e\text{-}06$ $\left[\frac{m}{s}\right]$

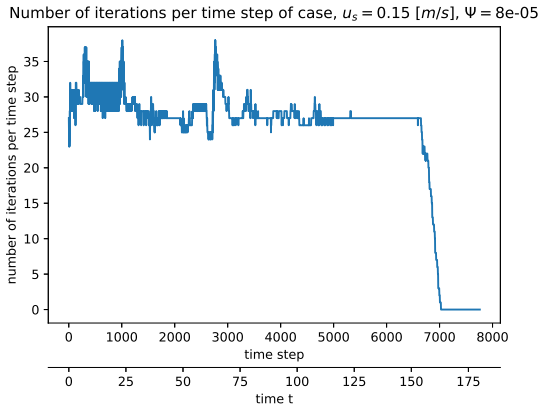

(b) Number of iterations per time step of case $u_s = 0.15$ $\left[\frac{m}{s}\right]$ and $\Psi = 8e\text{-}05$ $\left[\frac{m}{s}\right]$

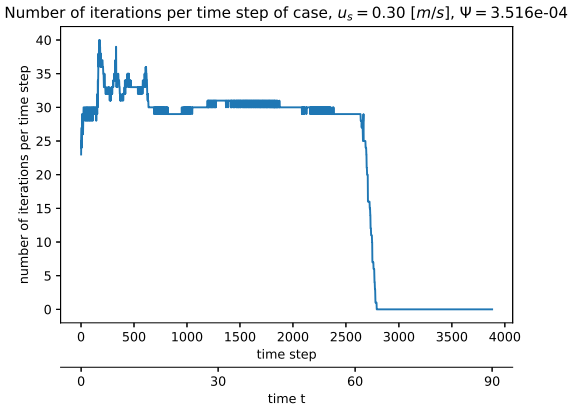

(c) Number of iterations per time step of case $u_s = 0.30$ $\left[\frac{m}{s}\right]$ and $\Psi = 3.516e\text{-}04$ $\left[\frac{m}{s}\right]$

Figure 5.26: The number of iterations per time step is visualised for the cases (a) $u_s = 0.06$ $\left[\frac{m}{s}\right]$ and $\Psi = 9e\text{-}06$ $\left[\frac{m}{s}\right]$, (b) $u_s = 0.15$ $\left[\frac{m}{s}\right]$ and $\Psi = 8e\text{-}05$ $\left[\frac{m}{s}\right]$ and (c) $u_s = 0.30$ $\left[\frac{m}{s}\right]$ and $\Psi = 3.516e\text{-}04$ $\left[\frac{m}{s}\right]$.

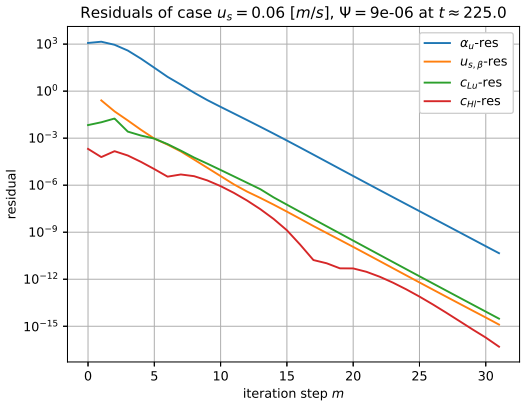

(a) Residuals of case $u_s = 0.06$ $[\frac{m}{s}]$ and $\Psi = 9e\text{-}06$ $[\frac{m}{s}]$

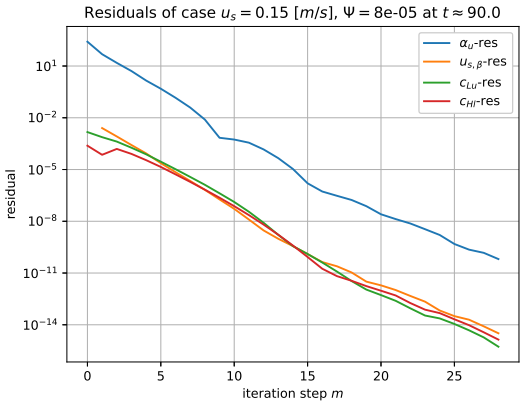

(b) Residuals of case $u_s = 0.15$ $[\frac{m}{s}]$ and $\Psi = 8e\text{-}05$ $[\frac{m}{s}]$

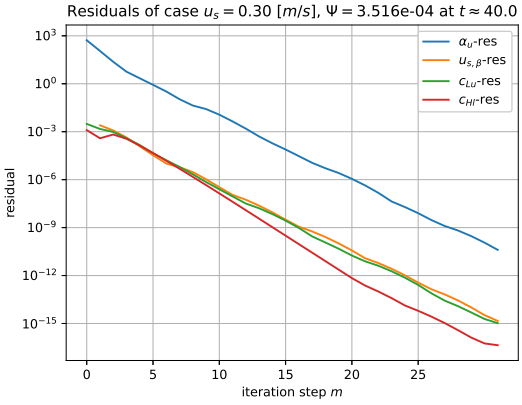

(c) Residuals of case $u_s = 0.30$ $[\frac{m}{s}]$ and $\Psi = 3.516e\text{-}04$ $[\frac{m}{s}]$

Figure 5.27: The residuals are visualised for the cases (a) $u_s = 0.06$ $[\frac{m}{s}]$ and $\Psi = 9e\text{-}06$ $[\frac{m}{s}]$, (b) $u_s = 0.15$ $[\frac{m}{s}]$ and $\Psi = 8e\text{-}05$ $[\frac{m}{s}]$ and (c) $u_s = 0.30$ $[\frac{m}{s}]$ and $\Psi = 3.516e\text{-}04$ $[\frac{m}{s}]$.

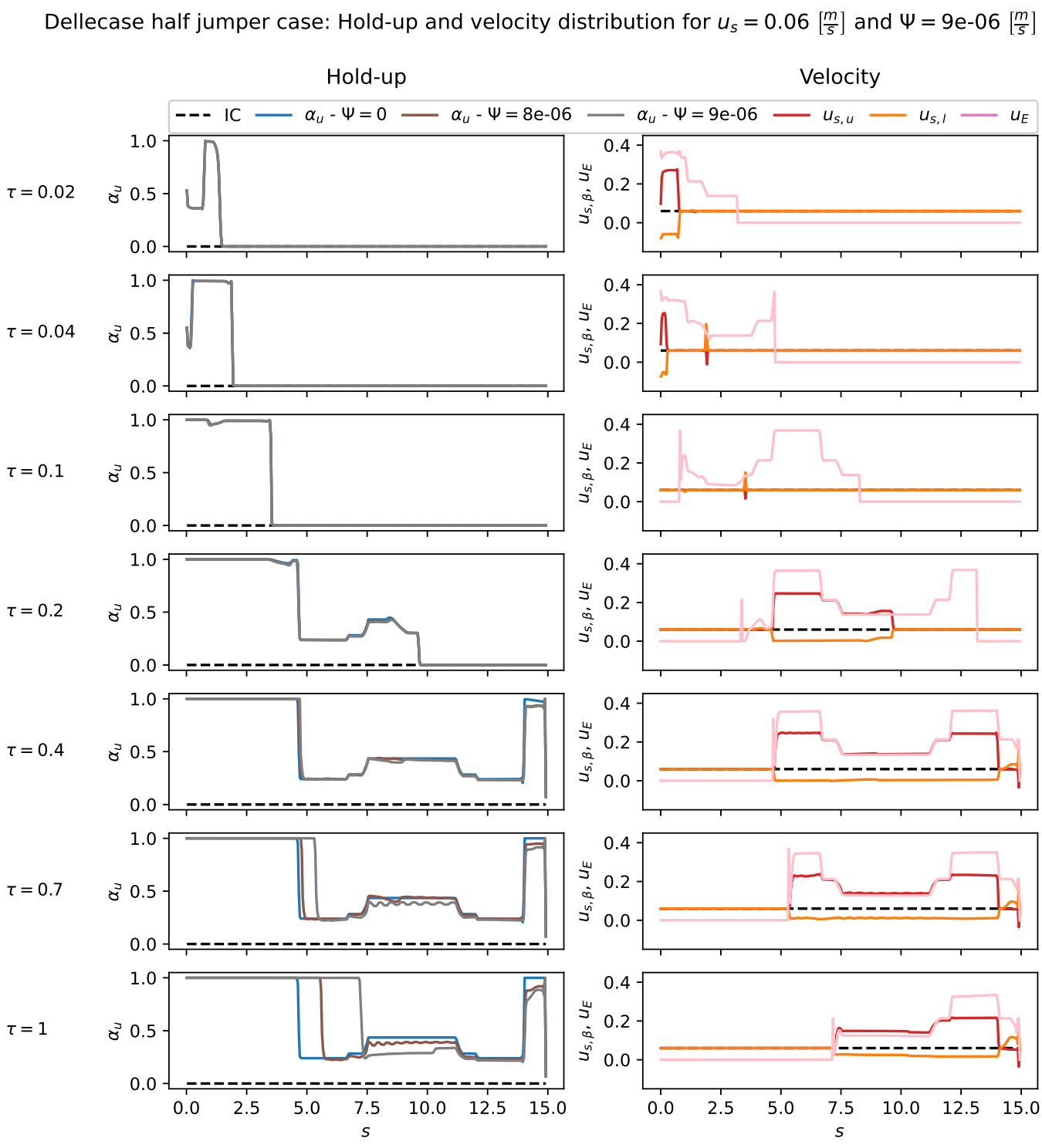

Figure 5.28: The distributions of the hold-up and the velocity variables are visualised for the Dellecase case: $u_s = 0.06$ $[\frac{m}{s}]$. The distributions are given at seven time steps.

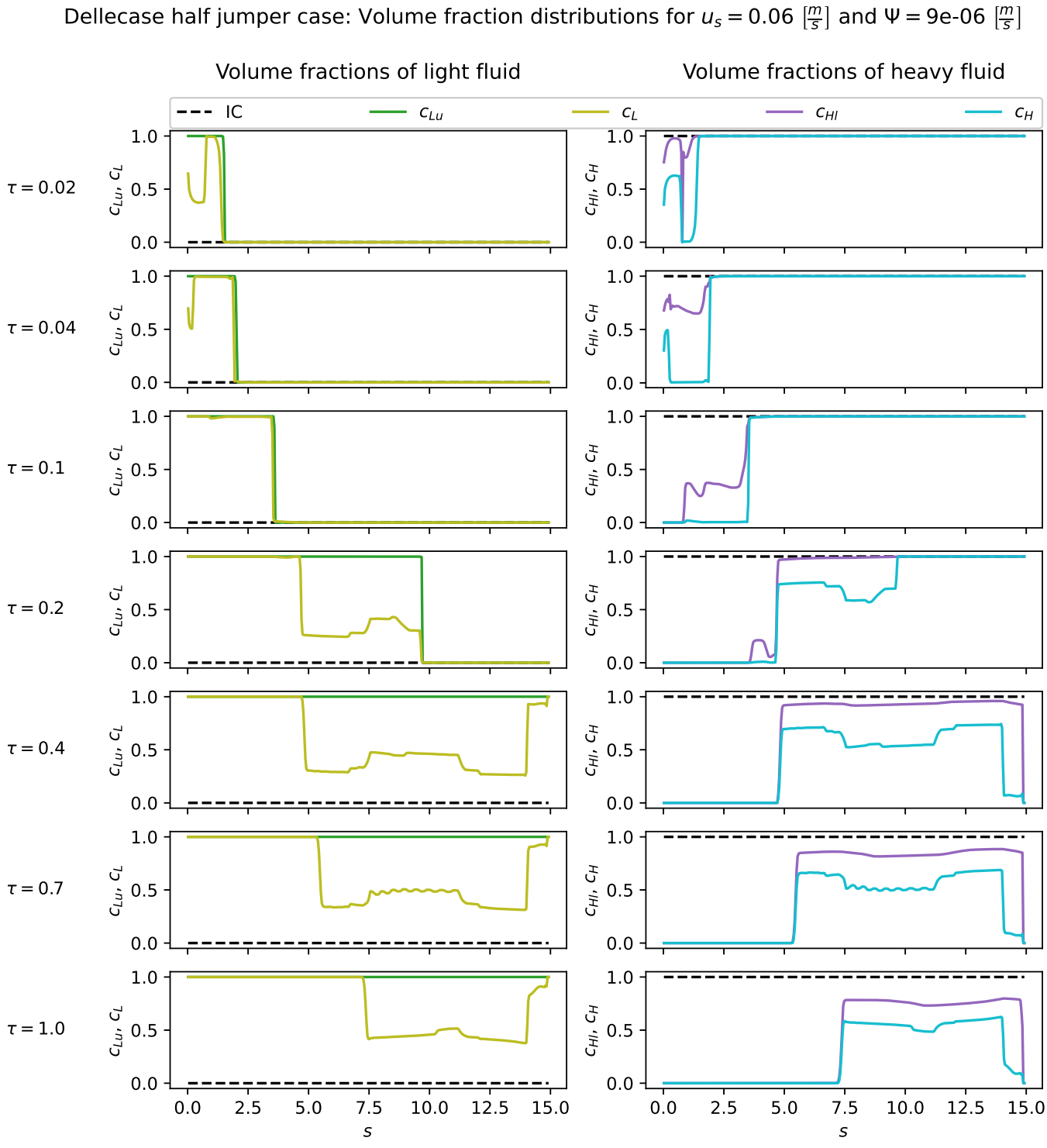

Figure 5.29: The distributions of the volume fraction variables of the light and heavy fluid are visualised for the Dellecase case: $u_s = 0.06$ $[\frac{m}{s}]$. The distributions are given at seven time steps.

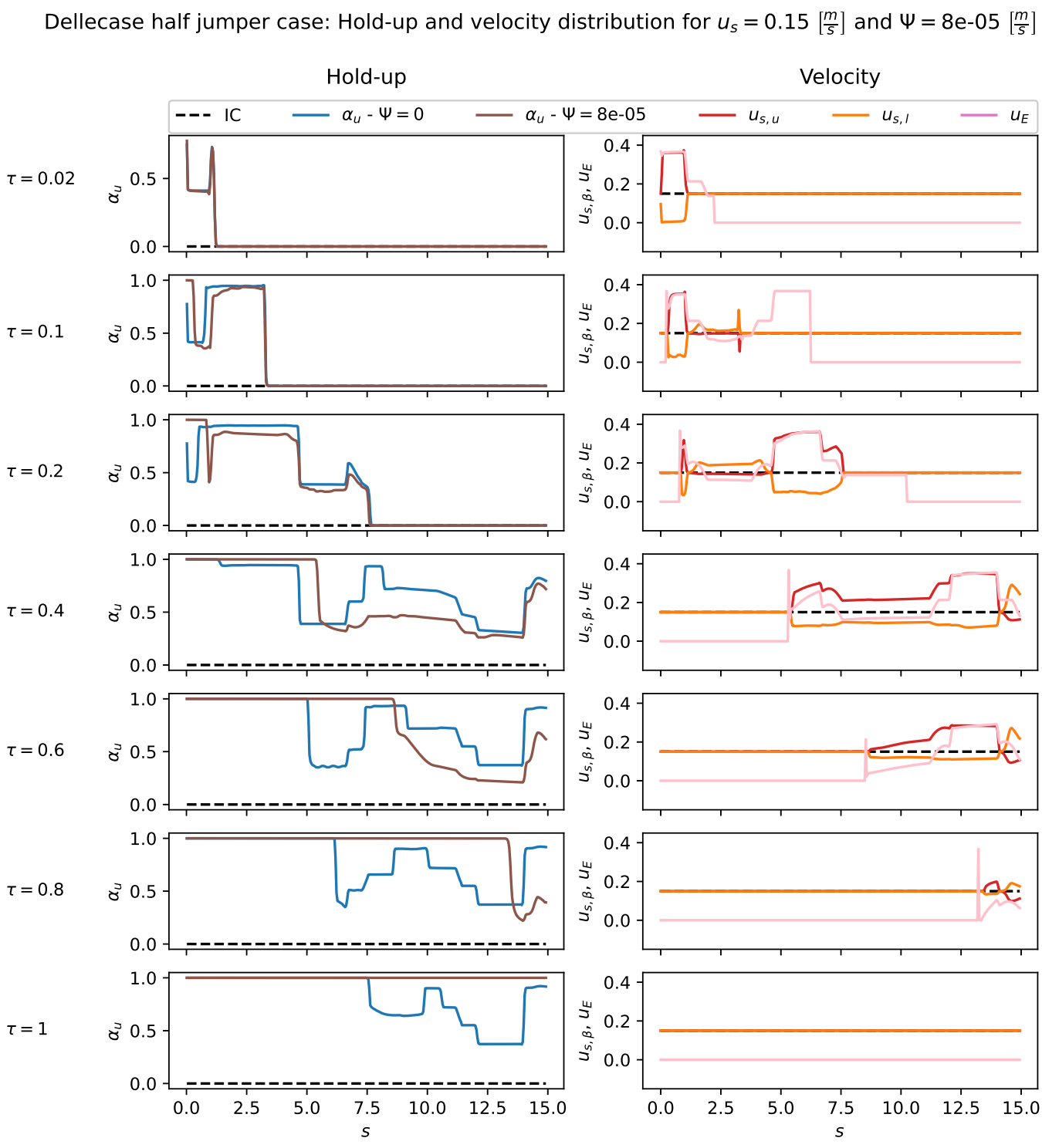

Figure 5.30: The distributions of the hold-up and the velocity variables are visualised for the Dellecase case: $u_s = 0.15$ $[\frac{m}{s}]$. The distributions are given at seven time steps.

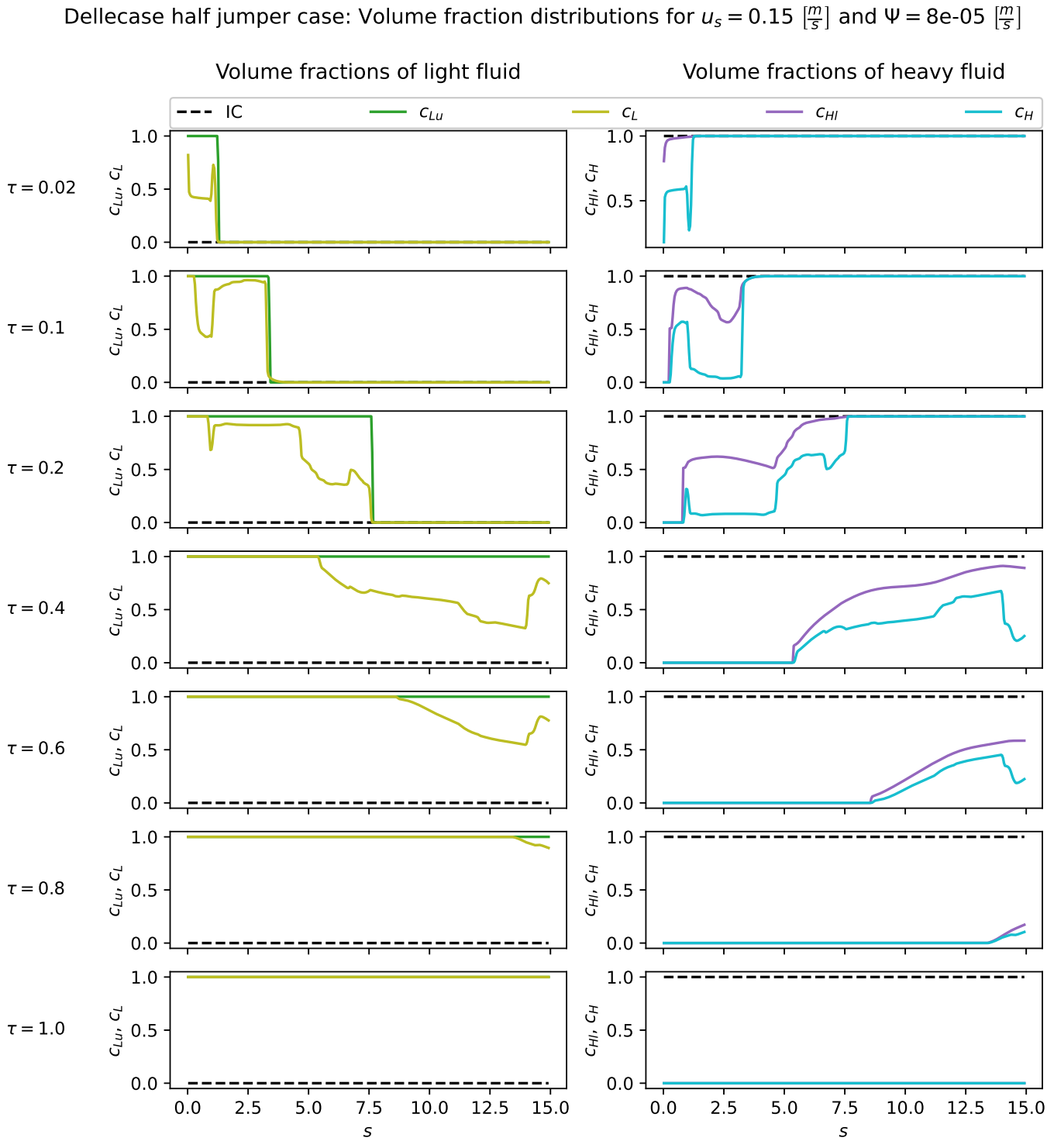

Figure 5.31: The distributions of the volume fraction variables of the light and heavy fluid are visualised for the Dellecase case: $u_s = 0.15$ $[\frac{m}{s}]$. The distributions are given at seven time steps.

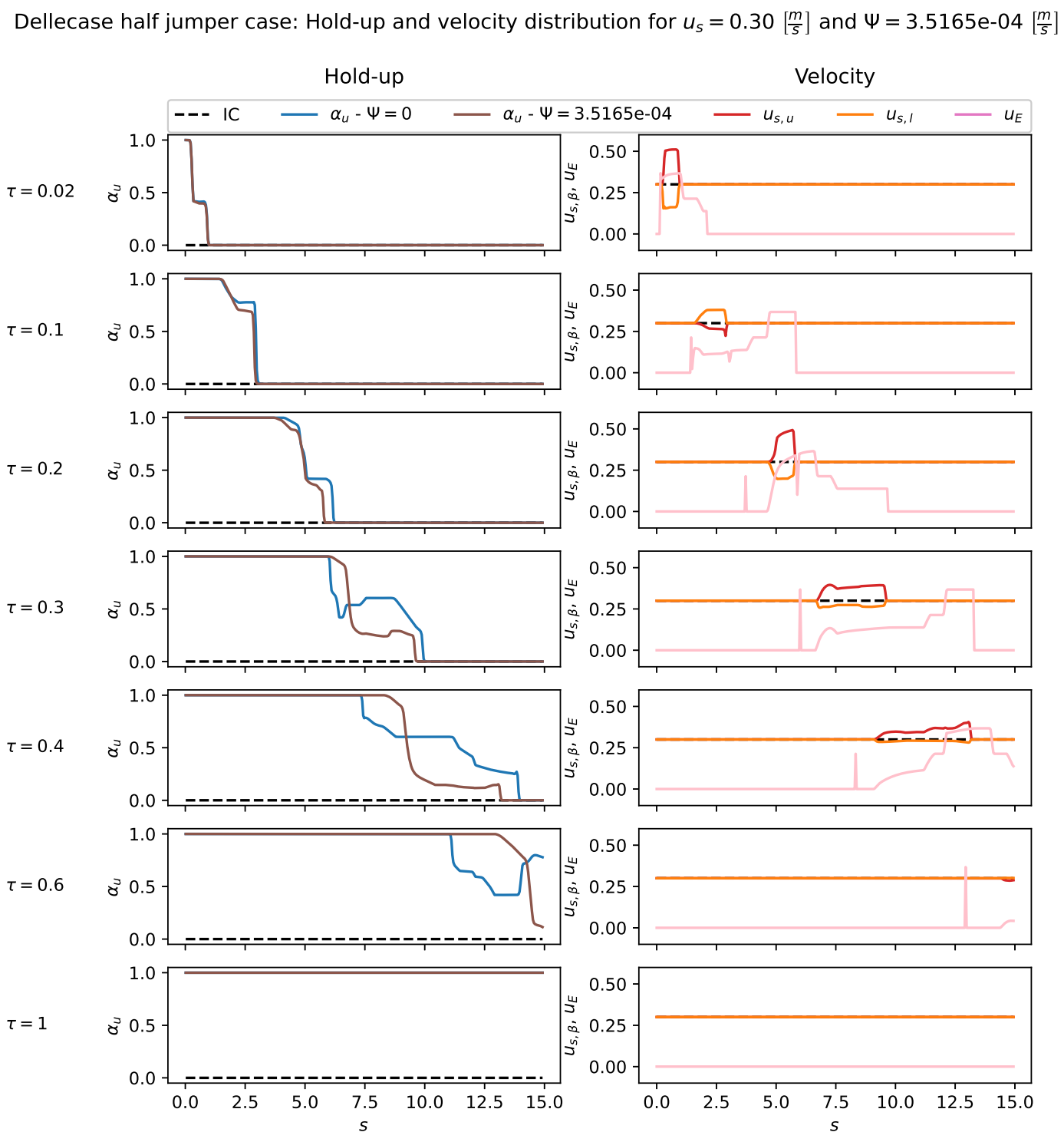

Figure 5.32: The distributions of the hold-up and the velocity variables are visualised for the Dellecase case: $u_s = 0.30$ $[\frac{m}{s}]$. The distributions are given at seven time steps.

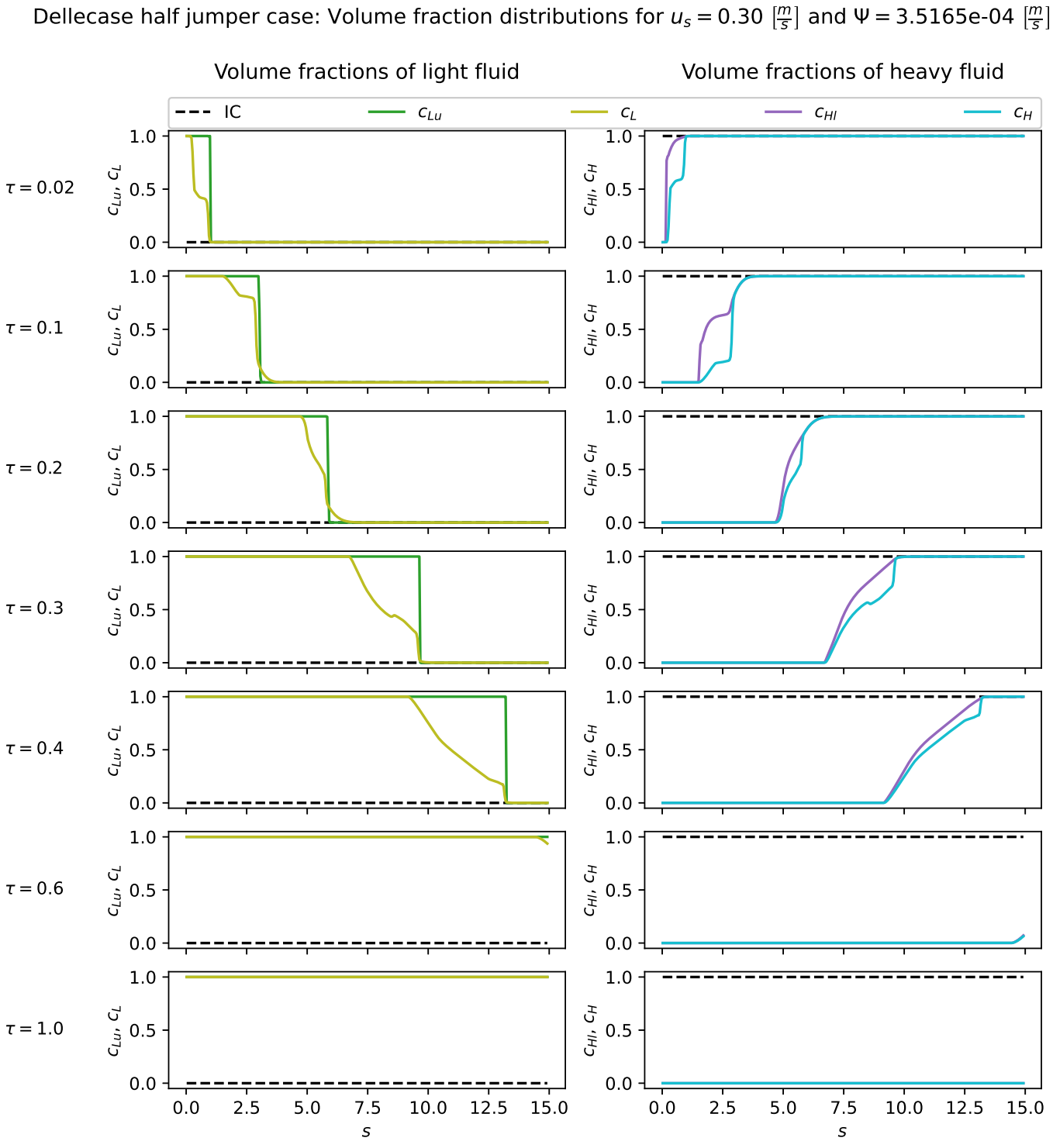

Figure 5.33: The distributions of the volume fraction variables of the light and heavy fluid are visualised for the Dellecase case: $u_s = 0.30$ $[\frac{m}{s}]$. The distributions are given at seven time steps.

5.5. Froude number and W-shaped pipe case with mass transfer

In this section the W-shaped pipe case and the Froude number case are redone to review the effect of the volumetric transfer term estimated by equation (5.1) on the flow solution. The initial conditions of the cases are not alternated, and these cases are again simulated for both flushing characteristics: *LH* and *HL*.

Froude number It is chosen to simulate the Froude number cases $Fr = 0.25$ and $Fr = 4$ with a volumetric transfer term determined by the linear empirical relation of equation (5.1), as these cases represent mixture Reynolds numbers in the critical and turbulent flow region. The mixture Reynolds number for the Froude number $Fr = 0.25$ is $Re_{\text{mix}} = 6759.6$ and its superficial velocity is $u_s = 0.1504 \left[\frac{m}{s}\right]$. This results in a volumetric transfer term of $\Psi = 3.471\text{e-}05 \left[\frac{m}{s}\right]$. The mixture Reynolds number for the Froude number $Fr = 0.4$ is $Re_{\text{mix}} = 27038$ and its superficial velocity is $u_s = 0.6017 \left[\frac{m}{s}\right]$ which results in a volumetric transfer term of $\Psi = 7.461\text{e-}04 \left[\frac{m}{s}\right]$.

In Figs. 5.34 & 5.35 the hold-up distribution of the Froude numbers $Fr = 0.25$ and $Fr = 4$ are illustrated for *LH* and *HL*, respectively. Again, only the hold-up distribution is given, as it provides a good understanding whether stratification effects are seen within the pipe section or not. The hold-up variables of the old Froude number cases are plotted as well to compare both results.

It is observed in Fig. 5.34 that the hold-up distribution for $Fr = 0.25$ does not deviate much from its reference case of $\Psi = 0 \left[\frac{m}{s}\right]$. The stratified flow is still observed for this Froude number. At the last two time steps it is shown that the volumetric transfer term case results in lower values of the hold-up variable in the stratified layer for both flushing characteristics.

The hold-up distribution of for $Fr = 4$ is totally different for $\Psi = 7.461\text{e-}04 \left[\frac{m}{s}\right]$ compared to the case of $\Psi = 0 \left[\frac{m}{s}\right]$, as is visualised in Fig. 5.35. Stratified layers are no longer observed in the horizontal pipe sections for both flushing characteristic. In Section 5.2 it was suspected that the mass transfer between the regions is required for the stratification to vanish at the high Froude numbers for *LH*. This hypothesis has been proven to be right. The results for $Fr = 4$ are more symmetrical for $\Psi = 7.461\text{e-}04 \left[\frac{m}{s}\right]$ than for $\Psi = 0 \left[\frac{m}{s}\right]$.

Furthermore, it is observed that the front of the bubble has propagated less distance for $Fr = 4$ under the influence of the volumetric transfer term. Nonetheless, the model still predicts the axial distance between the front and the tail of the bubble to be larger for *LH* than for *HL*. These axial distances are not given in this report.

W-shaped pipe The mixture Reynolds number of the W-shaped pipe case is $Re_{\text{mix}} = 22402$ and its superficial velocity is $u_s = 0.10 \left[\frac{m}{s}\right]$. This results in a volumetric transfer term of $\Psi = 1.010\text{e-}04 \left[\frac{m}{s}\right]$ using the linear empirical relation of equation (5.1). As it is observed that the hold-up and velocity distribution do not show great deviation in comparison to their previous distribution for a $\Psi = 1\text{e-}05 \left[\frac{m}{s}\right]$, they are not included in this section. The volume fraction distribution of the light fluid is plotted in Fig. 5.36 for *LH* and *HL*, and the volume fraction distribution of the heavy fluid is plotted in Fig. 5.37. The total volume fraction of the fluids of the old case with $\Psi = 1\text{e-}05 \left[\frac{m}{s}\right]$ is given as well to compare the both cases.

It is observed that the modified W-shaped pipe cases are affected by the updated volumetric transfer term. The stratified layers which remained in the W-shaped pipe geometry at $t^* = 560.3$ for the $\Psi = 1\text{e-}05 \left[\frac{m}{s}\right]$ case, are still present in the geometry. For *LH* the total volume fraction of the light fluid has increased compared to the old case, whereas the total volume fraction of the heavy fluid has decreased compared to the $\Psi = 1\text{e-}05 \left[\frac{m}{s}\right]$ cases. The exact opposite is shown for the flushing characteristic *HL*. The updated volumetric transfer terms do not yet result in a substantial decrease of the value of the effective bubble velocity at the beginning of the stratified layer, so that this layer is flushed out of the geometry.

Iterations The number of iterations per time step and the residuals of the flow variables are not visualised for the updated fluid-fluid displacement cases, as the outcome of these plots is similar to the ones shown in the respective previous sections.

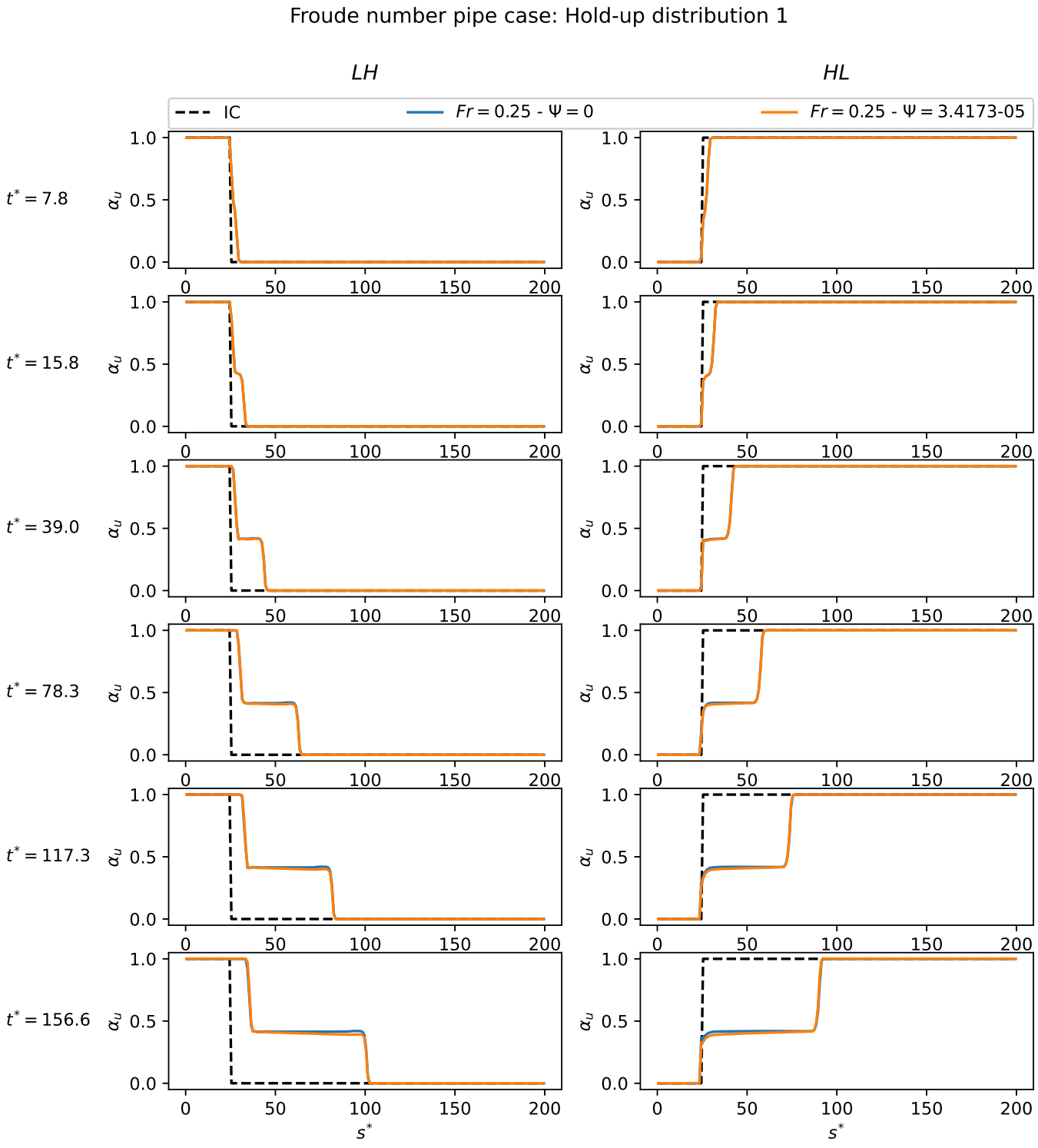

Figure 5.34: The distribution of the hold-up variables of the upper region is visualised for Froude number $Fr = 0.25$ and for the cases $\Psi = 0$ and Ψ = 3.471e-05 $\left[\frac{m}{s}\right]$. The distributions are given for both *LH* and *HL*.

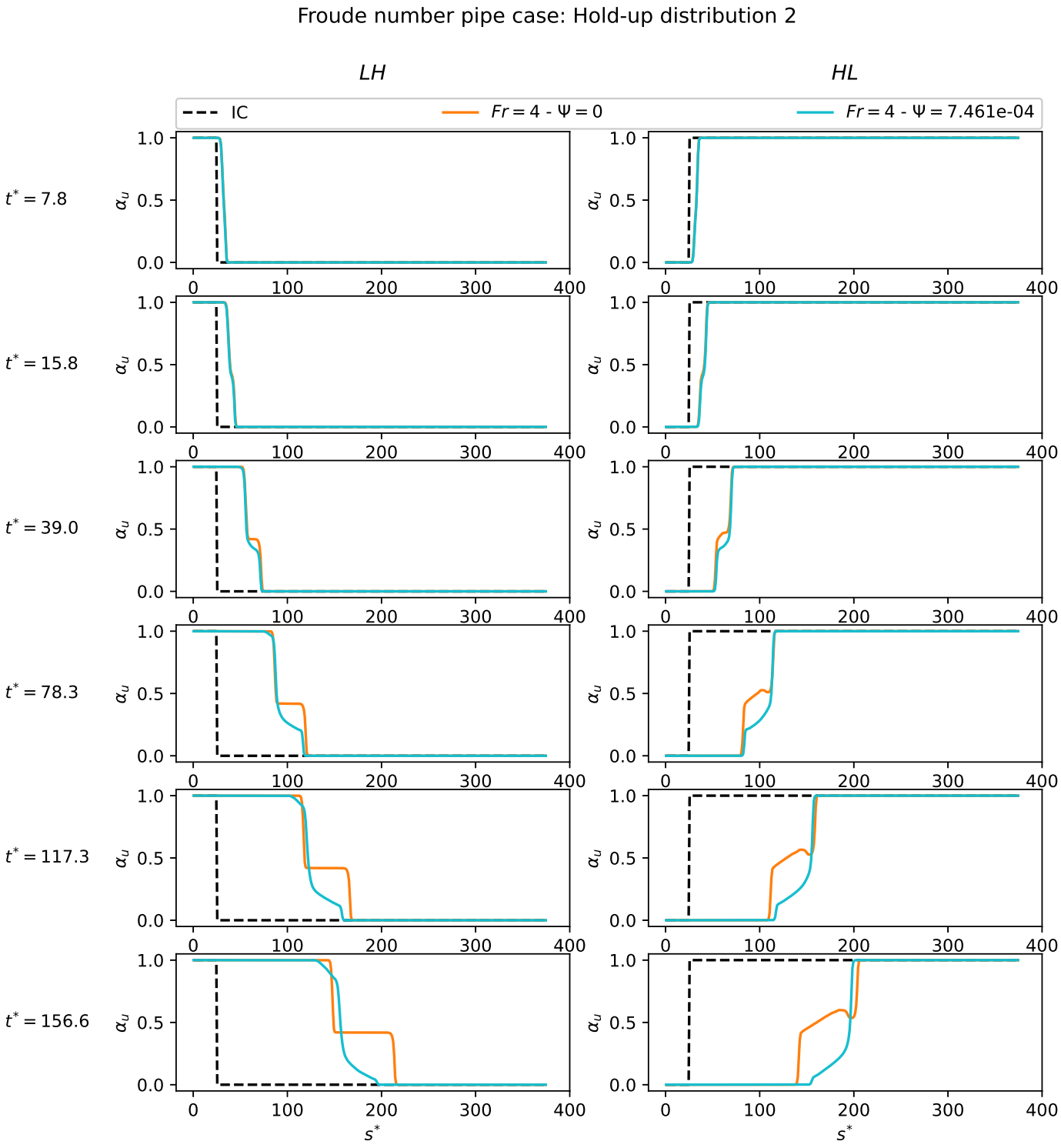

Figure 5.35: The distribution of the hold-up variables of the upper region is visualised for Froude number $Fr = 4$ and for the cases $\Psi = 0$ and Ψ = 7.461e-04 $\left[\frac{m}{s}\right]$. The distributions are given for both *LH* and *HL*.

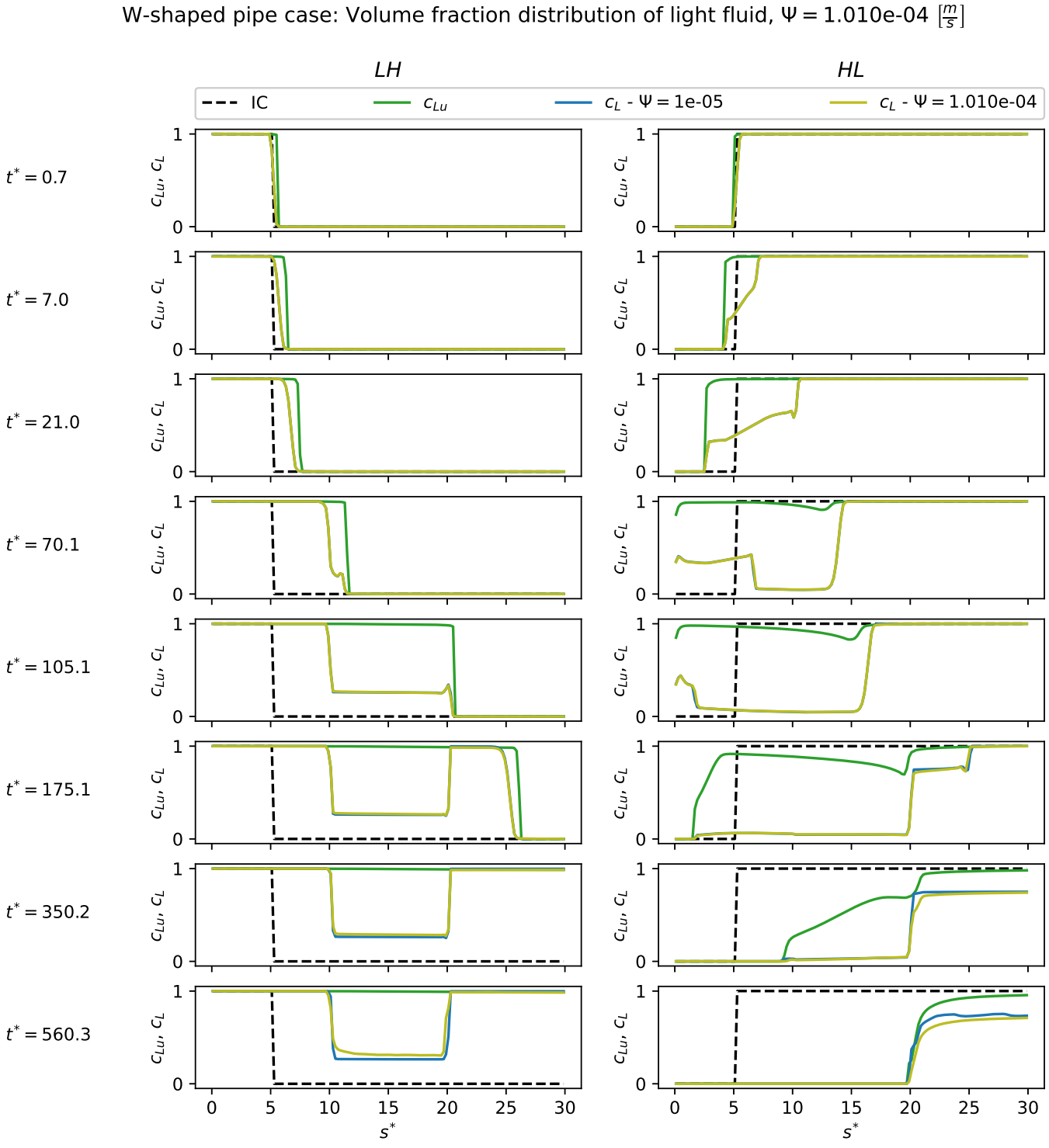

Figure 5.36: The distribution of the volume fraction variables of the light fluid of the W-shaped pipe case is visualised for Ψ = 1e-05 and Ψ = 1.010e-04 $\left[\frac{m}{s}\right]$. The distributions are shown for both *LH* and *HL*.

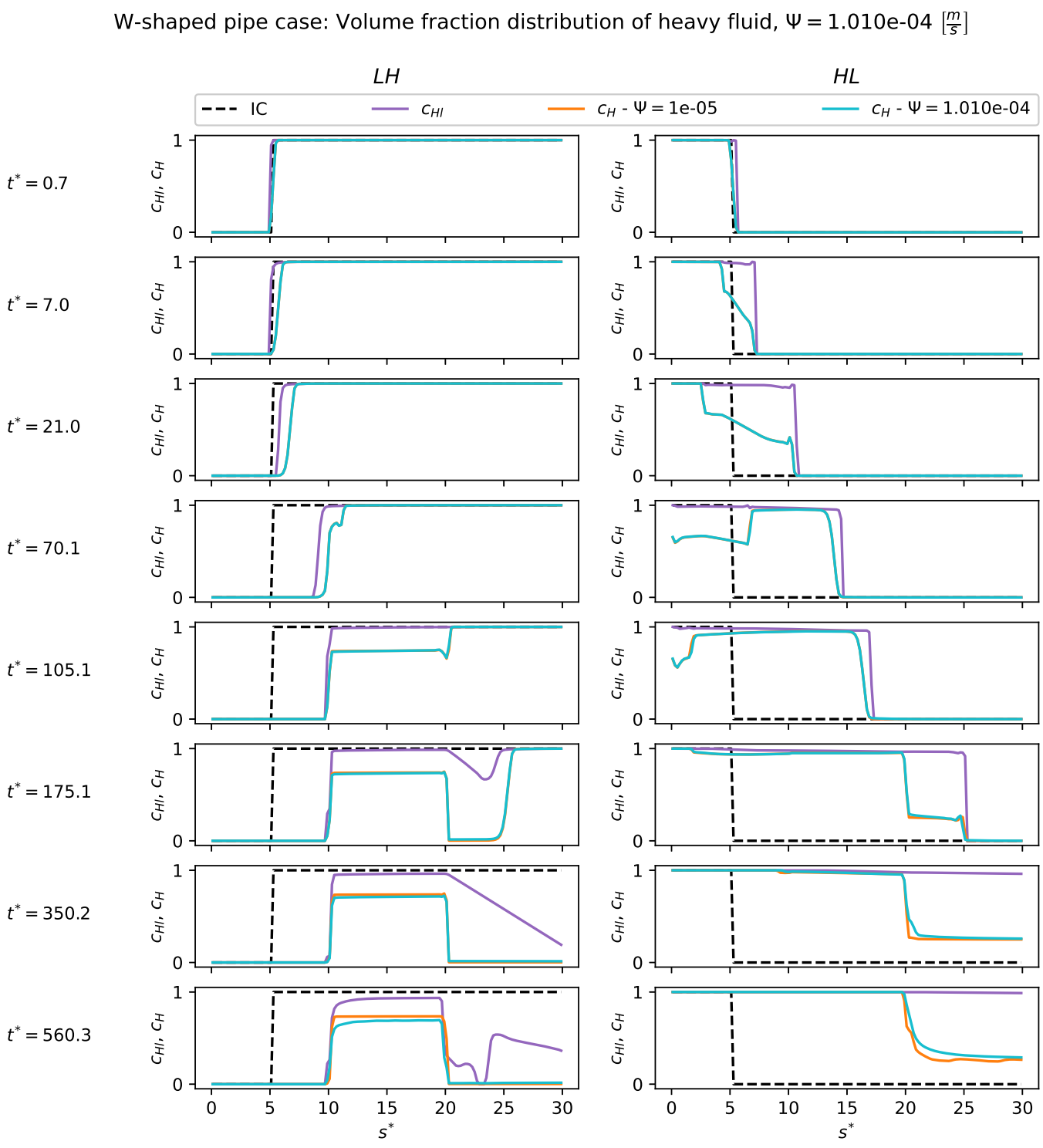

Figure 5.37: The distribution of the volume fraction variables of the heavy fluid of the W-shaped pipe case is visualised for Ψ = 1e-05 and Ψ = 1.010e-04 $\left[\frac{m}{s}\right]$. The distributions are shown for both *LH* and *HL*.

6

Conclusions

In the present study, a one-dimensional model has been developed which is able to predict miscible fluid-fluid displacement including the impact of density variations within the aqueous phase. To do so, the conservation of mass and the transport equation have been cross-sectionally averaged to track the transient behaviour of mass and the transient behaviour of the volume fraction of the fluid particles. Two virtual regions were introduced to track these particles: the upper region denoted by $(.)_u$ and the lower region denoted by $(.)_l$. Within the model, these regions are assumed to be separated by a sharp interface. The miscible displacement of the two fluids is tracked in each of the regions, namely: the light fluid denoted by $(.)_L$ and the heavy fluid by $(.)_H$. The derived one-dimensional multiphase conservation of mass equation and the multiphase transport equation include transfer terms which are connnected to each other and allow the exchange of mass and volume between the regions.

The axial velocity for each region is modelled using a slip relation and a velocity equation, in which the latter is derived from the incompressibility condition. No momentum equations are solved within the model. The slip relation is an artefact that couples the relative velocity between the regions to the effective bubble velocity relation proposed by Bendiksen [3]. The slip relation functions are designed to translate the correct form of the effective bubble velocity to the relative velocity of the regions.

To include turbulent axial dispersion in the aqueous phase, the empirical relation of Hart was incorporated in the multiphase transport equation [12]. The empirical relation of the axial dispersion coefficient is a function of the Reynolds number and is valid for Reynolds numbers between 3,000 and 50,000, i.e. the axial dispersion coefficient adapts its magnitude to the density, the axial velocity, the hydraulic diameter, the dynamic viscosity of the region.

The partial derivative terms with respect to time in the miscible set of equations of Eqn. (3.68) are discretised using the Crank-Nicolson method. The advective terms within these equations are discretised by the high-resolution scheme and the central approximation method is applied to the diffusive terms. The numerical model is up to second-order accurate in space and time for a smooth flow solution. The numerical model is validated for the single-phase transport equation by a turbulent diffusion equation of which the diffusion coefficient is determined by the empirical relation of Hart. The results of the numerical model are within 10% of the analytical solution for low Reynolds numbers and within 0.4% for Reynolds numbers above 20,000. Furthermore, it is shown that the accuracy of the results of the simulations performed with an implicit Euler time integration are low compared to the results of the simulations performed with the Crank-Nicolson time integration. The simulations of the experiments of Hart are also in good agreement with Hart's experimental data, as all simulation results are within 12% of the experimental results. Furthermore, through carrying out grid sensitivity simulations the numerical model was proven to be accurate for coarse grids as well.

The numerical model is solved by a coupled approach using Picard's method to linearise to nonlinear terms. The coupled approach has been selected after a reference case was employed. In this reference case, the coupled approach proved to be more stable than the segregated approach.

For an immiscible model, the possibility of applying Newton's method for the linearisation of the nonlinear terms has been studied, and its results were found to be promising. Nearly exponential convergence rates were found for this method, while Picard's method gave linear convergence rates. The averaged number of the iterations per time step and the total simulation time were less for Newton's method as well. However, Picard's method has been chosen to linearise the miscible model, as it was noticed that the introduction of one new linearisation within the immiscible model led to an extensive increase in the simulation time. It was expected that the introduction of the many linearisations required to apply Newton's method would result in larger simulation times than when Picard's method is applied.

The coupled solver is actually not fully coupled, as Picard's method is applied. Furthermore, a flipflopping process can be observed when a region is arriving in a cell and its respective hold-up has a magnitude greater than the threshold value ε_3 = 1e-03 in one iteration step, and a magnitude smaller than ε_3 in the subsequent iteration step (and so on). The model reacts by activating and deactivating flow variables in the particular cell which leads to no convergence within the specific time step. This has been resolved by taking the respective flow variables that depends on the threshold value ε_3, out of the iteration loop. The variables are now determined in the time loop and are constant in the iteration loop. Unfortunately, this leads to further decoupling of the coupled solver, as the model needs more time to rapidly react to changes in the flow solution. Another flipflopping process can be observed in the model. The axial velocities of the regions could flipflop between a positive and negative value within the iteration loop in specific cases. The high-resolution scheme uses their sign to determine the value and the orientation of the cell edge variables. Flipflopping of the sign between the iterations leads to no convergence within a time step as well. This has been resolved by determining cell edge variables using the high-resolution scheme in which the axial velocities of the previous time step are used.

In Chapter 5 it is shown that the model is capable of reproducing a slip velocity between the regions which is able to capture changes in thermodynamic properties, the pipe inclination angle, the slip relation functions and the transfer terms. Furthermore, the model is able to capture gravity currents by incorporating the slip functions. Another good feature of the model is that it handles both cases: a light fluid flushing a heavy fluid and a heavy fluid flushing a light fluid. In the horizontal pipe sections, this leads to symmetrical results for the Benjamin bubble cases, where the numerical model correctly predicts the movement of the bubble; the axial velocity of the upper region moves at the Benjamin bubble velocity and the axial velocity of the lower region moves at the water front velocity. Moreover, the model predicts longer mixing lengths for the flushing characteristic in which a light fluid is flushing out a heavy fluid. This is in line with literature. For inclined pipe sections, the equilibrium interface and the bubble interface are reproduced by the model. If the superficial velocity is able to overcome the effective bubble velocity in the inclined pipe sections, a bubble interface is formed by the flushing fluid which pushes out the other fluid. When the superficial velocity is not able to overcome the effective bubble velocity, a stagnant segregated layer is established in this section. This stratified layer is exposed to mass transfer and diffusion and will eventually enable this low spot to be flushed out of the inclined pipe section.

In Section 5.4 the experiments of Dellecase are reproduced by the numerical model with the goal of matching the numerical results with the experimental data in order to determine the Ψ term per superficial velocity case. Only for the superficial velocity case $u_s = 0.06 \left[\frac{m}{s}\right]$ a clear match was found, as it was hard to find a match for the other cases without having any transient data for the Dellecase configuration. This transient data for the Dellecase case were obtained by a CFD model as part of this study. By matching the numerical results to the CFD results a linear empirical relation of the volumetric transfer term was derived as a function of the mixture Reynolds number. The effect that Ψ has on the model was studied by simulating the test cases with and without the derived empirical correlation. For the Dellecase simulations plausible results with characteristics observed in the real experiments were confirmed.

It can be concluded that the goal of the present study has been achieved: the one-dimensional model has proven to be of high accuracy (even for coarse grids) and to convergence quickly. The model is able to capture slip velocities and gravity currents in pipe sections. Furthermore, the model also includes turbulent dispersion, mass transfer and changes in the pipe inclination.

7

Recommendations

The model performs well within the current set of assumptions. Nonetheless, the model can be extended to improve its functionalities and be further validated in future studies.

The empirical relation of Hart is implemenented in the model to predict an axial dispersion coefficient for the different regions. This relation is valid for Reynolds numbers in the critical and turbulent flow domain; i.e. Reynolds numbers between $Re = 3,000$ and $Re = 50,000$. However, a small superficial velocity is required in pipelines to predict the dispersion of the fluids with Hart's empirical relation, as the pipeline diameter is typically much larger than the diameters considered in this study. The flow inside these pipelines is often highly turbulent. The current model is not able to simulate the lowest superficial velocity case, $u_s = 0.02 \left[\frac{m}{s}\right]$, as it falls in the laminar domain. Laminar flow is mostly encountered in pipe sections where the flow becomes almost stagnant. Therefore, empirical relations are also required to reproduce axial dispersion coefficients for laminar and highly turbulent flow in the model. This is one of the improvements that can be done.

The dynamic viscosity per region is determined by the volume fraction of the fluid in the different regions. It is only used within the model to determine the Reynolds number per region, which is required to calculate the axial dispersion coefficient per region. The magnitude of the dynamic viscosity of a fluid quantifies its resistance to flow through a pipe. Besides, an absolute viscosity difference influences the mixing lengths between fluids. In the current model the batch transports of two gasolines and two diesels would result in a similar mixing length and a similar time of arrival at the destination of the transport, when it is assumed that the density difference and the superficial velocity of the batches are the same. These results will only be slightly different due to different axial dispersion coefficients for the fluids within the batch transports. On the contrary, the batch transport of the diesels is expected to arrive later at its destination and have a smaller mixing length than the batch transport of the gasolines due to the larger magnitude of the viscosities. [1] Therefore, one improvement can be to include the impact of viscosities in the model. A possible solution is to extend the relation of the effective bubble velocity relation of Bendiksen [3] with a viscosity term.

The current model is designed to match the slip velocity between the region to a correct form of the effective bubble velocity using slip relation functions. However, the functions used in the model are derived for horizontal pipe sections and for inclined pipe sections and they will be different when the pipe inclination angle changes from zero to a nonzero value. In the elbow corners, encountered in the simulations of Dellecase's experiments in Section 5.4, this transition from a horizontal pipe orientation to an inclined pipe orientation is observed. These transitions resulted locally in sharp spikes for the flow variables and slow convergence rates. This was resolved by applying smoothening over the slip relation functions from $\theta = 0$ to θ_{smooth}. However, the smoothening of the slip relations is a numerical artefact. Further testing of the model is recommended to explore the impact that this modelling choice can have on the results of the model.

In Section 5.4 a first empirical relation for the volumetric transfer terms is given in Eqn. (5.1). The relation is a function of the mixture Reynolds number and is constructed by using extrapolation between two points based on the CFD results of the Dellecase experiments. The relation serves as an initial estimation of the volumetric transfer term in fluid-fluid displacement of methanol - fresh water mixtures. However, it is not expected that extrapolating this relation would directly lead to accurate results. Therefore, a new experimental reference case is required to provide new miscible fluid-fluid displacement data for deriving an improved empirical relation for the volumetric transfer term outlined in Eqn. 3.66.

To increase the speed of the code and also be able to benefit from parallelization, it is recommended to rewrite the code in a compiled language such as C++..

Bibliography

[1] J. E. Austin and J. R. Palfrey. Mixing of Miscible but Dissimilar Liquids in Serial Flow in a Pipeline. *Proceedings of the Institution of Mechanical Engineers*, 178(1):377–389, 1963. ISSN 0020-3483. doi: 10.1177/002034836317800160.

[2] Yong Bai and Qiang Bai. *Subsea engineering handbook*. 2018. ISBN 9780128126226. doi: 10.1016/C2016-0-03767-1.

[3] Kjell H. Bendiksen. An experimental investigation of the motion of long bubbles in inclined tubes. 10 (4):467–483, 1984.

[4] Kjell H. Bendiksen, Dag Mainee, Randl Moe, and Sven Nuland. The Dynamic Two-Fluid Model OLGA : Theory and Application. *Inst. for Energy Technology*, (May), 1991.

[5] T. Brooke Benjamin. Gravity currents and related phenomena. 31:209–248, 1968.

[6] Dag Biberg. An explicit approximation for the wetted angle in two-phase stratified pipe flow. *Canadian Journal of Chemical Engineering*, 77(6):1221–1224, 1999. ISSN 00084034. doi: 10.1002/cjce.5450770619.

[7] Thijs Bouwhuis. *Prediction of the Immiscible and Miscible Fluid-Fluid Displacement in Pipelines*. PhD thesis, University of Twente, 2017.

[8] Christopher E. Brennen. Fundamentals of multiphase flow. *Fundamentals of Multiphase Flow*, 9780521848:1–345, 2013. doi: 10.1017/CBO9780511807169.

[9] Angelina Coletta, S P T Group Pty, Michael Volk, and Emmanuel Delle-case. IPTC 14592 Investigations of Flow Behavior in Well-Head Jumpers during Restart with Gas and Liquid. 2012.

[10] E. Dellecase, S. Mele Solano, H. Lu, and M. Volk. Hydrate inhibitor displacement experiments in jumper-like pipe configurations. *BHR Group - 16th International Conference on Multiphase Production Technology 2013*, pages 151–164, 2013.

[11] D. T. Dumitrescu. Strömung an einer Luftblase im senkrechten Rohr. *ZAMM - Journal of Applied Mathematics and Mechanics / Zeitschrift für Angewandte Mathematik und Mechanik*, 23(3):139–149, 1943. ISSN 15214001. doi: 10.1002/zamm.19430230303.

[12] J.R. Hart, I Guymer, F Sonnenwald, and V.R. Stovin. Residence Time Distributions for Turbulent, Critical and Laminar Pipe Flow. 2016.

[13] A M I Harten. High Resolution Schemes for Hyperbolic Conservation Laws. *Journal of Computational Physics*, 49(3):357–393, 1983.

[14] Hassan Hassanzadeh, Jalal Abedi, and Mehran Pooladi-Darvish. A comparative study of flux-limiting methods for numerical simulation of gas-solid reactions with Arrhenius type reaction kinetics. *Computers and Chemical Engineering*, 33(1):133–143, 2009. ISSN 00981354. doi: 10.1016/j.compchemeng.2008.07.010.

[15] Ruud Henkes. Hydraulic Guidelines - part on fluid-fluid displacement. .

[16] Ruud Henkes. Shell - Lab expriments - miscible fluids - Tempa Rossa, .

[17] William B. Krantz and Darsh T. Wasan. Axial Dispersion in the Turbulent Flow of Power-Law Fluids in Straight Tubes. 13(1), 1974.

[18] R. LaVeque. *Finite Volume Methods for Hyperbolic Problems*. 2002.

[19] B.P. Leonard and S. Mokhtari. BEYOND FIRST-ORDER UPWINDING : THE ULTRA-SHARP ALTERNATIVE FOR NON-OSCILLATORY STEADY-STATE SIMULATION OF CONVECTION. *International Journal for Numerical Methods in Engineerning*, 30(January):729–766, 1990.

[20] Haidan Lu, Noah Tracy, S. C. Johnson, Micheal Volk, Emmanuel Delle-Case, and Evren M. Ozbayoglu. Experimental and Computational study of Thermodynamic hydrate inhibitor mixing and displacement in subsea jumper. *Proceedings of the Annual Offshore Technology Conference*, 4:2361–2388, 2018. ISSN 01603663. doi: 10.4043/28823-ms.

[21] B. Müller. *Introduction to computational fluid dynamics*, volume 9780521853. Norwegain University of Science and Technology (NTNU), Trondheim, Norway, 2018. ISBN 9780511808975. doi: 10.1017/CBO9780511808975.

[22] Frans T M Nieuwstadt, Bendiks J Boersma, and Jerry Westerweel. *Turbulence: Introduction to Theory and Applications of Turbulent Flows*. Springer;, Delft, 2015. ISBN 9783319315973.

[23] A. Prosperetti and G. Tryggvason. *Compational Methods for Multiphase Flow*. 2007. ISBN 9780521847643.

[24] P.I. Rosen Esquivel and R.H.A. IJzermans. Calculation Method for flushing an Oil filled Pipeline with Water. (August), 2013.

[25] B. Sanderse. Governing equations of single- and multi-phase flow in one-dimensional pipelines. (December), 2013.

[26] B. Sanderse and M. Haspels. Prediction of an Elongated Bubble Moving in a Liquid-Filled Channel using a 1D Two-Fluid Model. (February), 2015.

[27] H.E. Skipness and P.I. Rosen Esquivel. Draugen Methanol Injection and Optimization for Hydrate Management. 2016.

[28] E. Dendy Sloan Jr., Carolyn A. Koh, and Carolyn A. Koh. Clathrate Hydrates of Natural Gases, 2007.

[29] Shell Global Solutions. Technical description Shell Flow Correlations Technical description Shell Flow Correlations.

[30] Geoffrey Taylor. The dispersion of matter in turbulent flow through a pipe. *Proceedings of the Royal Society of London. Series A. Mathematical and Physical Sciences*, 223(1155):446–468, 1954. ISSN 0080-4630. doi: 10.1098/rspa.1954.0130.

[31] Geoffrey Taylor and R.M. Davies. The mechanics of large bubbles rising through extended liquids and through liquids in tubes. pages 375–390, 1949.

[32] Frank M. White. *Viscous Fluid Flows*. Mcgraw-Hill Education - Europe, 2005. ISBN 9780071244930.

[33] Frank M. White. *Fluid Mechanics*. 8th (si un edition, 2016. ISBN 9789385965494.

Nomenclature

List of abbreviations

Abbreviation	Description
BC	Boundary Condition
CFD	Computational Fluid Dynamics
CFL	Courant-Friedrichs-Lewy
CN	Crank-Nicolson
COMPAS	Compositional MultiPhase Advanced Simulator
CPCE	Combined Phase Continuity Equation
FDM	Finite Difference Method
FVM	Finite Volume Method
HSE	Health, Safety and Environment
IC	Initial Condition
IPCE	Individual Phase Continuity Equation
NS	Navier-Stokes
ODE	Ordinary Differential Equation
OLGA	OiL and GAs simulator
PDE	Partial Differential Equation
THI	THermodynamic Inhibitor
TV	Total Variation
TVB	Total Variation Bounded
TVD	Total Variation Diminishing

List of Symbols

Subscripts and superscripts

$(.)_B$	General notation to denote: the light fluid $(.)_L$ and the heavy fluid $(.)_H$, $B \in \{L, H\}$
$(.)_\beta$	General notation to denote: the upper region $(.)_u$ and the lower region $(.)_l$, $\beta \in \{u, l\}$
$(.)_i$	Notation to denote a flow variable in the cell centre
$(.)_{i\pm1/2}$	Notation to denote a flow variable on the cell edge
$(\hat{.})$	Notation to denote the cell edge variables of the discretised advective terms
$(\tilde{.})$	Notation to denote the cell edge variables of the discretised diffusive terms
$(.)^n$	Notation to denote a flow variable at previous time level
$(.)^{n+1}$	Notation to denote a flow variable at next time level
$(.)^m$	Notation to denote a flow variable at previous iteration level
$(.)^{m+1}$	Notation to denote a flow variable at next iteration level
$(.)^*$	Notation to denote a dimensionless variable

Dimensionless variables

Π	Dimensionless variable in Buckingham Pi theorem
$Eö$	Eötvös number
Eu	Euler number
Fr	Froude number
$Pé$	Péclet number
Re	Reynolds number
Re_{cr}	Critical Reynolds number
Re_{mix}	Mixture Reynolds number
Sc	Schmidt number
h^*	Dimensionless interface height
Ψ^*	Dimensionless volumetric transfer term
s^*	Dimensionless axial distance
τ	Dimensionless time in Dellecase simulations to denote injected volume of methanol
t^*	Dimensionless time
u_s^*	Dimensionless axial velocity

Vector and matrices

$\mathbf{A}$	Solver matrix used of coupled approach[1]
Δ	Incremental vector[1]
$\mathscr{D}$	Dispersion coefficient vector $\left[m^2/s\right]$
$\mathbf{e}$	Unit vector $[-]$
$\mathbf{f}$	Flux vector $[m/s]$
∇	Divergence operator vector $[1/m]$
$\mathbf{n}$	Normal vector $[-]$
$\mathbf{r}$	Residual vector[1]
$\mathbf{u}$	Velocity vector $[m/s]$
$\mathbf{x}$	Coordinate system vector $[m]$

[1] These vectors and matrix consist of multiple different units, as they involve the miscible set of equations of Eqn. (3.68).

Geometry parameters

A	Pipe cross-sectional area $\left[m^2\right]$
D_H	Hydraulic diameter $[m]$
H	Channel height $[m]$
Ω	Arbitrary volume $\left[m^3\right]$
$\delta\Omega$	Arbitrary boundary of a volume $\left[m^2\right]$
Φ	Width of a initial step function $[m]$
R	Pipe radius $[m]$
s	Axial distance $[m]$
s_0	Initial position $[m]$
s_{mix}	Axial distance of a mixture $[m]$
s_{strat}	Axial distance of a stratified layer $[m]$
s_{total}	Total axial distance of a geometry $[m]$
s_{virtual}	Virtual axial distance due to a stratified layer $[m]$
S	Arbitrary surface $\left[m^2\right]$
θ	Pipe inclination angle $[°]$
θ_{smooth}	Pipe inclination angle until for the smoothening of the slip relation functions $[°]$
V	Pipe volume $\left[m^3\right]$
y	Pipe elevation $[m]$

Flow variables

A_l	Cross-sectional area of the lower region $\left[m^2\right]$
A_u	Cross-sectional area of the upper region $\left[m^2\right]$
A_{Hl}	Cross-sectional area of the heavy fluid in the lower region $\left[m^2\right]$
A_{Hu}	Cross-sectional area of the heavy fluid in the upper region $\left[m^2\right]$
A_{Ll}	Cross-sectional area of the light fluid in the lower region $\left[m^2\right]$
A_{Lu}	Cross-sectional area of the light fluid in the upper region $\left[m^2\right]$
α_l	Hold-up of the lower region [−]
α_u	Hold-up of the upper region [−]
c_{Hl}	Volume fraction of the heavy fluid in the lower region [−]
c_{Hu}	Volume fraction of the heavy fluid in the upper region [−]
c_H	Total volume fraction of the heavy fluid [−]
c_{Ll}	Volume fraction of the light fluid in the lower region [−]
c_{Lu}	Volume fraction of the light fluid in the upper region [−]
c_L	Total volume fraction of the light fluid [−]
$D_{H,l}$	Hydraulic diameter of the lower region [−]
$D_{H,u}$	Hydraulic diameter of the upper region [−]
$\mathscr{D}_{s,l}$	Axial dispersion coefficient of the lower region $\left[m^2/s\right]$
$\mathscr{D}_{s,u}$	Axial dispersion coefficient of the upper region $\left[m^2/s\right]$
γ_l	Wetted angle [°]
h	Interface height $[m]$
$(\mathrm{d}h/\mathrm{d}s)$	Gradient of the interface height with respect to the axial distance [−]
j_l	Volumetric flow rate of the lower region $\left[m^3/s\right]$
j_u	Volumetric flow rate of the upper region $\left[m^3/s\right]$
μ_l	Dynamic viscosity of the lower region $\left[kg/ms\right]$
μ_u	Dynamic viscosity of the upper region $\left[kg/ms\right]$
P_l	Wetted perimeter of the lower region $[m]$
P_u	Wetted perimeter of the upper region $[m]$
$P_{u,l}$	Interface length $[m]$
Ψ_{lu}	Mass transfer term from the lower region to the upper region $\left[kg/m^2s\right]$
Ψ_{ul}	Mass transfer term from the upper region to the lower region $\left[kg/m^2s\right]$
$\Psi_{H,lu}$	Volumetric transfer term of the heavy fluid from the lower region to the upper region $[m/s]$
$\Psi_{H,ul}$	Volumetric transfer term of the heavy fluid from the upper region to the lower region $[m/s]$
$\Psi_{L,lu}$	Volumetric transfer term of the light fluid from the lower region to the upper region $[m/s]$
$\Psi_{L,ul}$	Volumetric transfer term of the light fluid from the upper region to the lower region $[m/s]$
ρ_l	Density of the lower region $\left[kg/m^3\right]$
ρ_u	Density of the upper region $\left[kg/m^3\right]$
t	time $[s]$
$u_{s,l}$	Axial velocity of the lower region $[m/s]$
$u_{s,u}$	Axial velocity of the upper region $[m/s]$

Model function variables

$\mathscr{F}$	Hold-up function [−]
$\mathscr{F}_{\theta=0}$	Hold-up function [−] for $\theta = 0$ [°]
$\mathscr{F}_{\theta\neq0}$	Hold-up function [−] for $\theta \neq 0$ [°]
$\mathscr{G}$	Interface function [−]
$\mathscr{G}_{HL}$	Interface function for a heavy fluid flushing a light fluid [−]
$\mathscr{G}_{LH}$	Interface function for a light fluid flushing a heavy fluid [−]
$\mathscr{L}$	Slope limiter function [−]
u_E	Effective bubble velocity function $[m/s]$

Other model parameters

C	Palfrey coefficient [−]
$\mathscr{D}_{N,\text{adv}}$	Numerical diffusion term due to the discretised advective term [m^2/s]
$\mathscr{D}_{N,\text{diff}}$	Numerical diffusion term due to the discretised diffusive term [m^2/s]
$\mathscr{D}_{N,\text{t}}$	Numerical diffusion term due to the discretised time term [m^2/s]
f_B	Buoyancy force [N]
f_G	Gravitional force [N]
f_I	Inertia force [N]
f_P	Pressure force [N]
f_S	Surface tension force [N]
f_V	Viscous force [N]
$\bar{K}$	Virtual coefficient of dispersion [−] by Hart [12]
K_*	Virtual coefficient of dispersion [−] by Taylor [30]
λ	Smoothness gradient [−]
$\mathscr{O}$	Order of accuracy [−]
ϕ	Interface angle [°]
u_B	Benjamin bubble velocity [m/s]
u_E	Effective bubble bubble velocity [m/s]
u_F	Water front velocity [m/s]
u_g	Gravitional velocity [m/s]
u_s	Superficial velocity / total axial velocity / mixture velocity [m/s]
u_T	Taylor velocity [m/s]
u_*	Friction velocity [m/s]
Q	Scalar quantity [−]
$\dot{Q}$	Volumetric flow rate [m^3/s]

Simulation parameters

Co	Courant number [−]
ε_1	Threshold value in hold-up function $\mathscr{F}$ [−]
ε_2	Threshold value in interface function $\mathscr{G}$ [−]
ε_3	Threshold value for activation of cell [−]
ε_4	Tolerance value for convergence [−]
Δs	Spatial step size [m]
Δt	Temporal step size [s]
Δx	Mesh step size in x-direction of CFD simulations [m]
Δy	Mesh step size in y-direction of CFD simulations [m]
nt	Number of time steps [−]
N	Number of cells [−]

A

Advective terms in solver matrix

In this Appendix, the representation of the advective terms of equation (4.13) used in the coupled solver is derived. These terms are still defined at the nodes $i-\frac{1}{2}$ and $i-\frac{1}{2}$, whereas the solver matrix **A** requires the terms to be defined at the cell centres for the coupled approach. These terms are:

- $\Delta\hat{\alpha}^{m+1}_{u_{i+\frac{1}{2}}}\hat{\rho}^{n}_{u_{i+\frac{1}{2}}}u^{m}_{s,u_{i+\frac{1}{2}}}A_{i+\frac{1}{2}}$ and,
- $\Delta\hat{\alpha}^{m+1}_{u_{i-\frac{1}{2}}}\hat{\rho}^{n}_{u_{i-\frac{1}{2}}}u^{m}_{s,u_{i-\frac{1}{2}}}A_{i-\frac{1}{2}}$.

The scalar quantities at the $i\pm\frac{1}{2}^{\text{th}}$ nodes are defined in equation (4.39) using a high-resolution scheme. This equation makes it possible to rewrite the advective terms to the nodal notation used to indicate the cell centres. The residual side of the equation does not have to be altered, as the values of the advective terms on the $i\pm\frac{1}{2}^{\text{th}}$ nodes calculated by the model are directly used in the residuals.

The cross-sectional area is constant throughout the system and is not discretised by a high-resolution scheme. The axial velocity of the upper region is already defined at cell edges, as the staggered grid layout is used. Therefore, only the incremental hold-up of the upper region and the density of the upper region variables have to be discretised by the high-resolution scheme. The smoothness gradient of the hold-up is denoted by $\lambda^{\alpha_u}_{i\pm\frac{1}{2}}$ and the smoothness gradient of the density of the upper region is denoted by $\lambda^{\alpha_u}_{i\pm\frac{1}{2}}$.

As is shown in Section 4.5.3, the nodes which are used to determine the smoothness gradient and the value of scalar quantity Q at the cell edges depend on the sign of the velocity variable. The Leonard & Mokhtari notation is not repeated here. The time and iteration step dependencies are omitted for readability.

For $u_{s,u_{i+\frac{1}{2}}}\geq 0$, the variables of the advective term at the $i+\frac{1}{2}$ node are rewritten as:

$$
\begin{aligned}
&\Delta\hat{\alpha}_{u_{i+\frac{1}{2}}}\hat{\rho}_{u_{i+\frac{1}{2}}}u_{s,u_{i+\frac{1}{2}}}A_{i+\frac{1}{2}}\\
&=\left(\left(1-\frac{1}{2}\mathscr{L}\left(\lambda^{\alpha_u}_{i+\frac{1}{2}}\right)\right)\Delta\alpha_{u_i}+\frac{1}{2}\mathscr{L}\left(\lambda^{\alpha_u}_{i+\frac{1}{2}}\right)\Delta\alpha_{u_{i+1}}\right)\left(\left(1-\frac{1}{2}\mathscr{L}\left(\lambda^{\rho_u}_{i+\frac{1}{2}}\right)\right)\rho_{u_i}+\frac{1}{2}\mathscr{L}\left(\lambda^{\rho_u}_{i+\frac{1}{2}}\right)\rho_{u_{i+1}}\right)u_{s,u_{i+\frac{1}{2}}}A_{i+\frac{1}{2}}\\
&=\left(1-\frac{1}{2}\mathscr{L}\left(\lambda^{\alpha_u}_{i+\frac{1}{2}}\right)\right)\left(1-\frac{1}{2}\mathscr{L}\left(\lambda^{\rho_u}_{i+\frac{1}{2}}\right)\right)\Delta\alpha_{u_i}\rho_{u_i}u_{s,u_{i+\frac{1}{2}}}A_{i+\frac{1}{2}}\ldots\\
&+\left(1-\frac{1}{2}\mathscr{L}\left(\lambda^{\alpha_u}_{i+\frac{1}{2}}\right)\right)\frac{1}{2}\mathscr{L}\left(\lambda^{\rho_u}_{i+\frac{1}{2}}\right)\Delta\alpha_{u_i}\rho_{u_{i+1}}u_{s,u_{i+\frac{1}{2}}}A_{i+\frac{1}{2}}\ldots\\
&+\frac{1}{2}\mathscr{L}\left(\lambda^{\alpha_u}_{i+\frac{1}{2}}\right)\left(1-\frac{1}{2}\mathscr{L}\left(\lambda^{\rho_u}_{i+\frac{1}{2}}\right)\right)\Delta\alpha_{u_{i+1}}\rho_{u_i}u_{s,u_{i+\frac{1}{2}}}A_{i+\frac{1}{2}}\ldots\\
&+\frac{1}{4}\mathscr{L}\left(\lambda^{\alpha_u}_{i+\frac{1}{2}}\right)\mathscr{L}\left(\lambda^{\rho_u}_{i+\frac{1}{2}}\right)\Delta\alpha_{u_{i+1}}\rho_{u_{i+1}}u_{s,u_{i+\frac{1}{2}}}A_{i+\frac{1}{2}},
\end{aligned}
\tag{A.1}
$$

and for $u_{s,u_{i+\frac{1}{2}}} < 0$, the variables become:

$$
\begin{aligned}
&\Delta\hat{\alpha}_{u_{i+\frac{1}{2}}}\hat{\rho}_{u_{i+\frac{1}{2}}}u_{s,u_{i+\frac{1}{2}}}A_{i+\frac{1}{2}}\\
&=\left(\frac{1}{2}\mathscr{L}\left(\lambda^{\alpha_u}_{i+\frac{1}{2}}\right)\Delta\alpha_{u_i}+\left(1-\frac{1}{2}\mathscr{L}\left(\lambda^{\alpha_u}_{i+\frac{1}{2}}\right)\right)\Delta\alpha_{u_{i+1}}\right)\left(\frac{1}{2}\mathscr{L}\left(\lambda^{\rho_u}_{i+\frac{1}{2}}\right)\rho_{u_i}+\left(1-\frac{1}{2}\mathscr{L}\left(\lambda^{\rho_u}_{i+\frac{1}{2}}\right)\right)\rho_{u_{i+1}}\right)u_{s,u_{i+\frac{1}{2}}}A_{i+\frac{1}{2}}\\
&=\frac{1}{4}\mathscr{L}\left(\lambda^{\alpha_u}_{i+\frac{1}{2}}\right)\mathscr{L}\left(\lambda^{\rho_u}_{i+\frac{1}{2}}\right)\Delta\alpha_{u_i}\rho_{u_i}u_{s,u_{i+\frac{1}{2}}}A_{i+\frac{1}{2}}\cdots\\
&+\frac{1}{2}\mathscr{L}\left(\lambda^{\alpha_u}_{i+\frac{1}{2}}\right)\left(1-\frac{1}{2}\mathscr{L}\left(\lambda^{\rho_u}_{i+\frac{1}{2}}\right)\right)\Delta\alpha_{u_i}\rho_{u_{i+1}}u_{s,u_{i+\frac{1}{2}}}A_{i+\frac{1}{2}}\cdots\\
&+\left(1-\frac{1}{2}\mathscr{L}\left(\lambda^{\alpha_u}_{i+\frac{1}{2}}\right)\right)\frac{1}{2}\mathscr{L}\left(\lambda^{\rho_u}_{i+\frac{1}{2}}\right)\Delta\alpha_{u_{i+1}}\rho_{u_i}u_{s,u_{i+\frac{1}{2}}}A_{i+\frac{1}{2}}\cdots\\
&+\left(1-\frac{1}{2}\mathscr{L}\left(\lambda^{\alpha_u}_{i+\frac{1}{2}}\right)\right)\left(1-\frac{1}{2}\mathscr{L}\left(\lambda^{\rho_u}_{i+\frac{1}{2}}\right)\right)\Delta\alpha_{u_{i+1}}\rho_{u_{i+1}}u_{s,u_{i+\frac{1}{2}}}A_{i+\frac{1}{2}}.
\end{aligned}
\tag{A.2}
$$

The variables of the advective term at $i-\frac{1}{2}$ are rewritten for $u_{s,u_{i-\frac{1}{2}}} \geq 0$ as:

$$
\begin{aligned}
&\Delta\hat{\alpha}_{u_{i-\frac{1}{2}}}\hat{\rho}_{u_{i-\frac{1}{2}}}u_{s,u_{i-\frac{1}{2}}}A_{i-\frac{1}{2}}\\
&=\left(\left(1-\frac{1}{2}\mathscr{L}\left(\lambda^{\alpha_u}_{i-\frac{1}{2}}\right)\right)\Delta\alpha_{u_{i-1}}+\frac{1}{2}\mathscr{L}\left(\lambda^{\alpha_u}_{i-\frac{1}{2}}\right)\Delta\alpha_{u_i}\right)\left(\left(1-\frac{1}{2}\mathscr{L}\left(\lambda^{\rho_u}_{i-\frac{1}{2}}\right)\right)\rho_{u_{i-1}}+\frac{1}{2}\mathscr{L}\left(\lambda^{\rho_u}_{i-\frac{1}{2}}\right)\rho_{u_i}\right)u_{s,u_{i-\frac{1}{2}}}A_{i-\frac{1}{2}}\\
&=\left(1-\frac{1}{2}\mathscr{L}\left(\lambda^{\alpha_u}_{i-\frac{1}{2}}\right)\right)\left(1-\frac{1}{2}\mathscr{L}\left(\lambda^{\rho_u}_{i-\frac{1}{2}}\right)\right)\Delta\alpha_{u_{i-1}}\rho_{u_{i-1}}u_{s,u_{i-\frac{1}{2}}}A_{i-\frac{1}{2}}\cdots\\
&+\left(1-\frac{1}{2}\mathscr{L}\left(\lambda^{\alpha_u}_{i-\frac{1}{2}}\right)\right)\frac{1}{2}\mathscr{L}\left(\lambda^{\rho_u}_{i-\frac{1}{2}}\right)\Delta\alpha_{u_{i-1}}\rho_{u_i}u_{s,u_{i-\frac{1}{2}}}A_{i-\frac{1}{2}}\cdots\\
&+\frac{1}{2}\mathscr{L}\left(\lambda^{\alpha_u}_{i-\frac{1}{2}}\right)\left(1-\frac{1}{2}\mathscr{L}\left(\lambda^{\rho_u}_{i-\frac{1}{2}}\right)\right)\Delta\alpha_{u_i}\rho_{u_{i-1}}u_{s,u_{i-\frac{1}{2}}}A_{i-\frac{1}{2}}\cdots\\
&+\frac{1}{4}\mathscr{L}\left(\lambda^{\alpha_u}_{i-\frac{1}{2}}\right)\mathscr{L}\left(\lambda^{\rho_u}_{i-\frac{1}{2}}\right)\Delta\alpha_{u_i}\rho_{u_i}u_{s,u_{i-\frac{1}{2}}}A_{i-\frac{1}{2}},
\end{aligned}
\tag{A.3}
$$

and the variables for $u_{s,u_{i-\frac{1}{2}}} < 0$ become:

$$
\begin{aligned}
&\Delta\hat{\alpha}_{u_{i-\frac{1}{2}}}\hat{\rho}_{u_{i-\frac{1}{2}}}u_{s,u_{i-\frac{1}{2}}}A_{i-\frac{1}{2}}\\
&=\left(\frac{1}{2}\mathscr{L}\left(\lambda^{\alpha_u}_{i-\frac{1}{2}}\right)\Delta\alpha_{u_{i-1}}+\left(1-\frac{1}{2}\mathscr{L}\left(\lambda^{\alpha_u}_{i-\frac{1}{2}}\right)\right)\Delta\alpha_{u_i}\right)\left(\frac{1}{2}\mathscr{L}\left(\lambda^{\rho_u}_{i-\frac{1}{2}}\right)\rho_{u_{i-1}}+\left(1-\frac{1}{2}\mathscr{L}\left(\lambda^{\rho_u}_{i-\frac{1}{2}}\right)\right)\rho_{u_i}\right)u_{s,u_{i-\frac{1}{2}}}A_{i-\frac{1}{2}}\\
&=\frac{1}{4}\mathscr{L}\left(\lambda^{\alpha_u}_{i-\frac{1}{2}}\right)\mathscr{L}\left(\lambda^{\rho_u}_{i-\frac{1}{2}}\right)\Delta\alpha_{u_{i-1}}\rho_{u_{i-1}}u_{s,u_{i-\frac{1}{2}}}A_{i-\frac{1}{2}}\cdots\\
&+\frac{1}{2}\mathscr{L}\left(\lambda^{\alpha_u}_{i-\frac{1}{2}}\right)\left(1-\frac{1}{2}\mathscr{L}\left(\lambda^{\rho_u}_{i-\frac{1}{2}}\right)\right)\Delta\alpha_{u_{i-1}}\rho_{u_i}u_{s,u_{i-\frac{1}{2}}}A_{i-\frac{1}{2}}\cdots\\
&+\left(1-\frac{1}{2}\mathscr{L}\left(\lambda^{\alpha_u}_{i-\frac{1}{2}}\right)\right)\frac{1}{2}\mathscr{L}\left(\lambda^{\rho_u}_{i-\frac{1}{2}}\right)\Delta\alpha_{u_i}\rho_{u_{i-1}}u_{s,u_{i-\frac{1}{2}}}A_{i-\frac{1}{2}}\cdots\\
&+\left(1-\frac{1}{2}\mathscr{L}\left(\lambda^{\alpha_u}_{i-\frac{1}{2}}\right)\right)\left(1-\frac{1}{2}\mathscr{L}\left(\lambda^{\rho_u}_{i-\frac{1}{2}}\right)\right)\Delta\alpha_{u_i}\rho_{u_i}u_{s,u_{i-\frac{1}{2}}}A_{i-\frac{1}{2}}.
\end{aligned}
\tag{A.4}
$$

In total, four possibilities exist to implement these variables into the fully discretised IPCE of equation (4.13). This depends on the sign of the velocity of the upper region on the nodes $i+\frac{1}{2}$ and $i-\frac{1}{2}$:

1. $u_{s,u_{i+\frac{1}{2}}} \geq 0$ and $u_{s,u_{i-\frac{1}{2}}} \geq 0$;

$$
\begin{aligned}
&\frac{\Delta\hat{\alpha}_{u_{i+\frac{1}{2}}}\hat{\rho}_{u_{i+\frac{1}{2}}}u_{s,u_{i+\frac{1}{2}}}A_{i+\frac{1}{2}} - u_{s,u_{i-\frac{1}{2}}}\hat{\rho}_{u_{i-\frac{1}{2}}}\Delta\hat{\alpha}_{u_{i-\frac{1}{2}}}A_{i-\frac{1}{2}}}{A_i\Delta_s}\ldots \\
&= \frac{\Delta\alpha_{u_{i+1}}\left[\frac{1}{2}\mathscr{L}\left(\lambda^{\alpha_u}_{i+\frac{1}{2}}\right)\left(1-\frac{1}{2}\mathscr{L}\left(\lambda^{\rho_u}_{i+\frac{1}{2}}\right)\right)\rho_{u_i} + \frac{1}{4}\mathscr{L}\left(\lambda^{\alpha_u}_{i+\frac{1}{2}}\right)\mathscr{L}\left(\lambda^{\rho_u}_{i+\frac{1}{2}}\right)\rho_{u_{i+1}}\right]u_{u_{i+\frac{1}{2}}}A_{i+\frac{1}{2}}}{A_i\Delta s}\ldots \\
&+ \frac{\Delta\alpha_{u_i}\left[\left(1-\frac{1}{2}\mathscr{L}\left(\lambda^{\alpha_u}_{i+\frac{1}{2}}\right)\right)\left(1-\frac{1}{2}\mathscr{L}\left(\lambda^{\rho_u}_{i+\frac{1}{2}}\right)\right)\rho_{u_i} + \left(1-\frac{1}{2}\mathscr{L}\left(\lambda^{\alpha_u}_{i+\frac{1}{2}}\right)\right)\frac{1}{2}\mathscr{L}\left(\lambda^{\rho_u}_{i+\frac{1}{2}}\right)\rho_{u_{i+1}}\right]u_{u_{i+\frac{1}{2}}}A_{i+\frac{1}{2}}}{A_i\Delta s}\ldots \\
&- \frac{\Delta\alpha_{u_i}\left[\frac{1}{2}\mathscr{L}\left(\lambda^{\alpha_u}_{i-\frac{1}{2}}\right)\left(1-\frac{1}{2}\mathscr{L}\left(\lambda^{\rho_u}_{i-\frac{1}{2}}\right)\right)\rho_{u_{i-1}} + \frac{1}{4}\mathscr{L}\left(\lambda^{\alpha_u}_{i-\frac{1}{2}}\right)\mathscr{L}\left(\lambda^{\rho_u}_{i-\frac{1}{2}}\right)\rho_{u_i}\right]u_{u_{i-\frac{1}{2}}}A_{i-\frac{1}{2}}}{A_i\Delta s}\ldots \\
&- \frac{\Delta\alpha_{u_{i-1}}\left(\left(1-\frac{1}{2}\mathscr{L}\left(\lambda^{\alpha_u}_{i-\frac{1}{2}}\right)\right)\left(1-\frac{1}{2}\mathscr{L}\left(\lambda^{\rho_u}_{i-\frac{1}{2}}\right)\right)\rho_{u_{i-1}} + \left(1-\frac{1}{2}\mathscr{L}\left(\lambda^{\alpha_u}_{i-\frac{1}{2}}\right)\right)\frac{1}{2}\mathscr{L}\left(\lambda^{\rho_u}_{i-\frac{1}{2}}\right)\rho_{u_i}\right)u_{u_{i-\frac{1}{2}}}A_{i-\frac{1}{2}}}{A_i\Delta s}.
\end{aligned}
\tag{A.5}
$$

2. $u_{s,u_{i+\frac{1}{2}}} \geq 0$ and $u_{s,u_{i-\frac{1}{2}}} < 0$;

$$
\begin{aligned}
&\frac{\Delta\hat{\alpha}_{u_{i+\frac{1}{2}}}\hat{\rho}_{u_{i+\frac{1}{2}}}u_{s,u_{i+\frac{1}{2}}}A_{i+\frac{1}{2}} - u_{s,u_{i-\frac{1}{2}}}\hat{\rho}_{u_{i-\frac{1}{2}}}\Delta\hat{\alpha}_{u_{i-\frac{1}{2}}}A_{i-\frac{1}{2}}}{A_i\Delta_s}\ldots \\
&= \frac{\Delta\alpha_{u_{i+1}}\left[\frac{1}{2}\mathscr{L}\left(\lambda^{\alpha_u}_{i+\frac{1}{2}}\right)\left(1-\frac{1}{2}\mathscr{L}\left(\lambda^{\rho_u}_{i+\frac{1}{2}}\right)\right)\rho_{u_i} + \frac{1}{4}\mathscr{L}\left(\lambda^{\alpha_u}_{i+\frac{1}{2}}\right)\mathscr{L}\left(\lambda^{\rho_u}_{i+\frac{1}{2}}\right)\rho_{u_{i+1}}\right]u_{u_{i+\frac{1}{2}}}A_{i+\frac{1}{2}}}{A_i\Delta s}\ldots \\
&+ \frac{\Delta\alpha_{u_i}\left[\left(1-\frac{1}{2}\mathscr{L}\left(\lambda^{\alpha_u}_{i+\frac{1}{2}}\right)\right)\left(1-\frac{1}{2}\mathscr{L}\left(\lambda^{\rho_u}_{i+\frac{1}{2}}\right)\right)\rho_{u_i} + \left(1-\frac{1}{2}\mathscr{L}\left(\lambda^{\alpha_u}_{i+\frac{1}{2}}\right)\right)\frac{1}{2}\mathscr{L}\left(\lambda^{\rho_u}_{i+\frac{1}{2}}\right)\rho_{u_{i+1}}\right]u_{u_{i+\frac{1}{2}}}A_{i+\frac{1}{2}}}{A_i\Delta s}\ldots \\
&- \frac{\Delta\alpha_{u_i}\left[\left(1-\frac{1}{2}\mathscr{L}\left(\lambda^{\alpha_u}_{i-\frac{1}{2}}\right)\right)\frac{1}{2}\mathscr{L}\left(\lambda^{\rho_u}_{i-\frac{1}{2}}\right)\rho_{u_{i-1}} + \left(1-\frac{1}{2}\mathscr{L}\left(\lambda^{\alpha_u}_{i-\frac{1}{2}}\right)\right)\left(1-\frac{1}{2}\mathscr{L}\left(\lambda^{\rho_u}_{i-\frac{1}{2}}\right)\right)\rho_{u_i}\right]u_{u_{i-\frac{1}{2}}}A_{i-\frac{1}{2}}}{A_i\Delta s}\ldots \\
&- \frac{\Delta\alpha_{u_{i-1}}\left(\frac{1}{4}\mathscr{L}\left(\lambda^{\alpha_u}_{i-\frac{1}{2}}\right)\mathscr{L}\left(\lambda^{\rho_u}_{i-\frac{1}{2}}\right)\rho_{u_{i-1}} + \frac{1}{2}\mathscr{L}\left(\lambda^{\alpha_u}_{i-\frac{1}{2}}\right)\left(1-\frac{1}{2}\mathscr{L}\left(\lambda^{\rho_u}_{i-\frac{1}{2}}\right)\right)\rho_{u_i}\right)u_{u_{i-\frac{1}{2}}}A_{i-\frac{1}{2}}}{A_i\Delta s}.
\end{aligned}
\tag{A.6}
$$

3. $u_{s,u_{i+\frac{1}{2}}} < 0$ and $u_{s,u_{i-\frac{1}{2}}} \geq 0$;

$$
\begin{aligned}
&\frac{\Delta\hat{\alpha}_{u_{i+\frac{1}{2}}}\hat{\rho}_{u_{i+\frac{1}{2}}}u_{s,u_{i+\frac{1}{2}}}A_{i+\frac{1}{2}} - u_{s,u_{i-\frac{1}{2}}}\hat{\rho}_{u_{i-\frac{1}{2}}}\Delta\hat{\alpha}_{u_{i-\frac{1}{2}}}A_{i-\frac{1}{2}}}{A_i\Delta_s}\ldots \\
&= \frac{\Delta\alpha_{u_{i+1}}\left[\left(1-\frac{1}{2}\mathscr{L}\left(\lambda^{\alpha_u}_{i+\frac{1}{2}}\right)\right)\frac{1}{2}\mathscr{L}\left(\lambda^{\rho_u}_{i+\frac{1}{2}}\right)\rho_{u_i} + \left(1-\frac{1}{2}\mathscr{L}\left(\lambda^{\alpha_u}_{i+\frac{1}{2}}\right)\right)\left(1-\frac{1}{2}\mathscr{L}\left(\lambda^{\rho_u}_{i+\frac{1}{2}}\right)\right)\rho_{u_{i+1}}\right]u_{u_{i+\frac{1}{2}}}A_{i+\frac{1}{2}}}{A_i\Delta s}\ldots \\
&+ \frac{\Delta\alpha_{u_i}\left[\frac{1}{4}\mathscr{L}\left(\lambda^{\alpha_u}_{i+\frac{1}{2}}\right)\mathscr{L}\left(\lambda^{\rho_u}_{i+\frac{1}{2}}\right)\rho_{u_i} + \frac{1}{2}\mathscr{L}\left(\lambda^{\alpha_u}_{i+\frac{1}{2}}\right)\left(1-\frac{1}{2}\mathscr{L}\left(\lambda^{\rho_u}_{i+\frac{1}{2}}\right)\right)\rho_{u_{i+1}}\right]u_{u_{i+\frac{1}{2}}}A_{i+\frac{1}{2}}}{A_i\Delta s}\ldots \\
&- \frac{\Delta\alpha_{u_i}\left[\frac{1}{2}\mathscr{L}\left(\lambda^{\alpha_u}_{i-\frac{1}{2}}\right)\left(1-\frac{1}{2}\mathscr{L}\left(\lambda^{\rho_u}_{i-\frac{1}{2}}\right)\right)\rho_{u_{i-1}} + \frac{1}{4}\mathscr{L}\left(\lambda^{\alpha_u}_{i-\frac{1}{2}}\right)\mathscr{L}\left(\lambda^{\rho_u}_{i-\frac{1}{2}}\right)\rho_{u_i}\right]u_{u_{i-\frac{1}{2}}}A_{i-\frac{1}{2}}}{A_i\Delta s}\ldots \\
&- \frac{\Delta\alpha_{u_{i-1}}\left(\left(1-\frac{1}{2}\mathscr{L}\left(\lambda^{\alpha_u}_{i-\frac{1}{2}}\right)\right)\left(1-\frac{1}{2}\mathscr{L}\left(\lambda^{\rho_u}_{i-\frac{1}{2}}\right)\right)\rho_{u_{i-1}} + \left(1-\frac{1}{2}\mathscr{L}\left(\lambda^{\alpha_u}_{i-\frac{1}{2}}\right)\right)\frac{1}{2}\mathscr{L}\left(\lambda^{\rho_u}_{i-\frac{1}{2}}\right)\rho_{u_i}\right)u_{u_{i-\frac{1}{2}}}A_{i-\frac{1}{2}}}{A_i\Delta s}.
\end{aligned}
\tag{A.7}
$$

4. $u_{s,u_{i+\frac{1}{2}}} < 0$ and $u_{s,u_{i-\frac{1}{2}}} < 0$.

$$
\begin{aligned}
&\frac{\Delta\hat{\alpha}_{u_{i+\frac{1}{2}}}\hat{\rho}_{u_{i+\frac{1}{2}}}u_{s,u_{i+\frac{1}{2}}}A_{i+\frac{1}{2}} - u_{s,u_{i-\frac{1}{2}}}\hat{\rho}_{u_{i-\frac{1}{2}}}\Delta\hat{\alpha}_{u_{i-\frac{1}{2}}}A_{i-\frac{1}{2}}}{A_i\Delta_s}\ldots \\
&= \frac{\Delta\alpha_{u_{i+1}}\left[\left(1-\frac{1}{2}\mathscr{L}\left(\lambda^{\alpha_u}_{i+\frac{1}{2}}\right)\right)\frac{1}{2}\mathscr{L}\left(\lambda^{\rho_u}_{i+\frac{1}{2}}\right)\rho_{u_i} + \left(1-\frac{1}{2}\mathscr{L}\left(\lambda^{\alpha_u}_{i+\frac{1}{2}}\right)\right)\left(1-\frac{1}{2}\mathscr{L}\left(\lambda^{\rho_u}_{i+\frac{1}{2}}\right)\right)\rho_{u_{i+1}}\right]u_{u_{i+\frac{1}{2}}}A_{i+\frac{1}{2}}}{A_i\Delta s}\ldots \\
&+ \frac{\Delta\alpha_{u_i}\left[\frac{1}{4}\mathscr{L}\left(\lambda^{\alpha_u}_{i+\frac{1}{2}}\right)\mathscr{L}\left(\lambda^{\rho_u}_{i+\frac{1}{2}}\right)\rho_{u_i} + \frac{1}{2}\mathscr{L}\left(\lambda^{\alpha_u}_{i+\frac{1}{2}}\right)\left(1-\frac{1}{2}\mathscr{L}\left(\lambda^{\rho_u}_{i+\frac{1}{2}}\right)\right)\rho_{u_{i+1}}\right]u_{u_{i+\frac{1}{2}}}A_{i+\frac{1}{2}}}{A_i\Delta s}\ldots \\
&- \frac{\Delta\alpha_{u_i}\left[\left(1-\frac{1}{2}\mathscr{L}\left(\lambda^{\alpha_u}_{i-\frac{1}{2}}\right)\right)\frac{1}{2}\mathscr{L}\left(\lambda^{\rho_u}_{i-\frac{1}{2}}\right)\rho_{u_{i-1}} + \left(1-\frac{1}{2}\mathscr{L}\left(\lambda^{\alpha_u}_{i-\frac{1}{2}}\right)\right)\left(1-\frac{1}{2}\mathscr{L}\left(\lambda^{\rho_u}_{i-\frac{1}{2}}\right)\right)\rho_{u_i}\right]u_{u_{i-\frac{1}{2}}}A_{i-\frac{1}{2}}}{A_i\Delta s}\ldots \\
&- \frac{\Delta\alpha_{u_{i-1}}\left(\frac{1}{4}\mathscr{L}\left(\lambda^{\alpha_u}_{i-\frac{1}{2}}\right)\mathscr{L}\left(\lambda^{\rho_u}_{i-\frac{1}{2}}\right)\rho_{u_{i-1}} + \frac{1}{2}\mathscr{L}\left(\lambda^{\alpha_u}_{i-\frac{1}{2}}\right)\left(1-\frac{1}{2}\mathscr{L}\left(\lambda^{\rho_u}_{i-\frac{1}{2}}\right)\right)\rho_{u_i}\right)u_{u_{i-\frac{1}{2}}}A_{i-\frac{1}{2}}}{A_i\Delta s}.
\end{aligned}
\tag{A.8}
$$

The advective terms of the fully discretised volume fraction equations of (4.26) & (4.28) are constructed in a similar way. These terms are implemented in the Python code with the help of the sign-function.

B

Newton's method for an immiscible solver

Picard's method is applied to linearise the nonlinear terms in the current numerical method, although the method is only able to achieve a linear convergence rate. This appendix will show how Newton's method could be implemented in the current numerical model and that faster convergence rates can be achieved by applying Newton's linearisation.

It is chosen to implement Newton's process for an immiscible fluid-fluid displacement model, as less linearisation processes are required compared to a miscible model. The fluids do not dissolve into each other, which implies that only the hold-up equation is sufficient to track the fluid within the interior fluid domain. The volume fraction equations are not solved for an immiscible model. Furthermore, the mass transfer term is dropped out of the hold-up equation, as no mass transfer takes place between the fluid for immiscible flow. Also, the density variables of the upper region satisfy the material derivative for immiscible flow; the density variables are removed from the hold-up equation. The immiscible model is further simplified as channel flow is assumed. The slip relation and the incompressible velocity equation (and its boundary condition at node $N+\frac{1}{2}$) do not change for an immiscible model.

First, Newton's method is applied on the hold-up equation and the incompressible velocity equation, as the linearisation process is relatively easy. The linearisation process of the slip relation is more difficult and is described at last.

The immiscible hold-up equation is defined as:

$$\frac{\partial \alpha_u}{\partial t} + \frac{\partial}{\partial s}\left(\alpha_u u_{s,u} A\right) = 0. \tag{B.1}$$

The hold-up relation is discretised by the implicit Euler method in time and its advection term is discretised by the upwind scheme. The fully discretised hold-up equation for immiscible flow is defined as:

$$\frac{\alpha_{u,i}^{m+1} - \alpha_{u,i}^{n}}{\Delta t} + \frac{\hat{\alpha}_{u_{i-\frac{1}{2}}}^{m+1} u_{s,u_{i-\frac{1}{2}}}^{m+1} A_{i-\frac{1}{2}} - \hat{\alpha}_{u_{i-\frac{1}{2}}}^{m+1} u_{s,u_{i-\frac{1}{2}}}^{m+1} A_{i-\frac{1}{2}}}{A_i \Delta s} = 0. \tag{B.2}$$

The nonlinear terms, which require to be linearised by Newton's method are:

- $\hat{\alpha}_{u_{i-\frac{1}{2}}}^{m+1} u_{s,u_{i-\frac{1}{2}}}^{m+1}$ and;
- $\hat{\alpha}_{u_{i-\frac{1}{2}}}^{m+1} u_{u_{i-\frac{1}{2}}}^{m+1}$.

Here, only the term at node $i-\frac{1}{2}$ is linearised, as the term at node $i+\frac{1}{2}$ gives the same results with another nodal notation. The terms are approximated by the function f.

$$\begin{aligned}
f\left(\alpha_u^{m+1}, u_{s,u}^{m+1}\right) &= \hat{\alpha}_{u_{i-\frac{1}{2}}}^{m+1} u_{s,u_{i-\frac{1}{2}}}^{m+1} \\
f\left(\alpha_u^{m+1}, u_{s,u}^{m+1}\right) &= f\left(\alpha_u^{m} + \Delta\alpha_u^{m+1}, u_{s,u}^{m+1} + \Delta u_{s,u}^{m+1}\right) \\
f\left(\alpha_u^{m} + \Delta\alpha_u^{m+1}, u_{s,u}^{m+1} + \Delta u_{s,u}^{m+1}\right) &= \left(\hat{\alpha}_{u_{i-\frac{1}{2}}}^{m} + \Delta\hat{\alpha}_{u_{i-\frac{1}{2}}}^{m+1}\right)\left(u_{s,u_{i-\frac{1}{2}}}^{m} + \Delta u_{s,u_{i-\frac{1}{2}}}^{m+1}\right)
\end{aligned} \tag{B.3}$$

The advection term of function f can be approximated by:

$$\begin{aligned} f\left(\alpha_u^{m+1}, u_{s,u}^{m+1}\right) &\approx f\left(\alpha_u^m, u_{s,u}^m\right) &&+ \frac{\partial f}{\partial \alpha}\left(\alpha_u^m, u_{s,u}^m\right)\Delta\hat{\alpha}_{u_{i-\frac{1}{2}}}^{m+1} &&+ \frac{\partial f}{\partial u}\left(\alpha_u^m, u_{s,u}^m\right)\Delta u_{s,u_{i-\frac{1}{2}}}^{m+1}, \\ f\left(\alpha_u^{m+1}, u_{s,u}^{m+1}\right) &\approx \hat{\alpha}_{u_{i-\frac{1}{2}}}^m u_{s,u_{i-\frac{1}{2}}}^m &&+ \Delta\hat{\alpha}_{u_{i-\frac{1}{2}}}^{m+1} u_{s,u_{i-\frac{1}{2}}}^m &&+ \hat{\alpha}_{u_{i-\frac{1}{2}}}^m \Delta u_{s,u_{i-\frac{1}{2}}}^{m+1}, \end{aligned} \tag{B.4}$$

which is the same result as reported in equation (4.10). Substituting the terms of Eqn (B.4) back into the fully discretised hold-up equation of (B.2) yields:

$$\begin{aligned} \frac{\Delta\alpha_{u_i}^{m+1}}{\Delta t} &+ \frac{\Delta\hat{\alpha}_{u_{i-\frac{1}{2}}}^{m+1} u_{s,u_{i-\frac{1}{2}}}^m A_{i-\frac{1}{2}} + \hat{\alpha}_{u_{i-\frac{1}{2}}}^m \Delta u_{s,u_{i-\frac{1}{2}}}^{m+1} A_{i-\frac{1}{2}}}{A_i \Delta s_i} \\ &- \frac{\Delta\hat{\alpha}_{u_{i-\frac{1}{2}}}^{m+1} u_{s,u_{i-\frac{1}{2}}}^m A_{i-\frac{1}{2}} + \hat{\alpha}_{u_{i-\frac{1}{2}}}^m \Delta u_{s,u_{i-\frac{1}{2}}}^{m+1} A_{i-\frac{1}{2}}}{A_i \Delta s_i} = \\ -\frac{\alpha_{u_i}^m - \alpha_{u_i}^n}{\Delta t} &- \frac{\hat{\alpha}_{u_{i-\frac{1}{2}}}^m u_{s,u_{i-\frac{1}{2}}}^m A_{i-\frac{1}{2}} - \hat{\alpha}_{u_{i-\frac{1}{2}}}^m u_{s,u_{i-\frac{1}{2}}}^m A_{i-\frac{1}{2}}}{A_i \Delta s_i}. \end{aligned} \tag{B.5}$$

The discrete incompresible velocity equation at iteration level $m+1$ is defined as:

$$\hat{\alpha}_{u_{i-\frac{1}{2}}}^{m+1} u_{s,u_{i-\frac{1}{2}}}^{m+1} + \hat{\alpha}_{l_{i-\frac{1}{2}}}^{m+1} u_{s,l_{i-\frac{1}{2}}}^{m+1} - \hat{\alpha}_{u_{i-\frac{1}{2}}}^{m+1} u_{s,u_{i-\frac{1}{2}}}^{m+1} - \hat{\alpha}_{l_{i-\frac{1}{2}}}^{m+1} u_{s,l_{i-\frac{1}{2}}}^{m+1} = 0. \tag{B.6}$$

The nonlinear terms, which require to be linearised by Newton's method are:

- $\hat{\alpha}_{u_{i-\frac{1}{2}}}^{m+1} u_{s,u_{i-\frac{1}{2}}}^{m+1}$,
- $\hat{\alpha}_{l_{i-\frac{1}{2}}}^{m+1} u_{s,l_{i-\frac{1}{2}}}^{m+1}$,
- $\hat{\alpha}_{u_{i-\frac{1}{2}}}^{m+1} u_{u_{i-\frac{1}{2}}}^{m+1}$ and
- $\hat{\alpha}_{l_{i-\frac{1}{2}}}^{m+1} u_{s,l_{i-\frac{1}{2}}}^{m+1}$.

The linearisation process of these nonlinear terms is exactly similar to the process visualised for the nonlinear terms of the hold-up equation. Therefore, the fully discretised Incompressible velocity equation for immiscible flow is immediatelly given, together with its fully discretised boundary condition at node $N+\frac{1}{2}$.

$$\begin{aligned} &\hat{\alpha}_{u_{i-\frac{1}{2}}}^m \Delta u_{s,u_{i-\frac{1}{2}}}^{m+1} + \hat{\alpha}_{l_{i-\frac{1}{2}}}^m \Delta u_{s,l_{i-\frac{1}{2}}}^{m+1} &&- \hat{\alpha}_{u_{i-\frac{1}{2}}}^m \Delta u_{s,u_{i-\frac{1}{2}}}^{m+1} - \hat{\alpha}_{l_{i-\frac{1}{2}}}^m \Delta u_{s,l_{i-\frac{1}{2}}}^{m+1} \dots \\ &+ \Delta\hat{\alpha}_{u_{i-\frac{1}{2}}}^{m+1} u_{s,u_{i-\frac{1}{2}}}^m + \Delta\hat{\alpha}_{l_{i-\frac{1}{2}}}^{m+1} u_{s,l_{i-\frac{1}{2}}}^m &&- \Delta\hat{\alpha}_{u_{i-\frac{1}{2}}}^{m+1} u_{s,u_{i-\frac{1}{2}}}^m - \Delta\hat{\alpha}_{l_{i-\frac{1}{2}}}^{m+1} u_{s,l_{i-\frac{1}{2}}}^m = \dots \\ &- \hat{\alpha}_{u_{i-\frac{1}{2}}}^m u_{s,u_{i-\frac{1}{2}}}^m - \hat{\alpha}_{l_{i-\frac{1}{2}}}^m u_{s,l_{i-\frac{1}{2}}}^m &&+ \hat{\alpha}_{u_{i-\frac{1}{2}}}^m u_{s,u_{i-\frac{1}{2}}}^m + \hat{\alpha}_{l_{i-\frac{1}{2}}}^m u_{s,l_{i-\frac{1}{2}}}^m \end{aligned} \tag{B.7}$$

$$\hat{\alpha}_{u_{N+\frac{1}{2}}}^m \Delta u_{s,u_{N+\frac{1}{2}}}^{m+1} + \hat{\alpha}_{l_{N+\frac{1}{2}}}^m \Delta u_{s,l_{N+\frac{1}{2}}}^{m+1} + \Delta\hat{\alpha}_{u_{N+\frac{1}{2}}}^{m+1} u_{s,u_{N+\frac{1}{2}}}^m + \Delta\hat{\alpha}_{l_{N+\frac{1}{2}}}^{m+1} u_{s,l_{N+\frac{1}{2}}}^m = u_s - \hat{\alpha}_{u_{N+\frac{1}{2}}}^m u_{s,u_{N+\frac{1}{2}}}^m - \hat{\alpha}_{l_{N+\frac{1}{2}}}^m u_{s,l_{N+\frac{1}{2}}}^m \tag{B.8}$$

The slip relation is more difficult to linearise, as it contains three nonlinear terms, the three Slip functions. The discretised slip relation at iteration level $m+1$ reads:

$$u_{s,u_{i-\frac{1}{2}}}^{m+1} - u_{s,l_{i-\frac{1}{2}}}^{m+1} = \mathscr{F}_{i-\frac{1}{2}}^{m+1} \mathscr{G}_{B_1 B_2 i-\frac{1}{2}}^{m+1} u_{E_{i-\frac{1}{2}}}^{m+1}, \tag{B.9}$$

where the dependencies of the slip relations are omitted. A linearised slip relation is investigated for the Benjamin bubble case and the W-shaped channel case, which are already discussed in Chapter 5. In both cases it is assumed that the light fluid flushes out the heavy fluid. The nonlinear Slip functions take the form of:

- $\mathscr{F}\mathscr{G}_{LH} u_E = \mathscr{F}_{i-\frac{1}{2}}\left(\tilde{\alpha}_{u_{i-\frac{1}{2}}}, \tilde{\theta}_{i-\frac{1}{2}}, \varepsilon_1\right) u_{E_{i-\frac{1}{2}}}\left(\tilde{\rho}_{u_{i-\frac{1}{2}}}, \tilde{\rho}_{u_{i-\frac{1}{2}}}, \tilde{\theta}_{i-\frac{1}{2}}\right)$ for the Benjamin bubble case, as $\mathscr{G}_{LH} = 1$ for $\theta = 0$, and
- $\mathscr{F}\mathscr{G}_{LH} u_E = \mathscr{F}_{i-\frac{1}{2}}\left(\tilde{\alpha}_{u_{i-\frac{1}{2}}}, \tilde{\theta}_{i-\frac{1}{2}}, \varepsilon_1\right) \mathscr{G}_{LH_{i-\frac{1}{2}}}\left(\tilde{\theta}_{i-\frac{1}{2}}, \frac{\mathrm{d}\tilde{h}}{\mathrm{d}s}_{i-\frac{1}{2}}, \varepsilon_2\right) u_{E_{i-\frac{1}{2}}}\left(\tilde{\rho}_{u_{i-\frac{1}{2}}}, \tilde{\rho}_{u_{i-\frac{1}{2}}}, \tilde{\theta}_{i-\frac{1}{2}}\right)$ for the W-shaped channel.

B.1. Benjamin bubble case

For immiscible flow, the effective bubble velocity function does not depend on the volume fractions. The density of the regions are simply given the value of their fluid, when it is present in a particular cell; i.e. the hold-up has to satisfy the threshold value ε_3. Therefore, the effective bubble velocity function does not require linearisation and its values at iteration level $m+1$ are approximated by its value at m.

$$\begin{aligned} u_E^{m+1} &\approx u_E^m + \frac{\partial u_E}{\partial u_{s,u}}\Delta u_{s,u} + \frac{\partial u_E}{\partial u_{s,l}}\Delta u_{s,l} + \frac{\partial u_E}{\partial \alpha_u}\Delta \alpha_u + \frac{\partial u_E}{\partial \alpha_l}\Delta \alpha_l \\ u_E^{m+1} &\approx u_E^m \end{aligned} \tag{B.10}$$

Note that only the velocity and hold-up variables are included in the solver matrix **A**. Therefore, only dependencies of the Slip functions regarding these variables can be included into the coupled solver by applying Newton's method.

The hold-up function is defined for a channel and an inclination angle of $\theta = 0$, as:

$$\mathscr{F}(\alpha_u, \varepsilon_1) = \begin{cases} \dfrac{-2\left(\frac{\alpha_u}{\varepsilon_1}\right)^3 + 3\left(\frac{\alpha_u}{\varepsilon_1}\right)^2}{2(1-\alpha_u)}, & \text{for } 0 \le \alpha_u < \varepsilon_1 \\ \dfrac{1}{2(1-\alpha_u)}, & \text{for } \varepsilon_1 \le \alpha_u < \dfrac{1}{2} \\ \dfrac{1}{2\alpha_u}, & \text{for } \dfrac{1}{2} \le \alpha_u < (1-\varepsilon_1) \\ \dfrac{\left(2\left(\frac{\alpha_u-(1-\varepsilon_1)}{\varepsilon_1}\right)^3 - 3\left(\frac{\alpha_u-(1-\varepsilon_1)}{\varepsilon_1}\right)^2 + 1\right)}{2\alpha_u}, & \text{for } \alpha_u \ge (1-\varepsilon). \end{cases} \tag{B.11}$$

The hold-up function for channel flow shows symmetrical behaviour, as $h = \frac{D_H}{2}$ and $u_F = u_B$ in a channel. [5]

The hold-up function is dependent on the hold-up of the upper region and can be linearised by Newton's method as:

$$\begin{aligned} \mathscr{F}^{m+1}\left(\alpha_u^{m+1}, \varepsilon_1\right) &= \mathscr{F}^{m+1}\left(\alpha_u^m + \Delta\alpha_u^{m+1}, \varepsilon_1\right), \\ \mathscr{F}^{m+1}\left(\alpha_u^{m+1}, \varepsilon_1\right) &\approx \mathscr{F}^{m}\left(\alpha_u^m, \varepsilon_1\right) + \frac{\partial \mathscr{F}}{\partial \alpha_u}\Delta\alpha_u^{m+1}. \end{aligned} \tag{B.12}$$

This implies that the derivative of the hold-up function has to be determined with respect to the hold-up of the upper region.

$$\frac{\partial \mathscr{F}(\alpha_u, \varepsilon_1)}{\partial \alpha_u} = \begin{cases} \dfrac{\left(-\frac{6}{\varepsilon_1^3}\alpha_u^2 + \frac{6}{\varepsilon_1^2}\alpha_u\right)\cdot(1-\alpha_u) - \left(-2\left(\frac{\alpha_u}{\varepsilon_1}\right)^3 + 6\left(\frac{\alpha_u}{\varepsilon_1}\right)^2\right)\cdot -1}{2(1-\alpha_u)^2}, & \text{for } 0 \le \alpha_u < \varepsilon_1 \\ \dfrac{1}{2(1-\alpha_u)^2}, & \text{for } \varepsilon_1 \le \alpha_u < \dfrac{1}{2} \\ -\dfrac{1}{2\alpha_u^2}, & \text{for } \dfrac{1}{2} \le \alpha_u < (1-\varepsilon_1) \\ \dfrac{\left(\frac{6}{\varepsilon_1^3}(\alpha_u-(1-\varepsilon_1))^2 - \frac{6}{\varepsilon_1^2}(\alpha_u-(1-\varepsilon_1))\right)\cdot\alpha_u}{2\alpha_u^2} + \dots & \\ \dfrac{-\left(2\left(\frac{\alpha_u-(1-\varepsilon_1)}{\varepsilon_1}\right)^3 - 3\left(\frac{\alpha_u-(1-\varepsilon_1)}{\varepsilon_1}\right)^2 + 1\right)\cdot 1}{2\alpha_u^2}, & \text{for } \alpha_u \ge (1-\varepsilon_1) \end{cases} \tag{B.13}$$

The hold-up function and its partial derivative with respect to the hold-up of the upper region are plotted in Fig. B.1. The hold-up function is defined at the $i-\frac{1}{2}^{\text{th}}$ node, therefore the hold-up variables are approximated by the central scheme, as:

$$\alpha_{u_{i-\frac{1}{2}}} = 0.5\left(\alpha_{u_{i-1}} + \alpha_{u_i}\right). \tag{B.14}$$

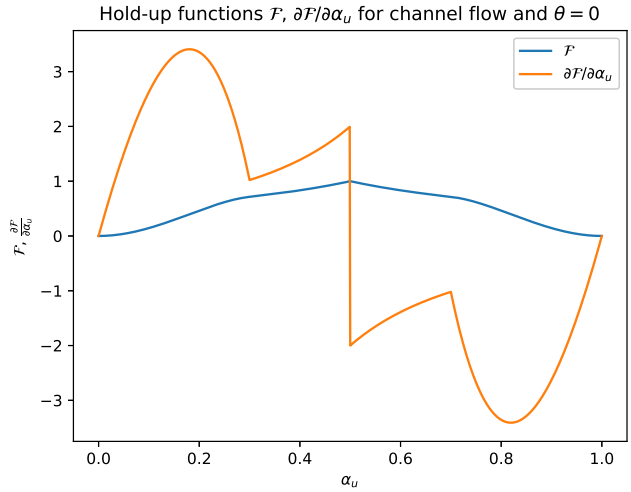

Figure B.1: The hold-up function $\mathscr{F}$ is presented together with its partial derivative with respect to the hold-up of the upper region for a horizontal channel.

So, the hold-up function at node $i-\frac{1}{2}$ solely depends on the hold-up variables at the nodes $i-1$ and i; i.e. $\mathscr{F}_{i-\frac{1}{2}} = \mathscr{F}_{i-\frac{1}{2}}\left(\alpha_{u_{i-1}}, \alpha_{u_i}, \varepsilon_1\right) = \mathscr{F}_{i-\frac{1}{2}}\left(\alpha_{u_{i-\frac{1}{2}}}, \varepsilon_1\right)$. The linearisation of equation (B.12) is extended to:

$$\mathscr{F}^{m+1}_{i-\frac{1}{2}}\left(\alpha^{m+1}_{u_{i-\frac{1}{2}}}, \varepsilon_1\right) \approx \mathscr{F}^{m}_{i-\frac{1}{2}}\left(\alpha^{m}_{u_{i-\frac{1}{2}}}, \varepsilon_1\right) + \left(\frac{\partial\mathscr{F}}{\partial\alpha_u}\right)^m_{i-\frac{1}{2}} \Delta\alpha^{m+1}_{u_{i-1}} + \left(\frac{\partial\mathscr{F}}{\partial\alpha_u}\right)^m_{i-\frac{1}{2}} \Delta\alpha^{m+1}_{u_i}. \tag{B.15}$$

The fully coupled discretised slip relation is defined for a horizontal channel section as:

$$\begin{aligned} &\Delta u^{m+1}_{s,u_{i-\frac{1}{2}}} - \Delta u^{m+1}_{s,l_{i-\frac{1}{2}}} - \left(\frac{\partial\mathscr{F}}{\partial\alpha_u}\right)^m_{i-\frac{1}{2}} u^m_{E_{i-\frac{1}{2}}} \Delta\alpha^{m+1}_{u_{i-1}} + \left(\frac{\partial\mathscr{F}}{\partial\alpha_u}\right)^m_{i-\frac{1}{2}} u^m_{E_{i-\frac{1}{2}}} \Delta\alpha^{m+1}_{u_i} = \dots \\ &\mathscr{F}^m_{i-\frac{1}{2}} u^m_{E_{i-\frac{1}{2}}} - u^m_{s,u_{i-\frac{1}{2}}} + u^m_{s,l_{i-\frac{1}{2}}}, \end{aligned} \tag{B.16}$$

where the dependencies of the hold-up function and the effective bubble velocity function are omitted for readability.

The same Benjamin bubble case as in Section 5.1 is applied, but now the gravity current travels in a channel instead of in a pipe. The most important simulation properties are summarised as:

- the channel section is completely horizontal; i.e. $\theta = 0$ [°];
- the channel height is $H = 0.1$ [m] corresponding to a hydraulic diameter of $D_H = 0.2$ [m];
- the flow is stagnant; i.e. $u_s = 0$ [$\frac{m}{s}$];
- the channel is 4 metres long; $s^* = 20$;
- the spatial step size is $\Delta s = 0.02$ [m], corresponding to $N = 200$;
- the Courant number is $Co = 0.5$, which leads to a temporal time step of $\Delta t \approx 0.007$ [s];
- the total simulation time is $t_{\max} = 10$ [s]; $t^* \approx 210$.

The flow solution results are not visualised, as the focus is purely on the difference in the convergence rates between Picard's and Newton's method. In Fig. B.2, the residuals of the hold-up and the velocity variables versus the iteration step are plotted. The residuals are shown at time $t = 1$ and $t = 5$ [s] for both Newton's and Picard's method.

The slopes of the residuals are given in Tab. B.1. A slope of minus two would indicate that an exponential convergence rate is achieved, whereas a slope of minus one would indicate that a linear convergence rate is obtained. Newton's method is capable of achieving exponential convergence rates, while Picard's method is only able to achieve linear convergence rates. It is seen that Newton's method achieves the expected convergence; it can be concluded that the method was correctly applied for the Benjamin bubble in a channel. The convergence rates for Picard's method are somewhat below one. Therefore, a completely linear convergence rate is not achieved for this method. The slopes of both methods over time are almost identical.

Furthermore, the average number of iterations per time step was 11.94 for Newton's method and 24.19 for Picard's method after a time of $t = 10$ $[s]$. This averaged number is normally higher; however when the equilibrium position is reached, low numbers of iterations per time step are seen for both methods. The flow solution does not change over time anymore as an equilibrium position is found; as a consequence the number of iterations goes down very rapidly. The number of iterations per time step required to meet the convergence criteria ε_4 = 1e-10, is plotted in Fig. B.3. Here, a second horizontal axis is added to relate a particular time step of the model to the physical time. The equilibrium position is reached at $t \approx 7$ $[s]$, which clearly has its influence on the number of iterations per time step.

Moreover, Newton's method was 1.9 times faster in finding the solution of the Benjamin bubble case in a channel.

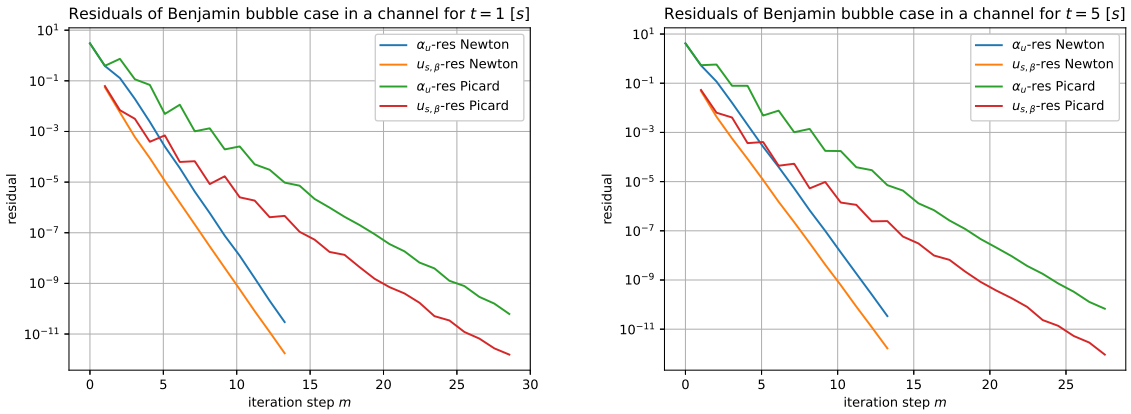

(a) Residuals at $t = 1$ $[s]$

(b) Residuals at $t = 5$ $[s]$

Figure B.2: Residuals of the hold-up of the upper region and the velocity variables for Newton's and Picard's method at $t = 1$ and $t = 5$ $[s]$ for a Benjamin bubble in a channel flow.

Table B.1: The slopes of residuals of the hold-up of the upper region and the velocity variables are presented for a Benjamin bubble case in a channel. The residuals include Newton's and Picard's method and are measured at $t = 1$ and $t = 5$ $[s]$.

Residual	**Slope at** $t = 1$ $[s]$	**Slope at** $t = 5$ $[s]$
Newton's α_u	-1.949	-1.964
Newton's $u_{s,\beta}$	-2.015	-2.007
Picard's α_u	-0.879	-0.920
Picard's $u_{s,\beta}$	-0.904	-0.953

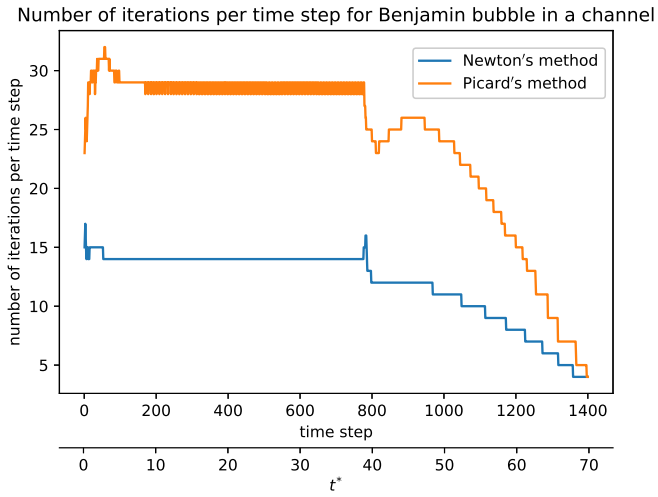

Figure B.3: Number of iterations per time step for a Benjamin bubble in a channel. The iterations of both Newton's and Picard's method are plotted.

B.2. W-shaped channel case

The effective bubble velocity function at the new iteration level $m+1$ can still be approximated by the function at the previous iteration level m for a W-shaped channel. The hold-up function $\mathscr{F}$ multiplied by the interface function $\mathscr{G}_{LH}$ forms the nonlinear term of the slip relation at iteration level $m+1$. Therefore, the terms have to be linearised by Newton's method.

The hold-up function $\mathscr{F}$ in an inclined channel is the same as earlier defined in equation (3.53). The hold-up function remains the same whether pipe or channel flow is seen, unlike what was seen for $\mathscr{F}$ if $\theta = 0$. Here, the flushing of a light fluid displacing a heavy fluid is assumed. Therefore, the interface function $\mathscr{G}$ defined in equation (3.38), is used. $\mathscr{G}$ depends on the hold-up of the lower region, as the gradient of the interface heigth with respect to the axial distance is determined by α_l. This gradient is defined at the $i-\frac{1}{2}^{\text{th}}$ node for a channel as:

$$\left(\frac{dh}{ds}\right)_{i-\frac{1}{2}} = \frac{\left(h_i^* - \frac{1}{2}\right)H - \left(h_{i-1}^* - \frac{1}{2}\right)H}{\Delta s}, \tag{B.17}$$

where H is the channel height and h^* is the dimensionless interface height, which is defined for a channel as:

$$h^* = \frac{A_l}{A} = \alpha_l. \tag{B.18}$$

So, the Biberg approximation is not required to approximate the interface height for a channel flow, which simplifies the linearisation process. Note that a channel and a pipe can be compared by using the hydraulic diameter.

The nonlinear term of the slip relation is approximated by a function g. Function g is defined as:

$$\begin{aligned}
g\left(\alpha_u^{m+1}, \alpha_l^{m+1}\right) &= \mathscr{F}_{i-\frac{1}{2}}^{m+1} \mathscr{G}_{i-\frac{1}{2}}^{m+1}, \\
g\left(\alpha_u^{m+1}, \alpha_l^{m+1}\right) &= g\left(\alpha_u^m + \Delta\alpha_u^{m+1}, \alpha_l^m + \alpha_l^{m+1}\right), \\
g\left(\alpha_u^{m+1}, \alpha_l^{m+1}\right) &\approx \mathscr{F}_{i-\frac{1}{2}}^m \mathscr{G}_{i-\frac{1}{2}}^m + \left(\frac{\partial \mathscr{F}}{\partial \alpha_u}\right)_{i-\frac{1}{2}}^m \mathscr{G}_{i-\frac{1}{2}}^m \Delta\alpha_u^{m+1} + \left(\frac{\partial \mathscr{G}}{\partial \alpha_l}\right)_{i-\frac{1}{2}}^m \mathscr{F}_{i-\frac{1}{2}}^m \Delta\alpha_l^{m+1}.
\end{aligned} \tag{B.19}$$

Both the hold-up function and the interface function have to be partially derivated by the hold-up of the upper and lower region, respectively. The partial derivative of the hold-up function with respect to the hold-up of the upper region for an inclined channel (and pipe) is defined as:

$$\frac{\partial \mathscr{F}(\alpha_u, \varepsilon_1)}{\partial \alpha_u} = \begin{cases} -\frac{6}{\varepsilon_1^3}\alpha_u^2 + \frac{6}{\varepsilon_1^2}\alpha_u, & \text{for } 0 \le \alpha_u < \varepsilon_1, \\ 0, & \text{for } \varepsilon_1 \le \alpha_u < (1-\varepsilon_1), \\ \frac{6}{\varepsilon_1^3}(\alpha_u - (1-\varepsilon_1))^2 - \frac{6}{\varepsilon_1^2}(\alpha_u - (1-\varepsilon_1)), & \text{for } \alpha_u \ge (1-\varepsilon_1), \end{cases} \tag{B.20}$$

and is plotted in Fig. B.4. The partial derivative of the interface function with respect to the hold-up of the lower region is defined for a light fluid flushing a heavy fluid as:

$$\frac{\partial \mathscr{G}_{LH}}{\partial \alpha_l} = \begin{cases} 0, & \text{for} \quad \tan(\theta) + \left(\frac{\mathrm{d}h}{\mathrm{d}s}\right) < -\varepsilon_2 \quad \text{and} \quad \theta < 0, \\ \frac{3}{2}\left(\frac{\tan(\theta) + \left(\frac{\mathrm{d}h}{\mathrm{d}s}\right) + \varepsilon_2}{\frac{1}{2}\varepsilon_2}\right)^2 \cdot \frac{\partial\left(\frac{\mathrm{d}h}{\mathrm{d}s}\right)}{\partial \alpha_l}, & \text{for} \quad -\varepsilon_2 \le \tan(\theta) + \left(\frac{\mathrm{d}h}{\mathrm{d}s}\right) < -\frac{1}{2}\varepsilon_2 \quad \text{and} \quad \theta < 0, \\ \frac{3}{2}\left(\frac{\tan(\theta) + \left(\frac{\mathrm{d}h}{\mathrm{d}s}\right)}{\frac{1}{2}\varepsilon_2}\right)^2 \cdot \frac{\partial\left(\frac{\mathrm{d}h}{\mathrm{d}s}\right)}{\partial \alpha_l}, & \text{for} \quad -\frac{1}{2}\varepsilon_2 \le \tan(\theta) + \left(\frac{\mathrm{d}h}{\mathrm{d}s}\right) < \frac{1}{2}\varepsilon_2 \quad \text{and} \quad \theta < 0, \\ \frac{3}{2}\left(\frac{\tan(\theta) + \left(\frac{\mathrm{d}h}{\mathrm{d}s}\right) - \varepsilon_2}{\frac{1}{2}\varepsilon_2}\right)^2 \cdot \frac{\partial\left(\frac{\mathrm{d}h}{\mathrm{d}s}\right)}{\partial \alpha_l}, & \text{for} \quad \frac{1}{2}\varepsilon_2 \le \tan(\theta) + \left(\frac{\mathrm{d}h}{\mathrm{d}s}\right) < \varepsilon_2 \quad \text{and} \quad \theta < 0, \\ 0, & \text{for} \quad \tan(\theta) + \left(\frac{\mathrm{d}h}{\mathrm{d}s}\right) > \varepsilon_2 \quad \text{and} \quad \theta < 0, \\ 0, & \text{for} \quad \theta \ge 0. \end{cases} \tag{B.21}$$

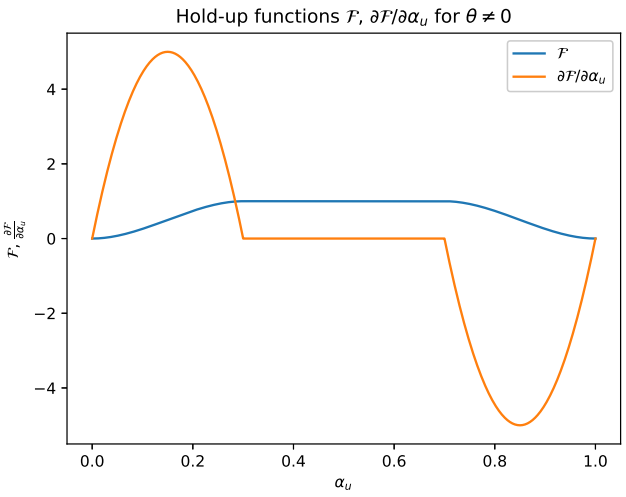

Figure B.4: The hold-up function $\mathscr{F}$ is presented together with its partial derivative with respect to the hold-up of the upper region. These functions are valid for both inclined channel and pipe sections.

The gradient of the interface height with respect to the axial distance at node $i-\frac{1}{2}$ depends on the hold-up of the lower region at node $i-1$ and i, as is shown in equations (B.17) & (B.18). Therefore, the partial derivative of the interface function of (B.21) has two different variants, as the partial derivatives of the gradients of the interface height with respect to $\alpha_{l_{i-1}}$ and α_{l_i} are distinct. These partials are defined as:

$$\frac{\partial\left(\frac{\mathrm{d}h}{\mathrm{d}s}\right)_{i-\frac{1}{2}}}{\partial \alpha_{l,i-1}} = -\frac{H}{\Delta s} \quad \text{and} \quad \frac{\left(\frac{\mathrm{d}h}{\mathrm{d}s}\right)_{i-\frac{1}{2}}}{\partial \alpha_{l,i}} = \frac{H}{\Delta s}. \tag{B.22}$$

The hold-up function also depends on the hold-ups of the upper region at the node $i-1$ and i, due to similar reasons explained in the Benjamin bubble case for a channel flow. Therefore, the linearisation of the non-linear term in the slip relation given in equation (B.19) needs to be extended to include the important nodal dependencies of the hold-ups. The extended linearisation of $\mathscr{F}$ and $\mathscr{G}$ is defined as:

$$\begin{aligned} g\left(\alpha_u^{m+1},\alpha_l^{m+1}\right) \approx \mathscr{F}^m_{i-\frac{1}{2}}\mathscr{G}^m_{i-\frac{1}{2}} &+ \left(\frac{\partial \mathscr{F}}{\partial \alpha_u}\right)^m_{i-\frac{1}{2}} \mathscr{G}^m_{i-\frac{1}{2}}\Delta\alpha^{m+1}_{u_{i-1}} + \left(\frac{\partial \mathscr{F}}{\partial \alpha_u}\right)^m_{i-\frac{1}{2}} \mathscr{G}^m_{i-\frac{1}{2}}\Delta\alpha^{m+1}_{u_i} \\ &+ \left(\frac{\partial \mathscr{G}}{\partial \alpha_{l_{i-1}}}\right)^m_{i-\frac{1}{2}} \mathscr{F}^m_{i-\frac{1}{2}}\Delta\alpha^{m+1}_{l_{i-1}} + \left(\frac{\partial \mathscr{G}}{\partial \alpha_{l_i}}\right)^m_{i-\frac{1}{2}} \mathscr{F}^m_{i-\frac{1}{2}}\Delta\alpha^{m+1}_{l_i}, \end{aligned} \tag{B.23}$$

where the nodal dependencies of the hold-ups for the partial derivative of the interface function are denoted to underline the different variants of the derivatives. As the partial derivative of the hold-up has only one variant, these nodal dependencies are not denoted for the hold-ups of the upper region.

The two partial derivatives of the interface function are plotted in Fig. B.5 together with the interface function as defined in equation (3.38). In this figure, the height of the channel is $H = 0.1$ $[m]$ and the pipe inclination angle is kept constant at $\theta = -40$ [°]. Three-dimensional representations of the partial derivative of the interface function are visualised in Fig. B.6 for the same channel height as just reported.

The fully coupled discretised slip relation for an inclined channel is defined as:

$$\begin{aligned} &\Delta u^{m+1}_{s,u_{i-\frac{1}{2}}} - \Delta u^{m+1}_{s,l_{i-\frac{1}{2}}} - \left(\frac{\partial \mathscr{F}}{\partial \alpha_u}\right)^m_{i-\frac{1}{2}} \mathscr{G}^m_{i-\frac{1}{2}} u^m_{E_{i-\frac{1}{2}}}\Delta\alpha^{m+1}_{u_{i-1}} - \left(\frac{\partial \mathscr{F}}{\partial \alpha_u}\right)^m_{i-\frac{1}{2}} \mathscr{G}^m_{i-\frac{1}{2}} u^m_{E_{i-\frac{1}{2}}}\Delta\alpha^{m+1}_{u_i} \dots \\ &- \left(\frac{\partial \mathscr{G}}{\partial \alpha_{l_{i-1}}}\right)^m_{i-\frac{1}{2}} \mathscr{F}^m_{i-\frac{1}{2}} u^m_{E_{i-\frac{1}{2}}}\Delta\alpha^{m+1}_{l_{i-1}} - \left(\frac{\partial \mathscr{G}}{\partial \alpha_{l_i}}\right)^m_{i-\frac{1}{2}} \mathscr{F}^m_{i-\frac{1}{2}} u^m_{E_{i-\frac{1}{2}}}\Delta\alpha^{m+1}_{l_i} = \dots \\ &\mathscr{F}^m_{i-\frac{1}{2}}\mathscr{G}^m_{i-\frac{1}{2}} u^m_{E_{i-\frac{1}{2}}} - u^m_{s,u_{i-\frac{1}{2}}} + u^m_{s,l_{i-\frac{1}{2}}}. \end{aligned} \tag{B.24}$$

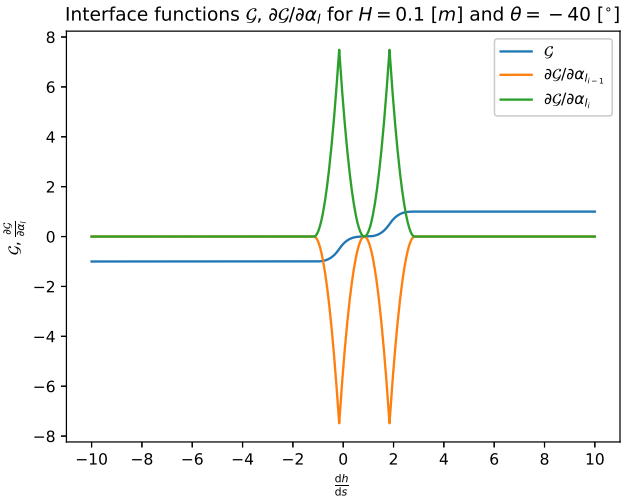

Figure B.5: The interface function $\mathscr{G}$ and its partial derivatives with respect to $\alpha_{l_{i-1}}$ and α_{l_i} are presented for a channel height $H = 0.1$ $[m]$ and a pipe inclination angle $\theta = -40$ [°].

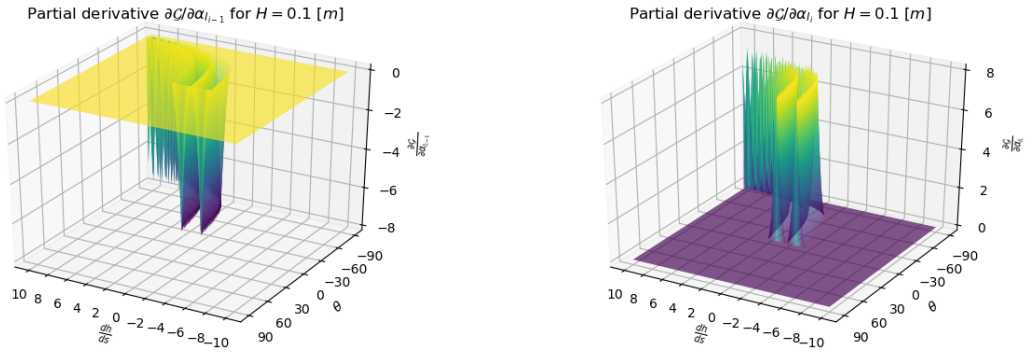

(a) $\frac{\partial \mathcal{G}}{\partial \alpha_{l_{i-1}}}$ (b) $\frac{\partial \mathcal{G}}{\partial \alpha_{l_i}}$

Figure B.6: Partial derivative of interface function G with respect to $\alpha_{l_{i-1}}$ and α_{l_i} in three-dimensional representation.

A similar W-shaped case as described in Section 5.3 is used to investigate the difference between Newton's and Picard's method for immiscible channel flow. The most important simulation properties are summarised as:

- the pipe inclination angles are $\theta = -40$ [°] for the downward-inclined sections and $\theta = -40$ [°] for the downward-inclined sections;
- the channel height is $H = 0.1$ [m];
- the superficial velocity is $u_s = 0.2$ $\left[\frac{m}{s}\right]$.
- the spatial step size is $\Delta s = 0.02$ [m], corresponding to $N = 300$;
- the Courant number is $Co = 0.5$, which leads to a temporal time step of $\Delta t \approx 0.007$ [s];
- the total simulation time is $t_{\max} = 30$ [s].

In Fig. B.7, the residuals of the hold-up of the upper region and the velocity variables are plotted for both Newton's and Picard's method. The residuals are visualised for $t = 1$, $t = 5$, $t = 15$ and $t = 30$ [s] in the W-shaped channel. Remarkably, it is seen in Fig. B.7a that Picard's method locally achieves almost as good as Newton's at $t = 1$ [s]. This can also be observed in the slope of both methods at $t = 1$ [s].

The results of Picard's method show about linear convergence rates for the other time frames, while Newton's method is not able to realise exponential convergence rates for this W-shaped channel case. Therefore, it must be concluded that Newton's method is not entirely correctly applied for this case.

The number of iterations per time step are plotted in Fig. B.8 for Newton's and Picard's method. The average number of iterations per time step for the Newton's linearisation was 13.56 and the average number of iterations per time step of Picard's linearisation was 20.89. As a consequence, the total simulation time for Newton's method was approximately 1.3 times faster than Picard's method for this particular case.

Table B.2: The slopes of residuals of the hold-up of the upper region and the velocity variables are presented for a W-shaped channel. The residuals include Newton's and Picard's method and are measured at $t = 1$, $t = 5$, $t = 15$ and $t = 30$ [s].

Residual	**Slope at** $t = 1$ [s]	**Slope at** $t = 5$ [s]	**Slope at** $t = 15$ [s]	**Slope at** $t = 30$ [s]
Newton's α_u	-1.847	-1.684	-1.777	-1.674
Newton's $u_{s,\beta}$	-1.512	-1.569	-1.500	-1.573
Picard's α_u	-1.649	-0.946	-1.055	-1.112
Picard's $u_{s,\beta}$	-1.423	-0.835	-0.872	-1.115

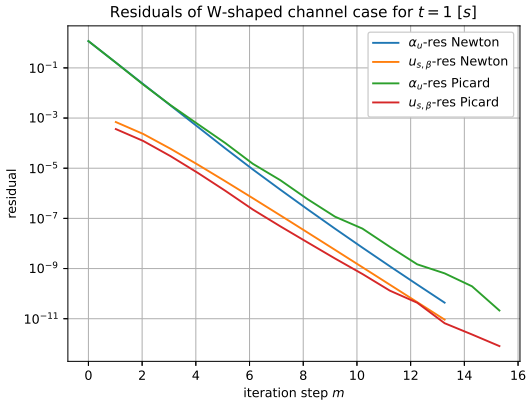

(a) Residual at $t = 1$ [s]

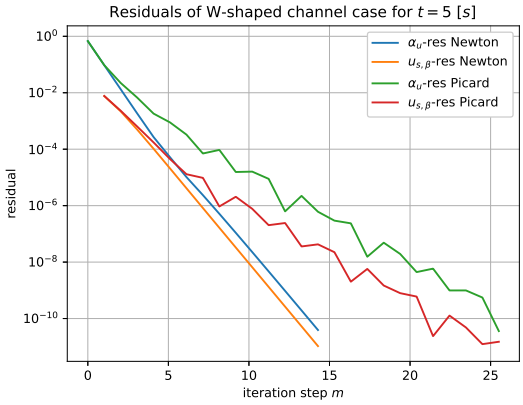

(b) Residual at $t = 5$ [s]

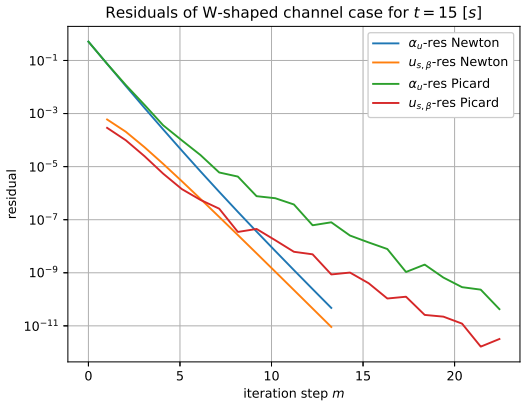

(c) Residual at $t = 15$ [s]

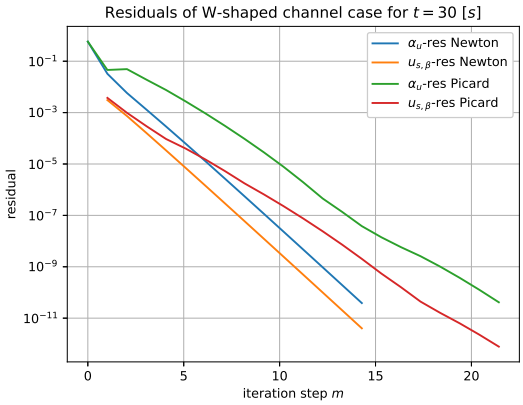

(d) Residual at $t = 30$ [s]

Figure B.7: Residuals of the hold-up of the upper region and the velocity variables are presented for Newton's and Picard's method at $t = 1$, $t = 5$, $t = 15$ and $t = 30$ [s] for a W-shaped channel.

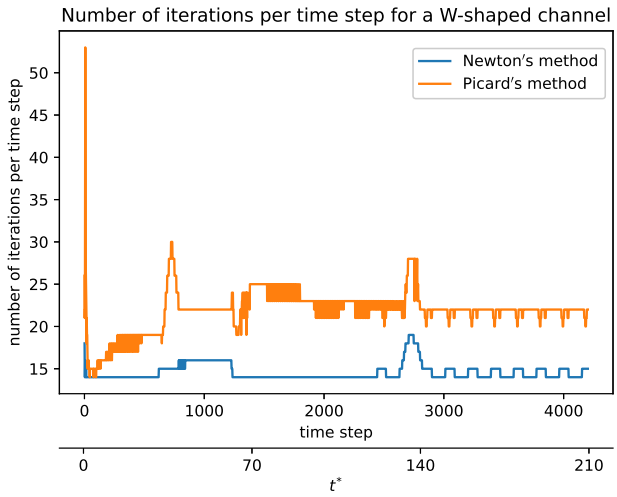

Figure B.8: Number of iterations per time step for a W-shaped channel. The iterations of both Newton's and Picard's method are plotted. Another horizontal axis is added to relate the time step to the physical time.

B.3. Conclusion Newton's method

Newton's method is applied to both horizontal and inclined immiscible channel flow and its convergence rate is compared for a Benjamin bubble case and a W-shaped case to Picard's method. It is found that Newton's method works as an excellement method for linearising the nonlinear terms of the implicit set of equations with immiscible behaviour. Its convergence rates are close to exponential or even exponential and the total simulation time is less than for Picard's method. The local slopes of the residuals evaluated at specific physical times are nearly constant for Newton's method, whereas these equivalent slopes of the residuals of Picard's method can show a wavy behaviour.

The miscible set of equations of (3.68) contains many more dependencies among the flow variables within the model. This implies that the introduction of Newton's method would result in many more linearisations to obtain a fully coupled implicit numerical model than is seen for immiscible channel flow. The shift from channel to pipe flow already makes the linearisation process more difficult. If one takes into account that Newton's method was only 1.3 times faster than Picard's method, while this factor was still 1.9 for the Benjamin bubble case, it must be concluded that the addition of one extra nonlinear term to the slip relation results into a huge number of extra calculations in the coupled solver; i.e. a longer simulation time. As many more linearisations are needed for the miscible model, it is expected that the flow solution is found quicker when Picard's method is applied.

C

CFD simulations Dellecase experiments

As part of the present study, CFD simulations are performed for Dellecase's experimental set-up for all volumetric flow rate cases. [10] Ansys Fluent is used to simulate the different cases. Unlike the Dellecase's simulations of the numerical model, the CFD simulations are executed for the full jumper-like geometry which is represented by a two-dimensional channel.

The CFD simulation case was carefully built up to capture all flow phenomena seen in the fluid-fluid displacement case of the Dellecase experiments. It started by simulating single-phase flow on a small periodic grid to retrieve the correct velocity profile for both laminar and turbulent flow, and this was followed up by a study to investigate the entrance effects of laminar and turbulent flow in a two-dimensional channel untill the flow was fully-developed. Literature research to these types of flow was done and reported. It was found that the k-ϵ model with enhanced wall functions for the near wall treatment gave the best results, which were in line with literature. Therefore, this turbulence model and its near wall treatment method are used in the Dellecase CFD simulations. The simulation results and literature research prior to the Dellecase experiments are not repeated in this report.

As only fluid-fluid displacement is observed within the Dellecase experiments, no multiphase model like Volume Of Fluid (VOF) is required in the CFD simulations. The species model suffices to simulate the Dellecase cases for which only the options: species transport and inlet diffusion are selected. Two different mixtures are computed: (1) methanol - fresh water and (2) methanol and brine 12%. For both mixtures a mass diffusivity of D = 1.6e-09 $\left[\frac{m^2}{s}\right]$ is initiated and the density and the viscosity of the mixtures are respectively determined by the volume and mass weighted mixing rule. In the inlet and outlet boundary conditions, the amount of turbulence is regulated by the specification method: intensity and hydraulic diameter. For the pressure-correction coupling, the coupled solver is chosen together with a Flow Courant number of 10, as it is found to result in faster convergence rates than the SIMPLE pressure-correction coupling method.

As the Dellecase experiments are performed in a pipe, the channel height within the simulations is determined by the definition of hydraulic diameter, which is given in Section 3.3.2. As mentioned, the Dellecase simulations are executed in Dellecase's full jumper-like geometry. Before the simulations are performed, a grid sensitivity analysis is executed in space and time to determine the correct cell size and time step at which all the required fluid-fluid displacement phenomena are captured. The channel height $H = D_H/2$ is used to define the cell size.

The cell size at which grid step independency in space is reached is $\Delta x = \frac{H}{20}$ $[m]$ and $\Delta y = \frac{H}{160}$ $[m]$. The cell size is finer in the y-direction, as it is found that this is necessary to capture the correct amount of stratification in the CFD model. The cell size in x-direction is set relatively coarse, as this size suffices to capture the advection of the fluid particles. By selecting the cell size in x-direction, one should take into account the cell size ratio $\Delta x : \Delta y$ which must be smaller than 10 : 1. When a cell ratio above 10 : 1 is used within the simulations, the flow solution is known to simply follow the direction of the widest cell which may suppress certain flow phenomena. The grid used for the CFD simulation is illustrated in Fig. C.1.

The time step per volumetric flow rate case is determined by the Courant number. It is found that a Courant number of $Co = 1$ with respect to Δx gives time step independent results. In the CFD simulations the Courant number is a function of the superficial velocity rather than the gravitational velocity used in the numerical model. The temporal time step per case is given in Tab. C.1 together with its mixture Reynolds number for both mixtures.

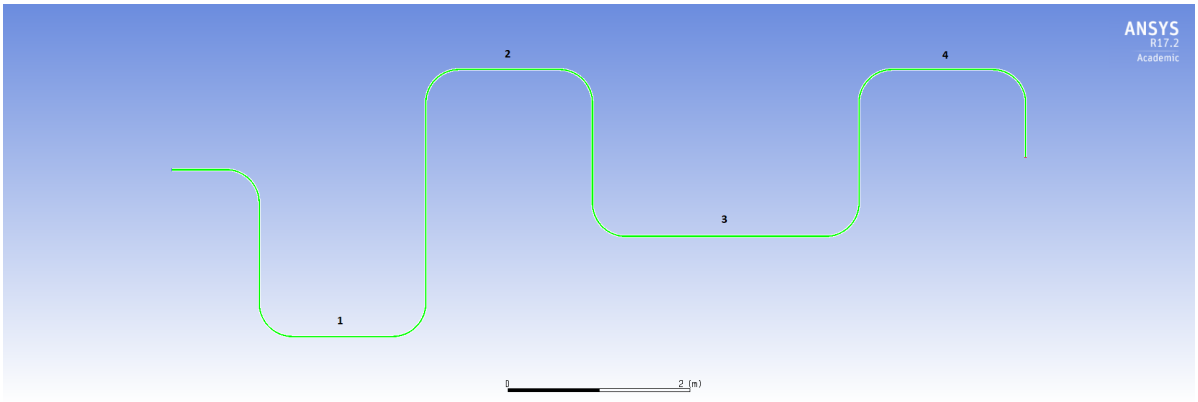

Figure C.1: The grid used for the CFD simulations of the Dellecase experiments is presented.

Table C.1: The mixture Reynolds numbers for both mixtures are given together with the temporal step size per superficial velocity observed in the Dellecase experiments.

Superficial velocity $u_s \left[\frac{m}{s}\right]$	**Mixture Reynolds number Methanol - fresh water** Re_{mix}	**Mixture Reynolds number Methanol - brine 12%** Re_{mix}	**Temporal step size** $\Delta t\ [s]$
0.02	1771.8	1494.6	0.09525
0.06	5135.5	4483.8	0.03175
0.15	12839	11210	0.0127
0.30	25677	22419	0.00635

The goal of the simulations is to obtain methanol concentration profiles similar to the ones reported by Dellecase and to capture stratification effects within the jumper volume. Although the mixture Reynolds number of the lowest superficial velocity cases is not in the turbulent domain, it is chosen to simulate the case with a turbulence model to capture the turbulent outbursts of the fluids.

In Figs. C.2, C.3, C.4 & C.5 the CFD results for the methanol concentration distribution are given for all Dellecase cases of the mixture methanol - fresh water at the dimensionless time $\tau = 1$. Recall that τ is the dimensionless time to quantify the amount of methanol volume inserted at the inlet of the jumper-like geometry, when $\tau = 1$, one full jumper volume of methanol is inserted which corresponds to approximately 34 gallons. The CFD results consist of line-averaged and top- and bottom-averaged methanol concentration data. The top -and bottom-averaged data are only measured at the top and the bottom of the channel at the horizontal sections of the jumper. The line-averaged data covers the averaged methanol concentration along a line which is equal to the channel height and perpendicular to the axial direction of the jumper. The CFD results of the methanol concentration distribution are given for all superficial velocity cases of the mixture methanol - brine 12% in Figs. C.6, C.7, C.8 & C.9. To compare the CFD results, Dellecase's experimental results are included in the figures together with the jumper elevation profile.

It is observed that for the superficial velocity cases $u_s = 0.02$ and $u_s = 0.06 \left[\frac{m}{s}\right]$ good agreement is found for the CFD results and Dellecase's experimental data for both mixtures. The only deviation between the simulations and the experimental results for these cases is that no more stratification is seen for mixture 1 at location 1 and that the stratified layer has almost disappeared for mixture 2 at location 1 as well. For the two larger superficial cases $u_s = 0.15$ and $u_s = 0.30 \left[\frac{m}{s}\right]$ the observed trend between Dellecase's experimental results and the CFD results at $\tau = 1$ along the jumper geometry deviates more. The CFD model predicts that the fresh and salt water has already been flushed out of the first half of the jumper geometry. For $u_s = 0.15 \left[\frac{m}{s}\right]$ a small stratified layer still remains at the horizontal channel section of location 3. For all cases the methanol has reached the outlet at $\tau = 1$.

The CFD stratification effect results for both mixtures are plotted in Figs. C.10. The stratification effects in the jumper geometry are measured by taking the absolute difference between the top and bottom measurement points. The results are plotted as a function of τ and are given at four different locations which correspond to the middle of the horizontal channel sections denoted by the numbers 1, 2, 3 and 4 in Fig. C.1. The results for mixture 1 and mixture 2 are respectively visualised at the left and right hand side of the figure. Likewise, the CFD line-averaged results are presented for both mixtures and the same locations in Fig. C.11.

The results with the stratification effects illustrate that a stratified layer remains at location 1 for the superficial case $u_s = 0.02 \left[\frac{m}{s}\right]$ for both mixtures after one jumper volume of methanol has been inserted at the inlet. The stratification effects of the other cases decrease over time until (almost) no stratified layer is observed anymore at the first location. This is also shown by the line-averaged results. The line-averaged concentration distribution for the cases $u_s = 0.15$ and $u_s = 0.30 \left[\frac{m}{s}\right]$ looks like a Gaussian impulse step function at the four locations. The role of axial dispersion for all cases can also be deduced from the results. The methanol of the case $u_s = 0.02 \left[\frac{m}{s}\right]$ arrives first at every location, while the methanol for the case $u_s = 0.30 \left[\frac{m}{s}\right]$ arrives last at every location. The amount of stratification effects seen in the jumper geometry decreases as the methanol moves further downstream.

C.1. Conclusions for CFD simulations of Dellecase experiments

It is concluded that the CFD results give a good representation of the trend of the fluid-fluid displacement phenomena in a jumper-like geometry. The CFD results of the superficial velocity cases $u_s = 0.02$ and $u_s = 0.06 \left[\frac{m}{s}\right]$ are in good agreement with the experimental results of Dellecase at $\tau = 1$, whereas the CFD results of the superficial velocity cases $u_s = 0.15$ and $u_s = 0.30 \left[\frac{m}{s}\right]$ show more deviations from the experimental results. These deviations are caused by an overestimation of the axial dispersion and mass transfer between the fluids for the higher volumetric flow rates by the CFD model. Besides, the simulations are performed in a two-dimensional channel. This leads to the suppressing of three-dimensional flow phenomena.

The CFD simulations of the Dellecase experiments in the present study prove to be a real improvement of the three-dimensional CFD simulations performed by Dellecase himself [20] where no stratification effects were reproduced in the horizontal section of the jumper-like geometry.

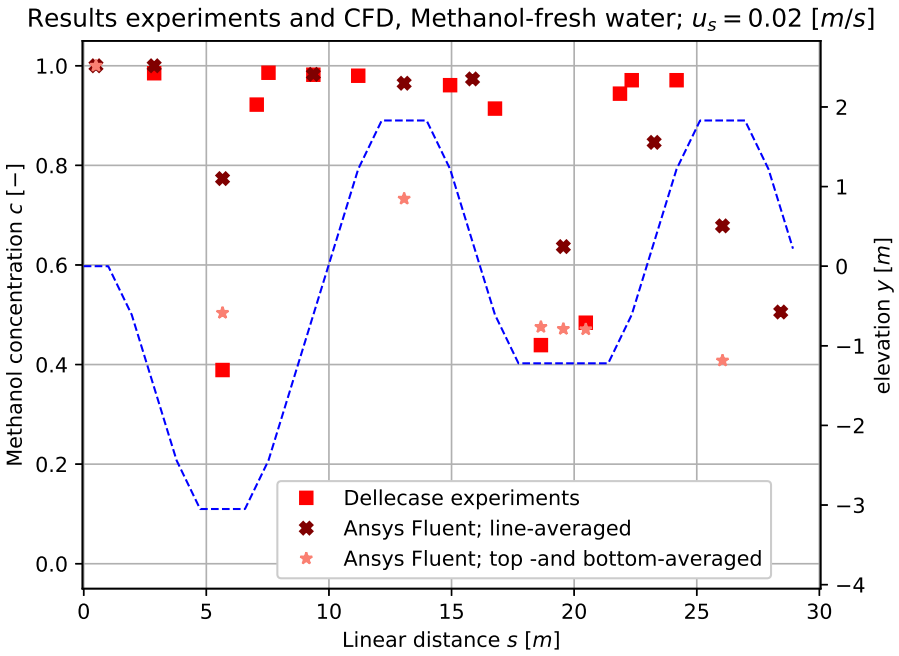

Figure C.2: The CFD results of Dellecase experimental case $u_s = 0.02$ [m/s] are visualised for methanol - fresh water mixture and directly compared with Dellecase's experimental results at $\tau = 1$.

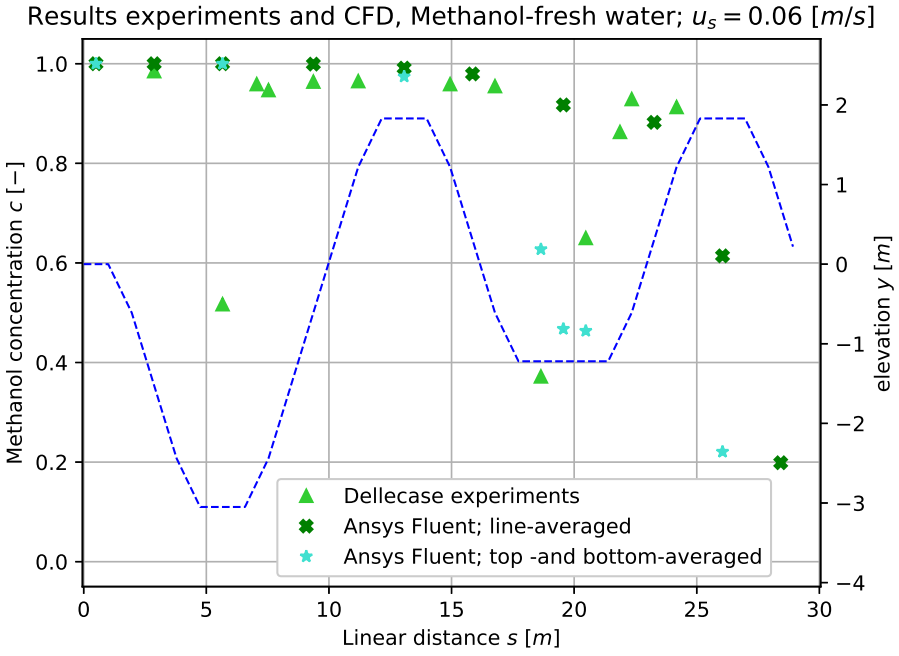

Figure C.3: The CFD results of Dellecase experimental case $u_s = 0.06$ [m/s] are visualised for methanol - fresh water mixture and directly compared with Dellecase's experimental resultsat $\tau = 1$.

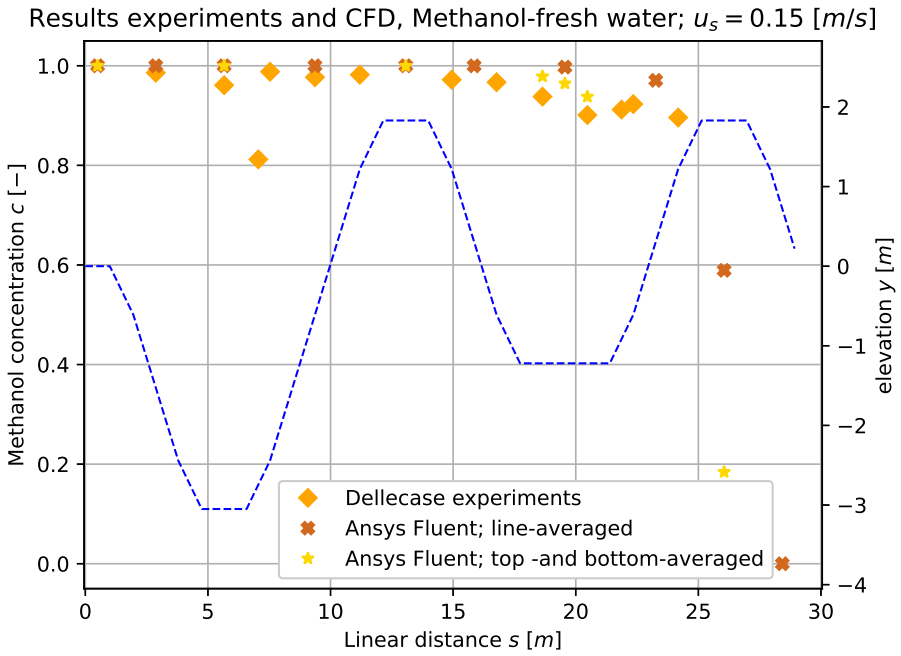

Figure C.4: The CFD results of Dellecase experimental case $u_s = 0.15$ [m/s] are visualised for methanol - fresh water mixture and directly compared with Dellecase's experimental results at $\tau = 1$.

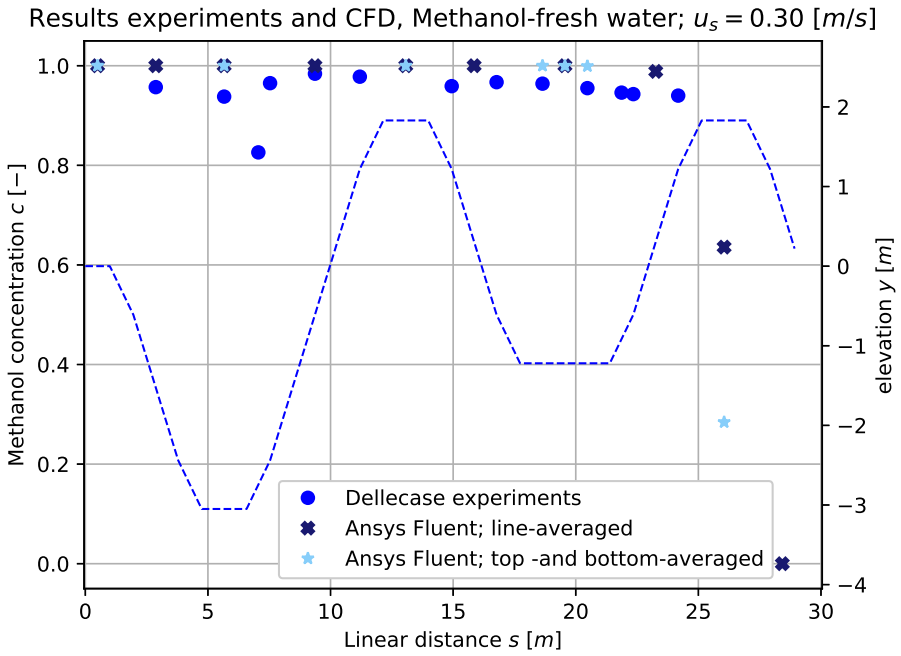

Figure C.5: The CFD results of Dellecase experimental case $u_s = 0.30$ [m/s] are visualised for methanol - fresh water mixture and directly compared with Dellecase's experimental results at $\tau = 1$.

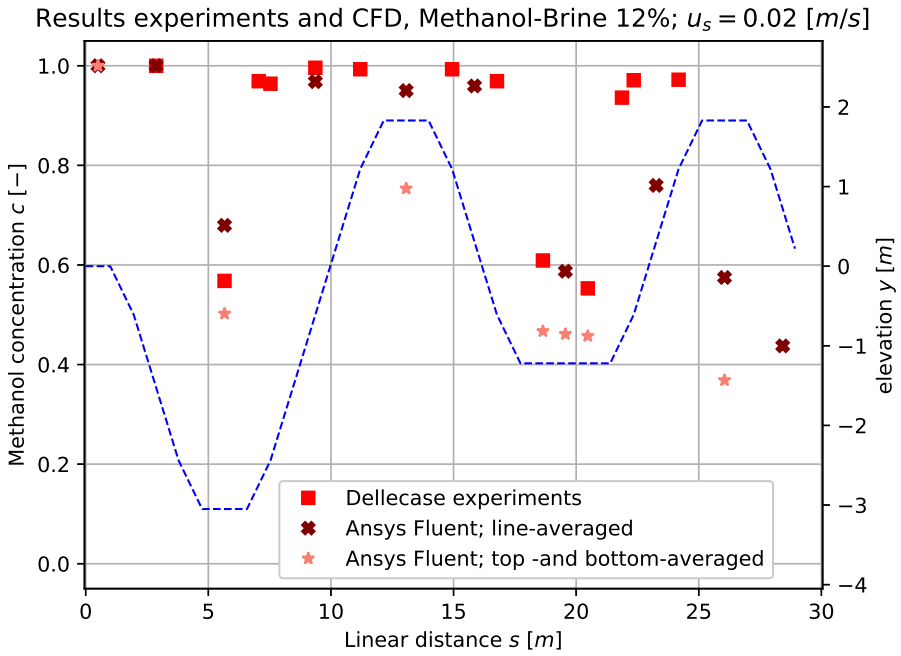

Figure C.6: The CFD results of Dellecase experimental case $u_s = 0.02$ [m/s] are visualised for methanol - brine 12% mixture and directly compared with Dellecase's experimental results at $\tau = 1$.

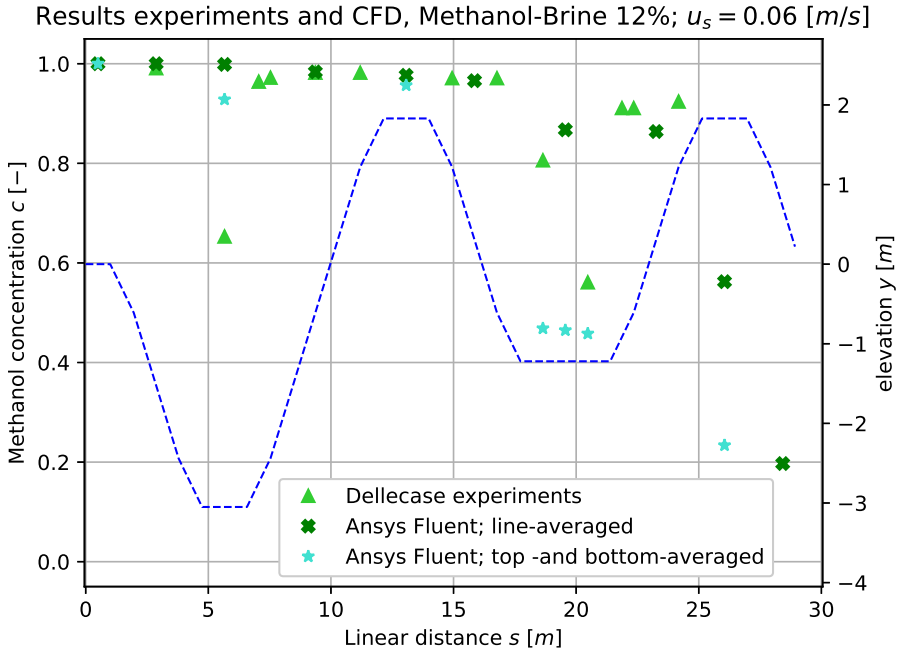

Figure C.7: The CFD results of Dellecase experimental case $u_s = 0.06$ [m/s] are visualised for methanol - brine 12% mixture and directly compared with Dellecase's experimental results at $\tau = 1$.

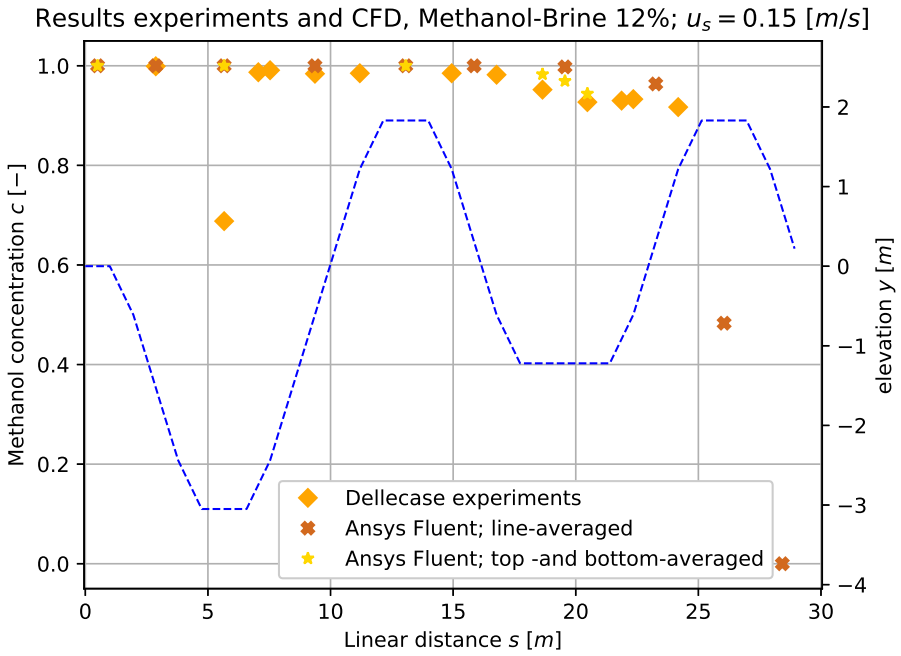

Figure C.8: The CFD results of Dellecase experimental case $u_s = 0.15$ [m/s] are visualised for methanol - brine 12% mixture and directly compared with Dellecase's experimental results at $\tau = 1$.

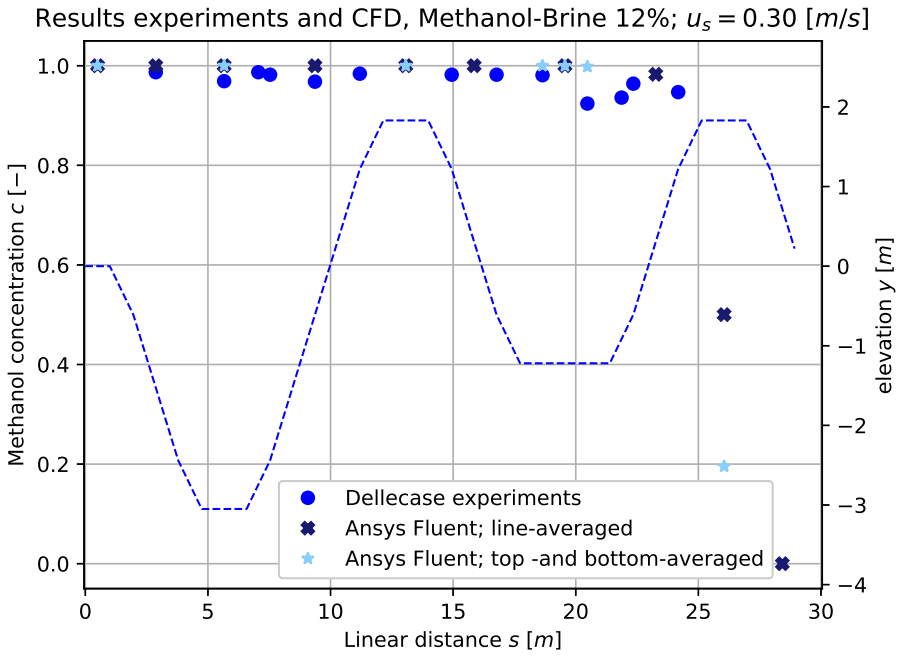

Figure C.9: The CFD results of Dellecase experimental case $u_s = 0.30$ [m/s] are visualised for methanol - brine 12% mixture and directly compared with Dellecase's experimental results at $\tau = 1$.

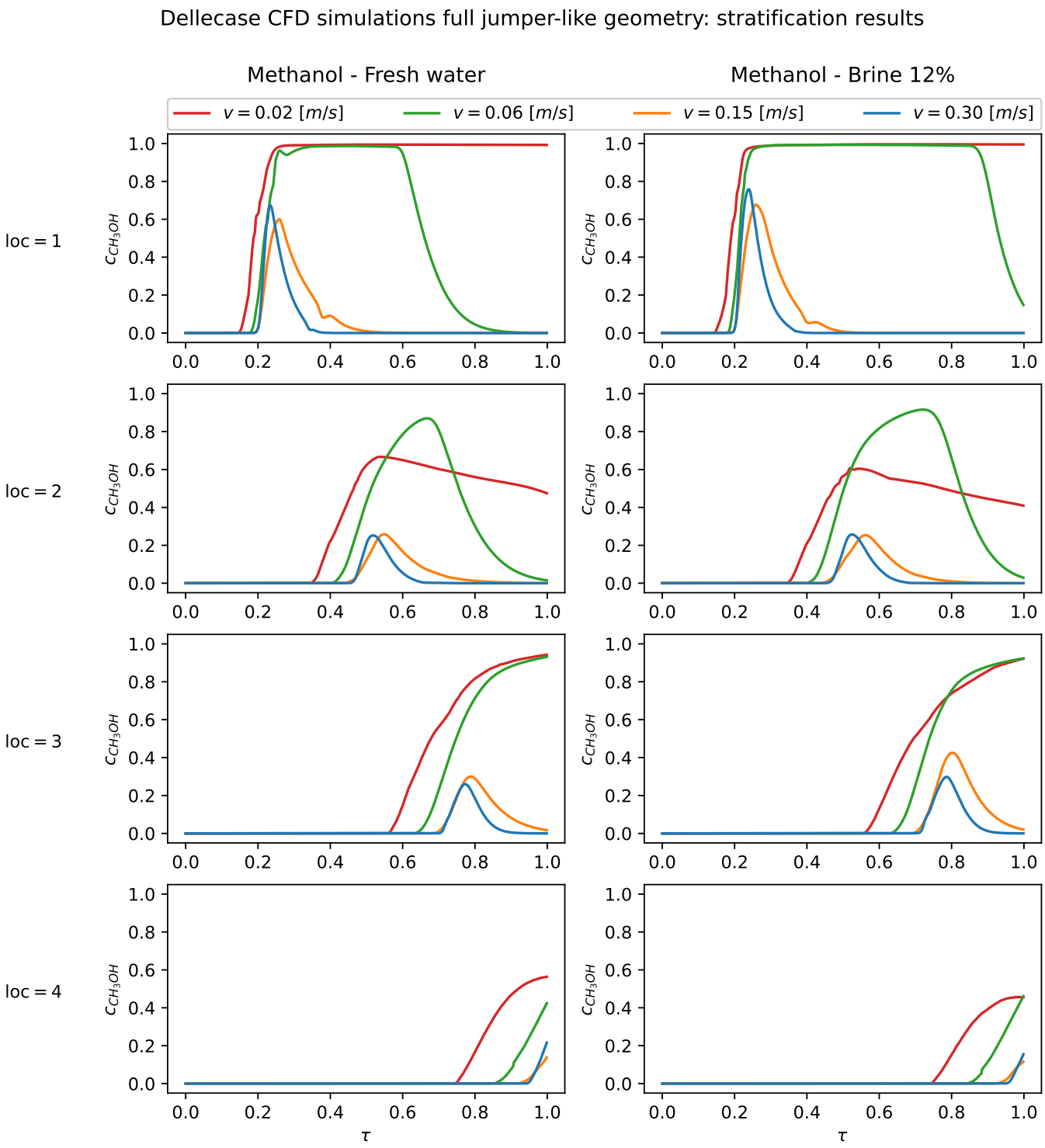

Figure C.10: The results with the CFD stratification effects are presented at the horizontal channel sections of the Dellecase jumper as a function of the dimensionless time τ. The volume fraction of methanol is measured at the top and bottom of the channel, by looking at the absolute difference between these two point the amount of stratification is quantified.

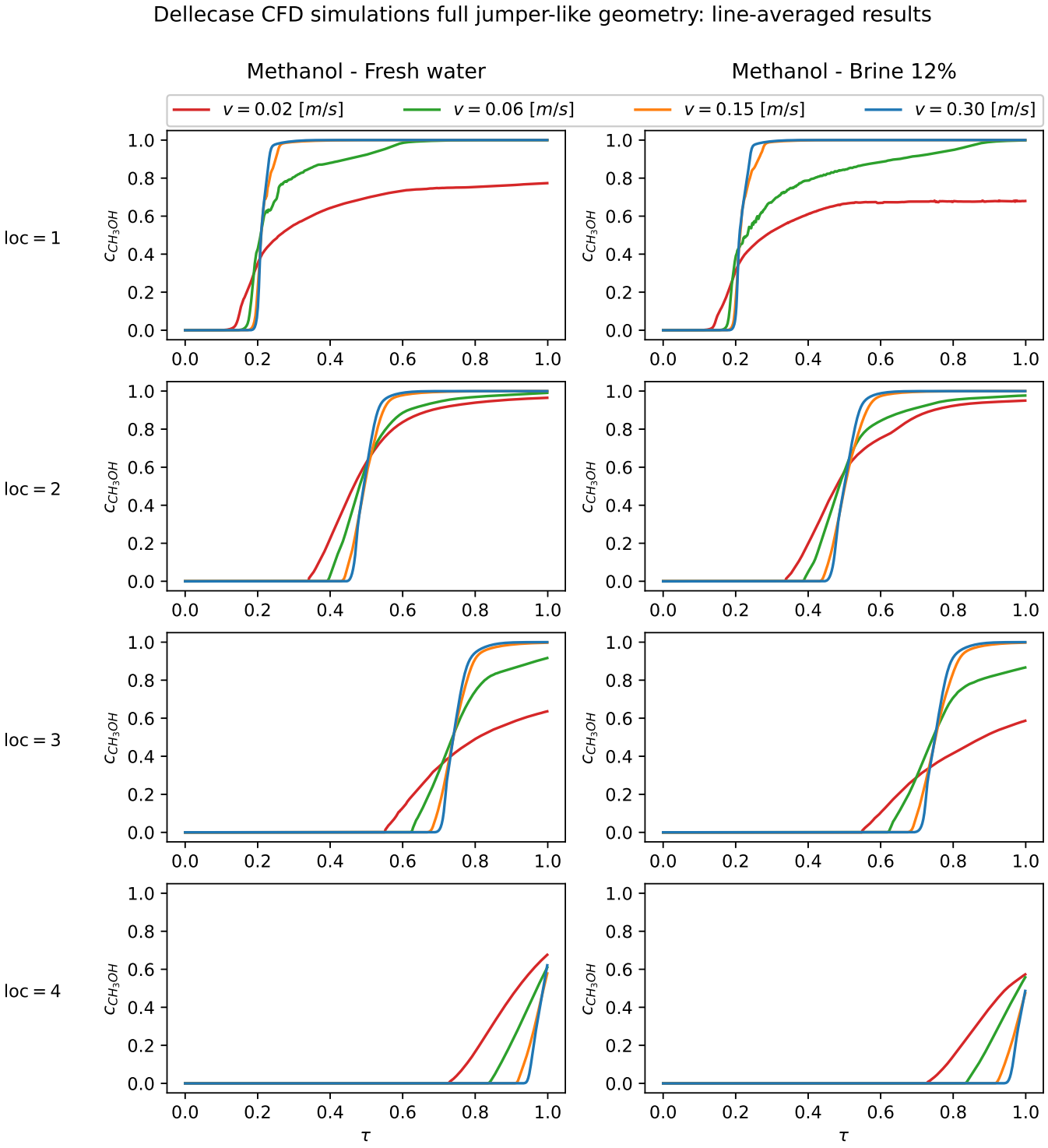

Figure C.11: The CFD line-averaged results are visualised at the horizontal channel sections of the Dellecase jumper as a function of the dimensionless time τ. The line-averaged methanol concentration is measured at a line of length H which is perpendicular to the axial axis of the jumper.